DISS. ETH NO. 15462

# Field experiments and numerical modelling of mass entrainment and deposition processes in snow avalanches

A dissertation submitted to the

## SWISS FEDERAL INSTITUTE OF TECHNOLOGY ZURICH

for the degree of

Doctor of Technical Sciences

presented by

BETTY SOVILLA

Civil Engineer, University of Padova, Italy
born 14.1.1967
in Italy

accepted on the recommendation of
Prof. Dr. Paolo Burlando
Dr. Mohamed Naaim
Dr. Perry Bartelt

2004

# Contents

# Abstract

Natural hazard mitigation strategies underwent a severe test during the winter of 1998/99 when the northern flank of the European Alps was struck by the worst snow avalanche period in over 50 years. Many alpine countries suffered damage and loss of life. In Switzerland, 12 people were killed in Evolène, Canton of Wallis; 38 people were killed in Galtür, Austria. The winter of 1998/99 revealed deficiencies in present hazard mapping procedures.

Hazard maps can be improved by using modern numerical calculation models that predict flow velocities and runout distances of extreme avalanche events. Because the corresponding processes are not well understood, current numerical models contain many simplifications, one of which concerns snow entrainment. Most avalanche dynamics models assume that avalanche mass is constant along the track, hypothesizing that no entrainment takes place. In reality, post-event observations of avalanche paths show that much of the snow cover has been entrained into the avalanche and that deposits are left along the avalanche path.

The aim of this work is to investigate mass entrainment and deposition processes in snow avalanches in order to determine the influence of these phenomena on avalanche motion. The primary goal is to improve hazard mapping procedures.

This work consists of the following parts:

1. *Design of experiments and field measurements.* First, we introduce experimental methods to determine the following: (1) avalanche mass evolution along the path, (2) the mass distribution in the avalanche body and (3) the interaction between the avalanche and the snow cover. The avalanche mass evolution is measured by: in situ measurements, photogrammetric measurements and orthophoto analysis. Avalanche mass distribution is estimated by measuring the avalanche flow depths using flow depth sensors. The avalanche - snow cover interaction, i.e. the entrainment location and the quantity of the entrained snow, is estimated by frequency modulated continuous wave (FMCW) radar. The mass balance of seventeen avalanches was measured.

iv

Experimental data were collected from the Pizzac and Vallèe de la Sionne test sites and at different sites during the catastrophic winter 1998/99. Indices to characterize entrainment and deposition processes in avalanches are defined.

2. *Data analysis and model inference.* A detailed analysis of the seventeen events shows that, on average, these avalanches increased their mass, with respect to the release mass, by more than a factor of four. On average avalanches erode snow down to a depth of two thirds the fracture depth. It is observed that entrainment is primarily controlled by snow characteristics. Snow cover entrainment at the avalanche front appears to dominate over bed erosion at the basal sliding surface. In our modelling approach, the avalanche is considered as a hydrodynamic continuum acting on a solid snow cover. Entrainment processes are formulated in terms of a dynamic stress exerted by the avalanche on the snow cover. It is assumed that the main mechanism responsible for snow entrainment is the impact between avalanche and snow cover, where impacting particles penetrate the snow cover, fracturing snow bonds.

3. *Model implementation and validation.* A one-dimensional, depth-averaged continuum model was modified to consider snow entrainment and different constitutive equations were tested. Flow was described by a Voellmy-fluid flow law and by a modified Criminale-Ericksen-Filbey (NIS) constitutive equation. In addition to the standard input parameters such as release depth, $d_0$, release area, $A_r$, and friction parameters, $\xi$ and $\mu$, the introduction of entrainment into the model requires additional parameters such as snow cover depth, $d_m$, and snow cover strength, $p_{lm}$. Sensitivity tests of the input parameters on model results (e.g. runout distances, velocities and flow depths) were performed. It is shown that in models with entrainment, the range of friction parameters decreases substantially. Since, the additional parameters $d_m$ and $p_{lm}$ can be measured, the model becomes less empirical. A validation of the model was performed by comparing simulation results with experimental data. Results show that non-entrainment models should only be used for the determination of runout distances and, under certain limits, for frontal speeds. Simulations performed without entrainment strongly underestimate flow and deposition heights. The introduction of entrainment helps to reduce these discrepancies and allows a more accurate simulation of the experimental data. The influence of the entrained mass is important for both large and small avalanches.

4. *Recommendations for practical calculations.* To verify the influence of entrainment

in practical calculations, six extreme avalanches from the winter 1998/99 were back-calculated using the Swiss Guidelines. At present, in practical applications, entrainment is not considered and the mass defined in the calculation is always smaller that in reality. Inclusion of entrainment leads to:

a) A better prediction of runout distances.

b) A more accurate determination of flow and deposition depths.

A simple rule for practical calculations that can help to define the correct avalanche mass is suggested. The avalanche mass can be defined as the sum of the release mass $M_{rSG}$ and the entrained mass $M_e$. The entrained mass $M_e$ is calculated by considering an entrainment depth over all the potential entrainment area equal to one half of the fracture depth.

# 1 Introduction

## 1.1 History and motivation

Snow avalanche dynamics became a research issue in Europe after the catastrophic avalanche winter of 1950/51 (SLF. 1951) when over 100 people were killed in Austria and Switzerland. Many of these people were killed in their homes when large avalanches reached the center of alpine villages (Fig. 1.1).



**Figure 1.1:** *Catastrophic avalanche winter of 1950/51. Airolo. Avalanche of Vallascia (photo SLF).*

Since the 1960s. mountain communities in the Alps have experienced considerable growth in terms of both population and economics. This growth resulted in the expansion of many alpine communities. putting them at increased risk from natural hazards. In the confined and densely populated areas of the Swiss Alps. correct land-use planning plays an important role in avoiding incidents and damage from natural hazards. Thus. the

1

concept of an avalanche hazard map, which zones land into different regions depending on the degree of danger, was developed in the 1970s. The official Swiss avalanche hazard map guideline was issued in 1984 (BBF and SLF, 1984) and today, most mountain areas in Switzerland are protected using the rules defined in the guidelines.

Avalanche hazard maps are based on information such as the magnitude and impact pressure of rare avalanche events. The maximum avalanche runout and avalanche pressure are plotted on topographic maps and different hazard zones are created based on these data and represented by different colors (see §1.3). Today, avalanche hazard maps are the primary tool that snow experts use for protection against snow avalanches.

Hazard mapping and calculation procedures have been strongly influenced by developments in computer science, namely numerical modelling.

One of the first avalanche dynamics model appeared in 1955 with the well known and often cited work of Voellmy (1955). Voellmy's model was continuously improved in the 1960s and 1970s, primarily by Salm et al. (1990).

In recent years a new generation of hydrodynamics continuum models (St.Venant models) (Bartelt et al., 1999) have been proposed and since the 1970s there has also been increased activity in the theoretical study of granular flows (for an overview see Savage & Hutter (1989) and Savage & Hutter (1991)) and gravity driven suspension currents (Bonnecaze et al., 1993; Simpson, 1997) with the aim to better describe the avalanche behavior. Presently however, calculation procedures used for the avalanche hazard mapping are still based on hydrodynamic models.

Avalanche prevention methods, developed after the catastrophic winter 1950/51, underwent a severe test during the winter 1998/99 (SLF, 2000). During this winter season, the northern flank of the Swiss, French and Austrian Alps were struck by three periods of heavy snow fall, which resulted in intense avalanche activity. The winter was in many ways comparable to the 1950/51 winter (SLF, 1951).

In Switzerland, between January $27^{th}$ and February $25^{th}$, 1999, three periods of intense snow fall brought a total of 500 cm of new snow in the Alps. Over 1200 destructive avalanches occurred along the northern flank of the Alps. During this period 17 people were killed and the damages were evaluated to be over CHF 600 million.

A post-event analysis indicated that many of the damages and the human lives lost were in places where such large avalanches were never seen or historically documented. The avalanche winter 1998/99 revealed the limits and shortcomings of existing hazard mapping procedures (see Fig. 1.2).

An analysis performed in the Obergoms Valley (Gruber & Bartelt, 2001), in the south-
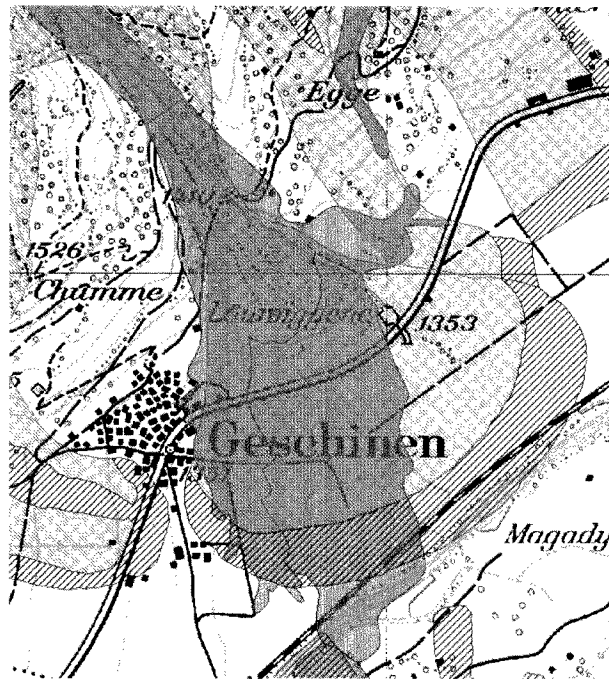
**Figure 1.2:** *An avalanche hazard map with an overlay showing the deposition area of a 1999 avalanche. The avalanche (grey area) exited the limits of the existing hazard map. The red zone represents high hazard level; the blue zone moderate hazard level.*

western part of Switzerland, showed that 80% of the avalanches stopped within the boundaries of the existing avalanche hazard maps. For the remaining 20% of the avalanches three main deficiencies were identifiable:

- The runout distances of powder snow avalanches were underestimated.

- The hazard caused by the occurrence of multiple avalanche events in the same avalanche path were not considered. Multiple avalanche events accumulate large amounts of mass in the deposition zone, changing its topography and influencing the natural lateral spreading. In addition, older deposits left by previous avalanches may smooth the avalanche bed, and diminish the friction along the track.

- Deflecting dams were frequently jumped over by the avalanches. The main reasons were the influence of the multiple avalanche events that transported a large amount of mass in the deposition area but also the deposition depths in general were underestimated.

These three deficiencies underscored the necessity of improving the hazard map quality by focusing snow research on (1) powder snow avalanches, (2) initiation conditions leading to the formation of multiple events and (3) the correct definition of the avalanche mass.

The aim of this thesis is to examine closely one of the questions raised after the 1998/99 avalanche winter: the correct definition of the avalanche mass. That is, what is the starting mass of an avalanche? How much snow does an avalanche entrain? And, how much snow does an avalanche lose during its downward flow?

These questions have puzzled avalanche dynamics experts since Voellmy. In particular, it has rarely been considered how the mass balance of an avalanche influences the flow and avalanche dynamics calculations and, as a result, the procedures used for hazard mitigation.

In this introductory chapter, several concepts are defined in greater detail before addressing the fundamental question of mass balance. Avalanche science basics are explained, including avalanche classification. Then, a review of avalanche dynamics is given focusing on experimental and numerical aspects, and finally a description of hazard mapping procedures in Switzerland is presented.

## 1.2 Avalanche classification and definitions

A snow avalanche is generated when a large part of the snow cover on a steep slope becomes unstable and starts to move downwards. The snow mass moves, due to gravity, towards the valley bottom following a trajectory that is primarily defined by the terrain topography. The avalanche can move in a well defined channel (*channelled avalanche*) or on an open slope (*open-slope avalanche*). Avalanches can move very close to the ground in a motion similar to a water torrent (*dense avalanche*) or might develop a snow cloud that can extend for hundreds of meters above the ground (*powder avalanche*). When the terrain characteristics change and the trajectory slope becomes more gentle the avalanche mass decelerates and forms a snow pile that may reach the height of tens of meters.

In avalanche science, avalanches are classified based on the characteristics of the *starting* or *release zone*, of the transition zone or *flowing zone* and of the *deposition zone*. A full description of the different avalanche typologies is given by the International Avalanche Classification published by the Unesco (1981).

In Fig. 1.4 a local and a global coordinate system are also defined. The *local coordinate system x, y, z* has the $x$-axis aligned with the local main flow direction. The $z$-axis is chosen perpendicular to the local avalanche path surface and the $y$-axis is perpendicular
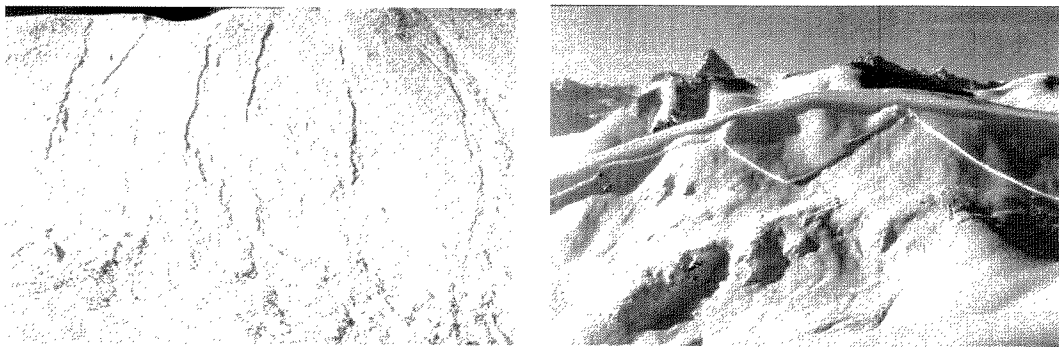
**Figure 1.3:** *On the left a loose snow avalanche: the starting points and the fan-like shapes are typical characteristics of loose avalanches. On the right a slab avalanche: the fracture line is easily recognized, on the contrary the stauchwall is almost erased by the avalanche passage (photos SLF).*

to both $x$ and $z$-axis and oriented in direction of the avalanche width. The local avalanche path slope angle is indicated with $\varphi$.

The *global coordinate system* $x'$, $y'$, $z'$ is an earth-based coordinate system. The coordinates $x'$, $y'$, $z'$ are chosen to represent latitude, longitude and geodetic height of each point.

## 1.2.1 Avalanche characterization in the release zone

Depending on its initiation an avalanche is defined as either a *loose snow avalanche* or a *slab avalanche*. *Loose snow avalanches* are usually confined to surface snow layers or to a limited snow depth and therefore are often small. They start from a point, collect mass progressively as they move downhill and develop into a fan-like shape. These avalanches require dry or wet cohesionless snow (see Fig. 1.3, left).

More hazardous are *slab avalanches*. For these avalanches snow mass is released simultaneously over a large area, involving one or more layers of cohesive snow. When considering the effect of large catastrophic avalanches, avalanche experts typically refer to slab avalanches.

Slab avalanches are easily recognized because they are characterized by a well defined fracture line which clearly confines the release zone. Figure 1.3, right, shows a typical picture of an avalanche slab. In Fig. 1.4 definitions of the different parts of a slab are given. The exact mechanism of failure is not yet well known (Schweizer, 1999) but it is supposed that a slab avalanche originates when a strong layer of cohesive snow is deposited

# 1. INTRODUCTION
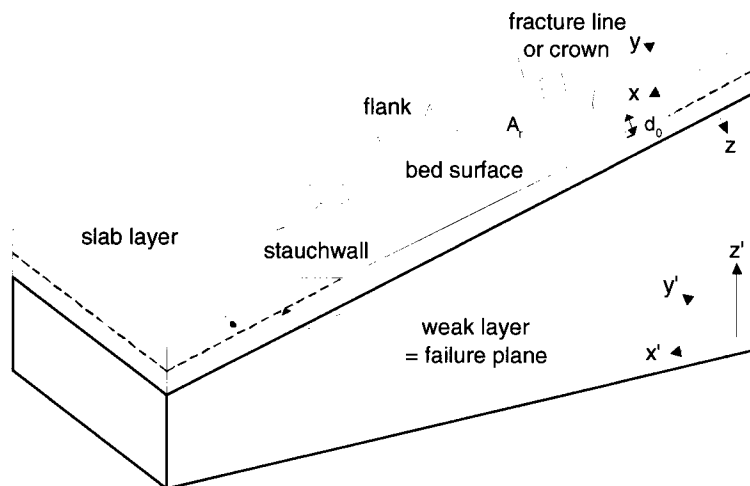


**Figure 1.4:** *Definitions of the different parts of a slab avalanche. A local coordinate system $x$, $y$, $z$ and a global coordinate system $x'$, $y'$, $z'$ are defined. $A_r$ is the release area and $d_0$ the release fracture depth.*

on a weak layer, or when weak bonding between layers exists. When the stress applied to the weak layer exceeds its strength a shear failure takes place. It is believed that local stresses concentrating in the weak layer are responsible for avalanches. Changes in snow strength due to a temperature increase and stress overloads due to new snow precipitation or skiers are the most common causes for avalanche releases (Schweizer et al., 2003).

Failures starting with a local stress concentration extend quickly through the instable area along a *failure plane*. At the upper border of the instable area, where the tension strength of the slab is exceeded, tension failure occurs and the *fracture line* is generated, defining the upper boundary of the slab, or *crown*. After the release, the sharp and well defined fracture line is always visible. The lower limit of the slab, the *stauchwall*, is more difficult to identify because it is frequently eroded by the passing avalanche. The lateral boundaries of the slab are defined as *flanks*.

The *bed surface* is the plane on which the slab flows. The bed surface usually lies immediately below the failure plane and is the surface we can observe after the avalanche release.

The *release fracture depth* $d_0$ [m] is defined as the depth of the fracture at the slab crown measured perpendicular to the terrain surface. The average value (taken from 200 dry slab measurements) is about 0.5–0.7 m with a range from about 0.1 to 2 m (McClung

& Schaerer, 1993). Fracture depths greater than 2 m occur less frequently but have been observed, for example, during the catastrophic winter 1998/99.

The *avalanche release area* $A_r$ [m$^2$] is defined as the area delimited by the crown, the stauchwall and the flanks.

The *avalanche release volume* $V_r$ [m$^3$] is defined as the snow volume delimited by the bed surface, the crown, the stauchwall and the flanks. Typical avalanche volumes range between a few cubic meters to thousands of cubic meters. Referring to the classification given by SLF (1999) small avalanches have volumes $V_r \leq 25\,000$ m$^3$, medium avalanches have volumes $25\,000$ m$^3 < V_r < 60\,000$ m$^3$ and large avalanches have volumes $V_r \geq 60\,000$ m$^3$.

The *avalanche release mass* or *initial mass* $M_r$ [kg] represents the amount of snow contained in the avalanche release volume. The average slab density is about 200 kg m$^{-3}$ with a range from 50 to 450 kg m$^{-3}$. The prevalent range of densities is between 100 and 350 kg m$^{-3}$ (McClung & Schaerer, 1993), i.e. masses can range from a few tons to several hundred thousand metric tons.

The *mean release zone slope* is often used to define the release zone. The most hazardous slab avalanches originate on slope angles between 30° and 45°. They seldom occur below 28°. Above 45° small, frequent avalanches are more common (McClung & Schaerer, 1993).

## 1.2.2 Avalanche characterization in the flowing zone

After the avalanche is released it moves towards the valley bottom. As a result of the impact between the slab and the irregularities of the ground, the slab breaks down to form rounded snow particles. Figure 1.5 shows the particles when they come to rest. The interstitial space is filled by air. The most frequent large avalanches have a powder component composed of a mixture of fine ice particles and air. This cloud surrounds a more dense core of larger snow particles. The different phases coexist as the avalanche moves downslope. In this case the avalanche is defined as *mixed*; Turnbull & Bartelt (2003) give a more detailed discussion.

A schematic view of the different components of a mixed avalanche is shown in Figure 1.6. A mixed avalanche is composed of three main components or layers: the *avalanche core* or *dense layer*, the *saltation layer* and the *powder cloud*.

The *avalanche core* is the densest part of the avalanche and is comprised of rounded particles with a diameter of few centimeters to rounded lumps of several meters. In general, the greater the cohesion in the snow the larger the particles. The particles have an average density between 400–600 kg m$^{-3}$. A *dense avalanche* is an avalanche composed

7
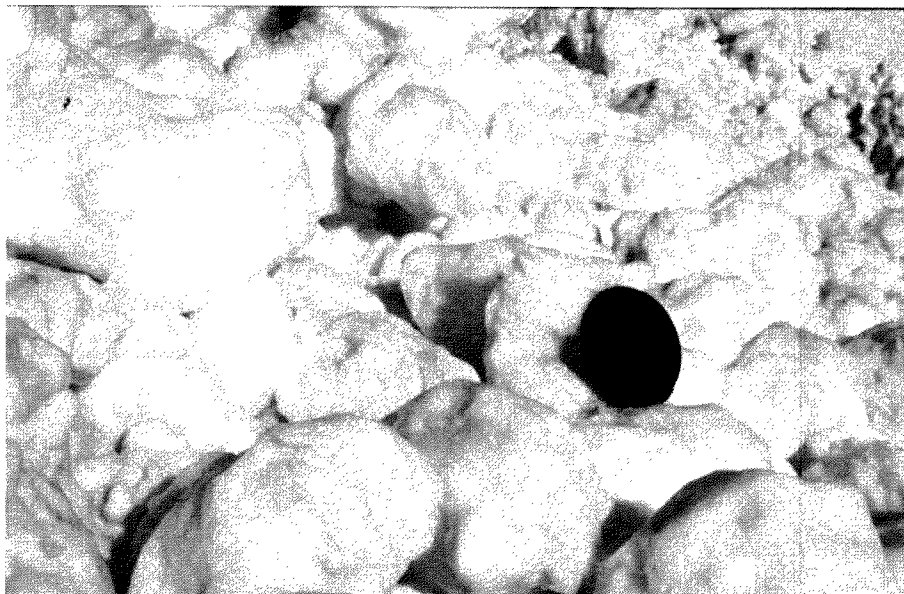
**Figure 1.5:** *Deposit of rounded particles generated by a slab avalanche. Particles of different dimensions are observed. The interstitial space is filled by air. Reference size is provided by lens-cap in the image (photo SLF).*

only of this granular layer.

The motion of the avalanche core is governed by the collisional and friction dynamics of the moving snow particles; the interstitial air does not play a fundamental role. The avalanche core is easily perturbed by irregularities in the terrain.

So far, the *avalanche core density* $\rho$ has been measured only one time by Dent et al. (1998). More numerous measurements concern the deposition density, i.e. the avalanche density after it comes to rest, and density measurements of the undisturbed snow cover.

In section 3.3 measurements of deposit densities are reported. It is shown that the deposit density of dry avalanches is between two and three times larger than the density of the undisturbed snow cover from which the avalanche was generated.

In this work, it is assumed that the density of the avalanche[1] while in motion is 300 kg m$^{-3}$, i.e. considerably higher than the undisturbed snow cover and slightly lower than the deposit density (average maximum density for dry avalanche deposits is approximately 370 kg m$^{-3}$, see Table 3.6) in order to take into account deposit densification of the snow

---

[1]Swiss Guidelines define an average avalanche density while in motion of 300 kg m$^{-3}$. The Swiss guidelines use snow density only to calculate impact pressure; speed and runout distances are independent of snow density.
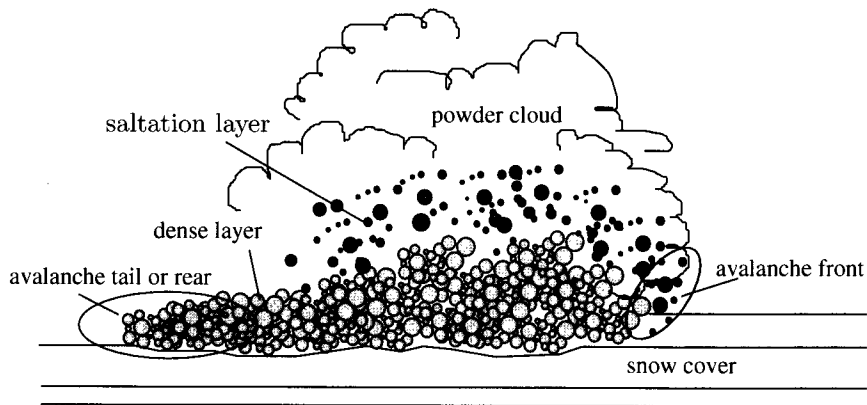
**Figure 1.6:** *A mixed avalanche is composed of three main components: the avalanche dense core, the saltation layer and the powder cloud. Dense avalanches are formed only by the dense layer and powder avalanches only by the powder layer.*

while stopping.

The snow *particle volume concentration* $c_c$ is calculated using the relation:

$$c_c = \frac{(\rho - \rho_{air})}{(\rho_p - \rho_{air})} \cong \frac{\rho}{\rho_p} \qquad (1.1)$$

where $\rho_p$ is the snow particle density and $\rho_{air}$ is the air density. We assume that the particle volume concentration is 50–75% for particle densities of 400–600 kg m$^{-3}$.

The second component of a mixed avalanche is the *saltation layer*, which is thought to form from particles ejected from the dense layer. It is located above and ahead of the dense layer (see Fig. 1.6). The saltation layer contains particles ranging in size from fine-grained snow to snowballs up to about 50 centimeters in diameter.

As for the dense layer, measurements of saltation layer density do not exist. The saltation layer has, however, been identified in videos and analyzing pressure measurements (Schaer & Issler, 2001; Schaerer & Salway, 1980). The density of the saltation layer $\rho_{sal}$ is assumed to vary between 10–100 kg m$^{-3}$ corresponding to a particle volume concentration of 1–15% (Schaer & Issler, 2001).

Particles from the saltation layer or directly from the snow cover are brought into suspension by the airborne shear stress to form the *powder cloud*. Powder clouds and saltation layer may move independently from the dense layer and are less influenced by terrain irregularities. Powder snow avalanches are driven by the higher density of the suspended particles and the dynamics are dominated by the turbulent air flow. Powder

9

avalanches are normally generated from a dry, low density and non-cohesive new snow cover. They can reach heights of hundreds of meters and are frequently observed to have a longer runout distance than the dense and saltation layers. A *powder avalanche* is an avalanche dominated by this component.

In the powder cloud, typical particle sizes range from 0.1 mm to 1–2 mm. The powder cloud is characterized by a particle volume concentration on the order of 0.1–1%. Average powder cloud densities have been estimated at 10 kg m$^{-3}$ or less.

Powder clouds reach very high velocities. During the catastrophic winter 1998/99 measurements performed at the Vallée de la Sionne test site confirm that the largest powder avalanche of the period was able to reach a front velocity of up to 80 m s$^{-1}$ (Gruber et al., 2002).

The velocity is one of the most important parameters characterizing avalanche motion. Two main velocities must be distinguished: the *avalanche front velocity* and the *internal velocity*.

The *front velocity* characterizes the translation velocity of the avalanche front along the $x$-axis direction, i.e. along the main flow direction. Measurements of front velocities are quite common and characterized by a high variability depending on avalanche type, dimension and topographic factors. Typical velocity values for small dense avalanches are in the range of 20–30 m s$^{-1}$. For large dense avalanches containing a saltation layer, the velocity can be as high as 60 m s$^{-1}$. Wet dense avalanches are generally slower and typical velocities range from a few meters per second up to 30 m s$^{-1}$.

Avalanche front velocities can differ from the avalanche internal velocities. Internal velocity distributions are represented by speed profiles. A one dimensional *avalanche speed profile* describes the main velocity component $U_x(z)$ at different depths $z$ above the sliding surface of the avalanche, i.e along the $z$ direction (see Fig. 1.7).

Avalanche speed profiles differ for powder and dense avalanches, which are characterized by turbulent and laminar-like flow, respectively. The determination of the internal speed profile of an avalanche is of fundamental importance since the shear stresses in the flow are related to the velocity gradient. Internal velocities are generally difficult to measure and as a result, very few measurements have been accomplished (Tiefenbacher & Kern, 2003).

To the author's knowledge, the only measurements of vertical velocity profiles in real avalanches are by Gubler (1987) and Dent et al. (1998).
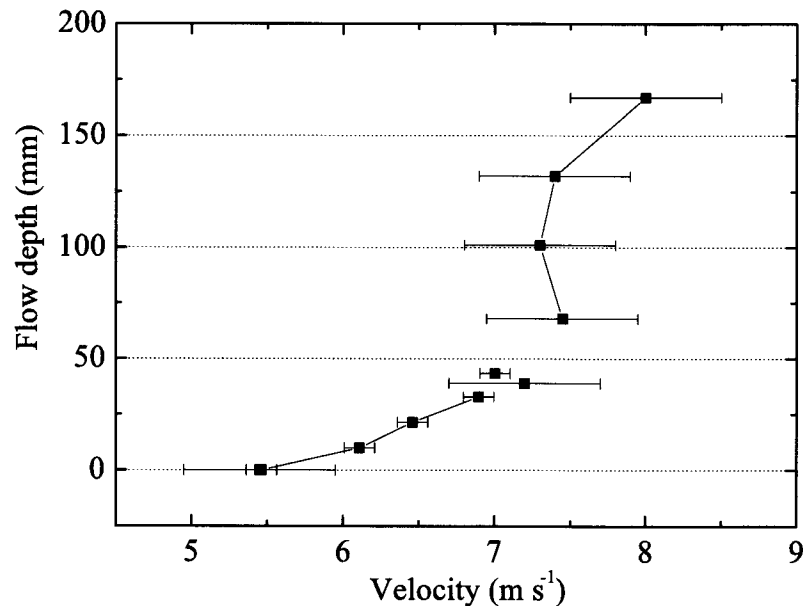
**Figure 1.7:** *Speed profile measured at the Weissfluhjoch snow chute. This velocity profile was measured for a 10 m³ experimental avalanche. Note the existence of a basal shear layer (Tiefenbacher, 2003) above the gliding horizon.*

## 1.2.3 Avalanche characterization in the deposition zone

The dense part of the avalanche comes to rest when the slope angle of the path decreases and the frictional forces are larger than the gravitational forces acting on the avalanche mass. Typical slope angles where avalanches decelerate and stop are 15° or less. However, it has been observed that smaller and slower avalanches may stop on steeper terrain. The area where the avalanche starts to deposit is defined as *deposition* or *runout zone*. Observation of the avalanche path after an event indicates that terrain variations along the flowing zone, such as gullies or small boulders, also create favorable conditions for snow deposition. As a result, the exact transition point between flowing zone and deposition zone is not always easy to identify.

The deposition area of an avalanche is easy to characterize for dense avalanches because of their sharp and well defined boundaries, since the deposit is composed of rounded particles having a dimension from a few centimeters to several meters (see Fig. 1.5).

The deposition area boundaries of powder avalanches are more difficult to distinguish

# 1. Introduction
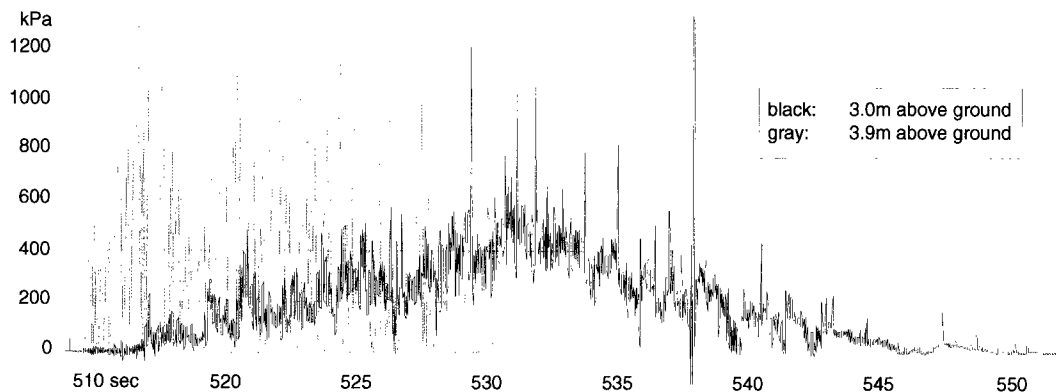


**Figure 1.8:** *Pressure data measured on load plates with diameter 10 cm at the experimental site Vallée de la Sionne, on February $10^{th}$, 1999. The diagram shows the pressure at different heights exerted by a dense avalanche (black line) with a saltation layer (grey line). The saltation layer was present only in the first avalanche part (shorter signal). From (Schaer & Issler, 2001)*

.

because the small rounded particles can be easily confused with the natural snow cover. In many cases, tree branches and rocks can also be part of the snow deposits. Terrain and tree scarring are also used to delimit the runout zone.

The *runout distance* $S$ is defined as the maximum distance reached by the avalanche. The distance is measured from the release zone.

In the deposition zone, buildings and defense structures can interfere with the avalanche motion, deflecting or stopping the avalanche. It is necessary to determine the avalanche impact pressures to dimension the defense structures.

The *avalanche impact pressure* $p$ exerted by a dense avalanche is considered to be proportional to the avalanche core density $\rho$ and to the square of the avalanche velocity $U$ multiplied by a form coefficient $c_f$, with $1 < c_f < 2$:

$$p = c_f \rho U^2 \tag{1.2}$$

Since density measurements do not exist and velocity profiles are very rare, the relation between these parameters has never been verified. Therefore, pressure data have been gathered by direct measurements of impact pressure against obstacles (Schaer & Issler, 2001) with different shapes and dimensions. Impact pressures can vary strongly based on the dimensions and form of the impact surface. Figure 1.8 shows an example of impact pressure measurements taken at the Vallée de la Sionne test site during the catastrophic winter 1998/99. The impact pressures of the dense and saltation layers of the February $10^{th}$ mixed avalanche are shown. A maximum pressure of about 500 kPa was measured in

12

**Table 1.1:** *Avalanche hazard levels defined by the Swiss Guidelines.*

| Zone | Hazard level | Avalanche parameters |
|------|--------------|----------------------|
| **Red** | High | $P_r < 30$ years or $P_r > 30$ years and $p > 30$ kPa |
| **Blue** | Moderate | $30 < P_r < 300$ years and $p < 30$ kPa or powder avalanches with $P_r < 30$ years and $p < 3$ kPa |
| **Yellow** | Low | $P_r > 300$ years or powder avalanches with $P_r > 30$ and $p < 3$ kPa |
| **White** | No hazard | no limits |

the dense part of the avalanche. A maximum pressure of about 1200 kPa, was measured in the saltation layer.

## 1.3 Avalanche hazard maps in Switzerland

Avalanche hazard maps are the most valuable tool that snow experts in Switzerland use as a basis for land-use planning and to develop technical or organizational protective measures against avalanches.

In the avalanche hazard maps the hazard is classified at different levels. In Switzerland, avalanche hazard levels are defined by a specific guideline issued in 1984 (BBF and SLF, 1984) and are defined on the basis of impact force, $p$, and avalanche return period, $P_r$. Four different zones are used to represent the avalanche hazard of an area (Table 1.1). An example of avalanche hazard map is shown in Figure 1.9.

Identification of avalanche hazard involves defining areas that are potentially endangered by avalanches. For this purpose it is necessary to have information regarding:

- Topographical and morphological features of the avalanche area. Topographical information such as path geometry and morphological information such as ground roughness and terrain irregularities are generally obtained from topographical maps, aerial pictures and field observations.

- Meteorological and nivological data of the region.

- Long-term data series of previous events. The analysis of long-term data series can help to define the avalanche characteristics. These data are sometimes contained in

13
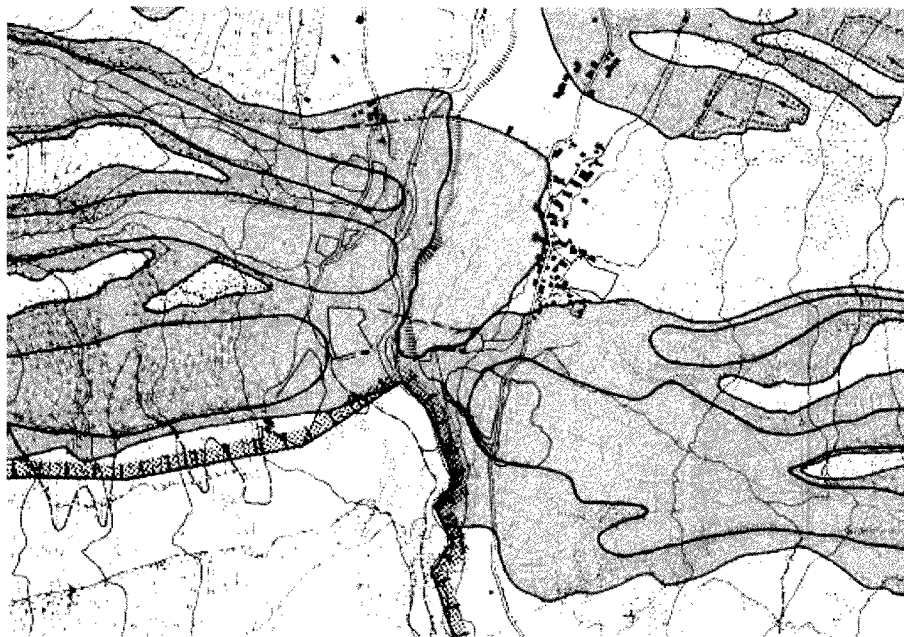
**Figure 1.9:** *Examples of avalanche hazard maps: in the red zone the hazard level is high and new buildings are not permitted. In the blue zone the hazard level is moderate and buildings are permitted only if designed to resist the avalanche forces. In the yellow zone the hazard is low.*

an *avalanche cadastre* which contains information regarding damage caused by previous avalanches, including the meteorological conditions at the time of the event. When this archive is well documented and a long-term series of avalanches is available, it can be used to define the typical dimension, return period and intensity of more extreme avalanches.

An overview of the procedure used for the identification of the avalanche hazard is shown if Figure 1.10.

Unfortunately, avalanche cadastres are generally incomplete and the length of the historical series is not long enough to include the most extreme and dangerous avalanches, which have a high return period (300 years). In addition, avalanche data such as avalanche velocity and avalanche impact pressure are usually not stated, because they are not measured.

When historical information on possible extreme events is missing, tools that predict the behavior of large avalanches are necessary. For this reason many physical, numerical and statistical models have been developed. For an overview, see the SAME European Union project report (Harbitz, 1998). These tools attempt to predict avalanche runout
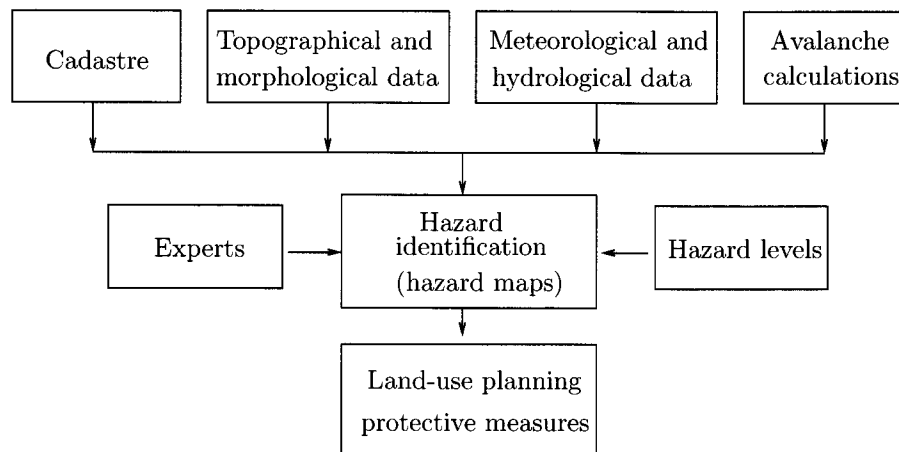
**Figure 1.10:** *Procedure for identification and assessment of the avalanche hazard.*

distances, flow velocities and impact pressures in the runout zone and are a fundamental aid for avalanche hazard identification.

The quality of hazard maps defines the quality of avalanche land planning measures. One possible way to improve hazard maps is to develop more precise and sophisticated methods to simulate the maximum runout distances, impact pressures and velocities of extreme avalanches.

## 1.4 Mathematical modelling of dense avalanches

As concluded from the previous section, an attractive option to improve our knowledge about avalanche hazards is that of building mathematical models which can simulate avalanche movements in space and time. A major concern in this respect is how accurate and representative such models can be made.

Avalanche models can be divided into two main categories: *empirical models*, which are based on statistical or comparative calculation methods, and *dynamic models* which try to reproduce the avalanche motion from initiation to runout. In this work we concentrate only on dynamic avalanche models and in particular on the simulation of dense avalanches.

Dynamic models of dense avalanche flow follow two main approaches: the *center-of-mass* approach where avalanche flow is described by the center of mass of a rigid body along a predefined trajectory and the *hydrodynamical* approach where the avalanche flow

# 1. INTRODUCTION

is described by a deformable fluid-like body.

One of the best-known examples of a center of mass model is the *Voellmy-Salm model* (Salm et al., 1990). Since 1990, in Switzerland, the Voellmy-Salm model has been integrated in the official hazard mapping procedure. It represents one of the earliest attempts to simulate avalanche motion (for both powder and dense avalanches) in a simplified and application-oriented way.

Since the avalanche motion is described only by the avalanche mass center, it is clear that many approximations had to be introduced into the calculation method. Specifically:

- The flow behavior is represented only by the motion of the avalanche mass center. That is the mass distribution around the center of mass, or the internal deformation of the avalanche body, does not enter into the flow physics.

- The mass of the avalanche remains constant along the path.

- The three-dimensional path is simplified into three segments identified along the main flow direction ($x$-axis). The three segments represent the release zone, the flowing zone and the deposition zone. Release and flowing zone have constant slopes. Only in the deposition zone changes of slope angle can be considered.

- Each segment has a constant flow width.

- The equation of motion is solved analytically for each segment considering steady and uniform flow; moreover, the velocity $U$ for each segment and runout distance $S$, are the main outputs of the calculations. As an example, for a laterally confined track the terminal velocity at the bottom of the track is given by:

$$U_p = \left[ \frac{Q}{w_p} \xi (\sin \varphi_p - \mu \cos \varphi_p) \right]^{1/3}, \qquad (1.3)$$

where $\mu$ and $\xi$ are *friction parameters*, $Q$ is the flow discharge, $w_p$ is the avalanche path width in a control section and $\varphi_P$ is the slope angle of the control section.

- The avalanche motion is controlled by the friction parameters $\mu$ and $\xi$.

The fracture depth and fracture width in the release zone and the friction parameters $\mu$ and $\xi$ must be specified.

16

The friction parameters are better termed *calibration parameters*, since they have no clear physical meaning. For example, they cannot be determined in experiments. The parameters are determined by model calibration simulating runout distances of real avalanches (Buser & Frutiger, 1980; Gruber, 1998).

The calibration parameters $\mu$ and $\xi$ significantly influence the results of the calculations. The model is relatively insensitive to the initial discharge rate, given by fracture depth and width. However, the runout distance is roughly proportional to the release depth.

When applied to avalanche tracks having a well defined and simple topography, the Voellmy-Salm model can accurately determine runout distances because it has been calibrated using a large number of observed avalanche runout distances. On the other hand, it is also clear that the model simplifications do not allow the modelling of more complex situations. It is important to stress that, during the catastrophic winter 1998/99, hazard maps that were based on this calculation method performed well. However, it is not surprising that powder avalanches or avalanches that entrained a lot of mass were not well reproduced by the Voellmy-Salm model (Gruber & Bartelt, 2001).

The Voellmy-Salm model is the most famous center-of-mass model used for practical calculation. However, other rigid-body models have been developed worldwide; the two-parameter PCM-model (Perla et al., 1980) in which the avalanche is described as a one-dimensional block of finite mass moving on a path of varying curvature or the McClung (1990) model that introduces concepts from dense granular flows to describe avalanche motion are other typical examples (for a more detailed description see (Harbitz, 1998)).

In recent years, new possibilities provided by the evolution of computer technologies and the increasing knowledge about physical processes in avalanches have permitted the development of new calculation models. These models (Harbitz, 1998) use a hydrodynamical approach and use equations similar to those commonly applied in the simulation of open-channel currents (St.Venant equations). Hydrodynamic models allow a more detailed simulation of observed avalanche events in comparison to the previous center of mass models.

Hydrodynamic models describe the avalanche motion from the release zone to the deposition zone. Mass and momentum equations are numerically solved under the assumption of non-uniform and unsteady flow. A possible set of equations is derived by averaging velocities and densities over the depth. For this reason the models are also called *depth-averaged* models.

Continuum models can be applied to the real avalanche topography and can mathematically describe avalanche motion in one, two or three dimensions, where the basic

17

# 1. INTRODUCTION

dimensionality of the deformable-body models is the number of space dimensions in the dynamics equations.

The avalanche described by a continuum model can flow over a realistic topography generated from high-quality maps. Runout distances and deposit distributions, flow depths along the avalanche path, spatial and temporal evolution of velocities and pressures are the main results from the numerical calculations.

However, as with the Voellmy-Salm model, many approximations are also made, in particular:

- Although the basic equations often include terms to describe avalanche mass variations along the path, few models implement these terms in the numerical solution, i.e. the mass, as in the Voellmy-Salm approach, is constant.

- The snow is considered incompressible, i.e. the flow density is constant.

- Since the equations are depth-averaged, the flow velocity is constant over the flow depth.

The term *quasi two-dimensional model* (Harbitz, 1998) means one dimensional-equation with depth averaging. For a quasi-two-dimensional model additional simplifications are introduced:

- The flow depth is the average flow depth across the avalanche path width.

- The flow width must be defined.

- A single velocity parallel to the slope is calculated.

A detailed description of the characteristic features of the dense flow avalanche models is reported in the SAME model survey report (Harbitz, 1998). Examples of quasi-two-dimensional models are: the NIS model (Norem et al., 1989) where the avalanche is described as a visco-elasto-plastic material, the Hungr (1995) model developed to describe the characteristics of non-steady rapid flowslides, debris flow and avalanches or the AVAL-1d model (Bartelt et al., 1999), developed at the Federal Swiss Institute for Snow and Avalanches Research and since 1999, used actively by practitioners for avalanche hazard assessment (SLF, 1999).

In spite of the large number of models, only few of them are actually used for practical calculations since the limited amount of data available from real events make it hard to evaluate or calibrate them.

18

Particularly evident is the lack of experimental data concerning entrainment and deposition processes, i.e. mass variations in avalanches. Therefore, the avalanche mass in model simulations is frequently assumed to be constant and corresponds to the release mass.

In analytical (center-of-mass) models the assumption of constant avalanche mass does not play a critical role in the prediction of runout distance and flow velocity since calculations are independent of the avalanche mass and it is assumed that the flow is uniform and steady and the discharge is constant.

Conversely, in depth-averaged models the avalanche is described as a continuum where significant variations in flow depth and velocity occur at each instant and for each location along the avalanche path. This means that flow depths and deposit distributions are strongly dependent on the avalanche mass.

Attempts to develop dense-snow models considering entrainment and deposition are shown in Table 1.2 (Barbolini et al., 1998); the main characteristic features are summarized.

It is shown that depth-averaged theories include terms for entrainment and deposition but few models implement these terms.

In the majority of models that implement the entrainment terms in the numerical solution, the entrained mass is not calculated as a function of the model variables like velocity or basal shear stress but must be specified by the user. The scarcity of entrainment models based on a description of the basic physical processes is apparent.

An exception are the models developed by the Moscow State University. The Russian work is not readily accessible. However, in the few accessible publications, the entrainment is systematically introduced into the models. Grigoryan et al. (1967) provides an example of how entrainment has been taken into account.

The entrainment theories behind these models are based on assumptions with little support from documented field data. Nonetheless, it is important to recognize that the Russian researchers observed that the avalanche mass is certainly not constant and that this process substantially influences the model calculation results.

In summary, there is little information on avalanche and deposition processes and this lack in knowledge is obviously apparent in both analytical and numerical calculation methods.

**Table 1.2:** *Summary of characteristic features of dense-snow avalanche models with snow entrainment from Barbolini et al. (1998). The model dimension refers to the number of space dimensions in the dynamics equations; a model dimension of 0 represent a block model; non-integer model dimensions represent averaging over a dimension.*

| Model | Dim. | Parameterization | Snow entrainment |
|---|---|---|---|
| PCM (Perla et al., 1980) | 0 | Coulomb friction $\mu$ $M/D$ for terms proportional to $U^2$ | Lumped into $M/D$ but not resolvable |
| Maeno & Nishimura (1987) | 0 | Coulomb friction $\mu$, viscous term B, turbulent term C | Related to velocity by an exponential function |
| MSU Grigoryan et al. (1967) | 1.5 | Coulomb with an upper limit. Hydraulic turbulent friction $k$. ($U^2$ and $U$ dependent) | Ostroumov (1972) extended entrainment to the whole flow. Entrainment rate given by propagation velocity of compression front, determined by hydrostatic plus dynamic pressure vs. compressive strength of snow cover |
| Brugnot & Pochat (1981) | 1.5 | Dry friction and dynamic drag coefficients | At the leading edge |
| NIS Norem et al. (1989) | 1.5 | Modified Criminale-Ericksen-Filbey fluid | Only theoretically described, not in numerical model |
| Kumar (1994) | 1.5 | Velocity-dependent Coulomb friction, laminar and turbulent drag. Additional equation for internal energy. | Fixed but unspecified entrainment rate along sides of avalanche |
| Hungr (1995) | 1.5 | Various rheological models can be selected. | Assumed to be a constant percentage of the cross-sectional area per unit displacement |

## 1.5 The importance of the avalanche mass balance

As briefly discussed in §1.4 a major limitation of the existing models may come from neglecting the influence of avalanche mass on snow avalanche flow dynamics.

Evidence of entrainment processes is given by deposit observations. Avalanche deposits often contain rock, debris and trees, recording material transport by avalanches. Avalanches are known to be geomorphic agents responsible for abrasion of bedrock and to have a significant erosional effect on debris slope surfaces. Recent research (see e.g.
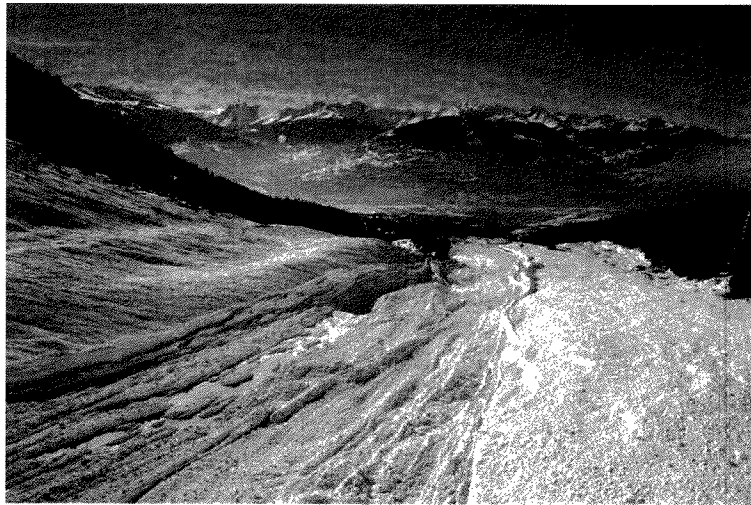
**Figure 1.11:** *A post-event avalanche path at the Vallée de la Sionne test site. February 1999. Part of the snow cover has been eroded and at the same time local or continuous deposits are distributed along the path (Photo SLF).*

Ackroyd (1987), Bell et al. (1990). Gardner (1983)) documenting erosion by wet snow avalanches attests that avalanches can entrain ground material. Terrain erosion occurs principally in the case of ground avalanches in which there is direct contact between the moving snow and the ground surface. It can be expected that if the avalanche moves on the ground all the snow lying above the ground, i.e. the snow lying along the avalanche path. will also be entrained.

Additional evidence of avalanche mass changes is given by surveys of release and deposition volumes of spontaneous avalanches, where deposit volumes are often larger than the release volumes, suggesting snow entrainment and transport during the events. Moreover. post-event observations of avalanche paths often show that while part of the snow cover is eroded. material is also deposited along the path. further indicating mass changes within the flowing avalanche (see Fig. 1.11).

Loose-snow avalanches are another typical example of mass entrainment along the avalanche path: they start from a point and collect mass progressively as they move downhill. developing a fan-like shape (see Fig. 1.3. left) with a growth rate proportional to the path length.

In recent years, interest in avalanche mass balance determination has grown due to the evolution of the calculation methods and the need for experimental data for model validation.

# 1. Introduction

Examples of rough mass balance observations are given by Förster (1999) and Issler et al. (1996). By digging three pits along the avalanche path, the old layer left by the avalanche passage and the new layer of deposited snow were distinguished. By comparing these profiles with the profiles of the undisturbed snow it was possible to determine the entrainment and deposition at particular locations. It was estimated that the avalanches almost doubled their mass from release to runout.

In 1998 the first systematic and extended field measurements of mass balance applied from the release to the deposition were carried out (Sovilla et al., 2001). These measurements were done for small avalanches and showed that an avalanche was able to increase its mass up to nine times the released mass. These measurements demonstrated the magnitude and importance of the entrainment process.

A second attempt to measure avalanche mass balance was performed during the catastrophic winter 1998/99 at the experimental test site Vallée de la Sionne. Using photogrammetric techniques, the release and the deposition volumes of three large avalanches were measured. In spite of the difficulties of applying such a technique to the snow cover, results allowed an estimation of the released and deposited masses of very large avalanches. It was estimated (Vallet et al., 2001) that one of the three avalanches increased its mass up to a factor of twelve in comparison to the released mass.

In Russia, systematic investigation of avalanche release and avalanche deposition masses confirmed that avalanches can entrain enormous quantities of snow along the avalanche track (Bozhinskiy A.N., 2000, personal communication). Unfortunately, these measurements are not published. Neither were detailed observations along the avalanche path or investigations of the physical forces responsible for erosion made.

Despite field observations suggesting entrainment by avalanches, the determination of the avalanche mass for avalanche dynamics calculations is based on estimations of the mass in the starting zone (the mass contained in the volume delimited by the bed surface, the crown, the stauchwall and the flanks). However, when modelling avalanche dynamics, because of the lack of information on the geometric features of the release zone, the release volume is frequently defined by rules related to return period of fracture depths and topographical factors such as average release slope. Depending on the model, these specifications can differ, introducing a high degree of subjectiveness in the calculations.

Since no contribution along the avalanche path due to entrainment or deposition is considered, avalanche masses are implicitly assumed to remain constant along the track. This is clearly an oversimplification given the evidence for erosion and deposition — that is, changes to the flowing mass — along many avalanche paths.

## 1.6 Goals and outline of the study

Since numerical models are being increasingly used as a tool for hazard assessment, it is important to understand what calculation errors are introduced by neglecting mass entrainment and deposition.

This thesis examines closely the erosion and deposition processes in snow avalanches. Field observations will be used to develop entrainment and deposition laws that will be implemented in numerical models that, at the same time, will be used to model avalanche events of variable mass.

In summary this work will involve:

- Designing the measurement techniques, the devices and the experiments to capture mass changes in avalanches.

- Performing entrainment and deposition experiments to collect detailed measurements related to a wide variety of avalanches.

- Analyzing the experimental results.

- Developing a theory of mass entrainment and deposition from the experiments and field observations.

- Developing and validating numerical models to treat mass entrainment and deposition and outline practical calculation methods that account for entrainment and deposition.

- Discussing the implications of the results on avalanche hazard estimation and on the corresponding guidelines.

In Chapter 2, a description of the methods and instruments used to measure the important parameters necessary to understand entrainment and deposition processes in avalanches are presented. Measurement results are discussed in Chapter 3. Chapter 4 aims at identifying the most important physical processes governing mass entrainment and deposition, thus developing the theory. An entrainment model is formulated in Chapter 4. It is used in conjunction with a depth-averaged numerical model. In Chapter 5, calculation and experimental data will be compared in order to validate the model. Finally, a discussion on the most important results and on their possible introduction into calculation guidelines is given.

Seite Leer /
Blank leaf

# 2 Avalanche investigation techniques

## 2.1 Introduction

Previous investigations of avalanche mass balance (Sovilla et al., 2001) have concentrated on the determination of the mass evolution $M(x)$ along the path. These investigations required large and complex field campaigns over widespread areas. Even then, the mass evolution could not always be determined because the measurements were frequently incomplete.

Two other aspects of the mass balance have been overlooked. One concerns the acceleration of the entrained mass (Sovilla & Bartelt, 2002). Entrained material, which is originally at rest, enters the moving mass and is accelerated up to the avalanche speed. This process can be almost instantaneous or can take a certain amount of time. In addition, the entrained snow can be piled up at the avalanche front or distributed along the avalanche length, strongly influencing the flow depth and, as a result, the flow dynamics.

In theory, experimental insight can be obtained by studying the distribution of velocity and density within the avalanche especially while entraining material. In practice, however, such experiments are difficult. Avalanche velocity profiles without entrainment are very rare (Tiefenbacher & Kern, 2003) (Gubler, 1987) (Dent et al., 1998). The same holds for density measurements. However, a representative parameter concerning the avalanche mass distribution is obtained by measuring the avalanche flow depth.

The other often overlooked problem is the interaction between the avalanche and the snow cover. The avalanche can increase its mass by entraining snow along the avalanche path (Sovilla et al., 2001). The mass source is represented by the snow cover lying along the avalanche path. However, the mass of an avalanche cannot increase indefinitely since the mass source is limited. The interaction is governed by the stress applied by the avalanche and the strength of the snow cover. Low-strength snow types are probably easily and almost instantaneously entrained. In contrast, more resistant snow types are slowly and partially entrained. The interaction between the avalanche and the snow cover can be observed, for instance, by means of special radar (see §2.3.2) installed at avalanche

test sites.

In summary, to investigate entrainment and deposition processes the following questions should be answered:

- How large is the mass of an avalanche and how is this mass varying in time and space?

- When is the snow cover entrained into the avalanche and how much snow can the avalanche entrain?

- How is the entrained mass accelerated and distributed inside the avalanche mass?

These problems cannot be resolved with a single measurement technique. A combination of methods must be employed. In this chapter, techniques required to resolve each of these problems are discussed.

In the next pages a detailed description of the conceptual and analytical methods used in this thesis is given.

## 2.2 Determining avalanche mass evolution

### 2.2.1 Conceptual model of data collection in the field

Estimating changes in mass during an avalanche can be carried out by post-event analysis of the avalanche path.

The snowpack consists of horizontal layers with dissimilar features (density, grain morphology, thickness). After the passage of the avalanche the layers are partially or completely eroded, moderately compacted and sometimes covered with the avalanche deposits. Figure 2.1 shows four typical situations observed after the avalanche passage; these are described below:

1. In the first case (see Fig. 2.1, $a$) the original snow cover (left) is composed of two or more different layers $i$ having different depths $d_i$ and densities $\rho_i$. After the avalanche passage (right) the upper layers have been entrained by the avalanche but the characteristics of the underlying layers are unchanged. This situation is typical of a flowing zone where a well defined snow crust between the two layers does not allow the avalanche either to entrain or compress the underlying layer. A similar situation can be recognized in the release zone of the avalanche when the initial slab slides over the underlying snow cover leaving it almost unchanged.

26

2. In the second case (see Fig. 2.1, $b$) a snow layer is partially entrained and moderately compressed by the avalanche passage. The initial layer depth $d_i$ and density $\rho_i$ change to $d_i^*$ and $\rho_i^*$, respectively. This situation is typical of the avalanche flowing zone.

3. The third case (see Fig. 2.1, $c$) is similar to the second case but the avalanche deposit covers the unentrained portion of the underlying snow cover. This situation is also typical of the avalanche flowing zone in areas where the avalanche deposits part of its mass (see Fig. 2.2).

4. In the last case (see Fig. 2.1, $d$) deposition depths are an order of magnitude larger than the original snow cover depth and it is very difficult to distinguish the original snow cover that normally is completely destroyed or compacted by the high pressure exerted by the overlaying mass. This situation is typical of the main avalanche deposition area.

Field measurements made before and after the avalanche passage allow the determination of the snow cover characteristics for all the cases shown in Figure 2.1. When the remaining layers are recognized and the post-event values are collected, it is easy to calculate the erosion using a simple proportion between the original and final values.

While deposition depths, $d_d$, are measured in the field, we estimate entrainment depths, $d_e$, by considering a layer having the initial characteristics density $\rho_i$ and depth $d_i$, which after the passage of the avalanche has a new density $\rho_i^*$ and depth $d_i^*$. If the relation

$$\rho_i \cdot d_i = \rho_i^* \cdot d_i^* \tag{2.1}$$

is fulfilled, then there has been no entrainment and the layer has only been compressed. The mathematical definition of entrainment can be consequently written as:

$$\rho_i \cdot d_i > \rho_i^* \cdot d_i^* \tag{2.2}$$

In this case the avalanche has entrained a snow depth $d_e$ with density $\rho_e$, equal to:

$$d_e = \frac{\rho_i \cdot d_i - \rho_i^* \cdot d_i^*}{\rho_e} \tag{2.3}$$

27

## 2. Avalanche investigation techniques

To measure the avalanche mass balance, measurements are made at numerous cross sections ($n$) along the flow path. The cross sections have a variable spacing ($\Delta x_i$); along each cross section avalanche snow profiles (see §2.2.3) are made to identify the various snow layers and their densities. Similarly, formal full snow profiles (see §2.2.3) are made outside of the avalanche zone in areas corresponding to the release, flow and deposition zones (see Fig. 2.3).

Average measured values for entrainment and deposition along a cross-section are used to calculate the cross-sectional entrainment $As_e$ and deposition $As_d$ areas using the following two relations:

$$As_e = \bar{d}_e \cdot w(x) \tag{2.4}$$

where

$$\bar{d}_e = \frac{1}{w} \int_0^w d_e(y) dy \tag{2.5}$$

is the average entrainment depth along the cross-section and $w(x)$ is the avalanche width.

$$As_d = \bar{d}_p \cdot w(x) \tag{2.6}$$

where $\bar{d}_d$ is the average measured deposition depth along a cross-section.

The average of the cross-sectional entrainment areas of two consecutive sections multiplied by the distance between the sections, $\Delta x_i$, provides the entrained volume in each sector. A similar procedure is used to determine the deposition volume. It is then possible to calculate the corresponding entrained mass $m_e$ and deposited mass $m_d$ since the average densities are known. The avalanche mass $M(x)$ at a specific section along the avalanche path is calculated by adding the difference between the entrained mass $m_{e_i}$ and deposited mass $m_{d_i}$ to the release mass $M_r$ for the $i^{th}$ sector.

The avalanche mass $M(x)$ can then be defined as follow:

$$M(x) = M_r + \sum_{i=1}^{n} (m_{e_i} - m_{d_i}) \tag{2.7}$$

28

before avalanche    after avalanche

a)    $d_2, \rho_2$        $d_e, \rho_e$

$d_1, \rho_1$     $d_1{}^*, \rho_1{}^*$

ground

before avalanche    after avalanche

b)    $d_1, \rho_1$        $d_e, \rho_e$

$d_1{}^*, \rho_1{}^*$

ground

before avalanche    after avalanche

c)    $d_1, \rho_1$        $d_e, \rho_e$

$d_d, \rho_d$    deposit

$d_1{}^*, \rho_1{}^*$

ground

before avalanche    after avalanche

d)                 $d_d, \rho_d$   deposit

$d_1, \rho_1$     $d_e, \rho_e$    $d_1{}^*, \rho_1{}^*$

old deposit    old deposit

ground
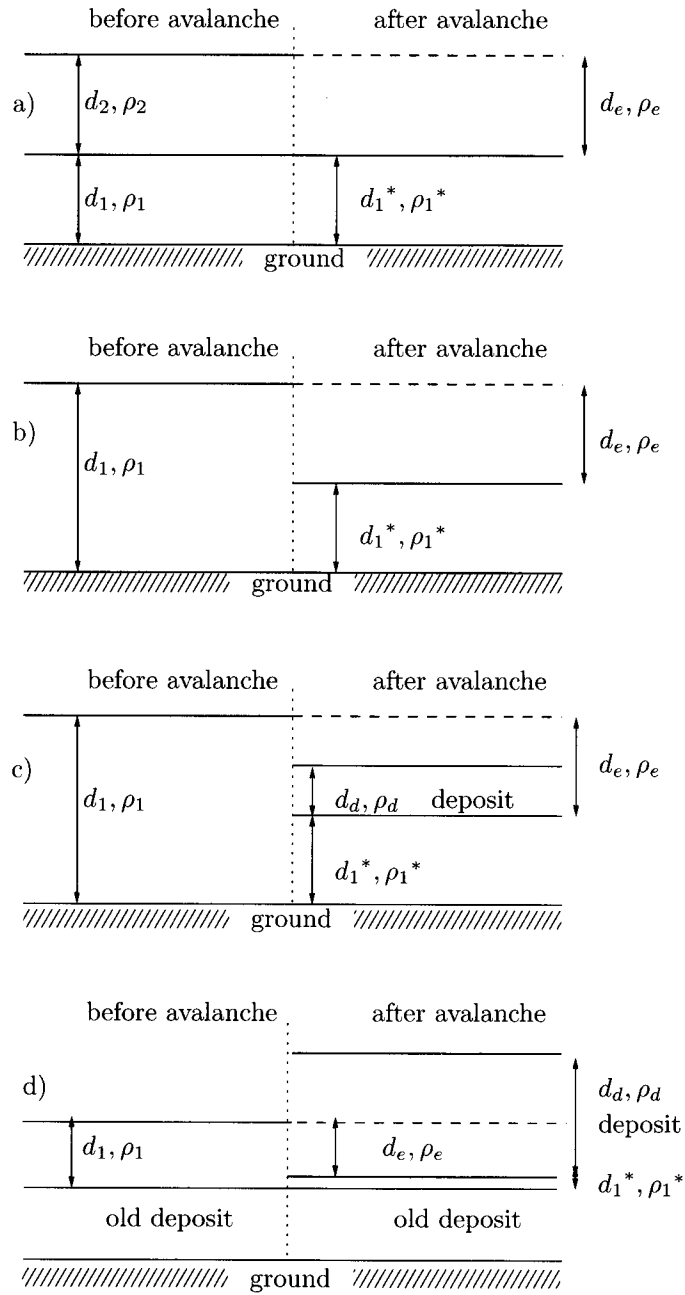
**Figure 2.1:** *Snow layers before and after the avalanche passage. Four characteristic situations are encountered: (a) an entire layer is entrained by the avalanche, (b) a layer is partially entrained and partially compressed, (c) a deposit is left by the avalanche on a partially entrained and partially compressed layer, (d) the deposit left by the avalanche destroyed the underlying layer. $d_e$ and $\rho_e$ are depth and density of the entrained layer; $d_d$ and $\rho_d$ are depth and density of the deposited snow. After the avalanche passage, the initial layer depth $d_1$ and density $\rho_1$ change to $d_1{}^*$ and $\rho_1{}^*$ respectively.*

where:

$$m_{e_i} = \frac{As_{e_{i-1}} + As_{e_i}}{2} \Delta x_i \bar{\rho}_{e_i}, \qquad (2.8)$$

$$m_{d_i} = \frac{As_{d_{i-1}} + As_{d_i}}{2} \Delta x_i \bar{\rho}_{d_i}, \qquad (2.9)$$

$\bar{\rho}_{e_i}$ is the average density of the entrained snow of the $i^{th}$ sector and $\bar{\rho}_{d_i}$ is the average density of the deposited snow of the $i^{th}$ sector.

The integral of the erosion $M_e$ and deposition $M_d$ masses along the avalanche trajectory are given by the relations:

$$M_e = \sum_{\Delta i=1}^{n} m_{e_i}, \qquad (2.10)$$

$$M_d = \sum_{\Delta i=1}^{n} m_{d_i}. \qquad (2.11)$$

## 2.2.2 Measurement techniques

The methods used for determining the avalanche mass evolution $M(x)$ are based on combinations of different techniques which can be divided into three main categories: a) manual measurements in the field, b) photogrammetric measurements and c) orthophoto analysis.

In general, field measurements (Sovilla et al., 2001) allow a more detailed and accurate definition of the avalanche mass but they require a large amount of manual work in very difficult conditions. The avalanche path must be followed from the release zone to the deposition zone and detailed information must be collected all along the path. This analysis is suitable for small avalanches where the volume is a few thousand cubic meters and where safety conditions allow to carry out measurements directly along the avalanche path.

For large avalanches, where the avalanche volume can reach millions of cubic meters, field campaigns that cover the entire avalanche area are impossible (see Fig. 2.2). In this case photogrammetric techniques in combination with field measurements are used. Photogrammetric techniques have two main advantages: measurements can be performed without entering the path and very large areas can be mapped in a very short time. However, only the snow volumes (from the difference between the snow cover surface before and after the avalanche passage), avalanche contours and release and deposition

**Figure 2.2:** *The flowing zone of the Vallée de la Sionne test site. Deposits are visible. Photo taken after the passage of the mixed avalanche of February $7^{th}$, 2003. The large dimension of the site makes it impossible to manually survey all the area. To determine the deposition volumes photogrammetry is used.*

areas can be determined. Information concerning the snow cover such as stratigraphy and densities are necessary to estimate the mass balance. Snow cover characteristics can only be collected by field measurements.

A third method for the determination of the avalanche mass balance is given by the combination of orthophoto analysis and again field measurements. The orthophoto analysis allows determination of the avalanche contours and release and deposition areas. However, as with photogrammetry, stratigraphy and density measurements are needed to estimate the avalanche mass balance. A combination of all three techniques is ideal.

The weather conditions after the avalanche occurrence is one of the most important factors that influence the measurements (Vallet et al., 2001). Bad visibility conditions, which frequently occur, do not allow the access to the field or the application of photogrammetry. In addition, if the measurements are not made soon enough, a successive snowfall can erase the information left by the avalanche passage, making the measurements impossible. Thus, determining the avalanche mass is a difficult task.

## 2.2.3 Field measurement methods and their use

Field measurement methods based on the conceptual model illustrated in §2.2.1 can be divided into the following categories:

1. Determination of the original snow cover characteristics.

2. Determination of the initial mass $M_r$ in the release zone.

3. Determination of the entrainment $m_{e_i}$ and deposition $m_{d_i}$ masses in the flowing and deposition zones.

### Determination of the original snow cover characteristics

As seen in the previous pages, the original snow cover layering and density before the avalanche passage plays an important role for the determination of the avalanche mass balance. However, the original snow cover in an avalanche field cannot be directly assessed prior to an event due to the inherent danger. Instead, measurements can only be performed after the avalanche release on small slopes close enough to the path to be representative of the snow conditions before the avalanche event. The representative undisturbed slopes (Föhn, 1989) must be chosen carefully in order to take into account the spatial variability of the snow cover (Birkeland et al., 1995).

Snow cover characteristics can change from place to place depending on the following factors:

- Topography: aspect, curvature, slope angle.

- Vegetation and soil conditions.

- Meteorological conditions: wind transport, radiation, temperature.

- Elevation: different snow depth and snow characteristics.

Therefore, information on the original snow cover is collected in areas adjacent the starting, flowing and deposition zones where there is no avalanche disturbance and where local variations of snow cover due to topographic, vegetation factors or meteorological influences can be neglected. The influence of elevation is taken into account by determining the original snow cover characteristics at representative places along the avalanche path.

Within the representative original slope area, the snow cover layer sequence and individual layer properties are determined by a *formal full snow profile* (McClung & Schaerer, 1993). This consists of digging a snow pit and recording the following:
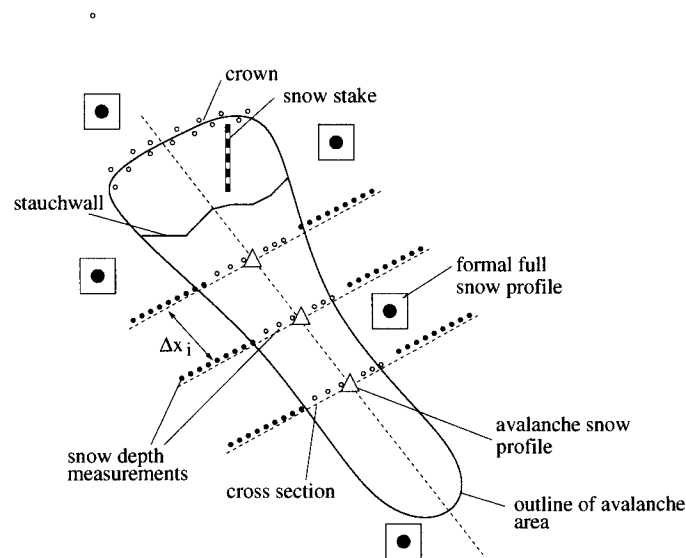
**Figure 2.3:** *Field measurements organization.*

- Observation of air and snow temperatures.

- Definition of the snow layers by variations in snow hardness and grain form.

- Identification of layer boundaries.

- Classification of the snow grain form and size in each layer using a crystal screen and magnifying glass.

- Classification of the hardness of each layer by hand and by ram profiles.

- Classification of the free water content.

- Measurements of the density of the snow layers using snow density sampler.

## Determination of the initial mass $M_r$ in the release zone

The definition of the initial avalanche mass $M_r$ is the second step for the determination of the avalanche mass balance and requires measurements of the release area and the average depth and density of the initial slab.

As seen in §1.2.1 the release area is estimated by defining its boundaries: crown, stauchwall and flanks (see Fig. 1.4). After the avalanche release, this area is identified by a combination of field mapping and photo analysis.

33

The area of the release zone is determined by plotting the observed border on a high-resolution topographic map.

The release area is multiplied by the average slab depth to calculate the release volume. The average slab height, $\bar{h}_0$, is calculated as average of many depth measurements taken:

- Along the crown, as the depth difference between the avalanche bed surface and the original snow surface (see Fig. 2.3).

- Measuring the depth of the layers involved in the avalanche release (determined by a *formal full snow profile*) in representative and undisturbed areas.

- Using special snow stakes, which are anchored to the ground and allow determination of the snow depth before and after the avalanche event even from a remote observation point. These stakes have a yellow-black scale which permits the snow height to be determined from a safe distance with a precision of 5–10 cm.

These data are then averaged to calculate the average slab depth. The deviation of data from the average gives an idea of data quality (see Vallet et al. (2001) for an analogous analysis).

Once the release area and average slab depth are defined, the initial avalanche volume $V_r$ is obtained. When the average density of the slab is defined the initial avalanche mass $M_r$ can be calculated.

The densities of the layers involved in the avalanche are determined by averaging many density measurements taken:

- Along the crown.

- In the layers involved in the avalanche release zone (determined by a *formal full snow profile*) in representative and undisturbed areas.

**Determination of the entrainment and deposition masses in the flowing and deposition zones**

The flowing and deposition zones are surveyed manually. For this purpose several representative locations are chosen along the avalanche track, that correspond to cross-sections oriented perpendicular to the flow direction (see Fig. 2.3). At each cross-section location the following information is collected:

- Flow width.

- Deposit width.

- Snow cover depth measured at 50 cm intervals along the cross-section.

- Avalanche snow profiles.

Special snow profiles are recorded along the avalanche path to determine entrainment and deposition. An *avalanche snow profile* requires a special survey technique and interpretation. On the basis of Fig. 2.1 the following should be carried out:

- Identification of snow layers not entrained by the avalanche.

- Identification of the avalanche deposits and distinction between deposits from different avalanches (new deposit, old deposit).

- Determination of depth and density of each layer or deposit.

- Identification of the layer formed after the passage of the avalanche in the case of new snow precipitation following the avalanche and preceding the field measurements or snow drift deposits.

In most cases the layers can be distinguished by their hardness, density, granulation, color and impurity. If the avalanche history of the site is well known, the correct origin can be attributed to each layer.

The deposition and entrainment quantities are then determined using equations 2.2 to 2.11.

In the next chapter (see §3.3) we show six avalanche events the mass balance of which has been determined using these methods.

## 2.2.4 Photogrammetry and field measurements

Photogrammetry (Kraus & Waldhäusl, 1998) is a well-established method for measuring $x$, $y$, $z$ coordinates of topographic points by means of photography.

Aerial photographs are acquired using specialized airborne cameras, carried by an aircraft or a helicopter. They are recorded in flight lines and each successive photo overlaps the previous image frame by approximately 60–80%. The overlap area between two successive frames allows for a three dimensional stereoscopic vision of the area in common, from which a digital elevation model (DEM) can be created.

If the technique is applied at the avalanche path before and after the avalanche event (Vallet et al., 2001) the snow volume variations along the avalanche path can be measured and the avalanche mass balance determined.

First photogrammetric measurements for determining local snow avalanche volumes were performed by Koelbl (1991). Castelle (1995) tried the same techniques to measure the snow distribution due to wind transport. Since 2001, the technique has been systematically applied at the experimental site Vallée de la Sionne (Vallet et al., 2001; Vallet, 2002) to determine avalanche event volumes with the aim of obtaining the mass balance of an avalanche.

The photogrammetry quality control consists of the determination of its spatial accuracy. Spatial accuracy refers to the location of a single measured point in reference to its true location on the surface of the earth. This accuracy can be tested looking at the displacement of control points[1] from their true location.

Photogrammetric measurements are performed:

1. Immediately before and after a triggered avalanche event (Vallet et al., 2001). The technique is applied to a specific avalanche track before a triggered avalanche release. In this way the DEM of the original snow cover surface is obtained. The same operation is performed after the avalanche event and the DEM relative to the new snow cover surface is obtained. The difference between each point on the two DEM allows the snow volumes (volume difference between original and new surface) to be determined. The fracture depth in the release zone can also be measured.

2. Immediately after a spontaneous event and during the summer. A sudden avalanche release (as during the catastrophic winter 1998/99) prevents photogrammetry measurements before the avalanche event. The measurements are performed immediately after the event and again after the snow melting to achieve the terrain DEM. The difference between each point on the winter and summer DEM allows the snow volumes on the terrain after the avalanche release to be determined. In the winter, if the DEM shows the top and bottom of the crown (see Fig. 1.4) the fracture depth in the release zone can be measured.

---

[1]Ground control points consist of any points whose position $x$, $y$, $z$ are known in a coordinate system and whose image can be positively identified in the photograph. These points should be well defined and well distributed over the image. These form the basis for the control and coordinate assignment through a process of triangulation.
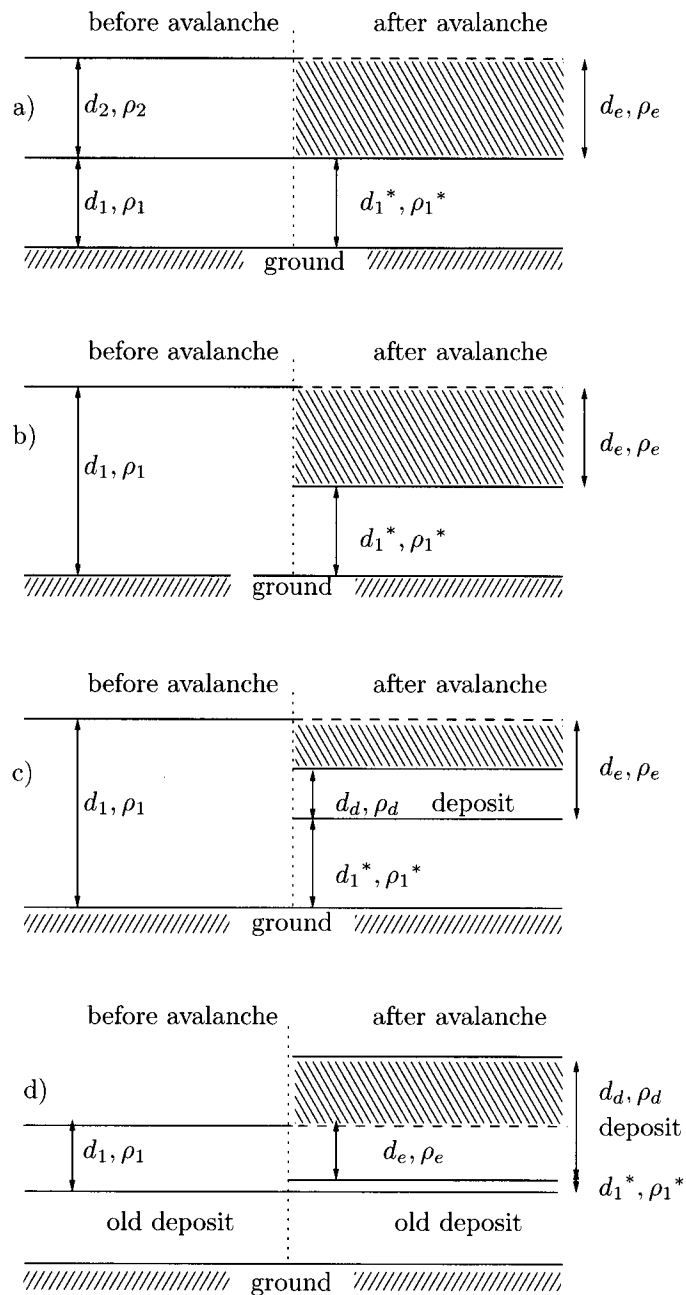
**Figure 2.4:** *The volumes measured by photogrammetry are represented by the hatched area. While in cases a and b photogrammetry allows the direct determination of the release/entrainment snow volumes (represented by the entrainment depth $d_e$), the entrainment and deposition volumes in cases c and d can be determined only after additional extended field measurements. $d_e$ and $\rho_e$ are the depth and density of the entrained layer; $d_d$ and $\rho_d$ are the depth and density of the deposited snow. After the avalanche passage, the initial layer depth $d_1$ and density $\rho_1$ change to $d_1{}^*$ and $\rho_1{}^*$, respectively.*

## 2. AVALANCHE INVESTIGATION TECHNIQUES

Photogrammetric analysis can be combined with field measurements to calculate the masses entrained and deposited by an avalanche. The volumes measured by photogrammetry are presented in Figure 2.4 by dashed areas. Each case is analyzed in the following manner.

1. Case $a$ and case $b$ are more typical for the release zone and the flowing zone where material is entrained. Photogrammetry allows the determination of the released and entrained volumes.

2. Case $c$ corresponds to the flowing zone where material is both entrained and deposited. This is the most difficult case to measure using photogrammetry. The entrained volume cannot be measured because part of it has been filled by deposition material. In addition, the deposition volume can not be measured because the position of the interface between the deposition material and the snow cover is not visible. Only extended field measurements allow the determination of the avalanche mass balance.

3. Case $d$ corresponds to the deposition zone where not entrainment occurs. Deposition depths are generally an order of magnitude larger than entrainment depths. As a result, the difference in volume due to the entrained mass can be neglected and photogrammetry used to estimate the deposition volume. To determine the deposition mass, the deposit density $\rho_d$ should be measured in the field.

In summary, photogrammetry is a useful technique for measuring release and deposition volumes. However, density measurements are required to determine entrainment and deposition masses. In particular, photogrammetry is less useful along the avalanche flowing zone, where large-scale field measurements are required to calculate the entrained and deposited masses.

The accuracy of the avalanche mass balance decreases if the technique is applied only after the avalanche event and during the summer. In this case each avalanche data set must be evaluated to understand whether mass balance measurements are possible.

The use of photogrammetry for the determination of snow volumes still faces some technical problems (Vallet et al., 2001):

- An undisturbed new snow cover has very little color contrast making precise measurements of snow cover volumes before an avalanche release very difficult.

38

- Aerial photographs should be taken immediately after the event in order to record important information. Weather conditions may render the collection of accurate information difficult.

- The ground control points are very difficult to identify since points have to be found that are visible even after a heavy snowfall period.

### 2.2.5 Digital orthophotos and field measurements

Orthophotographs (Kraus & Waldhäusl, 1998) are digital images that can be integrated into a geographic information system allowing direct measurements of distance, areas, slope angles and position of specific features. Here, we use them to determine the post-avalanche topography including release zone, flowing zone and deposition zone boundaries.

Orthopothos are obtained by making geometric corrections to scanned aerial photographs taken immediately after an avalanche event. Aerial photographs are acquired using specialized airborne cameras, carried by an aircraft or a helicopter.

As with photogrammetry, the quality control of an orthophoto consists of the determination of its spatial accuracy. Spatial accuracy refers to the location of a single pixel on the photo in reference to its true location on the surface of the earth. This accuracy can be tested observing the dislocation of the control points in comparison to their true location.

To determine the avalanche mass all information concerning the avalanche snow cover such as layer depth, stratigraphy and density but also the average depth of the slab in the release zone, should be collected by field measurements. When the avalanche is small, this combination of techniques is ideal for determining the avalanche mass. However, for medium to large avalanches the difficulty of collecting enough and precise field data does not allow an accurate evaluation of the mass balance.

## 2.3 Internal avalanche processes

After the snow cover is entrained, it is accelerated up to the avalanche speed. How the entrained mass is accelerated and how it is distributed along the avalanche length could be investigated by measuring internal velocities and densities in avalanches.

However, internal speed and density profiles are difficult to measure. Various attempts performed on real avalanches have not provided definite results (Issler, 2003). Due to the difficulties of performing experiments on real avalanches (the only known avalanche

speed profiles were measured by Gubler (1987) and Dent et al. (1998)) the internal flow structure is investigated by studying reproducible avalanche-like snow flows (Tiefenbacher & Kern, 2003). The majority of these experiments is performed using granular materials in a laboratory chute (Nishimura & Maeno, 1989; Tiefenbacher & Kern, 2003). However, experiments taking entrainment into account and particularly the influence of the entrained mass on the definition of the speed profiles, have never been performed. The mixing process between avalanche snow and entrained snow should modify the internal velocity profiles, at least for the region inside the avalanche where the entrainment takes place modifying the entire mass distribution process.

If internal processes cannot be measured, a representative parameter of the avalanche mass distribution is obtained by measuring the avalanche flow depth distribution. Comparison of the avalanche snow depth distribution at different locations along the avalanche path (see Fig. 3.5) indicates whether the snow is piled up at the avalanche front or is distributed along the avalanche length.

We have performed measurements using two techniques: flow depth sensors and Frequency Modulated Continuous Wave (FMCW) radar. These techniques are further described in the following sections.

## 2.3.1 Flow depth sensors

Flow depth sensors measure the avalanche flow height through contact with the moving snow mass. They consist of a series of mechanical and/or piezo-electric switches set at constant intervals along a pylon, which is placed in the path of an avalanche (see Fig. 2.5).

The piezo-electric switches consist of a small element of piezo-electric ceramic. Under pressure the element distorts its crystal structure in such a way as to create a voltage between its surfaces, which can be amplified and interpreted as a switching signal. The presence of this switching signal depends on the actuating force and the applied time of the force. Piezo-electric switches are characterized by a good reliability due to the high robustness in harsh conditions. They do not have moving parts. When the avalanche reaches the measuring pole, the sensors provide a voltage that is sampled with a defined frequency. At each time the position of each pressed sensor is known. In this way it is possible to record information about avalanche flow depth and pressure discontinuities inside the flowing mass. The pressure discontinuity, however, can not be related directly to a density or velocity distribution.

The mechanical toggle-switches (see Fig. 2.5) are less robust in harsh conditions since
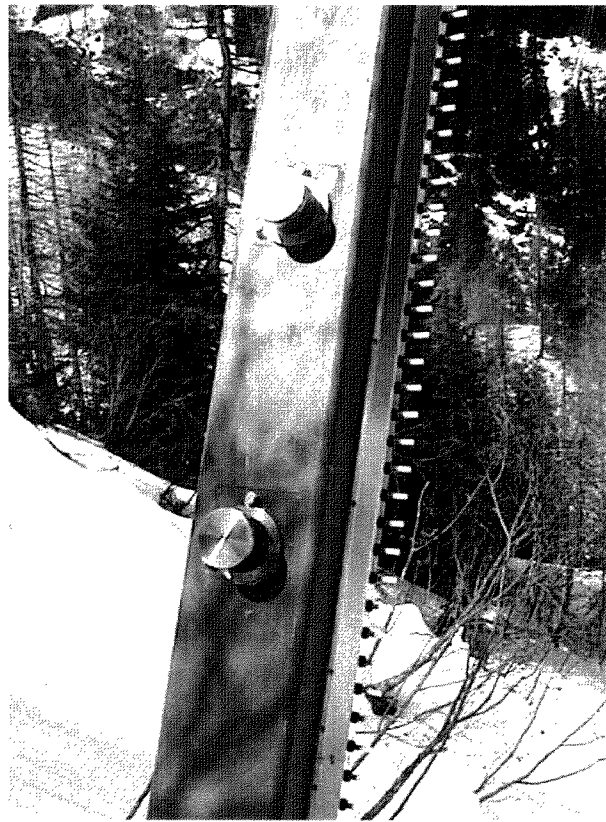
**Figure 2.5:** *At the Pizzac experimental site, Italy (see §3.2.1), mechanical sensors have been installed to check the flow height through contact with the moving snow mass on the side of 5 m high pylons. They consist of a series of mechanical switches set at intervals of 5 cm along the pylon.*

their moving parts can break easily under the pressure of a large avalanche. However, these sensors are cheaper than the piezo-electric sensors and they provide very good measurements in experiments with small avalanches where the exerted pressure is not large.

When the avalanche reaches the toggle-switches, the highest sensor affected by the avalanche provides a voltage that is sampled with a defined frequency. At each time the position of the highest affected sensor is known. In this way it is possible to record information about the maximum avalanche flow depth. Typical results are shown in Fig. 2.6.
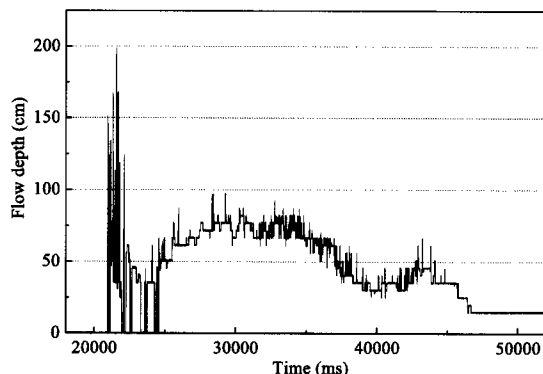
**Figure 2.6:** *The output of the mechanical switches at the Pizzac experimental site, Italy. At each instant the maximum flow depth is recorded.*

## 2.3.2 FMCW radar

FMCW (Frequency Modulating Continuous Wave) radars (Gubler & Hiller, 1984) are buried in the ground at points along the avalanche track. Each radar is pointed upwards and measures a vertical cross section of the avalanche during a defined time period.

Radars send electromagnetic waves that propagate through a medium. The waves are back-scattered by the target and collected by a receiver (Fig. 2.7). The electromagnetic scattering and wave propagation are both related to the properties of the target and the medium. The distance of the target from the transmitter is determined by the amount of time that an emitted signal takes to return to the receiver.

The FMCW radars measure the time it takes the signal to return after being reflected from a snow particle or clump. Hence measuring the intensity of the received signal and its corresponding height provides information regarding the avalanche height distribution.

The frequency of the transmitted signals is periodically increased and decreased according to the waveform of Fig. 2.8. Each FMCW radar has a clock which governs the frequency of the broadcasted signal. In the case of the radar installed at the Vallée de la Sionne experimental test site, the clock runs at 120 Hz (Dawes, 1999). The clock triggers a timer signal with a period of $\frac{1}{200}$ s, which in turn controls the frequency of the output signal. The frequency is increased from 8.5 to 10.25 GHz during the first third of the signal. This part of the signal is used to determine the flow depth of the avalanche. The signal then remains constant at 10.25 GHz and the Doppler effect is measured to detect particle velocities perpendicular to the slope.

42
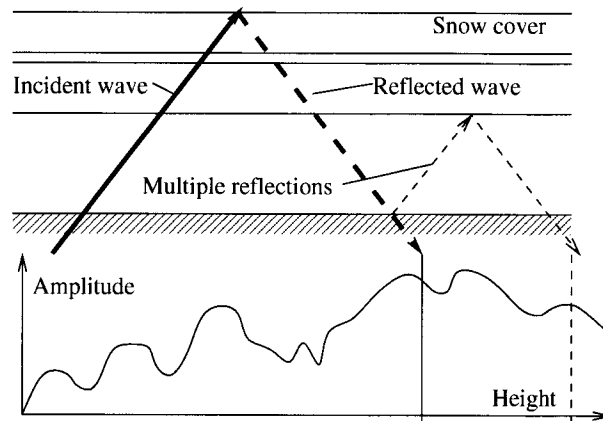
**Figure 2.7:** Radars send electromagnetic waves (incident wave) that propagate through a medium. The waves are back-scattered (reflected wave) by the target and collected by a receiver. The signal is not always necessarily reflected straight back to the radar. At layer boundaries, the signal may be re-reflected causing the signal to appear as though it was reflected from another layer higher up in the snowpack (multiple reflections).

The radar circuity compares the frequency received with the frequency being sent out at the time of receiving the signal. The recorded signal is Fourier-transformed and the spectra of the reflected signal amplitude for each difference in frequency are obtained at discrete time intervals. If the gradient of the increasing output signal is known, then the distribution of time differences between sent and received signals can be found. If the distribution of time differences is multiplied by the signal speed, then the amplitude reflected from different depths in the avalanche is found.

These amplitude depth distributions are plotted as a function of time (see Fig. 2.9). The flow depths can be read off the FMCW plots.

The main error associated with the radar measurements concerns multiple reflections (Dawes, 1999). When the signal is reflected from a snow particle or clump, it is not always necessarily reflected straight back to the radar. At layer boundaries, the signal may be re-reflected causing signal to appear as though it was reflected from another layer higher up in the snowpack (see Fig. 2.7). This error, which cannot be easily quantified, makes the estimation of the exact position of the snow cover surface and the evaluation of the layering of the snow cover difficult.
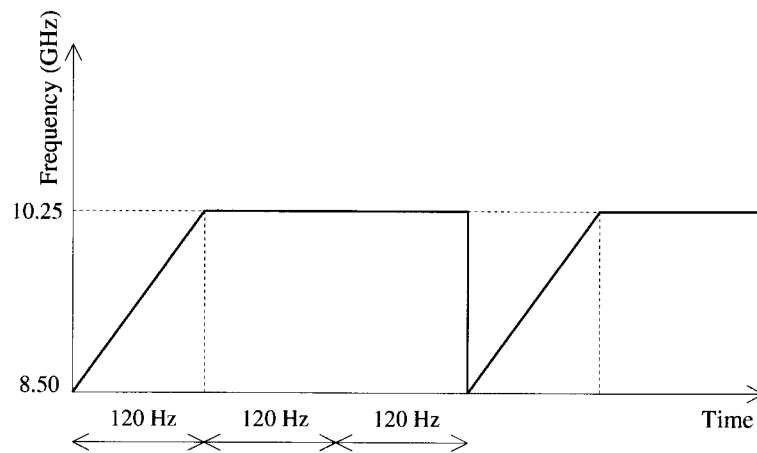
**Figure 2.8:** *The output frequencies of the FMCW radars.*

## 2.4 Avalanche-snow cover interaction

The avalanche mass and the mass distribution are obviously strongly related to the interaction between avalanche and snow cover. The entrainment location, the quantity of mass that the avalanche entrains, the forces that the avalanche exerts on the snow cover and the resistance the snow cover offers to these forces are all factors that modify the avalanche dynamics. Part of this information, i.e. the entrainment location and the quantity of entrained snow, can be measured with FMCW radars. We also attempted to quantify shear and normal forces exerted by the avalanche on the ground using the mechanical properties of the snow cover entrained by the avalanche, which must be investigated by means of field measurements. An alternative to the FMCW radar is offered by seismic investigations.

### 2.4.1 FMCW radar to measure entrainment location and rate

Investigations of the entrainment location can be performed with FMCW radars. At the left of Figure 2.9, the interaction between the original snow cover and the avalanche can be seen. The horizontal lines corresponding to the first 3–4 seconds in the plot represent the snow cover lying over the radar before the avalanche passage. After about 2 seconds the horizontal lines are interrupted by the avalanche. The disappearance of these horizontal lines suggests that all the snow cover, about 2.5 m of snow, is eroded at the avalanche front. Observation of different plots allows identification of typical avalanche-
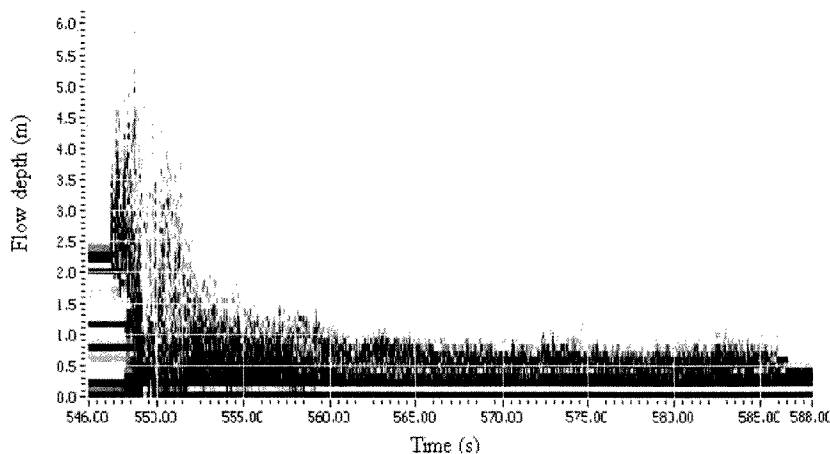
**Figure 2.9:** *A FMCW radars plot measured at the Vallée de la Sionne avalanche test site on December 27th, 1999. The amplitude-depth distributions are plotted as a function of time on an intensity 3D plot, a graphic of the avalanche depths and intensities is obtained. The flow depths can be read off the FMCW plots.*

snow cover interactions and quantification of the erosion depth and rate. Because of the multiple reflection problem the indication of snow cover depth and snow cover stratigraphy should be treated with particular attention. Field experiments on undisturbed snow covers demonstrated that only snow crusts and layers with a higher water content can be easily recognized by the radar because of their large reflection (black horizontal lines)(see §3.4.2).

## 2.4.2 Field measurements to define mechanical properties of the snow cover

The radar data can be correlated to the snow characteristics obtained from field measurements. Field measurements are performed after each event in order to collect as much information as possible on the snow cover characteristics and its mechanical properties. In particular layering. grain size. shape and density of the snow cover are measured.

Density measurements on snowpack layers are often incomplete because of problems sampling thin layers or time constraints on field work. The density values in these cases are determined from snow hardness and grain form using the methodology developed by Geldsetzer & Jamieson (2001).

Mechanical properties of the snow cover are not directly measured. The shear strength is calculated from density and grain form on the basis of the experience of Brun & Rey (1987) and Jamieson & Johnston (2001). In particular shear strength can be correlated

to snow density, crystal shape and water content of the snow.

Knowing the order of magnitude of the snow layer shear resistance and observing the effect of the avalanche passage over these layers (i.e. which layers were eroded and which were not), it is possible to quantify the order of magnitude of the stress exerted by the avalanche on the snow cover.

### 2.4.3 Seismic signals

Seismic signals can also be used to understand the interaction between avalanche and snow. Although the source of seismic signals generated by avalanches is not yet well understood (Suriñach et al., 2001), a comparison between FMCW radar and seismic signals helps to clarify where maximum stresses between avalanche and ground are applied. The high-frequency band (30–50 Hz) of the seismic signals yields information on the effect on the ground of the flux which passes over the sensor. Figure 2.10 shows a comparison between a FMCW and the corresponding seismic plot (top right).

Typically, the largest seismic amplitudes correspond to the breaking of the snow layers and do not necessarily correspond to large avalanche depths, i.e. is not the hydrostatic pressure exerted by the avalanche weight that causes the large seismic amplitude. Point 4 in Figure 2.10 is an example of this behavior: the avalanche flow depth does not change substantially but the changes in the seismic amplitudes suggest a change in the internal avalanche structure.
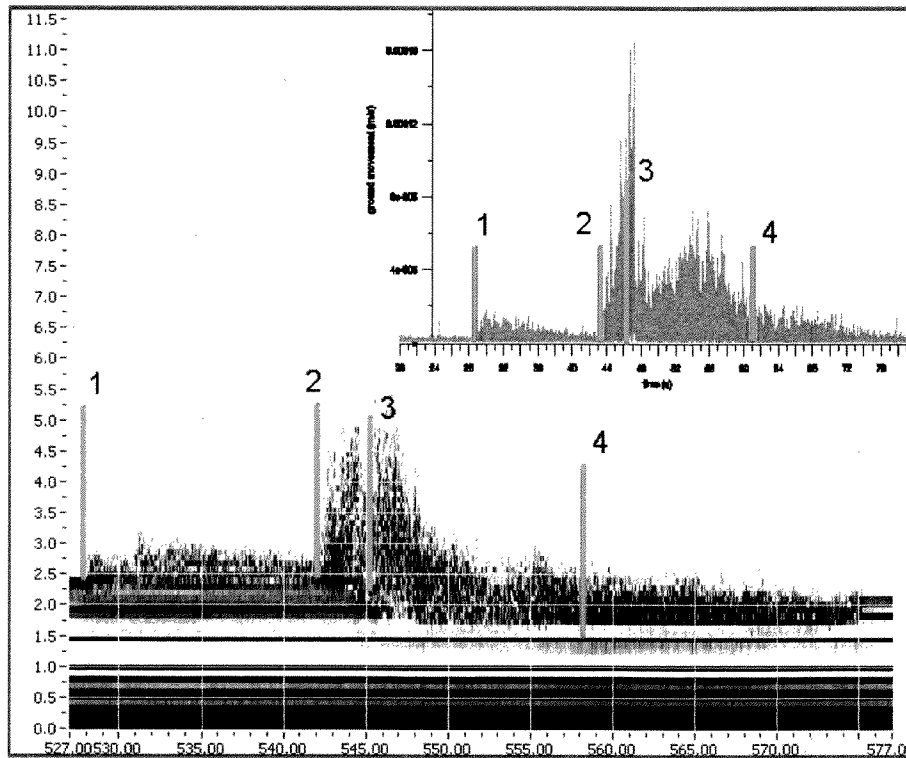
**Figure 2.10:** *Comparison between seismic and FMCW signals at the Vallée de la Sionne avalanche test site, February 21$^{st}$, 2000.*

# 3 Field experiments and observations

In this chapter the experimental sites are described and the mass balances of both natural and artificially released avalanche events are presented. The goal is to identify the important processes and conditions for snow entrainment and deposition.

The measurements used in this work were performed at two experimental sites: the Pizzac (Sommavilla & Sovilla, 1998), located in the northeastern Alps of Italy and the Vallée de la Sionne (Ammann, 1999) located in the canton Valais of Switzerland. A description of the test facilities is given in §3.2. Additional data have been collected during the catastrophic winter 1998/99 and in occasional avalanche paths. The studied avalanches are listed in Table 3.1.

The mass balance data collected at the experimental test sites are supplemented with additional dynamical data concerning speed, pressure, flow depth and additional information according to the installed instrumentation (see Tabs. 3.3, 3.4 and 3.5 for detailed information).

The measurements are representative of different avalanche types, in particular small, large and extreme avalanches have been investigated. The analysis of events having different scales is important for understanding whether physical processes in avalanches strongly depend on avalanche dimension. Data on extreme events, i.e. events having an extremely high return period (in avalanche science approximately 300 years)[1] have fundamental importance because they are the basis for hazard map calculations.

## 3.1 Avalanche indices and general definitions

The avalanches are characterized with respect to type (dense or mixed), topography (channelled or open slope), absolute and relative size. They are also classified on the basis of their release volume (SLF, 1999): small avalanches have volumes less than $25\,000$ m$^3$, medium avalanches have volumes between $25\,000$ and $60\,000$ m$^3$ and large avalanches have volumes larger than $60\,000$ m$^3$.

---

[1]In practical calculations, a 300-year avalanche is an avalanche whose fracture depth has a return period of 300 years.

## 3. FIELD EXPERIMENTS AND OBSERVATIONS

**Table 3.1:** *The table summarizes the avalanche events for which mass balance data were collected. MP = Monte Pizzac test site, VDLS = Vallée de la Sionne test site, Top. = topography, d = dense avalanche, m = mixed avalanche, c = channelled, os = open slope.*

| Event | Location | Type | Top. | Absolute dim. | Relative dim. | Dynam. Data |
|-------|----------|------|------|---------------|---------------|-------------|
| Dec. $5^{th}$, 1997 | MP | d | c | small | small | yes |
| Dec. $21^{st}$, 1997 | MP | d | c | small | medium | yes |
| Apr. $14^{th}$, 1998 | MP | d | c | small | small | yes |
| Apr. $28^{th}$, 1998 | MP | d | c | small | small | yes |
| Jan. $11^{th}$, 1999 | MP | d | c | small | small | yes |
| Mar. $5^{th}$, 1999 | MP | d | c | small | medium | yes |
| Feb. $9^{th}$, 1999 | Obergoms | d/m | c | large | large | no |
| Feb. $22^{nd}$, 1999 | Obergoms | d/m | os | large | catastr. | no |
| Feb. $22^{nd}$, 1999 | Obergoms | d/m | os/c | large | catastr. | no |
| Feb. $23^{rd}$, 1999 | Obergoms | d/m | os | large | catastr. | no |
| Feb. $23^{rd}$, 1999 | Obergoms | d/m | c | medium | catastr. | no |
| Feb. $25^{th}$, 1999 | Aulta | d/m | os/c | large | catastr. | no |
| Jan. $30^{th}$, 1999 | VDLS | m | os/c | large | large | yes |
| Feb. $10^{th}$, 1999 | VDLS | m | os/c | large | large | yes |
| Feb. $25^{th}$, 1999 | VDLS | m | os/c | large | catastr. | yes |
| Jan. $31^{st}$, 2000 | Braemabuel | d | c | small | medium | no |

The term *relative dimension* refers to the event dimension in relation to the site dimension; i.e. a small avalanche (absolute dimension) can be the largest (extreme) avalanche ever seen in the site (relative dimension). Extreme events are defined as events having extremely high return periods (300 years). All mass balance calculations were performed using three approaches for estimating the release mass:

1. Using photogrammetric data, geo-referenced aerial pictures or field measurements to determine the release mass.

2. Using the *Swiss Guidelines* (SLF, 1999) to define the release area and using photogrammetric data or field measurements to define release depth and density. In the following discussion, variables for volumes, masses etc. used for this case are indicated by the subscript *SG* (i.e. $A_{r_{SG}}$).

3. Using the *Swiss Guidelines* (SLF, 1999) to define the release area, fracture depth and density. The fracture depth refers to an avalanche having return period of 300

**Table 3.2:** *Indices and general definitions.*

| **Definition** | Observed | Swiss Guidelines SG | Swiss Guidelines extreme event SG300 |
|---|---|---|---|
| Release area | $A_r$ | $A_{r_{SG}}$ | $A_{r_{SG}}$ |
| Potential entrainment area | $A_e$ | $A_{e_{SG}}$ | $A_{e_{SG}}$ |
| Fracture depth | $d_0$ | $d_0$ | $d_{SG300}$ |
| Release mass | $M_r$ | $M_{r_{SG}}$ | $M_{r_{SG300}}$ |
| Deposit mass | $M_d$ | $M_d$ | $M_d$ |
| Entrainment depth | $d_e = \frac{M_d - M_r}{A_e \rho_e}$ | $d_{e_{SG}} = \frac{M_d - M_{r_{SG}}}{A_{e_{SG}} \rho_e}$ | $d_{e_{SG300}} = \frac{M_d - M_{r_{SG300}}}{A_{e_{SG}} 300}$ |
| Growth index | $I_g = \frac{M_d}{M_r}$ | $I_{g_{SG}} = \frac{M_d}{M_{r_{SG}}}$ | $I_{g_{SG300}} = \frac{M_d}{M_{r_{SG300}}}$ |
| Potential entrainment index | $I_{pe} = \frac{A_e}{A_r}$ | $I_{pe_{SG}} = \frac{A_{e_{SG}}}{A_{r_{SG}}}$ | $I_{pe_{SG300}} = I_{pe_{SG}}$ |
| Entrainment index | $I_e = \frac{d_e}{d_0}$ | $I_{e_{SG}} = \frac{d_{e_{SG}}}{d_0}$ | $I_{e_{SG300}} = \frac{d_{e_{SG}}}{d_{SG300}}$ |
| Compression index | $I_\rho = \frac{\rho_d}{\rho_r}$ | - | - |

years. Variables for volumes, masses etc. used for this case are indicated by the subscript $SG300$ (i.e. $A_{r_{SG300}}$).

These approaches are used to compare the observed measurements with the procedures used by practitioners.

In order to characterize the mass variation processes in avalanches and to facilitate the comparison between observations and procedures used by practitioners, definitions are introduced (see also Table 3.2 for an overview):

1. The *release area* $A_r$ is computed as the area delimited by the fracture line, the stauchwall and the flanks. It is determined from the geo-referenced aerial pictures or by field measurements. In several of the cases the lower edge of the initial slab was not recognizable, making it impossible to define this area.

2. The *SG release area* $A_{r_{SG}}$ is defined by the *Swiss Guidelines* as the area in the release zone having a slope angle larger than 30° for a maximum length of 500 m (SLF, 1999). The release area as defined in the guidelines $A_{r_{SG}}$ is usually larger than the observed release area $A_r$.

3. The *potential entrainment area* $A_e$ is computed as the area affected by the avalanche passage, excluding the release area $A_r$, having an average slope larger than 10°. It is assumed that avalanches do not have enough energy to erode the snow cover when the slope angle decreases under this limit.

4. The *SG potential entrainment area* $A_{e_{SG}}$ is computed as the area affected by the avalanche passage, excluded the release area $A_{r_{SG}}$, having an average slope larger than 10°.

5. The *fracture depth* $d_0$ is the observed fracture depth in the release zone and the *SG fracture depth* $d_{SG300}$ is the fracture depth as defined by the *Swiss Guideline* for extreme avalanches having a return period of 300 years.

6. The *release mass* $M_r$ is calculated from the observed release area $A_r$, slab density $\rho$ and fracture depth $d_0$. The *SG release mass* $M_{r_{SG}}$ is calculated from the SG release area $A_{r_{SG}}$, the observed slab density $\rho$ and observed fracture depth $d_0$. The *SG release mass for extreme avalanches*, $M_{r_{SG300}}$, is calculated from the SG release area $A_{r_{SG}}$, a slab density of $\rho = 300$ kg m$^{-3}$ and the fracture depth $d_{SG300}$.

7. The *average entrainment depth* $d_e$ and the *SG average entrainment depth* $d_{e_{SG}}$ are written as:

$$d_e = \frac{M_d - M_r}{A_e \rho_e}, \quad d_{e_{SG}} = \frac{M_d - M_{r_{SG}}}{A_{e_{SG}} \rho_e}, \tag{3.1}$$

where $\rho_e$ is the density of the entrained snow. Calculations are performed assuming that the density of the entrained snow is equal to the density of the released mass. $M_d$ is the deposition mass accumulated by the avalanche in the deposition zone. Secondary deposits left by the avalanche along the avalanche path are not taken into account for the definition of $M_d$. As a result, the average entrainment depth $d_e$ is not the observed snow cover depth entrained by the avalanche but is a balance between this depth and the deposition depth left by the avalanche along the avalanche path.

8. The *SG average entrainment depth for extreme avalanches* $d_{e_{SG300}}$ is calculated only for extreme avalanches with return period of about 300 years and is given by:

$$d_{e_{SG300}} = \frac{M_d - M_{r_{SG300}}}{A_{e_{SG}}300},$$ (3.2)

where the density of the entrained snow is $\rho_e = 300$ kg m$^{-3}$.

On the basis of these definitions, the following indices are then introduced:

1. The *growth index* $I_g$ and the *SG growth index* $I_{g_{SG}}$ are defined as:

$$I_g = \frac{M_d}{M_r}, \quad I_{g_{SG}} = \frac{M_d}{M_{r_{SG}}},$$ (3.3)

where $M_d$ is the deposit mass, $M_r$ and $M_{r_{SG}}$ are the release masses related to the areas $A_r$ and $A_{r_{SG}}$ respectively. These indices define the avalanche mass increase due to snow entrainment.

2. The *SG growth index for extreme avalanches* $I_{g_{SG300}}$ is defined as:

$$I_{g_{SG300}} = \frac{M_d}{M_{r_{SG300}}},$$ (3.4)

It is calculated only for extreme avalanches.

3. The *potential entrainment index* $I_{pe}$ and the *SG potential entrainment index* $I_{pe_{SG}}$ are defined as:

$$I_{pe} = \frac{A_e}{A_r}, \quad I_{pe_{SG}} = \frac{A_{e_{SG}}}{A_{r_{SG}}}.$$ (3.5)

These indices define the dimension of the snow entrainment basin in comparison to the release area. They are an indicator of the possible avalanche mass increase.

4. The *entrainment index* $I_e$ and the *SG entrainment index* $I_{e_{SG}}$ are defined as:

$$I_e = \frac{d_e}{d_0}, \quad I_{e_{SG}} = \frac{d_{e_{SG}}}{d_0},$$ (3.6)

where $d_0$ is the release fracture depth. They indicate the relation between the release fracture depth and the entrainment depth.

5. The *SG entrainment index for extreme avalanches* $I_{e_{SG300}}$ is defined as:

$$I_{e_{SG300}} = \frac{d_{e_{SG}}}{d_{SG300}},$$ (3.7)

It is calculated only for extreme avalanches.

6. The *compression index* $I_\rho$ is defined as:

$$I_\rho = \frac{\rho_d}{\rho_r},$$ (3.8)

where $\rho_d$ is the density of the deposition and $\rho_r$ is the density of the release. The index is an indicator of the degree of snow compression along the avalanche path.

## 3.2 Experimental sites and other data sources

In the last years full scale avalanche test sites were developed in order to collect as much data as possible about the dynamics of avalanches (Issler, 1999). At present, about nine experimental sites distributed all over the European territory (Switzerland, Italy, France, Norway, Spain and Austria) are operational. The experiments related to this work were performed at two of these sites: the Swiss Vallée de la Sionne and at the Italian Pizzac test sites.

At the Vallée de la Sionne test site the data collected are typical of powder and dense flow avalanches of large dimension which develop both on an open slope and along a channelled path. Typical release masses are on the order of several thousand tons.

At the Pizzac test site the collected information is typical of dense flow avalanches which have small dimension and flow primarily in a channelled path. The Pizzac avalanches are either dry or wet flowing avalanches with a small or no powder part. Typical release masses are smaller than 100 tons. The events at the site are typically wet dense flow avalanches that occur at the end of the winter season and dry or moist dense flow avalanches occurring during the central period of the winter season.

Data about extreme avalanches were collected during the winter 1998/99 at different sites.

### 3.2.1 The Pizzac avalanche test site: instruments and methods

Since 1993, the Avalanche Centre of Arabba, Italy has managed a test site to determine avalanche dynamics parameters (Sommavilla & Sovilla, 1998; Sommavilla et al., 1997). The system is located in an avalanche track which is representative of the North-Italian Alps (Dolomites). It monitors avalanche pressures, speeds, flow depths and variations of the avalanche shape and extent. In the winter seasons 1997/98 and 1998/99, together with the standard measurements, a series of new field measurements and observations of the snow cover in the avalanche path were conducted for the first time to accurately

determine the avalanche mass balance. The collected information is typical of dense flow avalanches which have small dimensions and develop mainly along a channelled path.

*Topography.* Relative to the maximum runout, the avalanches start at 2200 m a.s.l. and stop at 1745 m a.s.l. flowing down a slope with an average inclination angle of 31°. The release zone is characterized by an average slope of about 40° and absence of significant accumulation of drifted snow. The slope is oriented to the west, the exposition to the sun limited to 2–3 hours during December–January and reaches 5–6 hours at the end of the winter season. The maximum possible length of the starting zone is 170 m; the maximum area of the release zone is 5750 m², with a corresponding maximum volume of approximately 3450 m³. The track of the avalanche has a typical gully-shaped cross section characterized by some variations of sub-stratum; the slope angle varies between 31° and 36°. Below an altitude of 1832 m a.s.l. the gradient decreases to 25° and in the majority of the cases, at this point the avalanches stop or deposit a large part of the transported material. At 1783 m a.s.l., at the end of the channelled part, deposits develop on an open slope having an average slope angle of 23°. A creek stops the avalanche at an altitude of 1745 m a.s.l.

*Infrastructure.* The monitoring system is made up of an infrastructure formed by six steel poles, 5 m high, set perpendicularly to the ground along the length of the avalanche track. Each pole is equipped with eight pressure sensors. Five of the six poles are also equipped with flow depth sensors (see §2.3.1).

*Pressure sensors.* The avalanche dynamic pressure is recorded by sensors which are installed on the upward facing side of each pole (see Fig. 2.5). On each pole, eight sensors at an approximate spacing of 0.60 m have been installed, for a total of 48 pressure measuring devices. The sensors are mechanical with a resistive transducer. The dimension of the contact surface for each sensor is 78.5 cm², corresponding to a diameter of 0.10 m; the sensors can record a maximum pressure of 250 kPa. The acquisition system allows a sampling frequency of 160 Hz for an overall recording time of 5 minutes.

*Flow depth sensors.* On the side of five of the six equipped poles, flow depth sensors (see §2.3.1) have been installed. They consist of a series of mechanical switches set at intervals of 5 cm along the pole. The acquisition system allows a sampling frequency of 160 Hz for an overall recording time of 5 minutes.

## 3.2.2 The Vallée de la Sionne avalanche test site: instruments and methods

Since 1997 the Swiss Federal Institute for Snow and Avalanche Research (SLF) has managed a test site to study physical processes in avalanches for the development of avalanche dynamics models (Issler, 1999; Ammann, 1999). The data collection system is located along an avalanche track representative of the western part of the Swiss Alps, immediately to the north of the town of Sion, Canton du Valais. Avalanche pressures, speeds, flow depths and the avalanche mass balance of large avalanches are measured at the site. The collected data are typical of dry-snow avalanches which develop a powder snow component. Wet-snow avalanches mostly occur at the beginning and at the end of the winter season. Avalanches are both natural or artificially triggered.

*Topography.* With respect to the maximum runout, the avalanches start at 2700 m a.s.l. and stop at 1300 m a.s.l. The release zones, consisting of two major areas (termed Crêta Besse 1 and 2), are characterized by an average slope angle of about 40° and 35° respectively. The slopes are oriented towards ESE and SE. The maximum area of a observed release zone was 260 000 m². The tracks of Crêta Besse 1 and 2 are separated and consist of three sections. From 2350 m a.s.l. to 2050 m a.s.l. the avalanches develop on an open slope having average inclination of about 25–30°. Between 2050 and 1900 m a.s.l. the avalanches follow a track having a cross section in the shape of a typical gully where the slope angle exceeds 35°. Below an altitude of 1800 m a.s.l. the slope angle decreases to 25–30°. At the end of the channelled part of the track, the deposit develops on an open slope having a slope angle below 25°. Very large avalanches can reach the bottom of the valley at about 1300 m a.s.l, some 5 km from the avalanche release zone.

*Infrastructure.* A 20 m high pylon, a 5 m high narrow wedge steel construction and a roof section from a road protection gallery are placed within the avalanche track and equipped with various instruments. These are located at an altitude of about 1600 m a.s.l. at the beginning of the deposition zone so that data on both medium and large avalanches can be recorded. A shelter construction opposite the avalanche track at 1500 m a.s.l. (within the deposition zone) protects the staff members, observers and the Doppler radar units and serves as data storage center.

*Ground radars.* FMCW radars (see Fig. 2.9) are buried in the ground under the avalanche at three locations along the avalanche path (respectively 2300 (radars *a*), 1900 (radars *b*) and 1600 m a.s.l. (radars *c*)). The radars are situated in pairs (master and slave), 10 m apart, so that a cross-correlation may be carried out to find the flow velocities.

*Flow depth sensors.* On the side of the pylon, snow depth sensors were installed. These sensors allow the avalanche flow depth to be determined through contact with the moving snow mass. They consist of a series of slide-switches and piezo-switches set at intervals of 25 cm along the pole axis. They record the depth of the flow up to a height of about 8 m. Two lines of sensors were installed on the pylon, 1.20 m apart, so that a cross-correlation may be carried out to find the flow velocities. The acquisition system allows a sampling frequency of about 200 Hz. Both types of sensor open when the pressure reaches a minimum value of about 20 kPa.

*Pressure measuring devices.* In order to measure local impact forces the wedge-shaped steel construction and the pylon were equipped with pressure sensors.

*Normal and shear forces measuring devices.* The road gallery roof is equipped with four bi-axial load cells for determination of normal and shear forces exerted by the avalanche.

*Velocity-measuring devices.* The frontal speed of the avalanche is obtained by video analysis. Doppler radar is used to measure the front and internal velocity of dense-flow and powder-snow avalanches. Five units are placed in the upper floor of the shelter, each targeting different segments of the whole track. Optical sensors (Tiefenbacher & Kern, 2003) are installed on the 20 m high pylon in order to measure the velocity profiles in the avalanche.

*Density measuring devices.* Capacitance sensors (Louge et al., 1997) installed on the 20 m high tower allow avalanche density to be recorded .

*Mass balance measurements.* In order to establish the mass balance of an avalanche, the snow distributions along the path before and after the avalanche passage have to be measured. Since it is too dangerous to directly measure the snow depths in the slope before the avalanche triggering, remote sensing methods have to be applied. Therefore, a method of helicopter-based photogrammetry was developed to measure the snow depths before and after the artificial avalanche triggering. See section 2.2.4. In addition to the measurements by photogrammetry, field measurements are necessary to complete the information on the mass balance.

## 3.2.3 Data from the catastrophic winter 1998/99

The winter 1998/99 (SLF, 2000) was an extraordinary avalanche season. Between January $27^{th}$ and February $25^{th}$ three precipitation periods accompanied by stormy north-westerly winds brought large amounts of snow to the Swiss Alps, resulting in intense avalanche activity. In Switzerland, about 1200 avalanches caused damage to buildings, transportation, infrastructures and power lines; 28 people were caught in inhabited areas or on roads

3. FIELD EXPERIMENTS AND OBSERVATIONS

**Table 3.3:** *The geographic location, topography and characteristics of the Monte Pizzac and Vallée de la Sionne avalanche test sites.*

|  | Monte Pizzac (MP) | Vallée de la Sionne (VDLS) |
|---|---|---|
| **General information** |  |  |
| Site location | Arabba, Venetian Region, Italy | Canton Valais, Switzerland |
| Region | Venetian Dolomites | N-W part of the Swiss Alp |
| Climate | Maritime | Transitional |
| Ownership | ARPAV-Centro Valanghe di Arabba | SLF |
| **Avalanche characteristics** |  |  |
| Avalanche dimension | Small | Medium to large |
| Initial snow volume | 500–3 000 m$^3$ | 50 000–350 000 m$^3$ |
| Avalanche type | Dry and wet dense flow avalanches; sometimes mixed avalanches with weak powder part | Dry and wet dense flow avalanches; many mixed avalanches with large powder part |
| Path characteristics | Strongly channelled | Partly channelled |
| **Topography** |  |  |
| Starting zone | Funnel-like slope, 0.6 ha, 40° | Open slope, 30 ha, 30–40° |
| Starting zone aspect | WNW | ESE, SE |
| Track | Gully, 31–36° | Open slope, gully, 30–40° |
| Runout zone | Gully, open slope, 23–25° | Open slope, 15–20° |
| Drop height | 450 m | 1300 m |
| Path length | 800 m | 2700 m |
| Average inclination | 31° | 29° |
| **Release technique** | Artificial release by Cat.Ex. | Artificial release by helicopter |

**Table 3.4:** *Currently installed experimental facilities and implemented measurement techniques at the Monte Pizzac avalanche test sites.*

| Monte Pizzac (MP) | Measurement technique | Location |
|---|---|---|
| **Avalanche mass balance** | | |
| Snow properties (layering, density etc.) | Manual measurements | Whole path |
| Release volume | Established manual method, snow stakes, video | Release zone |
| Eroded/deposited volumes along flowing zone | Established manual method | Whole path |
| Final deposit volume | Established manual method | Deposit zone |
| Avalanche trajectory, width | Field observation, video | Whole path |
| **Depth-averaged flow variables** | | |
| Front velocity | From impact on poles | At 6 locations |
| | Video image processing | Whole path |
| Velocity distribution | Not measured | |
| Flow depth | Array of mechanical switches | At 5 locations |
| **Internal flow variables** | | |
| Velocity profile | Not measured | |
| Flow density profile | Not measured | |
| Pressure profile | 8 electro-mechanical pressure sensors | At 6 locations |
| **Interaction avalanche/ snow cover/ ground** | | |
| Erosion rate, entrainment position | Not measured | |
| Ground shear stress | Not measured | |
| Seismic and acoustic signals | Not measured | |

# 3. Field experiments and observations

**Table 3.5:** *Currently installed experimental facilities and implemented measurement techniques at the Vallée de la Sionne avalanche test sites.*

| Vallée de la Sionne (VDLS) | Measurement technique | Location |
|---|---|---|
| **Avalanche mass balance** | | |
| Snow properties (layering, density etc.) | Automatic weather station; Under safe conditions manual measurements | Release and deposit zone; rarely whole path |
| Release volume | Aerial photogrammetry, manual measurements, video image processing | Release zone |
| Eroded/deposited volumes along track | Under safe conditions established manual method | Whole path |
| Final deposit volume | Aerial photogrammetry, manual measurements | Deposit zone |
| Avalanche trajectory, width | Video image processing | Whole path |
| **Depth-averaged flow variables** | | |
| Front velocity | Video image processing | Whole path |
| | FMCW radar | At 3 locations |
| Velocity distribution | Doppler radar | Whole path |
| Flow depth | Array of mechanical switches | At 1 location |
| | FMCW radar | At 3 locations |
| **Internal flow variables** | | |
| Velocity profile | FMCW radar | At 3 locations |
| | Optical sensors | At 1 location |
| Flow density profile | Capacitance sensors | At 1 location |
| Pressure profile | 7 pressure sensors | At 1 location |
| | 10 pressure sensors | At 1 location |
| **Interaction avalanche/ snow cover/ ground** | | |
| Erosion rate, entrainment position | FMCW radar | At 3 locations |
| Ground shear stress | Shear/normal force plates installed on roof of avalanche shed | At 1 location |
| Seismic and acoustic signals | Geophone | At 3 locations |

60

and 17 of these died. In order to control and improve the quality of the avalanche hazard maps, aerial stereo-photographs were taken after the avalanche events. The photographs allowed a detailed mapping of all avalanches. For some tracks, the deposition volumes of the avalanches and the release fracture depth were measured by photogrammetry. The photogrammetry also provided snow depth along profiles parallel to the avalanche trajectories giving information on the erosion and deposition processes along the avalanche path. The photographs have been geo-referenced to localize the release area of each avalanche and its perimeter. The information collected during the winter 1998/99 has been used to determine the influence of entrainment in extreme avalanches.

### 3.2.4 Other avalanches

During the winter season 1999/2000, information about erosion and deposition processes in natural avalanches was collected also at other sites as the opportunity arose. The avalanche paths were investigated immediately after the avalanche event using the field observation technique described in §2.2.3. No additional information is associated to these measurements.

## 3.3 Avalanche experiments at the Monte Pizzac test site.

Avalanche events are frequent at the Pizzac site. In particular, four events occurred during the winter 1997/98, specifically on December $5^{th}$ and $21^{st}$ and on April $14^{th}$ and $28^{th}$ (Sovilla et al., 2001). Two events occurred during the winter 1998/99 on January $11^{th}$ and March $5^{th}$. The avalanche mass balance was determined by field observations. The avalanche mass distribution was obtained by analysis of dynamical data such as frontal velocities and avalanche flow depths.

### 3.3.1 Mass balance analysis

The determination of the mass balance by field measurements (see §2.2.3) has been applied to the Pizzac avalanche site. The Pizzac site is ideal for these measurements, for the following reasons:

1. It allows a fairly secure field access.

2. It has a small size with an average release width of about 35 m, maximum release length of 170 m, average flowing zone width between 5 and 20 m, and path length about 800 m.

3. The entire path faces west and therefore has uniform radiation exposure and temperature over the entire avalanche path.

4. There is no significant wind transport.

5. There are only small variations in terrain characteristics.

As previously seen in §2.2.3, the determination of the mass balance is divided into the following steps:

1. *Determination of the original snow cover characteristics.* At the Pizzac test site, variations in snow cover are typically observed in the first part of the flowing zone, where a deep gully section accumulates snow and consequently has a deeper snow cover. It has been observed that the snow cover is rather homogeneous along the rest of the path and there is no significant accumulation of drifted snow. However, in order to minimize data collection errors due to local ground irregularities, the snow cover profile used for the mass balance calculations is the average of the collected profiles. In particular, the depth and density of the layers have been determined by averaging the corresponding measurements in different profiles. The small size of the Pizzac site makes such an averaging possible.

2. *Determination of the initial mass $M_r$ in the release zone.* At the Pizzac site the area of the release zone is determined by plotting the observed border on a high-resolution topographic map (scale 1:500, contour line resolution 1 m). The area limits are determined by photos or video analysis and local observations. As pointed out in §1.2.1, the avalanche crown and flanks are generally well defined and easy to localize on the map since they are located at sudden changes of slope or along the border of the neighboring forest. In comparison, the determination of the avalanche stauchwall is more difficult since it is frequently erased by the passage of the slab. To avoid errors caused by the determination of the position of this border, at the Pizzac site we have assumed that it is located in the lowest possible position where the avalanche starts to be channelized and where there are evident signs of flow. In this way the release area $A_r$ is slightly over-calculated by an order of up to 15%. This means that if we calculate the increase of mass of the avalanche as the ratio between maximum mass and released mass, the increase in mass can be greater than calculated because of this error. That is, we are always underestimating the mass increase.

Release depth $d_0$ and densities are determined as described in §2.2.3.

3. *Determination of the entrainment and deposition masses in the flowing and deposition zones.* At the Monte Pizzac test site all avalanches flow through a narrow and strongly channelled path. For this reason, previous events complicate the field measurements because the snow cover stratigraphy is influenced by previous deposits distributed along the path or by previous erosions which have already collected parts of the original snow cover.

The determination of the avalanche indices was performed using the approaches defined in §3.1, however two modifications were necessary:

1. *The SG release area $A_{r_{SG}}$ is defined as the area in the release zone having slope angle larger than 35°.* The Swiss Guideline defined the area $A_{r_{SG}}$ as the zone having slope angle larger than 30° for a maximum length of 500 m. The Pizzac test site is characterized by its narrow, steep and short channel which has a slope angle larger than 30° for almost all its length. Since the maximum path length is about 800 m, it is not possible to define the release length on the basis of the guidelines, i.e. 500 m long. Defining a higher slope angle limit for the release zone definition reduces the release length to about 200 m.

2. *The growth indices $I_g$ and $I_{g_{SG}}$ are defined as the ratio between the maximum mass $M_{max}$ reached by the avalanche and the release masses $M_r$ and $M_{r_{SG}}$, respectively.* The calculation of the deposited mass $M_d$ at the Pizzac test site takes into account all the mass deposited by the avalanche from the starting zone to the final main deposition. Since at the Pizzac test site avalanches are characterized by strong deposition all along the path, the $M_d$ is not representative for the definition of the avalanche mass. Therefore, it is substituted by the maximum mass $M_{max}$ reached by the avalanche along the avalanche path.

## Mass balance of December $5^{th}$, 1997, event

The December $5^{th}$ avalanche was the first event of the season on the Pizzac site. After a snow fall of about 30 cm on a snowpack of about 60 cm, an attempt was made to release an avalanche. The explosion triggered a small dry-slab avalanche which affected a layer of about 25 cm with an area of about 1 000 $m^2$ and a corresponding volume of about 250 $m^3$. It was difficult to determine the release zone because the stauchwall of the slab was not recognizable. For simplicity we consider the stauchwall position at the same place as the first examined section.

The average density of the released snow was about 135 kg m$^{-3}$, corresponding to an initial avalanche mass of 33 750 kg. The avalanche entrained snow along the path, eroding very deep layers. The total mass eroded by the avalanche is estimated to 303 000 kg. Immediately downstream of the starting zone, the avalanche began to deposit material with a mean density of 280 kg m$^{-3}$. The maximum value of the avalanche mass along the path was about 61 600 kg, corresponding to a growth index $I_g$ of 1.8 (see Table 3.7). The avalanche moved downslope with an average front speed of 11 m s$^{-1}$, covering a total distance of 547 m (from the slab crown to the final deposit). The speed was characterized by many fluctuations because of the high friction along the undisturbed surface and was influenced by the morphology of the ground. These fluctuations almost stopped the avalanche after approximately two-thirds of the total path length (point $A$ in Fig. 3.1, $a$), but then, with a sudden change of slope, the avalanche recovered speed; see Fig. 3.2.

Figure 3.1, $a$, shows the integral of the entrainment (erosion = positive $y$-axis) and of the deposition (negative) along the avalanche trajectory. The sum of the integrals allows the evolution of the avalanche mass along the track (mass balance) to be determined. The figure also shows the evolution of the erosion and deposition values for unit of surface area (kg m$^{-2}$), where each point represents a section. The origin of the $x$-axis coincides with the slab crown. The first data point on the integral erosion curve is the released mass.

## Mass balance of December 21$^{st}$, 1997, event

The second trajectory of the avalanche, on December 21$^{st}$, was partially coincident with that of the first avalanche. The avalanche had a larger width than the avalanche of December 5$^{th}$. Consequently undisturbed areas of the snow cover were eroded. In some areas immediately downslope of the starting zone, an average snow cover depth of about 1.40 m was measured. This high value is also explained by the fact that the area is strongly gully-shaped and that a steep wall delimiting one side of the gully tends to discharge snow into the gully.
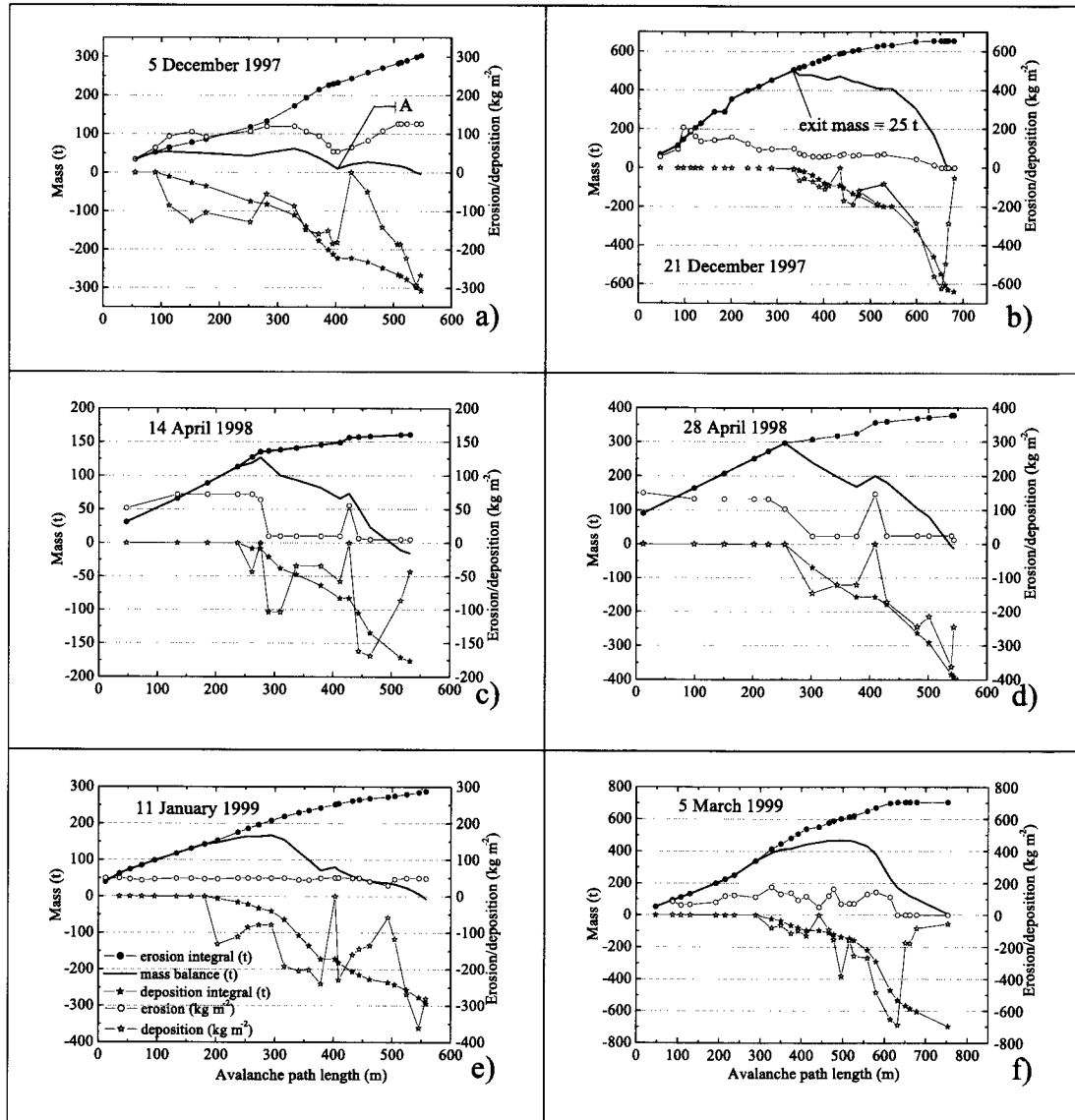
**Figure 3.1:** *Mass balance of the a) December $5^{th}$ event, b) December $21^{st}$ event, c) April $14^{th}$ event, d) April $28^{th}$ event, e) January $11^{th}$ event and f) March $5^{th}$ event. The measurements were performed at the Italian avalanche test site Pizzac.*

The avalanche was triggered artificially after a snow fall of about 40 cm. The explosion provoked a dry-slab avalanche. The total volume of the released mass was 600 m$^3$, of which 490 m$^3$ came from the main basin and 110 m$^3$ from a lateral branch. The initial mass was 84 450 kg. The avalanche collected snow along the flowing zone, including snow from basal layers. The total mass eroded by the avalanche was 654 000 kg. The avalanche covered a total length of 680 m and began to deposit after 300 m of flow. The density of the deposited snow was between 270 and 430 kg m$^{-3}$. The avalanche reached a maximum mass of 505 850 kg corresponding to a growth index $I_g$ of 6 (see Table 3.7) and had an average front speed of 17.9 m s$^{-1}$. Figure 3.1, b, shows the mass-balance analysis of this event. At about half-way point, a small part of the avalanche was deflected by a defence structure protecting a cable car pylon close to the flowing zone. This mass loss is included in the avalanche mass balance.

## Mass balance of April 14$^{th}$, 1998, event

After three months pause, a storm front deposited 80 cm of snow in 3 days. The high temperatures typical during spring had already caused the old snowpack to melt, except for a very thin layer of metamorphosed snow from the previous avalanche deposits less exposed to the solar radiation. On April 14$^{th}$ a moist-snow avalanche slab about 45 cm thick was artificially triggered. The total surface of the slab was 600 m$^2$ corresponding to a volume of 270 m$^3$ and a mass of 31 050 kg. The avalanche collected snow along the track, reaching the ice layer or the ground in the first part of the track, and the erosion progressively decreased towards the bottom of the slope. The eroded mass was 160 900 kg. The avalanche covered a total length of 530 m; deposition began after 250 m of track. The density of the deposited snow was 290–345 kg m$^{-3}$. The avalanche reached a maximum mass of 126 800 kg, corresponding to a growth index $I_g$ of 4.1 (see Table 3.7), and had an average front speed of 12.3 m s$^{-1}$. Figure 3.1, c, shows the mass-balance analysis of this event.

## Mass balance of April 28$^{th}$, 1998, event

New precipitation on April 27$^{th}$ and 28$^{th}$ produced 75 cm of snow. During the precipitation a natural release of a loose wet-snow avalanche resulted in a release depth of about 30 cm (all the fresh snow on the ground at the moment of the release). In this case it was not possible to access the starting zone, so data are missing from the first part of the flowing zone. Observation of the phenomenon from a moderate distance showed the presence of

a ground avalanche which followed more or less the same trajectory as the avalanche of April $14^{th}$.

The missing areas and volumes were therefore estimated on the basis of the previous avalanche. The release area and width of the flowing zone were set to the values determined for the April $14^{th}$ event, assuming that the densities in the first part of the track was equal to that measured along the second part of the track, i.e. 500 kg m$^{-3}$, the release mass is approximately 90 000 kg. The avalanche collected snow along the track, eroding down to the ground along the first part of the track. The erosion progressively decreased towards the bottom of the slope. The total eroded mass is estimated as 378 000 kg. The avalanche covered a total distance of 540 m; deposition began after 310 m. The density of the deposited snow was 500–560 kg m$^{-3}$. The avalanche reached a maximum mass of 296 700 kg, corresponding to a growth index $I_g$ of 3.3 (see Table 3.7) and had an average front speed of 7.6 m s$^{-1}$. Figure 3.1, $d$ shows the mass-balance analysis of this event.

## Mass balance of January $11^{th}$, 1999, event

On January $11^{th}$, 35 cm of new snow covered an old snow cover of about 18 cm. During the precipitation, at 9.30 a.m., a natural release of a dry-slab avalanche occurred. The fracture slab thickness was about 50 cm, the snow having an average density of about 100 kg m$^{-3}$. The avalanche was followed by a secondary event that influenced only the first part of the track. The deposits of the second avalanche were easily recognizable because of their different color and granular structure. The mass balance analysis was performed for the 9.30 a.m. avalanche. The total volume of the released mass was 400 m$^3$. The initial mass is estimated at 40 000 kg. The avalanche collected snow along the flowing zone, down to the ground; the erosion slightly decreased towards the bottom of the slope. The total mass eroded by the avalanche was 287 600 kg. The avalanche covered a total length of 555 m. The density of the deposited snow was 240–340 kg m$^{-3}$. The avalanche reached a maximum mass of 167 400 kg corresponding to a growth index $I_g$ of 4.2 (see Table 3.7) and had an average front speed of 13.7 m s$^{-1}$. Figure 3.1, graphic e, shows the mass-balance analysis of this event.

## Mass balance of March $5^{th}$, 1999, event

After two months of low precipitation, about 50 cm of new snow were deposited by a storm front between March $4^{th}$ and $5^{th}$. On March $5^{th}$ a dry-slab avalanche about 40 cm thick was artificially triggered. The avalanche collected snow along the track, down to the ice layer formed on the surface of the old deposits from the January $11^{th}$ avalanche.

This old deposit was characterized by a very smooth frozen hard surface over which the avalanche slid. The low friction between avalanche and sliding surface allowed a long runout distance. It was observed that the avalanche developed a small powder component, a very unusual phenomenon for the Pizzac avalanches. The total volume of the released mass was 330 m$^3$. The average density of the released slab was 160 kg m$^{-3}$. The initial mass reached the value of 53 120 kg. The total mass eroded by the avalanche was 705 550 kg. The avalanche covered a total length of 753 m. The density of the deposited snow was 200–375 kg m$^{-3}$. The avalanche reached a maximum mass of 468 200 kg corresponding to a growth index $I_g$ of 8.8 (see Table 3.7) and had an average front speed of 17.6 m s$^{-1}$. Figure 3.1, f, shows the mass-balance analysis of this event.

## Accuracy of measurements and error analysis

An assessment of the accuracy of the measurements through the estimation of the measurement error is an important aspect of field measurements. The main difficulty with field measurements is that the snow cover is not homogeneous. For example, a profile is only representative of a precise location; if we try to analyze another profile only a few meters away we will find something similar but not exactly equal.

A second problem is that the precision of the measurement (e.g. 1 m depth with a precision of 0.5 cm) is negligible in comparison to the problem of defining the point we want to measure. For example, the interface between two layers is not always well defined and its thickness can be greater than the instrument precision.

Considering these problems, we assume that the error has three main causes: (1) the difficulty in distinguishing and exactly defining the boundary of the original layers and deposits, (2) the assumption that local information is representative for the entire snow cover and (3) the error in the determination of the density of each layer or deposit.

These errors are very difficult to quantify. In order to show the order of magnitude of the possible errors and their effects, we will consider different scenarios assuming a realistic measurement error and calculating the influence of this error on the global mass-balance determination.

The error magnitude for the original snow cover, the released mass and the entrained/deposited masses have been calculated using three different methods. An error analysis is made for each case.

*Original snow cover.* In order to minimize data collection errors due to the local irregularity of the ground, the profile of the snow cover used for the mass balance calculations is the average of the measured profiles. Erosion masses are calculated on the basis of this

profile. In particular the depth and the density of the layers are determined as an average of the corresponding measurements in different profiles. The number of measurements are different from event to event; in general for each cross-section analyzed along the path (see Fig. 2.3) there are at least 5 measurements (in some cases up to 20) of the depth of the undisturbed snow cover and a *formal full snow profile* is available for up to 5 sections. Using the average depth and the deviation from this value, the realistic error associated with the depth measurements is about 5% (0.05 m over 1 m). Using an average density for each layer (averages were calculated using a minimum of 10 data points), we also compared the average of the density to the standard deviation of the data points from this value; we find that the realistic error associated with this measurement is about 10%.

*Release zone.* As seen in §2.2.3 the release area may be over-estimated by up to 15%. The error associated with the density measurements is approximately 10% as seen for the determination of the original snow cover characteristics.

*Flowing and deposition zone.* In a cross-section the snow cover depth is measured about every 0.50 m. *Avalanche snow profiles* allow determination of the depth corresponding to the deposit and to the original snow cover. These data are used to calculate the deposition and entrainment areas along the cross-section. Assuming a measurement errors, we assess the influence of this error on the calculation of the deposition area. For an average cross-section with the snow deposit depth varying between 0.7 and 1.9 m and a width of about 7 m, assuming an error of 0.10 m for each measurement, the variation of the global area is about 8%; an error of 0.05 m produces a difference of about 5%. Considering that there is an absolute error of 0.10 m over these depth values, and that it is difficult to repeat this error constantly for the entire measurement, we assume that the second case is more realistic. Assuming that density of the deposit is generally in the order of 300 kg m$^{-3}$, an error of 10% means a difference of 30 kg m$^{-3}$. The instruments have a precision of 10 kg m$^{-3}$ (3%). Since we do not use local information but the average of many data (10-20 data points) the final error should decrease. However, our application of the density data to the entire snow cover may influence the amount of error. As a matter of fact, the section and the profile are chosen carefully to represent the variation along the avalanche track and, in each case, we observed that the variations are small. Control of this kind of error is given by the fact that, when the avalanche stops, the sum of eroded and deposited snow must be zero, this means that the avalanche has deposited all the eroded snow.

For the examined events the calculated avalanche mass when it comes to rest is not zero, but the difference is small (see Fig. 3.1). The average error is 11.8% of the release mass and only 3.9% for the maximum mass obtained by the avalanche along the path.

An exception is represented by the April $14^{th}$ event, for which the percentage increased to 50% and 12.3%, respectively. Since erosion and deposition masses have been calculated with different methods, the respective errors are mutually independent. The fact that the final error is not so large means that in effect the local data represents the entire snow cover well. In conclusion, it is difficult to quantify a precise error, but is possible to state that the magnitude of the error does not influence the conclusion of this work.

## Velocity and runout analysis

There are six points, uniformly distributed along the track, where the time of the avalanche passage is recorded (Sommavilla & Sovilla, 1998; Sommavilla et al., 1997). These points are positioned at known distances, and when the release time has been recorded it is possible to determine the position of the avalanche along the track in function of the time. The recorded data points are then fitted with a third-order polynomial. The time derivative of the polynomial is the frontal speed of the avalanche at each point of its trajectory.

Figure 3.2 shows the speed as a function of the slope of the track, as well as the maximum runout distances reached by each avalanche. For a long segment of track between the release point and the first surveyed point, there is no information. Generally, the investigated avalanches start to decelerate when the slope angle is $< 30°$. Different runout distances are reached for the examined events. The maximum runout distance was reached for the March $5^{th}$, 1999 event followed by the event on December $21^{st}$, 1997. The other events reached more or less the same distance stopping immediately after a sudden change of slope. Interestingly, the wet snow avalanche on April $28^{th}$, which is characterized by a very low value of the frontal speed, reached the same runout distance as the other avalanches despite of it having a lower mean speed.

## Erosion and deposition analysis

Comparison of the mass-balance analysis for the examined events shows a consistent behavior whereby the avalanches entrain snow along their entire trajectory (see Fig. 3.1). In the first part of the track, where the avalanche accelerates, the part of snow cover eroded per unit surface area reaches the maximum value. Peak values of erosion are also reached after a sudden increase of slope. The analysis of the snow cover after an event shows the general tendency of the avalanche to erode the same layers for long sections over the entire track. It was also observed that the Pizzac avalanches eroded low-density snow down to the ground along the entire avalanche path. When an avalanche begins to decelerate and
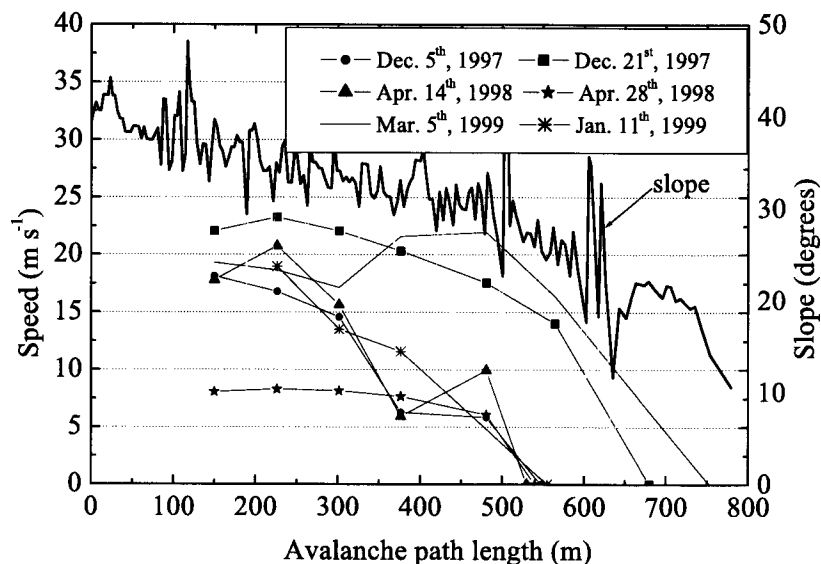
**Figure 3.2:** Frontal speed in relation to the slope of the track (bold line) and runout distances of the considered events.

the frontal speed begins to decrease, the avalanche starts to deposit. Figure 3.3 shows the comparison of different erosion and deposition rates. Bold lines represent the deposition and erosion rate averages calculated only along the track covered by all avalanches. It is observed that, on average, erosion takes place all along the avalanche path, decreasing only slightly towards the end of the path whereas the deposition increases significantly in the second part of the track (see Fig. 3.3). An exception is the December $5^{th}$ event, in which deposition started immediately after the release zone, probably because of the high friction value between the avalanche and the ground, which was not yet affected by the passage of previous events (see Fig. 3.1, $a$). In this case several acceleration and deceleration phases of the avalanche were observed (see Fig. 3.2). Erosion and deposition were uniformly distributed along the trajectory. Because of this behavior the avalanche did not reach a high speed. However, erosion maintained a positive mass balance allowing a considerable runout distance to be reached.

71
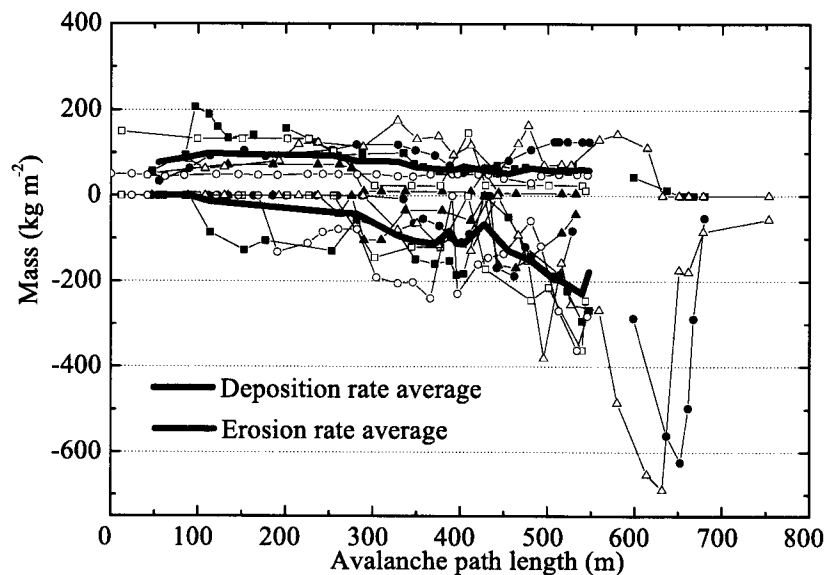
**Figure 3.3:** *Comparison of different erosion and deposition rates at the Pizzac test site. Bold lines represent the deposition and erosion rate averages calculated only along the track covered by all avalanches.*

## 3.3.2 Avalanche mass distribution

In the following we will use two of the avalanche events listed in Table 3.6: the avalanches of December $21^{st}$, 1997 ($A1$) and March $5^{th}$, 1999 ($A2$). These events were chosen because they were the largest and best documented events (i.e. larger runout distance, mass involved in the motion, flow velocity and pressure) recorded at the Pizzac test site.

Figure 3.4 shows the mass evolution along the avalanche trajectory as well as the frontal speed of the events. Both avalanches reach nearly the same maximum mass but the $A2$ avalanche has a longer runout distance. A comparison between the two events reveals that the $A1$ avalanche has a larger mass and a higher frontal speed along the first 400 m of the track. A comparison along the remaining part of the avalanche track shows different behavior: the $A1$ avalanche gradually starts to decelerate and deposit mass when it reaches the lower slopes; the $A2$ avalanche continues to accelerate, increases its mass and reaches a longer runout distance.

Figure 3.5 compares flow depths of the $A1$ and $A2$ events at two positions along the avalanche path. Flow depths are plotted as a function of time. Position $A$ is located at
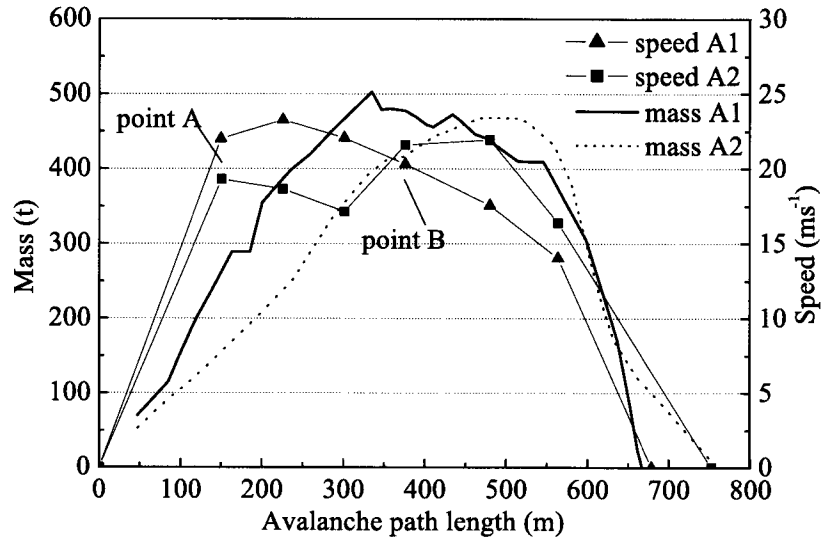
**Figure 3.4:** *Mass evolution and frontal velocity along the avalanche trajectory of December $21^{st}$ (A1) and March $5^{th}$ (A2) events.*
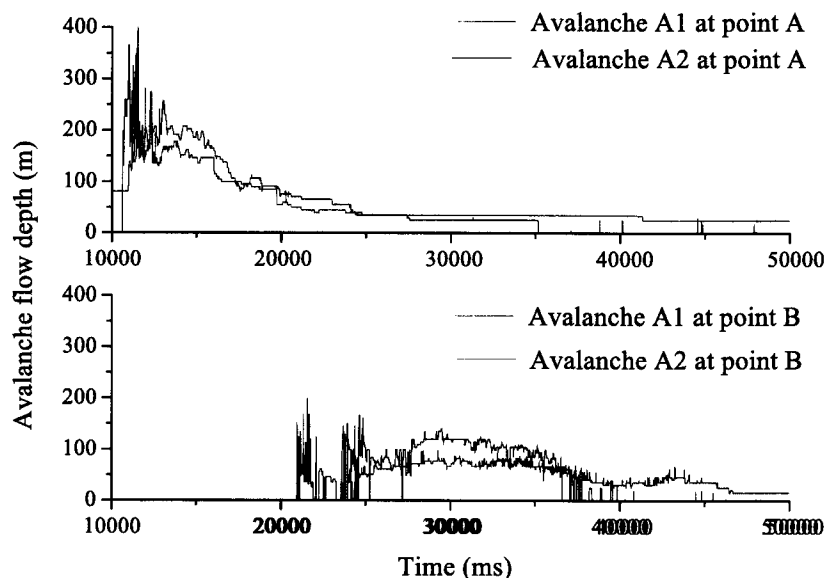
2024 m a.s.l. where the slope is about 40°; position $B$ is located at 1902 m a.s.l. where the slope is about 29°. At position $B$, the frontal speeds of the avalanches and their masses are similar but the $A1$ avalanche is decelerating while the $A2$ avalanche is accelerating. The flow behavior shows a completely different depth distribution over time. The $A2$ avalanche took about 13 seconds to pass through point $B$. The $A1$ avalanche took almost 26 seconds. It was characterized by lower flow depths and by an evident tail. On account of their similar masses, three hypotheses are possible:

1. The avalanche mass of $A1$ was distributed over a longer distance.

2. The body of $A1$ was moving slower than that of $A2$, even though their frontal speeds were similar.

3. $A1$ was both longer and slower.

Observations at the avalanche path immediately below point $B$ showed that $A2$ deposited only half of the mass deposited by $A1$, suggesting that in the $A1$ avalanche more mass was moving slowly and, as a consequence, not contributing to the dynamics of the avalanche, confirming the third hypothesis.

73

**Figure 3.5:** *Flow depths of the A1 and A2 events at two positions along the avalanche path. Flow depths are plotted as a function of time. Position A is located at 2024 m a.s.l. where the slope is about 40°; position B is located at 1902 m a.s.l. where the slope is about 29°.*

As an intermediate result we can state that not only is the avalanche mass important but that its spatial distribution can change the avalanche dynamics considerably. Avalanches with mass concentrated closer to the avalanche front and distributed more in the height than in the length tend to reach longer runout distances.

Another important observation corroborating this statement concerns the distribution of the maximum depths in the avalanche. At position $A$, avalanche $A1$ has a higher frontal speed and a larger mass. Avalanche $A1$ reaches maximum depth at the front while $A2$ reaches the maximum depth about three seconds after the passage of the avalanche front. (The sharp peaks at the avalanche front are due to the presence of a small powder component preceding the dense part.) At position $B$, where the slope angle is more gentle, maximum depths are found considerably behind the front in both avalanches. Also at each position, the faster avalanche is characterized by the maximum depth value closer to the avalanche front.

At this point it is important to understand what the boundary conditions are that allow the mass to move compactly close to the avalanche front. Gubler (1987), analyzing the

74

data measured with FMCW radar, stated that high track roughness increases the snow transfer from body to tail (i.e. lower avalanche depth and more snow mass in the avalanche tail). The reason why avalanche $A2$ is moving faster and as a compact mass is probably due to this basal sliding condition. The old deposit left by a previous avalanche (January $11^{th}$, 1999) was characterized by a very smooth frozen hard surface over which avalanche $A2$ slid. The low value of friction exerted by the slide-surface allowed the avalanche to go faster and decreased the transfer of mass to the avalanche tail. Because of its higher speed, the avalanche continued to collect mass also over low slopes and reached a longer runout distance.

### 3.3.3 Discussion of experimental survey

The six events are summarized in Tables 3.6 and 3.7. Four events were of small dimensions (December $5^{th}$, April $14^{th}$, April $28^{th}$ and January $11^{th}$) and two events of medium dimension (December $21^{st}$ and March $5^{th}$). We observed that the speed and mass of small avalanches are strongly related to sliding surface characteristics and density and strength of the snow cover. Two events (December $5^{th}$ and April $14^{th}$) started almost with the same initial mass, but because of the different substratum the April $14^{th}$ avalanche mass doubled that of the December $5^{th}$ event. Despite this, the speed and runout were almost the same, probably because of the different water content of the snow.

Depending on the external parameters, such as substratum, characteristics of the slope and snow water content, an avalanche can increase its mass while flowing. For example the avalanche on March $5^{th}$ grew to 8.8 times its initial mass.

An interesting observation concerns the increase of density of the deposited snow in comparison with the undisturbed snow cover. For most cases, the ratio is 2–3; only for wet snow is the ratio equal to 1.

The following conclusions can be drawn from the measurements:

1. The avalanche mass is not constant along the track. Analyzing the largest event (March $5^{th}$, 1999) we can observe that the mass increased 8.8 times ($I_g$), suggesting that the quantity of snow that an avalanche can potentially erode is more important than the release mass. The mass increase is especially important for avalanches having a small release area and a long flowing zone.

2. For the small Pizzac avalanches, the slope angle is the most important factor controlling the erosion and deposition processes. The erosion reaches a maximum value

# 3. Field experiments and observations

**Table 3.6:** *Summary of the mass balance data at the Pizzac avalanche test site.*

| Parameter | Symbol | 05.12.97 | 21.12.97 | 14.04.98 |
|---|---|---|---|---|
| Release area (m$^2$) | $A_r$ | 1 000 | 1 490 | 600 |
| Release area SG (m$^2$) | $A_{r_{SG}}$ | 1 940 | 4 350 | 1 740 |
| Fracture depth (m) | $d_0$ | 0.25 | 0.40 | 0.45 |
| Release volume (m$^3$) | $V_r$ | 250 | 600 | 270 |
| Release volume SG (m$^3$) | $V_{r_{SG}}$ | 480 | 1740 | 780 |
| Release snow density (kg m$^{-3}$) | $\rho_r$ | 135 | 140 | 115 |
| Release mass (tons) | $M_r$ | 33.8 | 84.5 | 31.1 |
| Release mass SG (tons) | $M_{r_{SG}}$ | 65.5 | 243.6 | 90.1 |
| Deposition snow density (kg m$^{-3}$) | $\rho_d$ | 280 | 270÷430 | 290÷345 |
| Deposition mass (tons) | $M_d$ | 307.0 | 638.5 | 176.5 |
| Max avalanche mass (tons) | $M_{max}$ | 61.6 | 505.9 | 126.8 |
| Potential entrainment area (m$^2$) | $A_e$ | 2 780 | 6 630 | 3 830 |
| Potential entrainment area SG (m$^2$) | $A_{e_{SG}}$ | 1 840 | 3 770 | 2 690 |
| Entrainment depth (m) | $d_e$ | 0.08 | 0.45 | 0.22 |
| Entrainment depth SG (m) | $d_{e_{SG}}$ | 0.0 | 0.5 | 0.12 |

| Parameter | Not. | 28.04.98 | 11.01.99 | 05.03.99 |
|---|---|---|---|---|
| Release area (m$^2$) | $A_r$ | 600 | 800 | 830 |
| Release area SG (m$^2$) | $A_{r_{SG}}$ | 1 820 | 3 160 | 3 200 |
| Fracture depth (m) | $d_0$ | 0.30 | 0.50 | 0.40 |
| Release volume (m$^3$) | $V_r$ | 180 | 400 | 330 |
| Release volume SG (m$^3$) | $V_{r_{SG}}$ | 550 | 1580 | 1280 |
| Release snow density (kg m$^{-3}$) | $\rho_r$ | 500 | 100 | 160 |
| Release mass (tons) | $M_r$ | 90.0 | 40.0 | 53.1 |
| Release mass SG (tons) | $M_{r_{SG}}$ | 273.0 | 158.0 | 204.8 |
| Deposition snow density (kg m$^{-3}$) | $\rho_d$ | 500÷560 | 240÷340 | 200÷375 |
| Deposition mass (tons) | $M_d$ | 390.4 | 294.0 | 697.4 |
| Max avalanche mass (tons) | $M_{max}$ | 296.7 | 167.4 | 468.2 |
| Potential entrainment area (m$^2$) | $A_e$ | 3 780 | 5 150 | 6 230 |
| Potential entrainment area SG (m$^2$) | $A_{e_{SG}}$ | 2 560 | 2 790 | 3 860 |
| Entrainment depth (m) | $d_e$ | 0.11 | 0.25 | 0.42 |
| Entrainment depth SG (m) | $d_{e_{SG}}$ | 0.02 | 0.03 | 0.43 |

on slopes > 30°; deposition starts when the slope angle drops below about 30° and the avalanche begins to decelerate.

3. The distribution of the mass *in the avalanche body* may be strongly influences flow

**Table 3.7:** *Calculated avalanche indices for the Pizzac avalanches. $I_{pe}$ = potential entrainment index, $Ipe_{SG}$ = SG potential entrainment index, $I_g$ = growth index, $I_{g_{SG}}$ = SG growth index, $I_e$ = entrainment index, $I_{e_{SG}}$ = SG entrainment index. $I_g$ and $I_{g_{SG}}$ refer to the maximum mass $M_{max}$ reached by the avalanche along the avalanche path and not to the total deposited mass $M_d$.*

| Event | $I_{pe}$ | $I_{pe_{SG}}$ | $I_g$ | $I_{g_{SG}}$ | $I_e$ | $I_{e_{SG}}$ | $I_\rho$ |
|---|---|---|---|---|---|---|---|
| **05.12.97** | 2.8 | 1.0 | 1.8 | 0.9 | 0.3 | 0.0 | 2.1 |
| **21.12.97** | 4.4 | 0.9 | 6.0 | 2.1 | 1.1 | 1.3 | 1.9 ÷ 3.1 |
| **14.04.98** | 6.4 | 1.5 | 4.1 | 1.4 | 0.5 | 0.3 | 2.5 ÷ 3.0 |
| **28.04.98** | 6.3 | 1.4 | 3.3 | 1.1 | 0.4 | 0.1 | 1.0 ÷ 1.1 |
| **11.01.99** | 6.4 | 0.9 | 4.2 | 1.1 | 0.5 | 0.1 | 2.4 ÷ 3.4 |
| **05.03.99** | 7.5 | 1.2 | 8.8 | 2.3 | 1.0 | 1.1 | 1.3 ÷ 2.3 |

height, velocity and runout distance of the avalanche. A comparison between two avalanches of equal mass shows that the avalanche with more mass concentrated at the avalanche front has higher front velocity and reaches a longer runout distance.

4. The distribution of mass in the avalanche it seems to be dependent on the entrainment location as well as how the mass is transferred within the avalanche.

5. The distribution of the mass within the avalanche it seems to be dependent on the terrain/snow cover friction. Lower friction decreases the snow transfer from the body to the tail of the avalanche. This conclusion corroborates that of Gubler (1987).

6. Avalanches with evident tails deposit mass along the avalanche path, suggesting that the deposition process begins at the tail, where velocities are lower.

7. For flowing avalanches the maximum flow depths are generally located behind the front. However, when the avalanche runs on a steep track (35–40°), the maximum depths move forward, closer to the avalanche front.

8. Maximum impact pressures correspond to the maximum depth position. Exceptions are due to the presence of a powder cloud moving at the front of the avalanche. In this case, particles exiting the flowing core can cause high point-impact pressures.

## 3.4 Avalanche experiments at the Vallée de la Sionne test site

The winter of 1998/99 in the Swiss Alps was extraordinary because of the unusually high number of extreme avalanche events that occurred, which seriously threatened transport routes and settlements. In the same period, powder avalanches of large dimensions were artificially released and measured at the Vallée de la Sionne test site. The first avalanche in the Vallée de la Sionne came down spontaneously on December $12^{th}$, 1998. From January $26^{th}$ three subsequent heavy precipitation events, characterized by strong NW winds, occurred. After each of these heavy snowfall periods there was a sunny spell, during which it was possible to artificially trigger and observe large avalanches. Each of these avalanches flowed over the instrumentation located in the path and reached the measuring bunker on the opposite slope. The avalanche on February $25^{th}$, because it was so exceptionally large, also caused damage to the instrumentation and to the surrounding forest (Gruber et al., 2002).

Two automatic snow and weather stations collected data about the development of the snow cover in the immediate vicinity of the testing site throughout the whole winter and three heavy snowfall periods could be clearly identified. In Vallée de la Sionne between 1.5 m and 2.0 m of new snow fell during each period.

Photogrammetry was used to measure the fracture depths and volumes for three avalanches. At the same time, three FMCW radars installed along the avalanche path measured the layers in the snow cover and in avalanches during their descent, providing additional information on snow cover–avalanche interaction.

### 3.4.1 Avalanche mass

The avalanche mass balance data collected and described herein concerns the avalanches of January $30^{th}$, February $25^{th}$ and February $10^{th}$ (Vallet et al., 2001), see Fig. 3.6. The data are also summarized in Table 3.8. The aim was to measure the release and deposition avalanche volumes by using photogrammetric techniques applied before and after the events. Unfortunately, difficulties were encountered in determining the release volume (Vallet et al., 2001); the bad contrast of the pre-event snow cover did not allow for accurate measurements. In addition, it was very difficult to distinguish the lower limit of the initial slab because it was erased by the avalanche passage.

For all three avalanches photogrammetric measurements allowed only the determination of the fracture depth $d_0$ along the fracture line. The release volumes were roughly
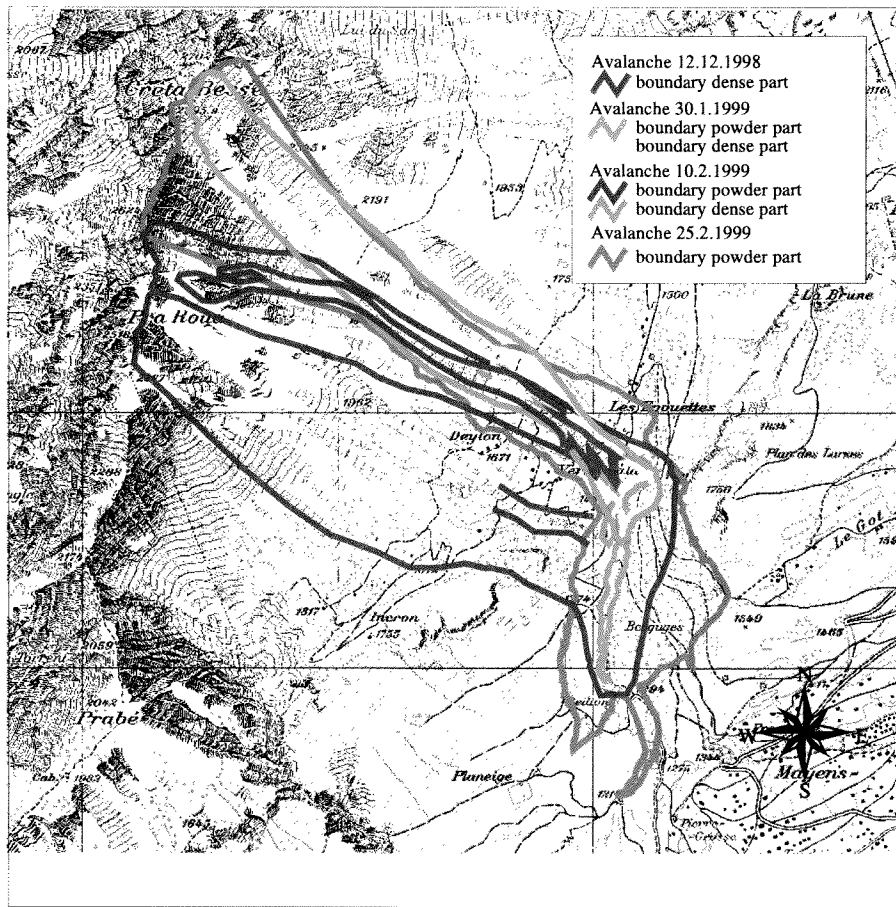
**Figure 3.6:** *Overview of avalanches in 1999 at the Vallée de la Sionne test site.*

estimated considering the average fracture depth and release area determined by video-analysis. In particular, the fracture height $d_0$ was determined by measuring the vertical fracture depth $h_0$ at several points along the fracture lines and correcting the average value in relation to the average slope angle of the entire release area. The release area was determined by geo-referencing the video images taken during the event. The release area was thus defined as the area of the slab that started to move downslope (a few seconds after the explosion).

The deposition volume was determined for all three avalanches as the volume difference between the situation before and after the avalanche release.

Table 3.8 summarizes the photogrammetric measurements for all three events.

**Table 3.8:** *Summary of the measurements collected during the winter 1998/99 at the Vallée de la Sionne test site by photogrammetry and video analysis.*

| Parameter | Not. | 30.01.99 | 10.02.99 | 25.02.99 |
|---|---|---|---|---|
| Release area $(m^2)$ | $A_r$ | 54 600 | 109 200 | 210 900 |
| Release area SG $(m^2)$ | $A_{r_{SG}}$ | 141 000 | 372 500 | 317 900 |
| Fracture depth (m) | $d_0$ | 1.31 | 0.77 | 1.5 |
| Fracture depth SG300 (m) | $d_{SG300}$ | - | - | 1.35 |
| Release volume $(m^3)$ | $V_r$ | 71 500 | 84 100 | 316 350 |
| Release volume SG $(m^3)$ | $V_{r_{SG}}$ | 184 700 | 286 800 | 476 850 |
| Release volume SG300 $(m^3)$ | $V_{r_{SG300}}$ | - | - | 429 160 |
| Release snow density $(kg\ m^{-3})$ | $\rho_r$ | 200 | 200 | 200 |
| Release mass (tons) | $M_r$ | 14 300 | 16 800 | 63 300 |
| Release mass SG (tons) | $M_{r_{SG}}$ | 36 940 | 57 400 | 95 400 |
| Release mass SG300 (tons) | $M_{r_{SG300}}$ | - | - | 128 750 |
| Deposition snow density $(kg\ m^{-3})$ | $\rho_d$ | 350 | 400 | 400 |
| Deposition volume $(m^3)$ | $V_d$ | 39 500 | 505 500 | 951 000 |
| Deposition mass (tons) | $M_d$ | 13 800 | 202 200 | 380 400 |
| Potential entrainment area $(m^2)$ | $A_e$ | 542 000 | 1 315 000 | 804 500 |
| Potential entrainment area SG $(m^2)$ | $A_{e_{SG}}$ | 455 600 | 1 051 700 | 697 500 |
| Entrainment depth (m) | $d_e$ | - | 0.7 | 2.0 |
| Entrainment depth SG (m) | $d_{e_{SG}}$ | - | 0.7 | 2.0 |
| Entrainment depth SG300 (m) | $d_{e_{SG300}}$ | - | - | 1.2 |

## Avalanche of January 30th, 1999

After a snowfall precipitation of about 1.5 m, accompanied by strong winds, a large powder avalanche was artificially released on January 30th (Gruber et al., 2002), see Fig. 3.6.

Photogrammetric measurements were performed both in the release and deposition zones. The accuracy of the measurement in the deposition was about ±0.2–0.3 m; in a shadow area close to the valley bottom the accuracy decreased to ±0.6 m.

In the release zone only the fracture depth was measured. The vertical fracture depth $h_0$ along the fracture line was taken over a distance of approximately 500 m as the average of 31 point measurements. The average amounted to 1.63 m, which corresponds to a fracture depth perpendicular to the surface of 1.31 m ($sd = 29$) cm. The average slope angle in the release zone was 36.6°. The approximate volume was about 71 400 $m^3$ (see Fig. 3.7, upper). The deposition volume was also measured by photogrammetry (see Fig.

3.7, lower). Field measurements performed after the event allowed the approximate definition of the densities in the release and deposition zones. The average snow densities were determined to be 200 and 350 kg m$^{-3}$ in the release and deposition zones, respectively. In spite of the large potential entrainment index ($I_{pe} = 9.9$) the release and deposition masses almost coincided (growth index $I_g = 1$, see Table 3.9).

The January avalanche did not entrain much snow. This is probably due to a previous natural avalanche on January 28$^{th}$ that already had eroded most of the existing snow along the track.

## Avalanche of February 10$^{th}$, 1999

After a new snowfall of about 2 m on February 10$^{th}$, a large powder avalanche was artificially released. Photogrammetric measurements were performed before and after the event. Because of the extreme size of the avalanche, it overpassed the usual site boundaries and the release zone extended to a sector where no photogrammetric measurement were performed before the avalanche release (see Fig. 3.8, upper panel). The accuracy of the deposition measurements was evaluated to be ±0.2–0.3 m.

The average fracture depth was measured over a length of about 550 m and amounted to 0.77 m ($sd = 25$ cm). This average fracture depth was used to calculate the total release volume of 84 100 m$^3$. The average release snow density was 200 kg m$^{-3}$, thus leading to an initial mass equal to 16 800 tons.

The deposition volume was 505 500 m$^3$ for a corresponding mass of 202,200 tons (average deposit density = 400 kg m$^{-3}$), see Fig. 3.8, lower panel. The avalanche was characterized by a large potential erosion area $A_e$ 12 times larger than the release area ($I_{pe} = 12$). This large basin allowed the avalanche to increase its mass 12 times with respect to the initial mass ($I_g = 12$), the largest growth index calculated in our analysis (see Table 3.9).

## Avalanche of February 25$^{th}$, 1999

The third and largest avalanche was released on February 25$^{th}$ following a new snow precipitation of 1.9 m. Photogrammetry was applied before and after the avalanche event in both the release and deposition areas (see Fig. 3.9). The avalanche on February 25$^{th}$, because it was so exceptionally large, caused damage to the control points along the avalanche path (Gruber et al., 2002), destroying all the control points used to reference aerial photographs. As a result, temporary control points had to be rearranged and the accuracy of the photogrammetry decreased to ±0.60 m. However, because of the large deposition depth that in some areas reached 30 m, the accuracy is judged to be acceptable.
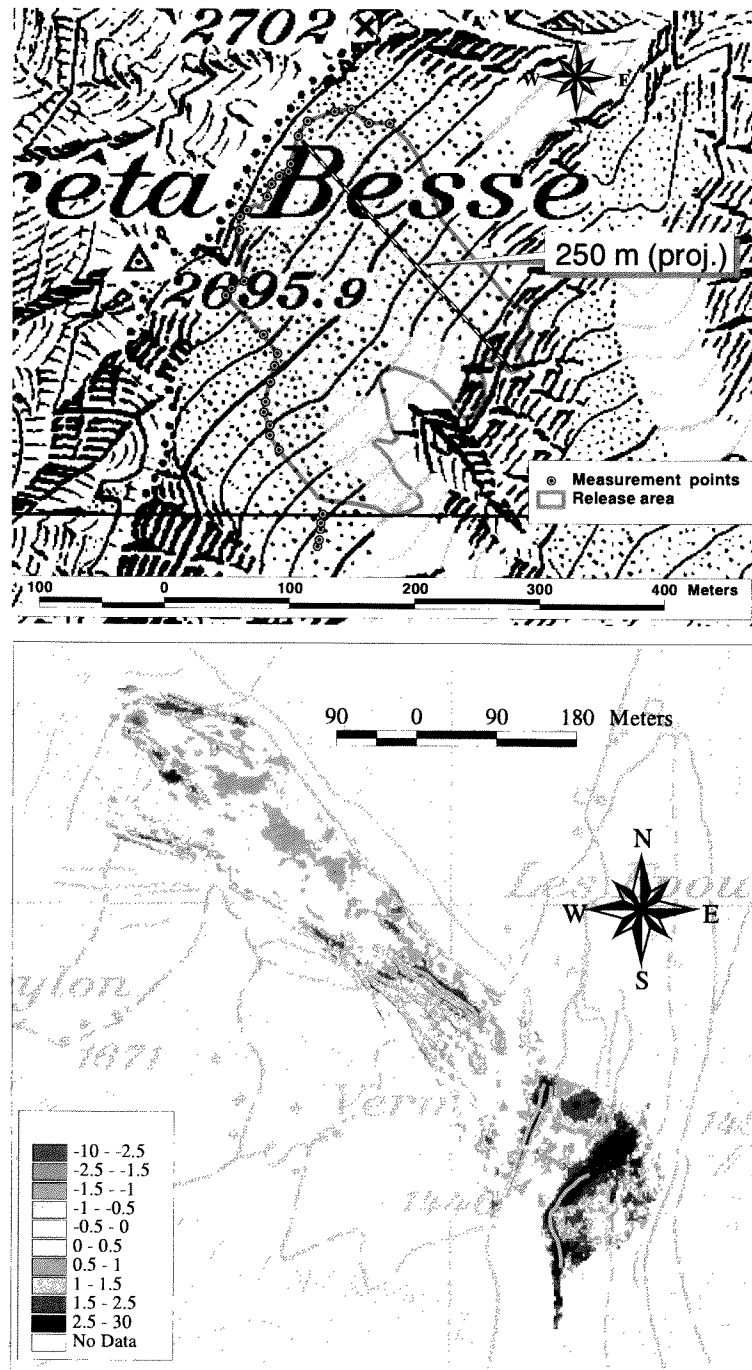
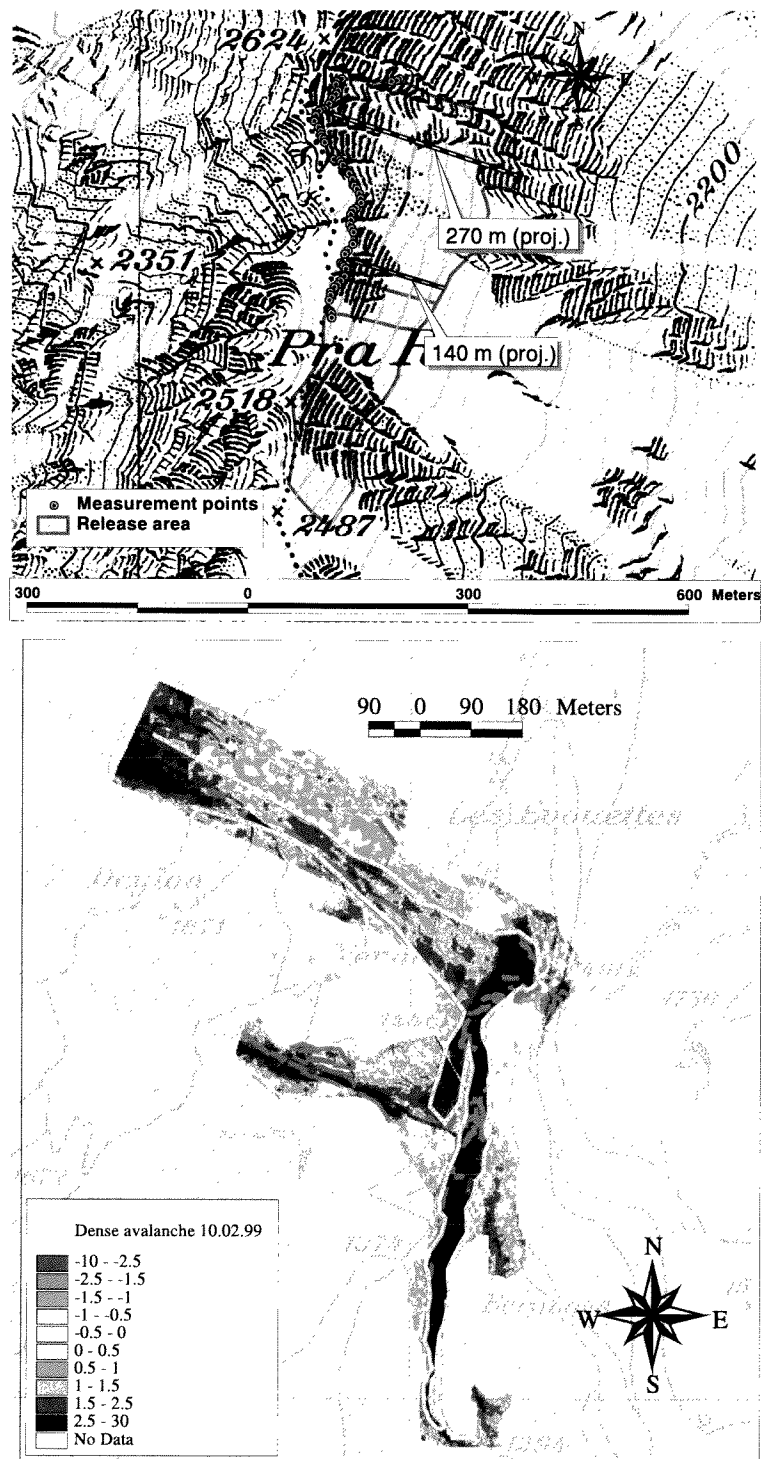**Figure 3.7:** *Avalanche of January 30$^{th}$ at the Vallée de la Sionne test site. Release area (upper panel) and deposition depths (lower panel) measured by photogrammetry (Gruber et al., 2002).*

**Figure 3.8:** *Avalanche of February 10th. 1999, at the Vallée de la Sionne test site. Release (upper panel) and deposition (lower panel) measured by photogrammetry (Gruber et al.. 2002).*

**Table 3.9:** *Vallée de la Sionne avalanche indices.* $I_{pe}$ = *potential entrainment index,* $Ipe_{SG}$ = *SG potential entrainment index,* $I_g$ = *growth index,* $I_{g_{SG}}$ = *SG growth index,* $I_{g_{SG300}}$ = *SG growth index for extreme avalanche,* $I_e$ = *entrainment index,* $I_{e_{SG}}$ = *SG entrainment index,* $I_{e_{SG300}}$ = *SG entrainment index for extreme avalanche.*

| Event | $I_{pe}$ | $I_{pe_{SG}}$ | $I_g$ | $I_{g_{SG}}$ | $I_{g_{SG300}}$ | $I_e$ | $I_{e_{SG}}$ | $I_{e_{SG300}}$ |
|---|---|---|---|---|---|---|---|---|
| **30.01.99** | 9.9 | 3.2 | $\sim 1$ | 0.4 | - | - | - | - |
| **10.02.99** | 12 | 2.8 | 12 | 3.5 | - | 0.9 | 0.9 | - |
| **25.02.99** | 3.8 | 2.2 | 6.0 | 4.0 | 3.0 | 1.3 | 1.4 | 0.9 |

The fracture depth was measured over a length of about 1 100 m and had an average depth of 1.5 m ($sd$ = 41 cm) (see Fig. 3.9, upper). This average fracture depth was used to calculate the total release volume of 316 300 m$^3$. The average snow density in the release was 200 kg m$^{-3}$; the initial mass was 63 300 tons.

The deposition volume and mass were 951 000 m$^3$ and 380 400 tons respectively. The avalanche increased its mass six times with respect to the initial mass ($I_g$ = 6) (see Table 3.9).

The avalanche crossed a potential erosion area of about 800 000 m$^2$ with an entrainment depth $d_e$ of about 2 m. The FMCW radar plot for this event shows, in effect, that the avalanche eroded all the snow cover to the ground (see Fig. 3.10, $a$) (Vallet et al., 2001).

## 3.4.2 Entrainment location and entrainment rate

Investigation of the entrainment location and rate is possible through analysis of the FMCW radar plots. Figure 3.10 shows four typical examples of FMCW radar output. At the bottom left of each plot it is possible to observe how the avalanche interacts with the snow cover. These measurements can be used to understand physical processes taking place between the avalanche and the snow cover and to determine the entrainment rate $\dot{E}$ [kg m$^{-2}$ s$^{-1}$]. When snow stratification and densities of the snow cover are known it is possible to measure the mass entrained by the avalanche per unit time and width.

Unfortunately, the stratigraphy and density of the snow cover in correspondence to the FMCW radar location can not be read directly from the FMCW plots and local field observations are difficult due to safety reasons. However, indication of snow cover stratigraphy and densities can be achieved from the data collected at the SLF meteorological station (*Donin du Jour*) located close to the avalanche path at an altitude of 2390 m a.s.l.
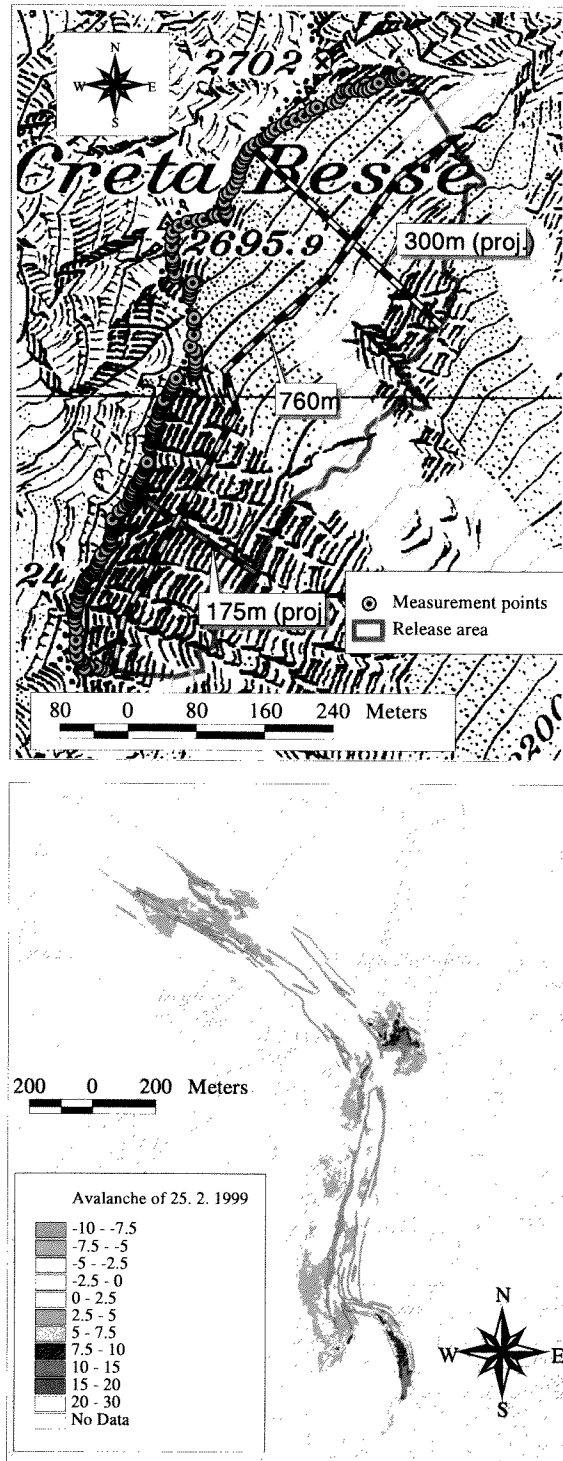
**Figure 3.9:** *Avalanche of February 25th, 1999, at the Vallée de la Sionne test site. Release (upper panel) and deposition (lower panel) measured by photogrammetry (Gruber et al., 2002).*
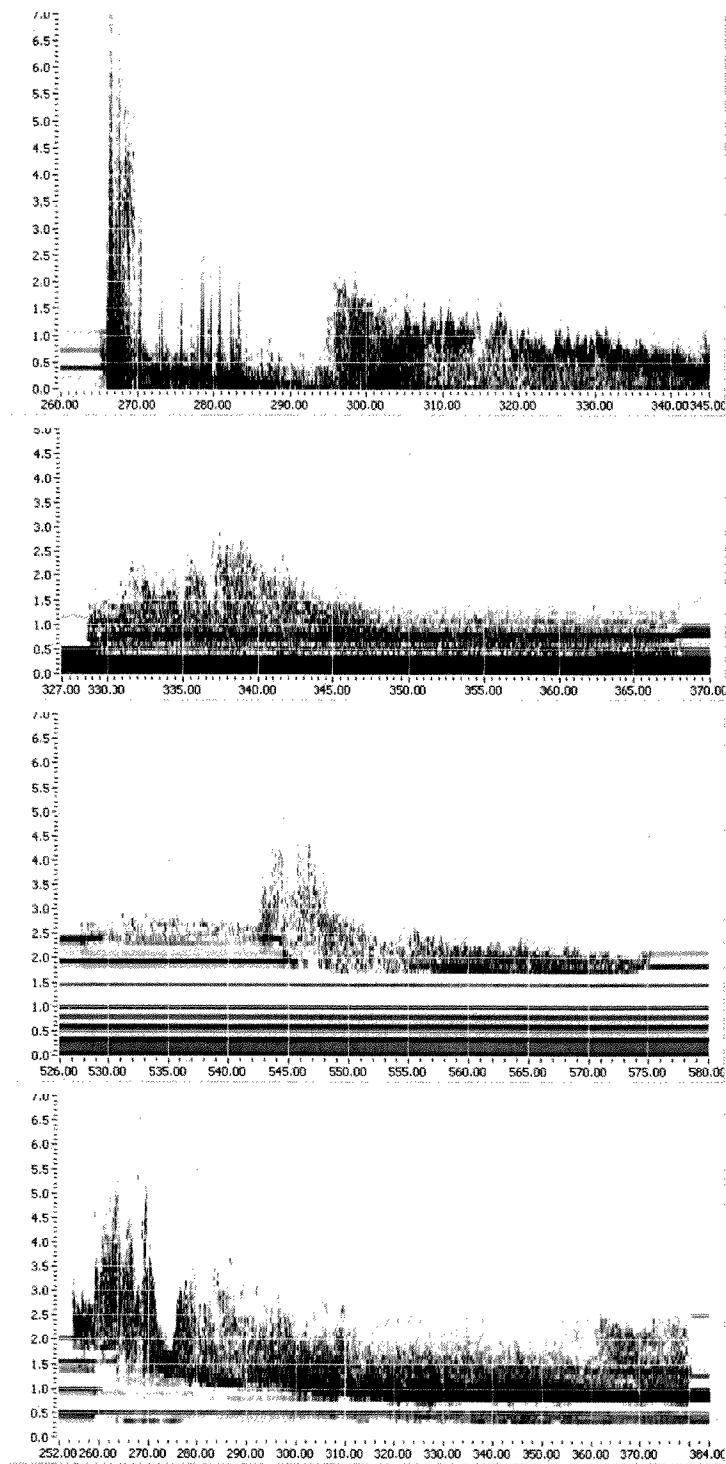
**Figure 3.10:** *FMCW radar height-intensity time plots measured at the Vallée de la Sionne test site (x-axis: time in seconds, y-axis: avalanche height in m). From the top to the bottom: avalanches of February 25<sup>th</sup>, 1999, radar b: January 29<sup>th</sup>, 2000, radar b: February 21<sup>st</sup>, 2000, radar a, December 29<sup>th</sup>, 2001, radar b.*
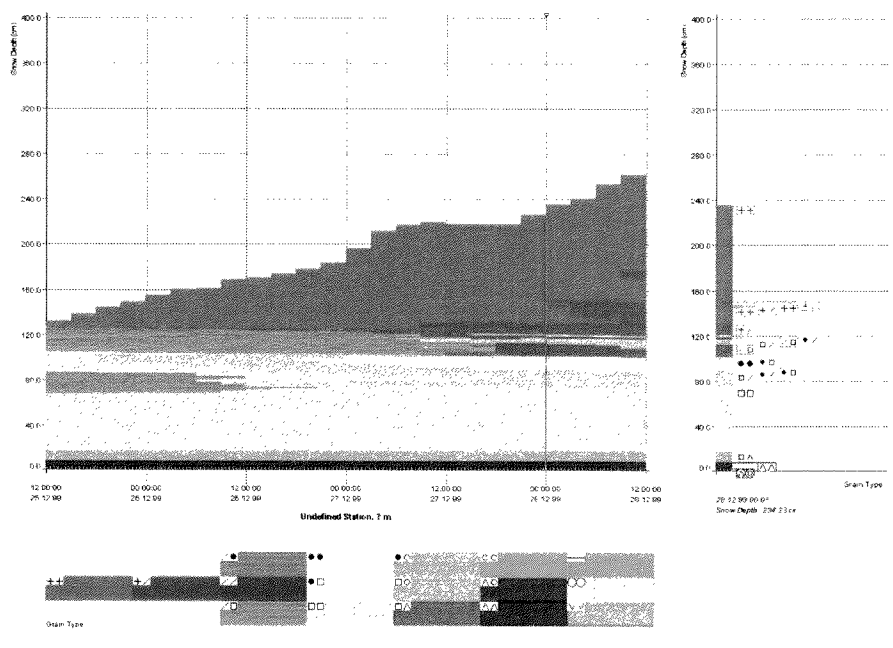
**Figure 3.11:** *The missing snow characteristics are calculated by SNOWPACK, an operational snow cover model that predicts, on the basis of the meteorological data obtained from the automatic station, snow settlement and layering in terms of depth, density and microstructure.*

Meteorological data such as new snow, snow and air temperature, wind intensity and direction are calculated with the finite-element based snow cover model *SNOWPACK* (Bartelt & Lehning, 2002; Lehning et al., 2002a,b). This is an operational model that predicts, on the basis of the meteorological data obtained from automatic stations, snow settlement and layering in terms of depth, density and microstructure (i.e. shape, dimension, bonding of the crystals composing the snow cover). Figure 3.11 shows a typical calculated snow cover. Snowpack modelling is not representative for the entire avalanche track because of the difference in altitude and because the snow cover layering in the avalanche path is frequently influenced by previous avalanche passages. However, it does provide an indication of the new snow precipitation in the area, especially for the FMCW radar positioned at an altitude of 2300 m a.s.l. (radar $a$), i.e. at about the same altitude as the meteorological station. The layering and the density plots in Fig. 3.11 correspond to the situation on December $28^{th}$, 1999, at midnight, two hours after the avalanche event on December $27^{th}$ shown in Fig. 3.12, recorded by the FMCW radar $a$. In the main plot of Fig. 3.11 the three-day snow cover evolution is shown. The snow cover (total depth 2.34 m) is composed of a 1.15 m thick superficial layer which corresponds to the new
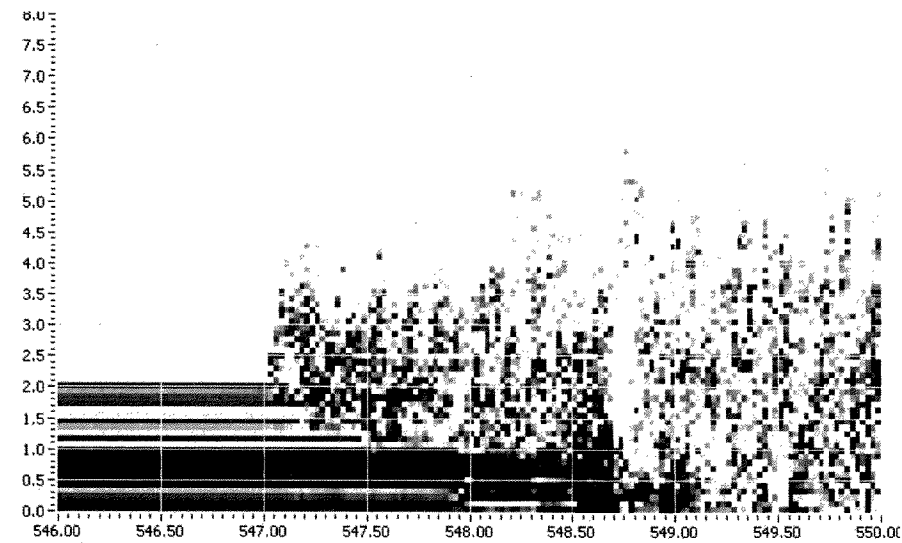
**Figure 3.12:** *FMCW radar plot from the avalanche of December 27$^{th}$, 1999, radar a. Detail of entrainment.*

snow precipitation in the last three days. This is underlain by an older snow cover mainly composed of metamorphosed particles and about 1.2 m thick. The average densities of the new and old snow cover were evaluated by *SNOWPACK* to be 160 and 330 kg m$^{-3}$, respectively.

The FMCW radar plot (Fig. 3.12) shows analogous snow cover characteristics. The total snow cover depth before the avalanche passage was 2.30 m. The avalanche entrained the first 1.30 m. more or less corresponding to the new snow layer of average density 160 kg m$^{-3}$), in about 1 sec. The avalanche then slid for 0.5 sec over a layer and then suddenly entrained all the remaining snow cover. which was about 1 m thick (average density 330 kg m$^{-3}$). The entrainment rates $\dot{E}$ were respectively 200 and 330 kg m$^{-2}$ s$^{-1}$. The avalanche was moving at a front velocity of 40 m s$^{-1}$; it was not possible to determine internal velocities. The analysis of the FMCW radar data revealed that:

1. Erosion may be concentrated at the avalanche front (see Fig. 3.10, *a*). The Figure shows the FMCW radar plot of a very large powder avalanche artificially released on February 25$^{th}$. 1999. radar *b*. The avalanche eroded a large quantity of snow immediately at the front. Normally. frontal erosion takes place when the snow cover has low density and low water content (powder snow).

2. Erosion may be distributed along the avalanche body (see Fig. 3.10, *d*). The fig-

ure shows a medium dimension dense avalanche naturally released on December 29$^{th}$, 2001. The avalanche progressively eroded 1 m of snow in about 50 sec. The entrainment was distributed along a large part of the avalanche length.

3. Erosion may be limited by the presence of a layer with high water content. Figure 3.10, b, shows a wet natural avalanche recorded on January 29$^{th}$, 2000. The avalanche entrained 1 m of snow immediately at the front and slid over a snow layer approx. 0.50 m thick without entraining any more mass. The sliding surface was formed by a layer with high water content, easily recognizable because of its large reflection (darker color). It is observed that layers with high water content are normally not eroded. Similar as in the Pizzac events discussed in section 3.3, the maximum height and intensity of the signal occur almost 10 seconds behind the avalanche front, corresponding to a distance of 200-500 m. The fact that the erosion is located in the front but the maximum flow height is located behind the front suggests that there is mass transfer from the avalanche head to the avalanche body, i.e. the collected snow requires a certain amount of time before it is accelerated up to the avalanche speed.

4. Erosion may be limited by the presence of an ice crust in the snow cover (see Fig. 3.10, c). The figure shows a medium dimension dense avalanche naturally released on February 21$^{st}$, 2000. The snow cover was characterized by two ice crusts easily recognizable in the plot because of the high reflection (dark lines at about 2.5 and 2 m respectively). The avalanche slid over the superficial crust for almost 15 seconds. The middle of the avalanche body (on the part with the highest flow height) eroded through this layer to a lower ice crust, where no more mass was entrained.

### 3.4.3 Discussion of experiment results

In most of the case studies presented here, the avalanche release volumes were considerably smaller than the deposit volumes, indicating entrainment of snow lying along the avalanche paths (see Tables 3.8 and 3.9). FMCW radar measurements confirm the photogrammetric findings that all the new snow cover and even parts of the old snow cover were entrained. However, even though all factors were favorable to mass entrainment (large potential entrainment area, light density snow conditions, formation of a powder avalanche) the avalanche of January 30$^{th}$ did not vary its mass ($I_g = 1.0$). The reason for this is not clear but does shows that the entrainment process can be quite irregular.

In general, the FMCW radar plots show that:
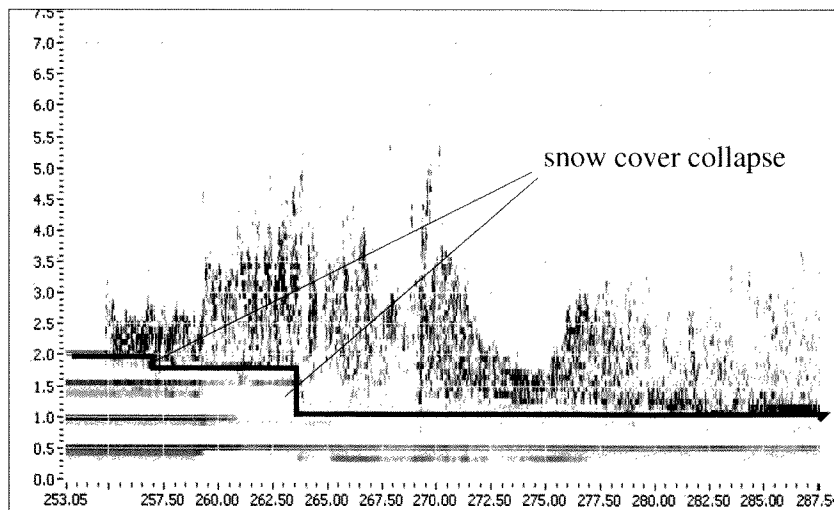
**Figure 3.13:** *FMCW radar $b$ plot from the December $29^{th}$, 2001 avalanche. The interface between avalanche and snow cover is shown by the dark line.*

1. When a clear sliding layer exists (i.e. an ice crust). the avalanche does not erode mass from this layer. Therefore, we conjecture that a pure shear stress is not responsible for erosion.

2. We observe that avalanches generally entrain the snow cover down to a more resistant, older snow layer or the ground. Frontal impact between the avalanche front and the snow cover takes place and the avalanche may collect all the snow immediately at the front. Powder snow is usually collected at the avalanche front.

3. Entrainment can also occur along the avalanche length (distributed or bed entrainment). As an avalanche starts to slide over a more resistant layer, sudden fracturing of the sliding plane can occur. changing the sliding plane. This process may occur many times during an avalanche. Figure 3.13 shows an example of this process. Entrainment is located at the step created between two different sliding surfaces. where again a frontal impact between the avalanche and the snow cover takes places. i.e. as in the *ploughing* case. We call the process as *step entrainment.*

## 3.5 Further investigated avalanches of the catastrophic winter 1998/99

### 3.5.1 The Obergoms avalanches

The Obergoms valley is located in the north-eastern part of the Canton Valais, near the Central Swiss Alps at the origin of the Rhône River. The main valley extends from NE to SW. Many small, mostly narrow side valleys exist, through which the avalanches flow into the main valley. Several small villages are situated near the entrances of these side valleys. During the winter 1998/99, especially between February $20^{th}$ and $25^{th}$, avalanches of extraordinary size occurred in nearly all known avalanche tracks (Gruber & Bartelt, 2001). They damaged and destroyed buildings, roads, power lines, railway lines and caused one fatality. We will focus on an area between the villages of Geschinen and Oberwald. In this area four avalanches were studied. The avalanches developed both on open slopes and in narrow gullies.

During the winter 1998/99 there were three large snowfall periods within a time period of less than one month (Wilhelm et al., 2001). The first period between January $27^{th}$ and $29^{th}$ brought a total new snow amount of 0.80 to 1.30 m, measured at the valley bottom. The snowfall was accompanied by strong winds. The second snowfall (February $5^{th}$ $10^{th}$) accumulated another 0.80 1.30 m of snow. The snowfall was again accompanied by strong north-westerly winds. During this period, avalanches with very large fracture depths were observed. The last of the three large snowfall periods started on February $17^{th}$. At that time the snow depth in the upper part of the Obergoms Valley reached 1.2 to 1.8 m. Between February $17^{th}$ and $25^{th}$, 1.90 to 2.80 m of new snow was deposited. Between February $20^{th}$ and $22^{th}$ the temperature increased remarkably and it rained up to an altitude of 1600 1800 m a.s.l. During this period the snow became very wet and the snow cover settled (Lauber, 1999). For example, in the village of Obergoms a new snow depth of 1.09 m was measured between February $20^{th}$ and $22^{nd}$ but the snow depth increased by only 0.21 m. The avalanches analyzed in this work occurred on February $9^{th}$, $22^{nd}$ and $23^{rd}$. Part of the avalanches recorded on February $22^{nd}$ and $23^{rd}$ were wet dense snow avalanches; however, several of the avalanches also had a powder component.

### 3.5.2 The Obergoms avalanche data

Aerial stereo-photographs of the area (scale 1:10 000) were taken immediately after the avalanche events and during the summer (SLF, 2000) by the Swiss Federal Office of

Topography. The difference between the terrain heights in winter and in summer allowed the snow volumes on the ground to be determined (§2.2.4). Photogrammetric calculations were performed by different private engineer offices. The photographs were also used to localize the release area of each avalanche and its flow perimeter. The volume in the deposition area could be determined by photogrammetry, but the determination of the fracture depths was not precise.

We assume a fracture depth of 2 m for all avalanches (based on the photographs taken in the release zone after the Loeuewenebach event of February $9^{th}$). Photogrammetry provided snow depth data along profiles parallel to the avalanche trajectory, thereby giving information on the erosion and deposition processes along the avalanche path. In the following a detailed description of the data collected for each avalanche is given.
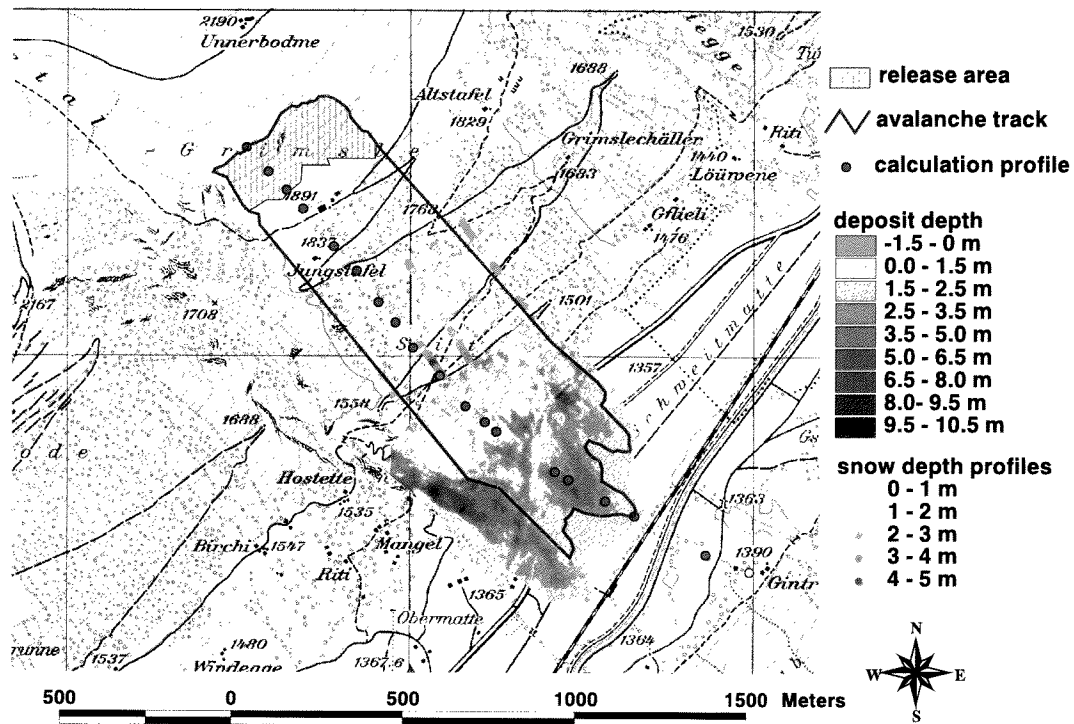
*The Jungstafel avalanche.* On February $22^{nd}$ at 14:15 p.m., an avalanche north-east of the village of Obergesteln descended into the main valley from a south-east facing release zone. The Jungstafel avalanche started from an open slope and discharged directly into the main valley. The starting zone was between 2 080 and 1 920 m a.s.l. The type of deposition suggested that the avalanche had a powder component but the exact distinction between the dense and the powder component is not clear in this case.

Aerial stereo-photographs of the area (scale 1:10 000) were taken immediately after the avalanche. The photogrammetry provided: deposition depths, deposition volumes and snow depth along profiles parallel to the avalanche trajectory providing information on the erosion and deposition processes along the avalanche path. An overview of the measurements made is given in Fig. 3.14. The release area was determined by geo-referencing the aerial pictures. Both upper and lower limits of the initial slab were visible in the photographs.

The spatial accuracy of the photogrammetric measurements was tested over small random areas by manual measurements (581 points). The accuracy of the data can be expressed by the root-mean-square error $rms$ and by the standard deviation $sd$. We found: $rms = 0.4$ m and $sd = 0.34$ m.

Deposition heights up to 6 m were measured. The total deposition volume of the avalanche is approx. 215 000 $m^3$. Measured values and those calculated using the Swiss Guidelines are summarized in Table 3.11. The calculated compression index $I_\rho$ varies between 2–3 (1 for very wet snow, see Table 3.7). We assume that the release density is equal to 200 kg $m^{-3}$, the deposition average density is 400 kg $m^{-3}$; that is we used a compression factor $I_\rho = 2$. Indices are summarized in Table 3.12. The snow depth in the flowing zone after the avalanche passage was measured along 5 profiles via photogrammetry (see Fig.

**Figure 3.14:** *Jungstafel avalanche. Release area, perimeter and deposition of the avalanche of February 22$^{nd}$, 1999, are shown. Deposition depth and snow depth in the avalanche track along five profiles are determined by photogrammetry. The accuracy of the measurements is ± 0.4 m*

3.14). Figure 3.15 shows an example of the photogrammetric measurements; diagram $d$ shows the snow depth in the valley bottom in an area adjacent to the deposition zone. The horizontal solid bold line represents the calculated average snow depth value (1.95 m, accuracy ± 0.4 m). The solid lines in diagrams $a$, $b$ and $c$ show the snow depth after the avalanche passage in the flowing zone along three profiles. The difference between the snow depth and the average snow depth at the valley bottom (horizontal lines) gives an idea of the erosion along the avalanche path. In this case, this difference indicates that the avalanche eroded mass all along the path, but also that a lot of snow was left on the ground. This is likely due to the high water content in the snow cover that limited the erosion (see §3.4.2).

*The Cheer and Cheer-west avalanches.* On February 23$^{rd}$, at 9.00 a.m., close to the village of Oberwald, two avalanches flowed into the main valley from an avalanche area of north-westerly aspect. The main avalanche (Cheer avalanche) started on an open

93
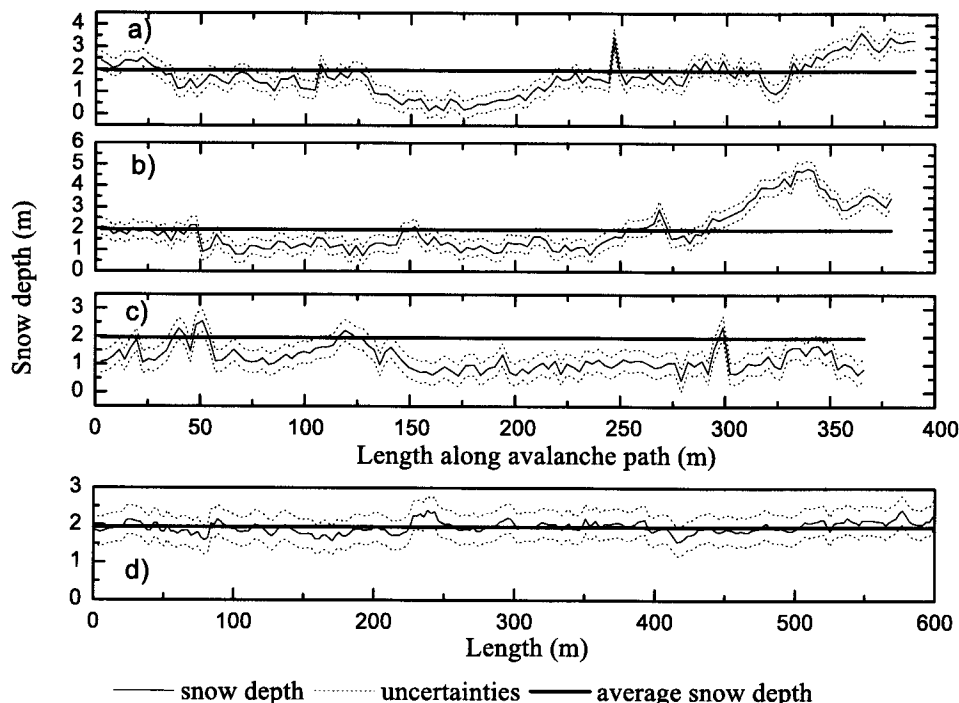
**Figure 3.15:** *Photogrammetry results for Jungstafel avalanche. Diagrams a, b and c show the snow depth (solid lines) in the avalanche path after the avalanche passage for 3 of the 5 profile represented in Figure 3.14 . Diagram d shows the snow depth (solid line) at the valley bottom. The bold horizontal lines represent the average snow depth at the avalanche bottom. The accuracy of all measurements is ± 0.4 m (dotted lines).*

slope at an altitude between 2115 and 1960 m a.s.l. A secondary avalanche (Cheer-west) released simultaneously from an adjacent narrow channel. Both avalanches reached the railway line located at about 1355 m a.s.l. Aerial photographs taken after the events and photogrammetry analysis allowed the deposition volumes to be determined (see Fig. 3.16). The deposition volume is approx. $337\,000$ m$^3$ and $125\,000$ m$^3$ for the Cheer and Cheer-west avalanches, respectively. Deposition depths up to 6 m were measured. The release perimeters were clearly defined and the area determined by geo-referencing the aerial photographs. Tables 3.11 and 3.12 summarize the measurements and the calculated indices.

*The Loeuewenebach avalanche.* On February $9^{th}$, at 22.00 hours, close to the village
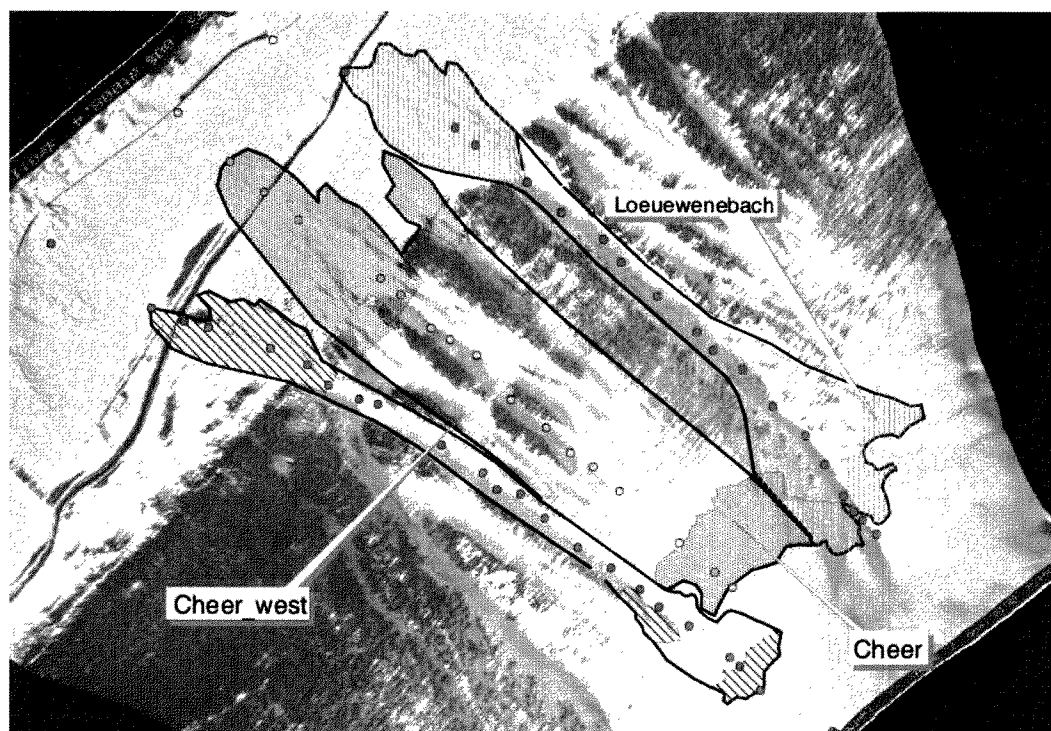
**Figure 3.16:** *Cheer, Cheer-west and Louewenebach avalanches. The release (hatched area on lower right corner), the deposition (hatched area on upper left corner) and the avalanche outline of February $9^{th}$ (Louewenebach) and February $22^{nd}$, 1999, (Cheer and Cheer-west) avalanches are shown. The avalanches are plotted on a geo-referenced aerial photograph taken on February $26^{th}$, 1999.*

of Oberwald, a large avalanche flowed into the main valley from a north-west exposed avalanche area. This avalanche was still visible in the aerial pictures of February $26^{th}$. The avalanche started at an altitude between 1980 and 2120 m a.s.l. and developed along a narrow channel as a mixed (powder/dense snow) avalanche. At the time of the measurements only the dense avalanche deposits were still visible. The deposition volume and release area were calculated by photogrammetry and analysis of aerial photographs, respectively. Tables 3.11 and 3.12 compile a summary of the measurements and of the indices.

*The Ulrichen avalanche.* On February $22^{nd}$, at 13.00 hours, close to the village of Ulrichen, a large dense avalanche flowed into the main valley from a south-southeast exposed channelled path. The avalanche started from a large basin between 2300 and 1700 m a.s.l. The analysis of the geo-referenced aerial pictures shows that the avalanche release area was composed of multiple zones. Figure 3.17 shows a map of the avalanche site. Snow
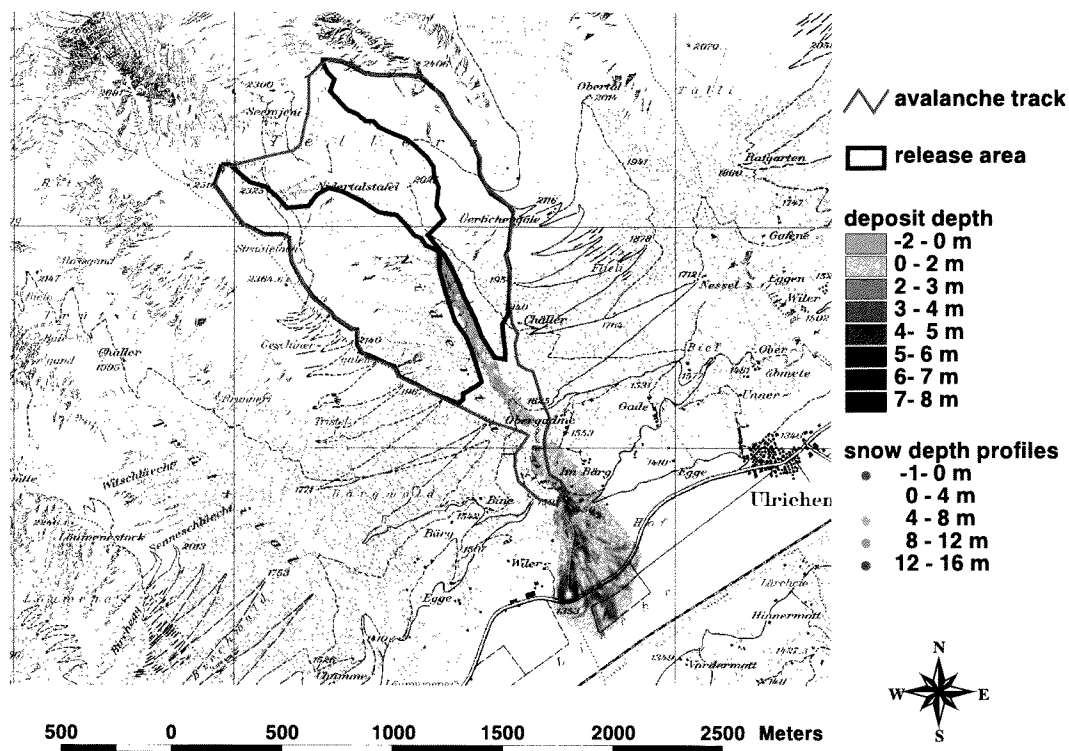
**Figure 3.17:** *Ulrichen avalanche. Avalanche track, release areas and photogrammetric measurements.*

was released from the valley sides respectively S-SW and E exposed and converged in the S-SE exposed main channel, through which the avalanche flowed. The deposition volume was determined by photogrammetry as $770\,000$ m$^3$. The mean deposition depths were about 7 m in the last part of the channel and about 3 m in the open field. Measured values and indices are shown in Tables 3.11 and 3.12. Previous smaller events on January 28th and 29th complicated the analysis of the main event. Due to the difficulty of associating correct release areas and corresponding deposition volumes to each avalanche, Table 3.11 is incomplete. This avalanche was characterized by a very large release area in comparison with the potential erosion area, making the erosion process insignificant (see Fig. 3.17).

## 3.5.3 The Aulta avalanche

The Medel valley is located in the Canton of Grisons in the Central Alps. During the winter 1998/99, between January 26th and February 25th, snow precipitation frequently accompanied by strong winds from the north-west brought a large amount of snow. On

February $25^{th}$ a large avalanche was artificially released from a S-SE exposed lateral valley (Val Aulta). The Aulta avalanche started on an open slope at an altitude between 2580 and 2200 m a.s.l. and descended into the main valley, following a narrow channel. The Aulta avalanche was released simultaneously to an adjacent smaller avalanche (Sparsa). The avalanches converged in the deposition zone (see Fig. 3.18).

## 3.5.4 The Aulta avalanche data

Aerial stereo-photographs of the area (scale 1:16 000) were taken immediately after the avalanche. The photogrammetry provided (Clement, 1999): fracture depth, snow depth measurements in the avalanche track after the avalanche passage, snow depth measurements outside the avalanche track and deposition depths and volumes. The photogrammetry also provided snow depths along profiles parallel to the avalanche's trajectory. Additional pictures and manual measurements were taken in the release zone after the event. In the following a detailed description of the collected data is given. An overview of the measurements is given in Fig. 3.18.

*Fracture depth.* It was possible to measure the fracture depth along 1110 m of fracture line from the aerial photos. Figure 3.18 shows an overview of the measurements. The average accuracy of the snow depth point measurements along the release crown is calculated to be ± 14 cm. Larger errors should be expected due to the low contrast of the snow cover at particular points along the fracture line.

The accuracy of a single point measurement (noise in the measurement) can be estimated by comparing fracture depth measurements of neighboring points $d_{0_i}$, $d_{0_{i-1}}$, assuming that they have approximately the same depth. The noise $N$ is then calculated with the equation:

$$N = d_{0_i} - d_{0_{i-1}} \qquad (3.9)$$

Note that the noise of a single point (Fig. 3.19, right) does not significantly affect the average fracture depth since the average value of the noise is about zero (Vallet et al., 2001).

The average fracture depth perpendicular to the slope, $d_0$, was calculated for three fracture line segments. Table 3.10 shows the average fracture depth $d_0$, the standard deviation of the measurements, $sd$, and the length of the fracture line for the three segments in Fig. 3.18. The segment $a - b$ has the largest fracture depth ($d_0 = 1.35$ m). Since this value corresponds to the fracture zone released directly into the Aulta valley, it is considered
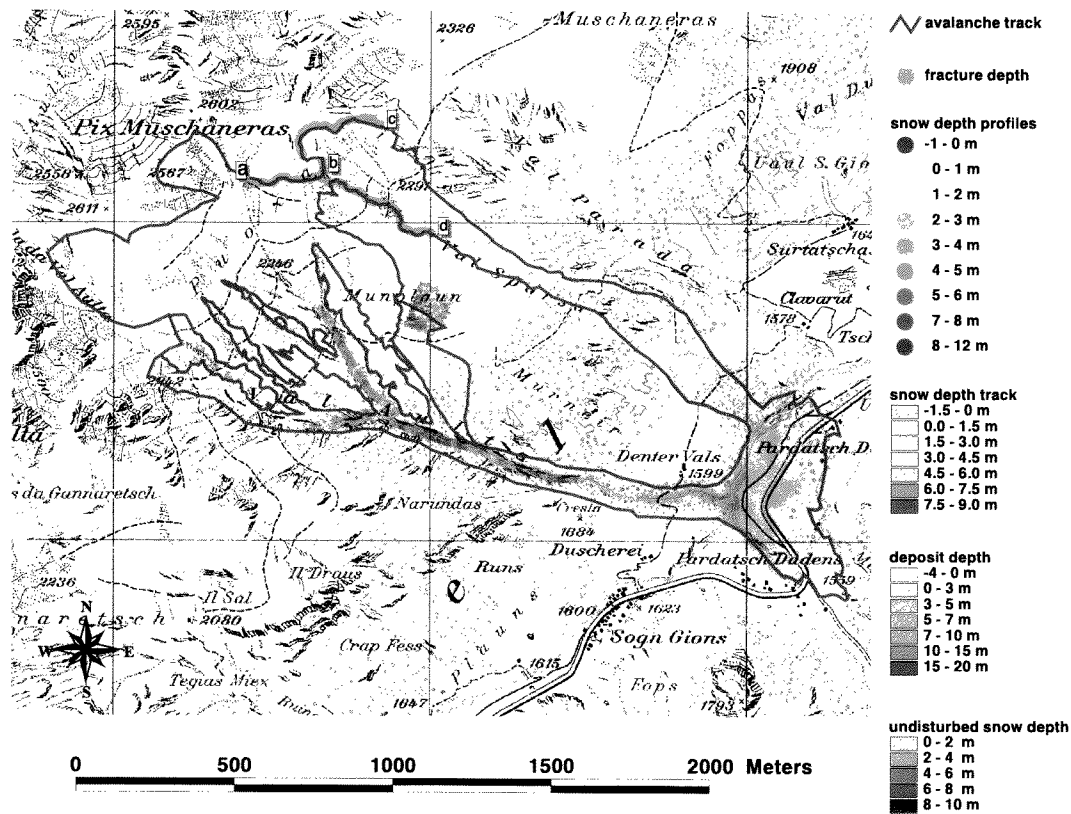
**Figure 3.18:** *Overview of the Aulta (left) and Sparsa (right) avalanche paths. The blue line delineates the avalanche outlines. Red lines at the crown: fracture line; yellow area: snow depth measurements in the avalanche track after the avalanche passage; green area: snow depth measurements outside the avalanche track; red lines in the avalanche channels: snow depth profiles in the avalanche track; pink area: deposition depths. All measurements were made by photogrammetry (Clement, 1999).*

**Table 3.10:** *Aulta avalanche. Average fracture depth, standard deviation and fracture length. Measurements were determined by photogrammetry.*

| Parameter | Notation | segment a-b | segment b-c | segment b-d | segment a-b-c-d |
|---|---|---|---|---|---|
| Fracture depth (m) | $d_0$ | 1.35 | 1.30 | 0.82 | 1.12 |
| Standard deviation (m) | $sd$ | 0.50 | 0.63 | 0.48 | 0.59 |
| Fracture length (m) | $w_r$ | 280 | 370 | 460 | 1110 |

the most representative of the fracture depth. The avalanche volume in the release area is estimated on the basis of this value.
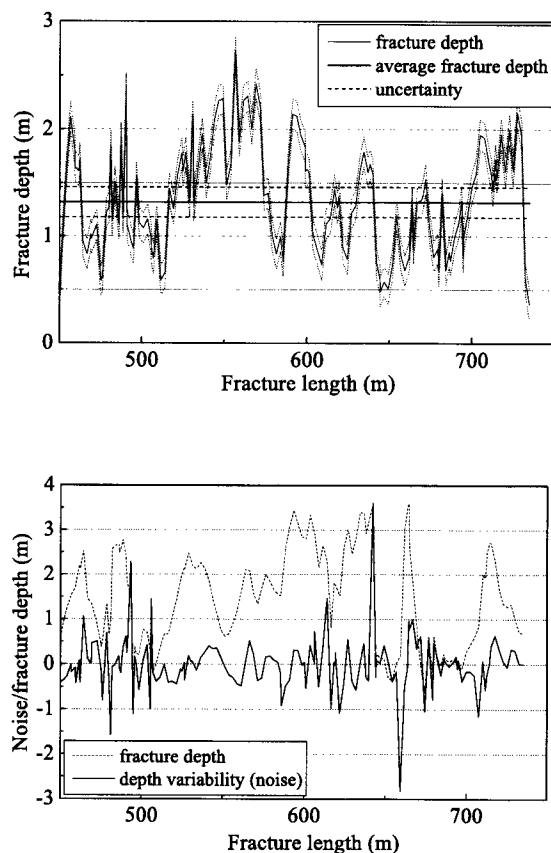
**Figure 3.19:** *Aulta avalanche. Top: fracture depths along the fracture line measured by photogrammetry. Results concerning the segment a − b are shown (see Fig. 3.18). Dotted lines indicate error of single point measurements (± 14 cm). Bottom: noise of the fracture depth measurements.*

*Release area, volume and mass.* In the geo-referenced pictures the release crown was visible but the lower boundary of the fracture slab was not recognizable because it was erased by the avalanche passage. This made it impossible to determine $A_r$. The SG release area $A_{r_{SG}}$ was defined on the basis of the the Swiss Guideline (SLF, 1999). The measurements are summarized in Table 3.11.

The release volume was calculated on the basis of the release area $A_{r_{SG}}$ using a fracture depth of 1.35 m. An average snow density of 200 kg m$^{-3}$ was measured in a snow pit dug adjacent to the release area immediately after the event.

The areas inside and outside the avalanche track were investigated. The data collected consists of grid measurements with a spatial resolution of 5 m. Figure 3.18 shows the
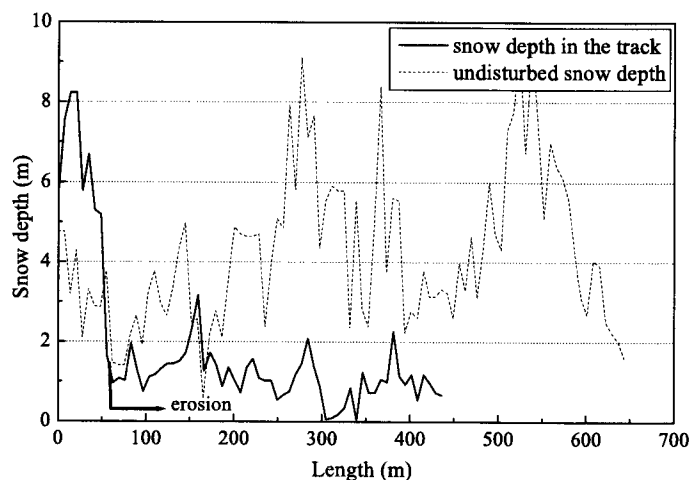
**Figure 3.20:** *Aulta avalanche. Snow depth measurements inside and outside the avalanche track. Single point measurement error was evaluated in ± 14 cm.*

position and extent of the analyzed areas. The dotted line in Figure 3.20 shows the snow depth along a profile in the undisturbed area (green area), the solid line shows the snow depth along a profile in the avalanche track (yellow area). It is observed that the snow cover depth in the avalanche track (1.45 m) is lower than the snow cover depth in the undisturbed area (3.9 m), suggesting that a snow layer approx. 2.45 m deep was entrained.

The variability of the snow cover height prior to the avalanche suggests that a large quantity of snow was re-distributed by the wind. The volume in the deposition zone was determined on a grid of locations with a spatial resolution of 2.5 m. The grid covers the final part of the channel (see Fig. 3.18). Maximum deposition depths of up to 20 m were found at the bottom of the valley, but deposition along the narrow channel was also observed. The upper part of the channel was covered by snow depth profile measurements. The contribution from the Sparsa avalanche was excluded from the analysis. The overall volume in the deposition zone was estimated to be 560 000 m³. Assuming an average deposition density of 400 kg m$^{-3}$ the final mass reached 224 000 t.

## 3.5.5 Discussion of survey results

The rough photogrammetric data (total volumes and depths in the release and deposition zone) were made available by the Swiss Federal Institute for Snow and Avalanche Research.

The data were analyzed during this work also by geo-referencing aerial photographs taken after each event. Table 3.11 shows a summary of the measurements collected during the winter 1998/99.

In the Obergoms valley, the calculated entrainment depths $d_e$ and $d_{e_{SG}}$ varied between 0.55–1.4 m and 0.4–1.1 m, respectively, for avalanches on NW facing slopes. The minimum values come from the Jungstafel avalanche.

In comparison with previous studies on mass entrainment (Sovilla et al., 2001; Vallet et al., 2001; Sovilla & Bartelt, 2002), snow entrainment was relatively minor for the present avalanches. The high snow water content due to the rain precipitation had obviously an important influence on the entrainment process and as a consequence on the runout distances. Experiments at the Swiss experimental site Vallée de la Sionne, at the Italian site Pizzac and general field observation (Sovilla et al., 2001) showed that the entrainment process is strongly influenced by the snow water content. In particular high water content in the snow decreases the ability of the avalanche to erode snow along the avalanche path. In this case entrainment only occurs in the steeper parts of the track (see §3.4.2). For the Jungstafel avalanche, on average, 0.55 m of snow were entrained. Figure 3.15 ($a$, $b$ and $c$) shows that the entrainment reaches higher values in the steeper parts of the track (from 50 to 250 m) but, over less steep terrain, the entrainment was limited (from 250 m to the end).

The growth index and the SG growth index varied between: $I_g$= 2.5–4.5 and $I_{g_{SG}}$= 1.4–2.0, respectively.

The situation was quite different for the Aulta avalanche where the entrainment depth $d_e$ reached 2.3 m. In this case the dry snow cover allowed the entrainment of a large quantity of snow. The SG growth index was $I_{g_{SG}}$ = 2.0 (see Table 3.12).

A third case is represented by the Ulrichen avalanche. As shown in Figure 3.17 the avalanche had large multiple release areas and a very small flowing area (approximately the red area in Fig. 3.17). The avalanche did not have the possibility to erode large quantities of snow along the path and entrainment did not play a fundamental role in the avalanche motion.

101

# 3. FIELD EXPERIMENTS AND OBSERVATIONS

**Table 3.11:** *Summary of the measurements collected during the winter 1998/99 by photogrammetry and analysis of the geo-referenced aerial photographs. (SG = Swiss Guidelines).*

| Parameter | Not. | Loeue. | Jungs. | Ulrichen |
|---|---|---|---|---|
| Release area (m$^2$) | $A_r$ | 60 200 | 85 800 | - |
| Release area SG (m$^2$) | $A_{r_{SG}}$ | 192 200 | 134 700 | - |
| Fracture depth (m) | $d_0$ | 2.00 | 2.00 | - |
| Fracture depth SG300 (m) | $d_{SG300}$ | 1.40 | 1.20 | - |
| Release volume (m$^3$) | $V_r$ | 120 400 | 171 600 | - |
| Release volume SG (m$^3$) | $V_{r_{SG}}$ | 384 400 | 269 400 | - |
| Release volume SG300 (m$^3$) | $V_{r_{SG300}}$ | 269 100 | 161 700 | - |
| Release snow density (kg m$^{-3}$) | $\rho_r$ | 200 | 200 | - |
| Release mass (tons) | $M_r$ | 24 080 | 34 320 | - |
| Release mass SG (tons) | $M_{r_{SG}}$ | 76 880 | 53 880 | - |
| Release mass SG300 (tons) | $M_{r_{SG300}}$ | 80 730 | 48 500 | - |
| Deposition snow density (kg m$^{-3}$) | $\rho_d$ | 400 | 400 | 400 |
| Deposition volume (m$^3$) | $V_d$ | 272 700 | 214 050 | 771 900 |
| Deposition mass (tons) | $M_d$ | 109 100 | 85 600 | 308 750 |
| Potential entrainment area (m$^2$) | $A_e$ | 298 500 | 470 750 | - |
| Potential entrainment area SG (m$^2$) | $A_{e_{SG}}$ | 166 500 | 421 850 | - |
| Entrainment depth (m) | $d_e$ | 1.40 | 0.55 | - |
| Entrainment depth SG (m) | $d_{e_{SG}}$ | 1.00 | 0.40 | - |
| Entrainment depth SG300 (m) | $d_{e_{SG300}}$ | 0.60 | 0.30 | - |
| **Parameter** | **Not.** | **Cheer** | **Cheer w.** | **Aulta** |
| Release area (m$^2$) | $A_r$ | 80 200 | 28 100 | - |
| Release area SG (m$^2$) | $A_{r_{SG}}$ | 163 700 | 87 100 | 426 000 |
| Fracture depth (m) | $d_0$ | 2.00 | 2.00 | 1.35 |
| Fracture depth SG300 (m) | $d_{SG300}$ | 1.35 | 1.45 | 1.35 |
| Release volume (m$^3$) | $V_r$ | 160 400 | 56 200 | - |
| Release volume SG (m$^3$) | $V_{r_{SG}}$ | 327 400 | 174 200 | 575 100 |
| Release volume SG300 (m$^3$) | $V_{r_{SG300}}$ | 221 000 | 126 300 | 575 100 |
| Release snow density (kg m$^{-3}$) | $\rho_r$ | 200 | 200 | 200 |
| Release mass (tons) | $M_r$ | 32 080 | 11 240 | - |
| Release mass SG (tons) | $M_{r_{SG}}$ | 65 480 | 34 840 | 115 020 |
| Release mass SG300 (tons) | $M_{r_{SG300}}$ | 66 300 | 37 900 | 172 500 |
| Deposition snow density (kg m$^{-3}$) | $\rho_d$ | 400 | 400 | 400 |
| Deposition volume (m$^3$) | $V_d$ | 337 300 | 124 300 | 560 800 |
| Deposition mass (tons) | $M_d$ | 134 900 | 49 700 | 224 300 |
| Potential entrainment area (m$^2$) | $A_e$ | 393 700 | 163 250 | - |
| Potential entrainment area SG (m$^2$) | $A_{e_{SG}}$ | 310 200 | 104 250 | 235 600 |
| Entrainment depth (m) | $d_e$ | 1.30 | 1.20 | - |
| Entrainment depth SG (m) | $d_{e_{SG}}$ | 1.10 | 0.70 | 2.30 |
| Entrainment depth SG300 (m) | $d_{e_{SG300}}$ | 0.75 | 0.40 | 0.75 |

**Table 3.12:** Avalanche index. $I_{pe}$ = potential entrainment index, $I_{pe_{SG}}$ = SG potential entrainment index, $I_g$ = growth index, $I_{g_{SG}}$ = SG growth index, $I_{g_{SG300}}$ = SG growth index for extreme avalanches, $I_e$ = entrainment index, $I_{e_{SG}}$ = SG entrainment index, $I_{e_{SG300}}$ = SG entrainment index for extreme avalanches. SG = Swiss Guidelines.

| Event | $I_{pe}$ | $I_{pe_{SG}}$ | $I_g$ | $I_{g_{SG}}$ | $I_{g_{SG300}}$ | $I_e$ | $I_{e_{SG}}$ | $I_{e_{SG300}}$ |
|---|---|---|---|---|---|---|---|---|
| **Loeuewenebach** | 5.0 | 0.9 | 4.5 | 1.4 | 1.4 | 0.70 | 0.50 | 0.40 |
| **Jungstafel** | 5.5 | 3.1 | 2.5 | 1.6 | 1.8 | 0.30 | 0.20 | 0.25 |
| **Cheer** | 4.9 | 1.9 | 4.2 | 2.0 | 2.0 | 0.65 | 0.55 | 0.55 |
| **Cheer–west** | 5.8 | 1.2 | 4.4 | 1.4 | 1.3 | 0.60 | 0.35 | 0.25 |
| **Aulta** | — | 0.6 | — | 2.0 | 1.3 | – | 1.70 | 0.55 |

The avalanche mass could only be described by a correct definition of the multiple release areas.

In summary, the avalanche mass evolution is strongly controlled by the snow cover characteristics. More specifically, dry snow is more favorable to entrainment than wet snow. When the snow characteristics are favorable, a large amount of snow entrainment takes place.

The entrainment index $I_e$ (see Table 3.12) varied between 0.30–0.7 ($I_{e_{SG}}$ between 0.20–0.55). The relatively low values are due to the high snow water content that limited the entrainment.

The Aulta avalanche had an entrainment index $I_e$ = 1.7. The entrainment was favored by the dry low–density snow condition.

The analysis of the photogrammetric measurements collected during the winter 1998/99 in the Obergoms Valley demonstrated that the entrainment process can strongly influence the mass balance not only for small avalanches (Sovilla et al., 2001) but also for large avalanches. The mass evolution is also influenced by the deposition rate. Depositions were observed at different locations along the avalanche paths; however, the main deposits were generally located on gentle slopes. An example corresponding to the Aulta avalanche is shown in Fig. 3.21. Figure 3.21 shows a box chart with a statistical distribution of the snow depth in areas where deposition was observed as a function of the corresponding slope angle. The snow depth does not correspond only to the deposition depth but also to the snow lying on the ground after the avalanche passage. No manual profiles were performed to distinguish the layering of the deposits. In spite of this, the results show that even if snow deposition is observed along all the channel, the deposition depth increases
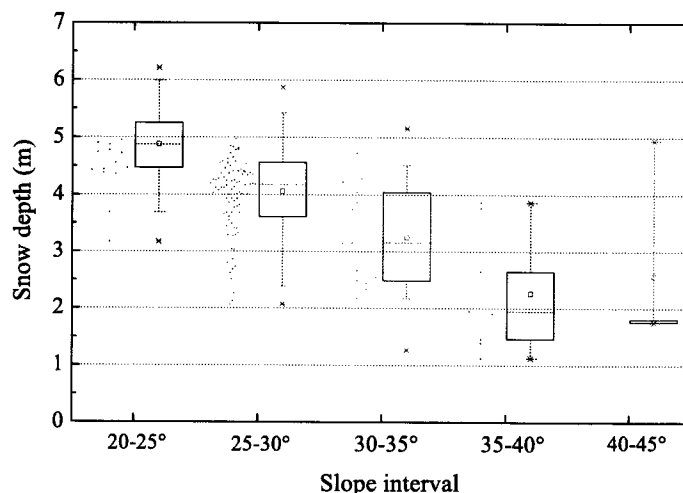
**Figure 3.21:** *Deposition depth along the avalanche path as a function of slope measured by photogrammetry. It is observed that the deposition depth increases significantly when the slope drops below 30°. The increase appears to be linear. The box plots show the mean (square in box), the median (line in box), 25/75% quantiles (box), 5/95% quantiles (whiskers) and 0/100% quantiles (cross).*

significantly when the slope drops below 30°.

# 3.6 The Braemabuel avalanche

In January 2000, field measurements of a natural avalanche were performed on the Braemabuel avalanche near Davos. The aim of these measurements was to collect information about entrainment and deposition processes in a spontaneous, medium-sized avalanche.

The avalanche occurred on January 31$^{st}$ on a NE exposed open slope. Defence structures located in the release area retained part of the initial mass, but a large part of the mass passed through. The avalanche descended into the Dischma valley following two parallel narrow channels and reached the valley road (see Fig. 3.22).

## 3.6.1 Avalanche data

Field measurements were performed immediately after the event and included: fracture depth in the release zone, snow depth and information on the deposition and entrainment processes along the avalanche track, snow depth outside the avalanche track and depths
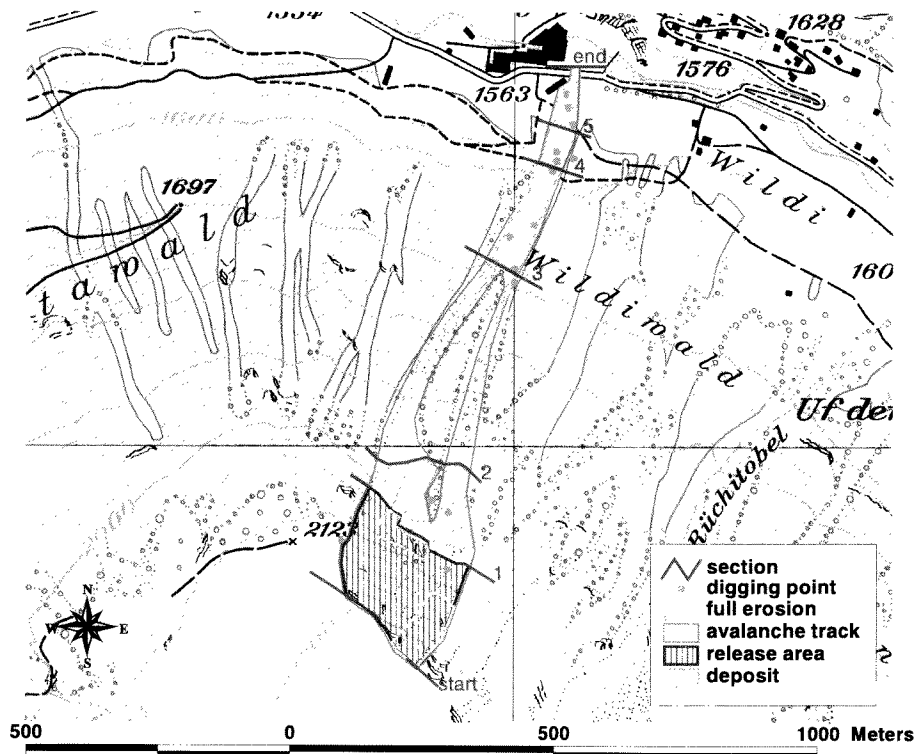
**Figure 3.22:** *Braemabuel measurements. Field measurements allowed the determination of the release area, fracture depth, deposition along the track and entrainment. Characteristics of the snow cover were determined by snow pits. The snow pit distribution is represented in the figure by red points.*

and volumes in the deposition area. In the following a detailed description of the collected data is given. An overview of the measurements is given in Fig. 3.22 and data are summarized in Tables 3.13 3.15. *Snow cover characteristics.* Information on the original snow cover was collected in areas adjacent to the starting and flowing zones where the snow was not influenced by the passage of the avalanche and where local variations of the snow cover due to topographic factors (small differences in slope) or meteorological influence (wind transport) were not evident. On average, the snow cover consisted of three layers: a 40 cm new snow layer having an average density of 200 kg m$^{-3}$ and an old layer about 50 cm thick having an average density of 300 kg m$^{-3}$: these two layers were separated by a thin ice crust. The bottom-most layer was 10 cm thick and composed of faceted crystals.

*Starting zone.* The avalanche started at 2240 m a.s.l: the stauchwall of the slab was located between 2070 and 2030 m a.s.l. The avalanche removed the fresh snow layer (40 cm thick) over all the release area. In some areas the old snow cover was also removed.

**Table 3.13:** *Calculation of the mass in the release, flowing and deposition zones for the Braemabuel avalanche. In the release zone the total mass, the mass retained by the structures and the release mass are shown. In the flowing and deposition zones entrainment and deposition masses are calculated.*

| Location (sector) | Area $m^2$ | Layer depth $m$ | Density $kg\ m^{-3}$ | Volume $m^3$ | Mass tons |
|---|---|---|---|---|---|
| **Release zone** | | | | | |
| Released mass (start–1) | 45200 | 0.4 | 200 | 18100 | 3600 |
| **Flowing zone** | | | | | |
| Erosion first layer (1–2) | 23500 | 0.4 | 200 | 9400 | +1880 |
| Erosion first layer (2–3) | 30000 | 0.4 | 200 | 12000 | +2400 |
| Erosion second layer (1–2) | 1500 | 0.5 | 300 | 750 | +220 |
| Erosion second layer (2–3) | 10800 | 0.5 | 300 | 5400 | +1620 |
| Left deposit below release | 8800 | 0.7 | 280 | 6160 | −1730 |
| Right deposit below release | 6200 | 0.7 | 280 | 4340 | −1200 |
| Upper deposit in the channel | 550 | 0.4 | 420 | 220 | −90 |
| Lower deposit in the channel | 1800 | 0.6 | 420 | 1080 | −450 |
| **Deposition zone** | | | | | |
| Erosion first layer (3–4) | 12400 | 0.4 | 200 | 4960 | +990 |
| Erosion second layer (3–4) | 9800 | 0.25 | 300 | 2450 | +730 |
| Deposit (3–4) | 10600 | 0.75 | 420 | 7950 | −3330 |
| Deposit (4–5) | 3600 | 2.0 | 470 | 7200 | −3380 |
| Deposit (5–end) | 4000 | 0.5 | 420 | 2000 | −840 |

The defence structures retained only a small part of the initial mass. We assume that the retained mass is equal to the mass removed from the old layer, thus the calculated release mass equals that for the new snow layer. The mass retained by the structures and the total mass in the release zone were also calculated (see Table 3.13 and Fig. 3.22).

*Flowing zone.* We define the flowing zone as the area between the lower part of the release zone and the end of the channelled part (area between sections 1 and 3 in Fig. 3.22). The avalanche entrained the fresh snow layer over the entire flowing zone. The layer of old snow was only partially eroded, with full erosion occurring only on the steepest slopes and in the channelled parts of the avalanche track. A large amount of snow was deposited immediately below the structures in an area having an average slope of 26° (2050–1980 m a.s.l.). Two small deposits were also located in the lower part of the right channel (see Table 3.13 and Fig. 3.22).

**Table 3.14:** *Braemabuel avalanche mass balance.*

| Section | Release mass tons | Erosion mass tons | Deposition mass tons | Avalanche mass tons |
|---------|-------------------|-------------------|----------------------|---------------------|
| start–1 | 3600 | — | — | +3600 |
| 1–2 | — | +2100 | −2930 | +2270 |
| 2–3 | — | +4020 | −540 | +6250 |
| 3–4 | — | +1720 | −3380 | +4640 |
| 4–5 | — | 0 | −3380 | +1260 |
| 5–end | — | 0 | −840 | +420 |

**Table 3.15:** *Braemabuel avalanche indices. $I_{pe}$ = potential entrainment index, $I_g$ = growth index, $I_e$ = entrainment index, $I_\rho$ = compression index.*

| Event | $I_{pe}$ $(A_e/A_r)$ | $I_g$ $(M_{max}/M_r)$ | $I_e$ $(d_e/d_0)$ | $I_\rho$ $(\rho_d/\rho_r)$ |
|-------|----------------------|-----------------------|-------------------|----------------------------|
| Braemabuel | 1.46 | 1.7 | 1.4 | 1.70 |

*Deposition zone.* The main deposit started at an altitude of 1690 m a.s.l. Between 1690 m a.s.l. and 1590 m a.s.l. the deposit was uniformly distributed over all the area. Maximum deposit depths were localized below 1590 m a.s.l. From 1590 m a.s.l to 1580 m a.s.l. the deposit depth increased progressively. The presence of eroded snow layers below the deposit was checked by snow profiles: the first (new snow) layer was fully eroded; the second (old layer) only partially. Below 1580 m a.s.l. little erosion was observed (see Table 3.13 and Fig. 3.22).

## 3.6.2 Braemabuel avalanche mass balance

The avalanche mass balance was calculated for the 5 sections shown in Fig. 3.22. The sections are positioned: (1) immediately below the release zone, (2) at 1980 m a. s. l. below the upper deposits, (3) at the end of the channelled part, (4) at 1580 m a.s.l. and (5) at 1565 m a.s.l. in the deposit. The initial mass was 3600 tons. The avalanche reached a maximum mass of 6250 tons, which is 1.7 times the initial mass. Results are shown in Tables 3.14 and 3.15. Figure 3.23 shows the mass balance analysis of this event. Figure 3.24 shows deposition and entrainment distributions along the avalanche path.
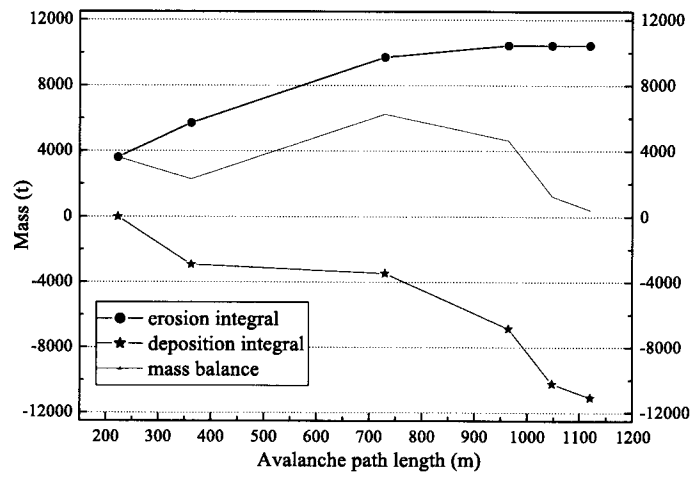
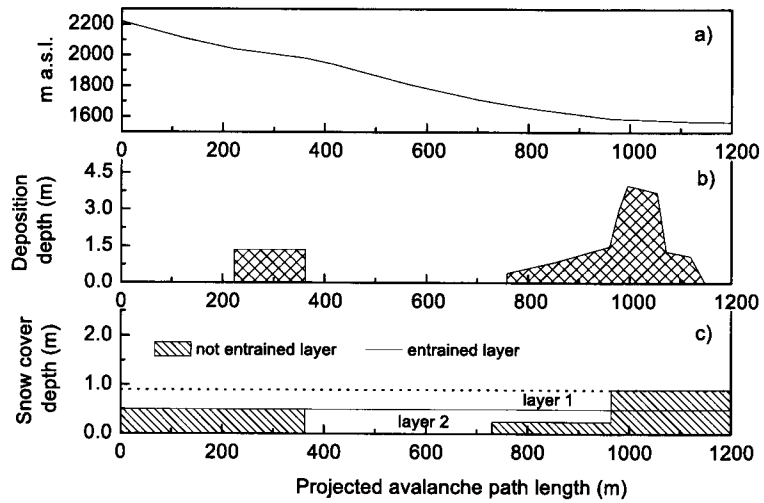**Figure 3.23:** *Braemabuel avalanche mass balance.*



**Figure 3.24:** *Braemabuel avalanche. Simplified description of the data. Avalanche profile, deposits distribution and layer erosion along the path.*

# 4 A theory of mass entrainment and deposition

As a prerequisite to understanding basic physical processes of snow entrainment and deposition the following questions must be answered:

- Under what conditions do entrainment and deposition occur?

- What are the dominant driving mechanisms leading to mass variations within an avalanche (collisions, scouring, erosion)?

To answer the first question, the avalanche dimension, the flow regime, the path topography and the snow cover characteristics are compared against potential entrainment, entrainment and growth indices to identify possible relationships.

The mechanical processes are investigated by analysis of FMCW radar plots.

We propose an entrainment theory based on these comparisons and observations.

## 4.1 Conditions for entrainment and deposition

The avalanche mass balance of seventeen avalanches of different dimensions and typologies have been determined in the preceding chapter. The potential entrainment index $I_{pe}$, the growth index $I_g$ and the entrainment index $I_e$ have been calculated for all the observed avalanches. Figure 4.1 shows the calculated avalanche indices in relation to the avalanche release mass. The indices are plotted on a logarithmic scale to represent the large avalanche mass variability in the analysis.

A statistical analysis of the avalanche indices is shown in Fig. 4.2. Both avalanche indices and practice avalanche indices have been studied.

### Growth index analysis

The growth index $I_g$ (see Figs. 4.1, $b$, and 4.2) indicates to what degree the avalanche masses increased. As shown by the graphs, the $I_g$ index can vary significantly.
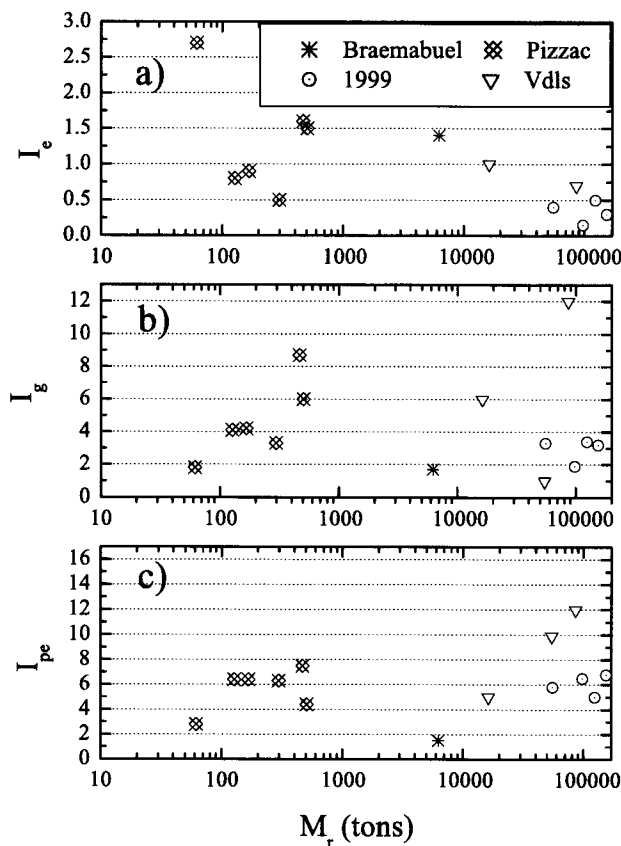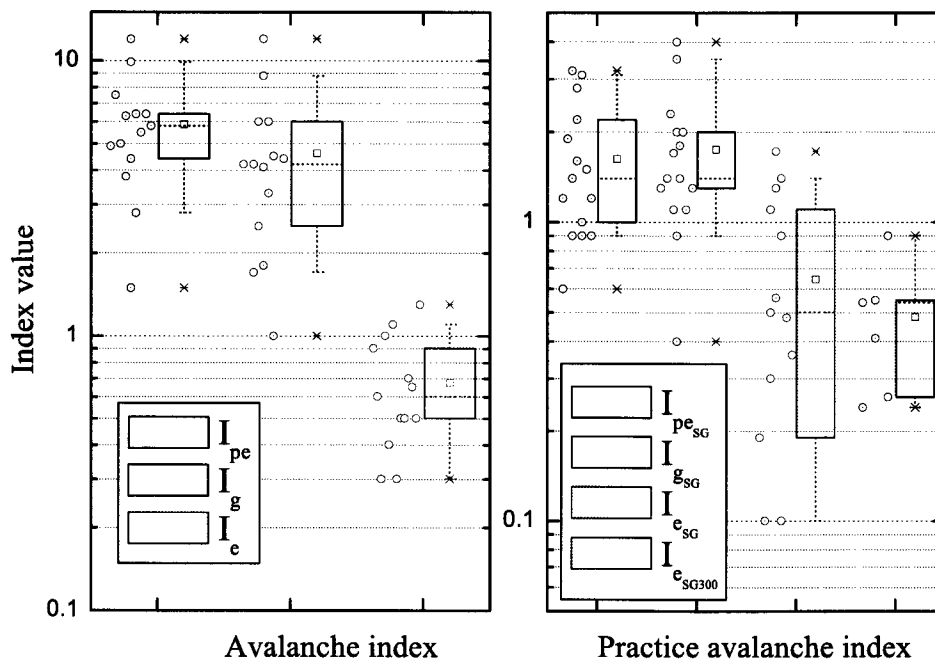
**Figure 4.1:** *The potential erosion $I_{pe}$, growth $I_g$ and entrainment $I_e$ avalanche indices are plotted as a function of the avalanche release mass. Vdls = Vallée de la Sionne.*

It is observed that:

- On average avalanches increase their mass by a factor $I_g = 4.6$.

- Entrainment is independent of topographic characteristics; at the Vallée de la Sionne site alone the growth index varies between $I_g = 1$ and $I_g = 12$ and at the Pizzac site between $I_g = 1.8$ and $I_g = 8.8$. This suggests that terrain characteristics are not the most important cause for entrainment.

- Entrainment is independent of avalanche size; small avalanches can increase their mass as large avalanches do. Extreme avalanches can increase their mass substantially, as in the case of the Vallée de la Sionne event of December $25^{th}$ ($I_g = 6.0$),

110

**Figure 4.2:** *Avalanche indices. On the left: potential erosion $I_{pe}$, growth $I_g$ and entrainment $I_e$ indices. On the right: practice potential erosion $I_{pe_{SG}}$, practice growth $I_{g_{SG}}$ and practice entrainment $I_{e_{SG}}$ indices. The practice entrainment index for extreme avalanches $I_{e_{SG300}}$ is also shown. The box plots show the mean (square in box), median (line in box), 25/75% quantiles (box), 5/95% quantiles (whiskers) and 0/100% quantiles (cross).*

or only slightly, as in the case of the avalanches of the Obergoms Valley (minimum value $I_g = 2.5$).

The analysis of the studied events attributes small growth indices to the following causes:

- Avalanche of December $5^{th}$, Pizzac test site, $I_g = 1.8$. The entrainment was quite large (see §3.3) but the avalanche began to deposit snow immediately below the release zone, therefore its mass did not increase. This was probably due to a combination of factors: the high roughness of the ground (it was the first avalanche of the season) did not allow the avalanche to increase its speed, while, at the same time, the avalanche was hindered by the large entrained mass. The avalanche had only a dense flow regime.

- Avalanches of the catastrophic Winter 1998/99, Obergoms valley, $I_g = 2.5$. The entrainment was limited by the high water content in the snow due to a rainfall preceding the event. The avalanche had a dense flow regime.

- Avalanche of January $30^{th}$, Vallée de la Sionne site, $I_g = 1$. The low growth index of this avalanche is yet not well understood. However, it is believed that the low snow entrainment is due to the lack of new snow available for entrainment. A previous avalanche (January $28^{th}$) entrained the available snow. The avalanche had a mixed flow regime.

The highest growth indices are attributed to the following causes:

- Avalanche of March $5^{th}$, Pizzac test site, $I_g = 8.8$. The combination of a very smooth, icy sliding surface and a low-density snow cover allowed the avalanche to reach high entrainment rates. Very little snow was deposited by the avalanche along the path. This was the only avalanche at the Pizzac test site that showed a mixed flowing regime.

- Avalanche of February $10^{th}$, Vallée de la Sionne site, $I_g = 12$. The potential entrainment index $I_{pe} = 12$ indicates that the avalanche had a very large potential entrainment area. This, together with the low density snow of the snow cover, allowed the avalanche to increase its mass. The avalanche had a mixed flow regime.

## Entrainment index analysis

The analysis of the entrainment index $I_e$ shows that:

- Avalanches entrained a snow depth $d_e$ between 30% (smallest entrainment index) and 130% (largest entrainment index) of the release depth $d_0$, underscoring the variability of the phenomenon (see Figs. 4.1 $a$ and 4.2).

- On average avalanches entrain along the avalanche path a snow depth $d_e = 0.67\ d_0$.

- Entrainment depends on the snow characteristics. Avalanche of the catastrophic Winter 1998/99, Obergoms valley, $I_e = 0.30$; the entrainment was limited by the high water content of the snow. Avalanche of February $25^{th}$, $I_e = 1.3$; the high entrainment was favored by the lightlow density and the low cohesion of the snow cover.
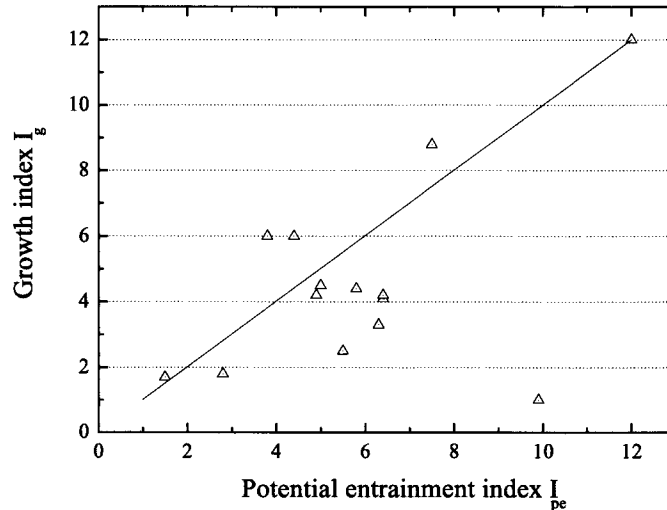
**Figure 4.3:** *The growth avalanche index $I_g$ plotted as a function of the potential entrainment index $I_{pe}$. The line $I_g = I_{pe}$ shows that $I_g$ cannot be easily be much larger than $I_{pe}$ because the entrained mass must come from the avalanche path.*

- Entrainment is dependent on sliding surface conditions. Avalanche of March $5^{th}$, Pizzac test site, $I_e = 0.3$; the avalanche entrained a large quantity of snow (see §3.3.3) but at the same time the avalanche deposited snow along all the avalanche path. Therefore, the avalanche increased its mass only slightly. The reason is probably due to the high friction between the avalanche and the sliding surface (first avalanche of the season). The avalanche was not able to accelerate the large entrained mass, while decelerating and depositing snow.

## Potential entrainment index analysis

Figure 4.3 shows the avalanche growth index $I_g$ plotted versus the potential entrainment index $I_{pe}$; the straight line represents the equation: $I_{pe} = I_g$. The plot shows that avalanches tend to increase their mass in proportion to the potential erosion area. However, exceptions exist.

Extreme situations are represented by the following cases:

- Avalanche of January $30^{th}$, Vallée de la Sionne test site, $I_{pe} = 9.9$, $I_g = 1$. In spite of the large potential entrainment index the avalanche did not substantially increase

its mass. The reason of the avalanche behavior is not clear but it is more than possible that a previous avalanche already entrained the snow cover.

- Avalanche of February $10^{th}$, Vallée de la Sionne test site, $I_{pe} = 12$, $I_g = 12$. The avalanche crossed a huge potential entrainment area increasing its mass. In this case, the low density snow conditions together with the high potential entrainment area favored the avalanche mass increase.

## Index analysis summary

On the basis of these observations, large entrainment amounts can be expected for both small and large avalanches, moving on open slopes or in channels, when favorable snow conditions and sliding surfaces together with high potential erosion areas exist. Entrainment is independent does not strongly depends on avalanche dimension; however, the entrainment has a strong variability and small factors (for example ice layers) can reduce the mass variation to zero.

The main conditions favoring strong entrainment are:

- Large potential entrainment area.

- Favorable snow conditions: enough snow to entrain, low-density snow cover with low water content.

- Smooth sliding surface: previous avalanche event deposits or ice crusts immediately below the new snow layer.

- Flow regime: mixed avalanches; however, mixed avalanches are generated when a light snow cover exists. Therefore, this fact also depends on the snow cover characteristics.

Avalanches can also deposit snow along the avalanche path with the result that, despite entrainment, the mass may decrease or increase only slowly. The main reasons for this process are primarily that:

- The sliding surface is not smooth enough to allow sufficient avalanche acceleration, and deposition occurs.

- The entrainment volume is too large for the avalanche to accelerate the entire entrained amount.

**Practice index analysis**

A statistical analysis of the practice avalanche indices is shown in the right panel of Fig. 4.2.

Defining the release mass as prescribed by the Swiss Guidelines and calculating the practice indices as defined in §3.1, the following conclusions can be drawn:

- On average, avalanches increase their mass by a factor $I_{g_{SG}} = 1.7$ (see Fig. 4.2, right).

- On average, avalanches entrain a snow depth $d_{e_{SG}} = 0.64\ d_0$ along the avalanche path; if only extreme avalanches are considered in the analysis, the entrained depth is $d_{e_{SG300}} = 0.48\ d_{0_{SG300}}$.

## 4.2 Basic physical processes in snow entrainment and deposition

Entrainment processes in avalanches have been observed using FMCW radar measurements at the Vallée de la Sionne experimental site since the winter 1998/99. A general scheme for erosion and deposition processes is shown in Fig. 4.4. Entrainment processes are frequently localized at the avalanche front; however, they can also take place along the basal sliding surface. Deposits are left by the avalanche after its passage.

Since snow characteristics play a fundamental role in entrainment, before we attempt to model the dominant mechanical processes leading to mass variations, a description of important mechanical properties of snow is given.

### 4.2.1 The snow cover strength

Snow entrainment is a function of the stress imposed on a snow layer in relation to the strength of the snow layer. Therefore, to understand entrainment processes it is necessary to quantify the strength of the snow cover. Different measures will be used to define the snow *strength*, which is primarily a function of the density and bonding of the snow. The mechanical properties of snow are reviewed in Jamieson & Johnston (2001) and Brun & Rey (1987).

Two main snow cover strengths are considered: the snow cover shear strength and the snow cover penetration strength.
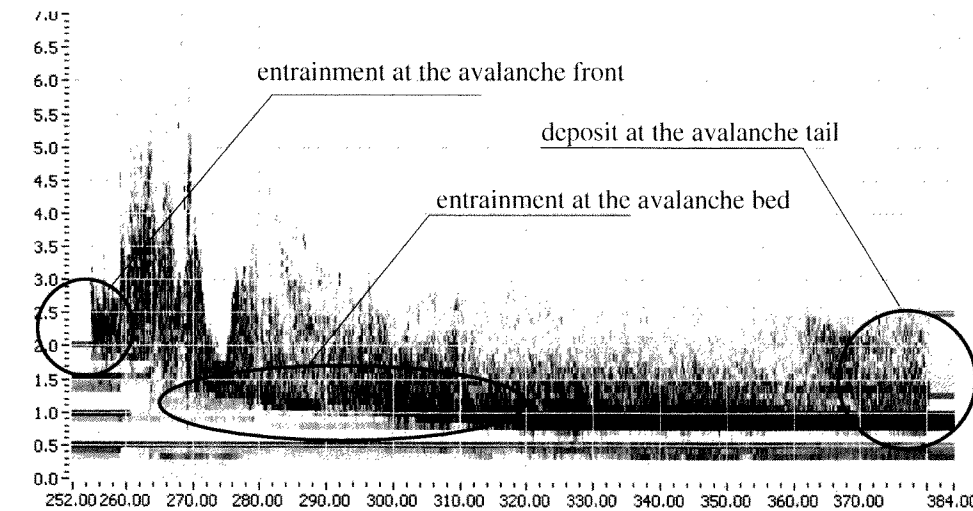
**Figure 4.4:** *FMCW radar plot. Avalanche of December $29^{th}$. 2001. Localization of entrainment and deposition processes is shown.*

## The snow cover shear strength

The shear strength of a snow layer $\tau_s$ can be given by a Mohr-Coulomb relation:

$$\tau_s = c + \sigma_z tg\phi \tag{4.1}$$

where $c$ denotes snow cohesion. $\phi$ is the internal friction angle and $\sigma_z$ the normal pressure on the layer. For a surface layer, where $\sigma_z$ is close to zero, the shear strength coincides with the cohesion.

The shear strength is strongly related to the snow density $\rho_m$ and the grain form. An empirical approximation describing this correlation was given by Perla et al. (1982):

$$\tau_s = a_1 \left(\frac{\rho_m}{\rho_{ice}}\right)^{a_2} \tag{4.2}$$

where $\rho_{ice}$ is the density of the ice (917 kg m$^{-3}$) and $a_1$ and $a_2$ are empirical constants that depend on grain form. Jamieson & Johnston (2001) determined these constants for weak snow pack layers of dry snow and obtained the following regressions:

$$\tau_s = 14.5kPa \left(\frac{\rho_m}{\rho_{ice}}\right)^{1.73} \tag{4.3}$$

related to precipitation particles, decomposed and fragmented particles and rounded grains (group I), and

$$\tau_s = 18.5 kPa \left(\frac{\rho_m}{\rho_{ice}}\right)^{2.11} \tag{4.4}$$

related to faceted crystals and depth hoar (group II), see Fig. 4.5.

On the basis of these regressions surface layers of fresh, low cohesion snow dry snow and a density between 80 and 200 kg m$^{-3}$ have an average shear strength between 0.2 kPa and 2 kPa. In the case of soft snow (density of about 100 kg m$^{-3}$) the average shear strength is about 0.3 kPa and rarely above 0.5 kPa. In general, older layers composed of faceted grains are weaker than layers of partly decomposed and/or rounded grains with the same density. A group II grain form with a density of 300 kg m$^{-3}$ has an average shear strength of 1.75 kPa, but can also reach 4 kPa, (see Fig. 4.5).

Additional measurements of the shear strength of homogeneous layers of dry and wet snow were performed by Brun & Rey (1987). They concentrated their attention on the influence of liquid water content on the bond resistance. They found that for the same density, a high water content can decrease the snow shear strength. On the other hand, the shear strength increases with density. Since the density of wet snow can reach 500 kg m$^{-3}$, the absolute shear resistance of a wet snow layer is higher. For instance, snow layers of wet snow having a density of 500–600 kg m$^{-3}$ have an average shear strength of about 18–26 kPa. Brun & Rey (1987) performed shear stress measurements also on dry and strong snow layers. For example, a dry snow layer having average density of 300 kg m$^{-3}$ can reach an average shear strength of about 10 kPa.

The shear strength of the entrained snow can provide helpful information on the force exerted by the avalanche on the snow cover.

### Snow cover penetration strength

The ploughing mechanism of entrainment consists of particle collisions between the avalanche and snow cover. The particles impact the snow cover and penetrate some distance before stopping. The depth of penetration can be related to layer entrainment height, $d_e$. Several investigations concerning particle-bed impact have been made to investigate aeolian snow/sand transport and erosion/abrasion of the snow cover (Rice et al., 1999). These investigations showed that colliding particles can eject grains from the snow cover and the

117
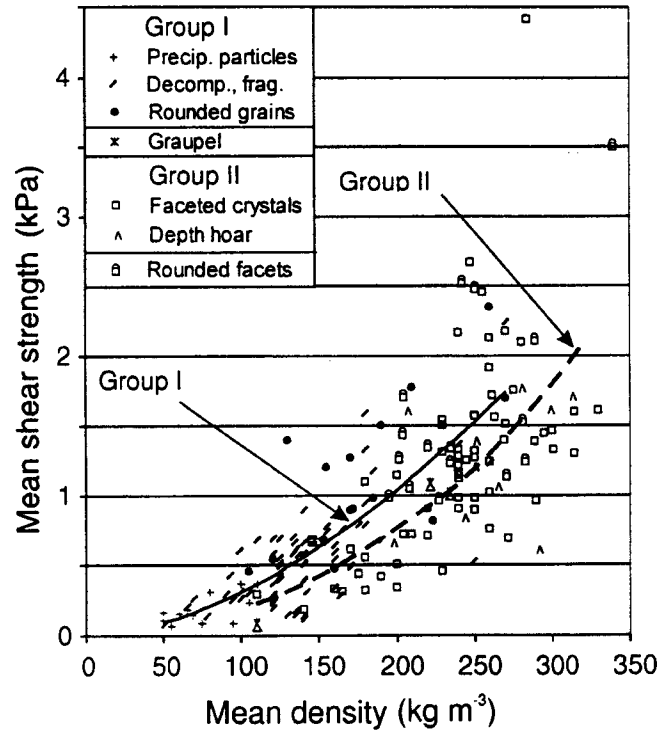
**Figure 4.5:** *Shear strength for weak snow layers of dry snow by density and grain form. Group I consists of precipitation particles, decomposed and fragmented particles and rounded grains but not graupel. Group II consists of faceted crystals and depth hoar but not rounded facets (Jamieson & Johnston, 2001).*

erosion rate is mainly controlled by the effective kinetic energy of the projectile and the bond strength of the target. The composition of the surface is important. Experiments on sand erosion reveal that particles are not easily eroded if they contain a high percentage of clay due to increasing cohesion between the particles. Erosion becomes increasingly difficult when a surface is crusted. Even a weak crust has been shown to reduce the rate of erosion significantly, protecting the underlying, less cohesive particles from the impact forces. Experiments also show that once the crust is broken the softer underlying snow is quickly eroded. Hence, the erosion rate is strongly dependent on the penetration resistance of the snow cover.

The entrainment rate is proportional to the total kinetic energy delivered to the surface

by the moving particles. Entrainment takes place when the energy of the impinging grains is high enough to rupture the interparticle bonds and penetrate into the snow cover.

The impact kinetic energy intensity $E_i$ can be calculated according to:

$$E_i = \frac{\frac{1}{2}m_p u_p{}^2}{A_i} = \frac{1}{3}D\rho u_p{}^2 \tag{4.5}$$

where the impacting particles are assumed to be spherical, $m_p$ is the particle mass, $D$ is the particle diameter, $u_p$ the particle velocity, $\rho_p$ the particle density and $A_i$ is the impact area.

Equation 4.5 can be extended to the particles moving in an avalanche. Avalanches are composed of roughly spherical particles having different dimensions (see Fig. 1.5). The horizontal lines in Fig. 4.6 show the kinetic energy intensity of a particle having a diameter $D = 10$ cm, a density of 300 kg m$^{-3}$ and different speeds $u_p$.

The energy intensity $E_b$ required to rupture the interparticle bonds on the snow cover was obtained using the relation:

$$E_b = \int \frac{F}{A_{so}} ds \tag{4.6}$$

where the force $F$ [N] was determined from snow hardness profiles measured by a micro penetrometer (Schneebeli et al., 1999), $ds$ is the increment in tip penetration depth and $A_{so}$ is the area of measurement, i.e. the area of the penetrometer tip.

The micro-penetrometer hardness (Schneebeli et al., 1999) is measured with a SnowMicroPen. The instrument records the penetration resistance of a small tip (area 20 mm$^2$) with high vertical layer resolution (4mm). The MicroPen measures the force necessary to break the bonds between crystals.

An analysis of snow hardness profiles collected during the winters 2001 and 2002 (Pielmeier & Schneebeli, 2002) shows that different snow types can have hardness values differing by more than one order of magnitude depending on crystal dimensions, density, water content and degree of refreezing. The snow types have been grouped as follows:

1. **Type I**: hard snow crust formed by refrozen melted snow.

2. **Type II**: refrozen melted snow.

3. **Type III**: hard snow composed by small dimension faceted and round crystals, with high density.
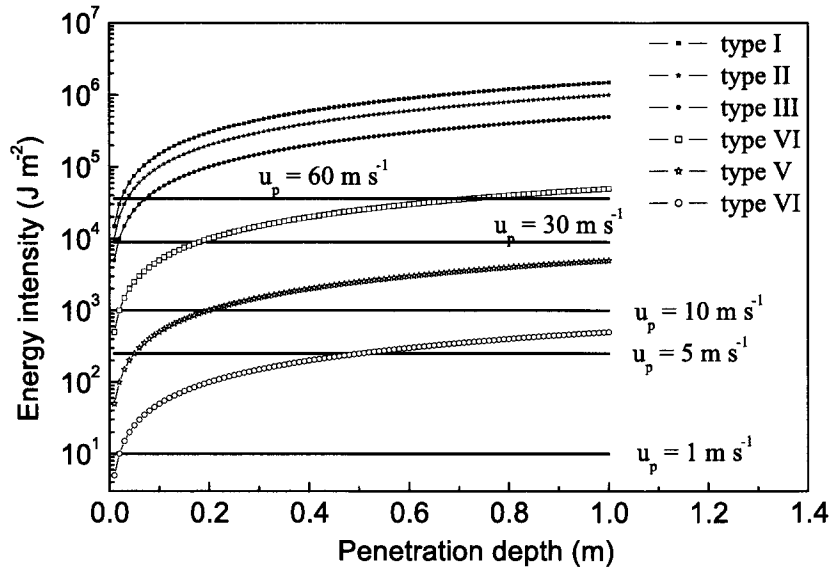
**Figure 4.6:** *Kinetic energy intensity of a particle having a diameter $D=10$ cm, a density of 300 kg m$^{-3}$ and different speeds $u_p$ (horizontal lines) in comparison with the penetration intensity energy for different snow types measured with SnowMicroPen. The energy intensities are plotted in function of the penetration depth.*

4. **Type IV**: wet snow with a large quantity of free water content; dry snow of medium density and crystal dimension.

5. **Type V**: new snow; rebuild snow with large crystals.

6. **Type VI**: new low density snow $(\rho_m < 100$ kg m$^{-3})$.

Figure 4.6 shows the penetration energy intensity for the different snow types as a function of the penetration depth.

It is assumed that jumping snow particles can break the bonds and penetrate into the snow cover when:

$$E_i > E_b \tag{4.7}$$

The rough estimation of the energy required to break the bonds in the snow cover corroborates the general observation that snow crust, refrozen melted snow and compact snow comprised of small grains need more energy to be broken up than new snow. Penetration resistance is thus a valuable parameter for assessing entrainment.

## 4.2.2 Entrainment at the avalanche front

New snow is typically dry, has a low-density and is cohesionless. Low density snow is characterized by a low shear resistance (Brun & Rey, 1987); for example, snow having a density of about 100 kg m$^{-3}$ has an average shear strength of about 0.3 kPa.

In comparison, the normal pressure exerted on a horizontal terrain by an avalanche having a flow depth of 2 m and an average density of 300 kg m$^{-3}$ is equal to 6 kPa. On a 45° slope the stress is 4.2 kPa.

Thus, the new snow layer cannot support the vertical pressure exerted by the avalanche, which tends to sink inside the snow cover, until it meets a stronger layer.

Observation of FMCW radar plots confirms this behavior. Avalanches tend to dive into the snow cover and slide over a more resistant and older layer or slide on the ground. As a result, frontal impact between the avalanche front and the snow cover takes place. Figure 4.7 shows an example of entrainment at the avalanche front. In this particular case the resistant layer over which the avalanche slides has a high water content with an approximate shear strength of 18–26 kPa (see §4.2.1). This process is referred to as *ploughing*. Ploughing entrainment rates depend directly on the density of the snow cover and the speed of the avalanche. In Vallée de la Sionne, ploughing entrainment rates of 330 kg m$^{-2}$ s$^{-1}$ were measured (see §3.4.2).

This large amount of snow suddenly entering the avalanche should influence the flow dynamics of the avalanche head, in particular, the avalanche flow depths. However, since avalanche flow depths at the front do not increase indefinitely and instantaneously, at least part of the entrained mass is transferred to the avalanche body. No information about these inner flow processes in avalanches is available. However, the avalanche flow depths can be used to determine where the mass is stored. Pizzac measurements show that the distribution of the mass within the avalanche is dependent on the terrain/snow cover friction. With lower basal friction the snow transfer from the head to the tail of the avalanche decreases. The same measurements also show that the avalanche with more mass concentrated close to the avalanche front has higher velocity and reaches longer runout distance (see §3.3.3). Thus, mass that is entrained and stored close to the avalanche front can contribute to increased flow velocities and runout distances.
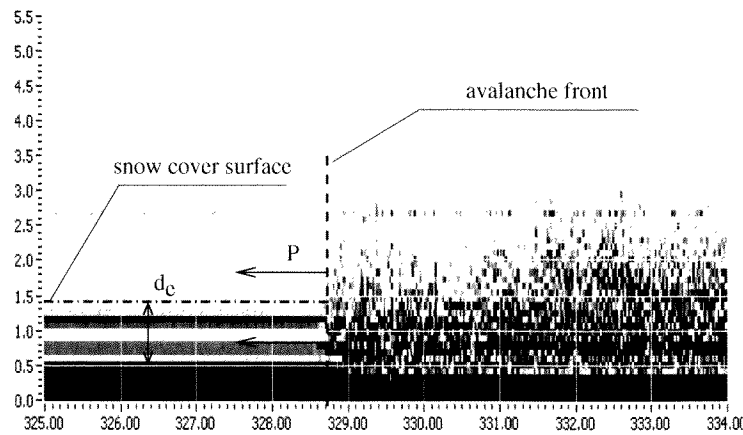
**Figure 4.7:** *FMCW radar plot of the avalanche of December 29$^{th}$, 2001. The avalanche ploughs into the snow cover and slides over a more resistant and older layer (in this case a wet snow layer). The snow cover is entrained immediately at the avalanche front. $d_e$ = entrainment depth; $p$ = impact pressure*

## 4.2.3 Entrainment along the avalanche basal surface

Analysis of the FMCW radar plot shows that avalanches may also entrain snow along the avalanche basal surface.

Two main mechanisms are observed from the FMCW radar:

- *Basal erosion.* Figure 4.4 shows an example of this mechanism. The avalanche entrained almost 1 m of snow in about 35 s ($x$-axis from 275 to 310 s). A second example is shown in Fig. 4.8. The FMCW radar plot corresponds to the December 27$^{th}$, 1999 avalanche passing over the radar positioned at 1900 m a.s.l. at the Vallée de la Sionne test site (see §3.2.2). Between section $a$ and $b$ the avalanche entrained about 0.5 m of snow in 10 s. In both cases there is no evident sliding surface and the avalanche dives progressively into the snow cover.

- *Step entrainment.* At section $b$ in Fig. 4.8, about 1.5 m of snow is instantaneously entrained and the avalanche starts to slide closer to the ground. Figure 4.9 shows another example of this mechanism. The twin FMCW radar plots correspond to the February 21$^{st}$, 2000 avalanche passing over the radar pair positioned at 2300 m a.s.l. at the Vallée de la Sionne test site. Both stratigraphies show two snow crusts separated by about 0.5 m of snow. Between sections $a$ and $b$ the avalanche slides over the upper snow crust without entraining any mass. At section $b$, the avalanche

122
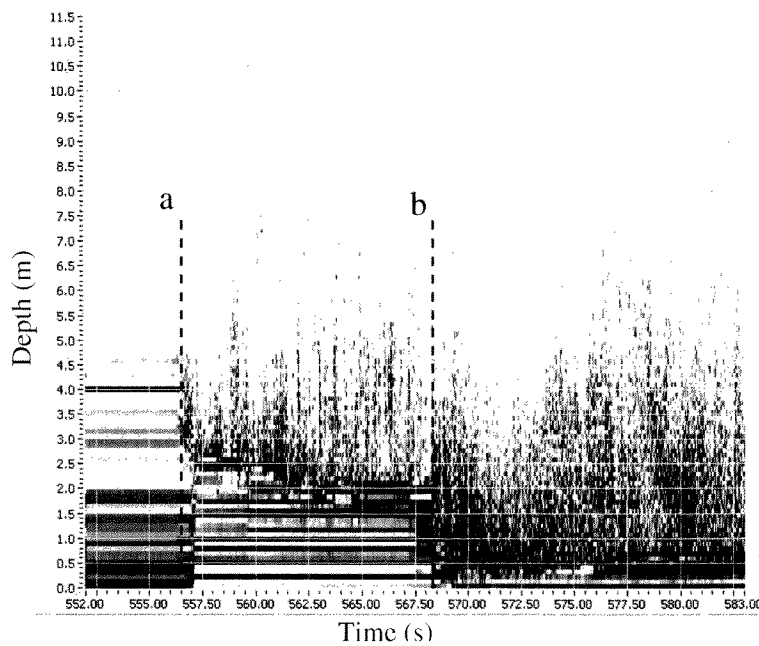
**Figure 4.8:** *FMCW radar plot of the avalanche of December 27th, 1999. The avalanche entrains part of the snow cover immediately at the front (front entrainment). Between sections a and b there is no evident sliding surface and the avalanche ploughs progressively into the snow cover (basal erosion). At section b, about 1.5 m of snow are instantaneously entrained (step entrainment).*

suddenly changes sliding surfaces and the snow layer between the two snow crusts is entrained. The avalanche then slides over the second crust without entraining any more snow. Both cases are characterized by a sudden change in the sliding surface, showing a clear step pattern.

The first mechanism, *basal erosion*, is observed when the snow cover is characterized by high strength. Typical examples of high-strength snow covers are refrozen melted snow, snow composed of small faceted and rounded crystals of high density, old avalanche snow deposits and snow with a high water content (see §4.2.1 and §4.2.1).

In basal erosion, the avalanche erodes mass from the sliding surface in proportion to the shearing force that it exerts on the basal surface. However, the entrainment rate is low. The values measured at the Vallée de la Sionne test site for the December 27th, 1999 and December 29th, 2001 avalanches are 10 kg m$^{-2}$ s$^{-1}$ and 6 kg m$^{-2}$ s$^{-1}$, respectively. These rates are a factor of 10 smaller than the observed frontal entrainments rates.

Other differences exist between frontal and basal entrainment. With basal entrain-
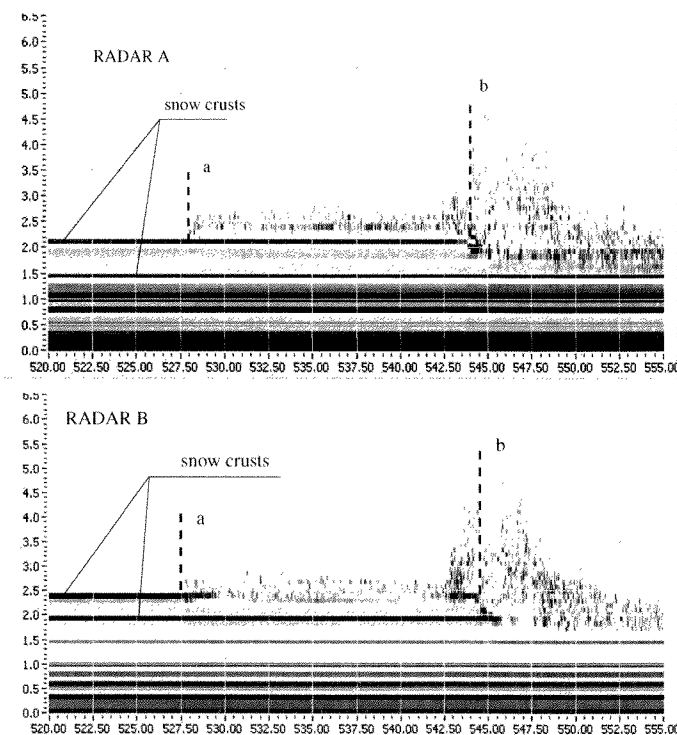
**Figure 4.9:** *Avalanche of February 21$^{th}$, 2000. The two twin plots are from the FMCW radar pair positioned at 2300 m a.s.l. at the Vallée de la Sionne test site. Between sections a and b the avalanche slides on a snow crust without entraining any snow. The avalanche suddenly changes sliding surface and the snow layer between the two crusts is entrained (step entrainment). Then the avalanche slides over the second crust without entraining any more snow.*

ment the snow is typically entrained in the avalanche interior, the entrainment is not instantaneous and its duration can strongly vary. Measured entrainment time intervals are between 1 and 40 s. The entrainment process automatically distributes the entrained mass over a large part of the avalanche length. Sometimes, basal erosion will even occur in the tail of the avalanche.

*Step entrainment* is observed when the snow cover is characterized by low-strength snow layers sandwiched between ice crusts.

Figure 4.10 shows a schematic view of the step entrainment mechanism. As the avalanche motion develops, the forces applied by the avalanche on the snow cover vary along the avalanche length. These different forces together with the spatial variability of the snow cover lead to different ploughing depths along the avalanche length. As a result, the avalanche slides on different layers along its length.

Initially, the avalanche slides over a resistant surface, for example a snow crust. If the
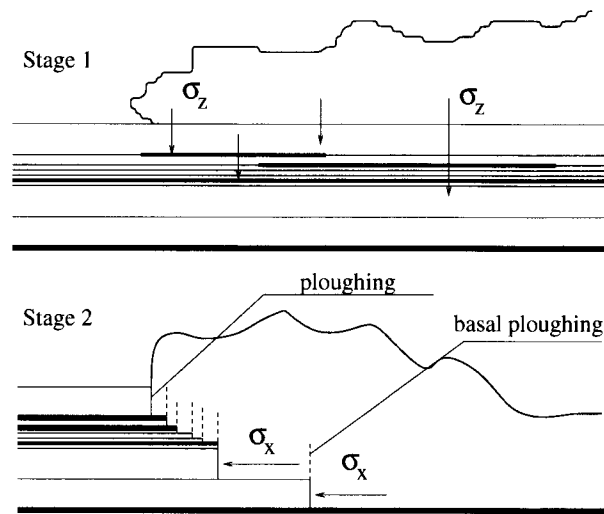
**Figure 4.10:** *Step entrainment. Stage 1: the avalanche sinks inside the snow cover. The distribution of the mass varies along the avalanche length. These differences together with the spatial variability of the snow cover produce different ploughing depths for different avalanche sectors. Stage 2: the avalanche slides over different surfaces along its length.*

avalanche changes the sliding surface, the snow between the two surfaces is entrained very rapidly (see Fig. 4.10, stage 2). If changing of the sliding surface occurs in fast succession, it appears as if the snow were gradually and continually entrained inside the avalanche, as in the case of basal erosion.

At each change of sliding surface a frontal impact between snow cover and avalanche occurs, as with the ploughing mechanism.

Step entrainment appears to be mainly controlled by the presence of snow crusts. Without a crust it is likely that all the snow cover is entrained immediately at the avalanche front.

The entrainment rate depends primarily on the snow cover characteristics; as in the case of the frontal erosion, it can reach very high values. The maximum value measured at the Vallée de la Sionne test site on December $27^{th}$, 1999 is about 350 kg m$^{-2}$ s$^{-1}$.

Analogous to the ploughing case, large amounts of snow suddenly enter the avalanche via basal or step erosion. However, the location is no longer directly at the front. Figure 4.9 shows that maximum flow depths are located close to the entrainment position, but distant from the leading edge of the avalanche.

### 4.2.4 Deposition at the avalanche tail

The mass distribution within the avalanche depends on the balance of forces within the avalanche. A reduction in the velocity of the avalanche, or an increase in the resistance may change this force balance and cause deposition. Reductions in the avalanche transport capacity can occur in a variety of ways, although reductions in the velocity are the most common reason. Velocity can be reduced locally by the topography effects, presence of vegetation or other obstructions. Avalanche deposition can also be observed in the FMCW radar plots. However, the physical interpretation of deposition is difficult and cannot always be determined from these plots. The experiments performed at the Italian Pizzac test site suggest that deposition processes begin at the avalanche tail, where flow depth and velocities are reduced. It was also observed that the distribution of the mass within the avalanche is dependent on the terrain/snow cover friction. Higher friction increases the snow transfer from the body to the avalanche tail, thus increasing the deposition mass (see §3.3.3).

### 4.2.5 Summary of the basic entrainment processes

Table 4.1 summarizes the characteristics of the different entrainment processes. Frontal and step entrainment have the highest influx rates; basal erosion is negligible in comparison to the other two processes. Hence, the frontal impact between the avalanche and the snow cover is often the main mechanism responsible for entrainment.

The avalanche exerts a normal stress $\sigma_x$ on the snow cover in the direction of flow. The stress is proportional to the speed of the avalanche squared, $U^2$. The normal stress breaks the bonds of the ice-matrix and a loose snow layer of height $d_e$ can be easily entrained into the flow.

## 4.3 A theory of entrainment

A theory of entrainment and deposition must be based on the physical observations and should answer two main questions: 1) When does entrainment and deposition occur and 2) how much mass is entrained and deposited. Our approach to answer these questions is described here.

In our modelling approach, the avalanche is considered as a continuum body acting on a solid snow cover. Entrainment processes are explained in terms of a global stress exerted by the avalanche on the snow cover.

**Table 4.1:** *Summary of the characteristics of the main entrainment mechanisms.*

| Definition | Ploughing | Step entrain-ment | Basal erosion |
|---|---|---|---|
| **Main features** | frontal entrain-ment | rapid change of sliding surface, ev-ident step | no evident sliding surface |
| **Location** | front | interior | interior |
| **Time scale** | $0.1 \div 2$ s | $0.1 \div 2$ s | $1 \div 40$ s |
| **Governing mechanism** | frontal im-pact between avalanche and snow cover | frontal impact be-tween avalanche and snow cover | shearing stress be-tween avalanche and snow cover |
| **Entrainment rate** | up to $350$ kg m$^{-2}$ s$^{-1}$ | up to $350$ kg m$^{-2}$ s$^{-1}$ | order of $10$ kg m$^{-2}$ s$^{-1}$ |
| **Snow cover characteristics** | low-density and cohesionless snow | low-strength snow sandwiched between ice layers | ice crust, high-strength snow layer and/or old avalanche deposits |
| **Snow cover shear strength** | $< 1$kPa | $1 \div 25$ kPa | $> 25$ kPa |

Based on observations, it is assumed that the main mechanism responsible for snow entrainment is the impact between the avalanche and the snow cover. The snow avalanche particles impact and penetrate the snow cover, fracturing the snow. The bonds of the ice lattice break when the impact pressure exerted by the avalanche exceeds the strength of the snow cover. We also assume that the avalanche impacts the snow cover perpendicularly.

The density of the snow cover changes under impact from $\rho_0$ to $\rho_1$. Depending on the snow cover properties, the eroded snow is either compressed or dilated (powderized). In the case of compression, the eroded snow is entrained into the dense flow, otherwise it is entrained into the powder-snow layer.

To describe the process we use an approach already presented by Ostroumov (1972) and Grigorian & Ostroumov (200). The avalanche impacts on the snow cover with mean velocity $U$. The entrainment front moves with velocity $u_f$ and is not necessarily perpen-dicular to the flow direction. With the approximation of one dimensional flow, in the time $dt$ the entrainment front moves $u_f dt$, breaking the bonds of all particles included in the
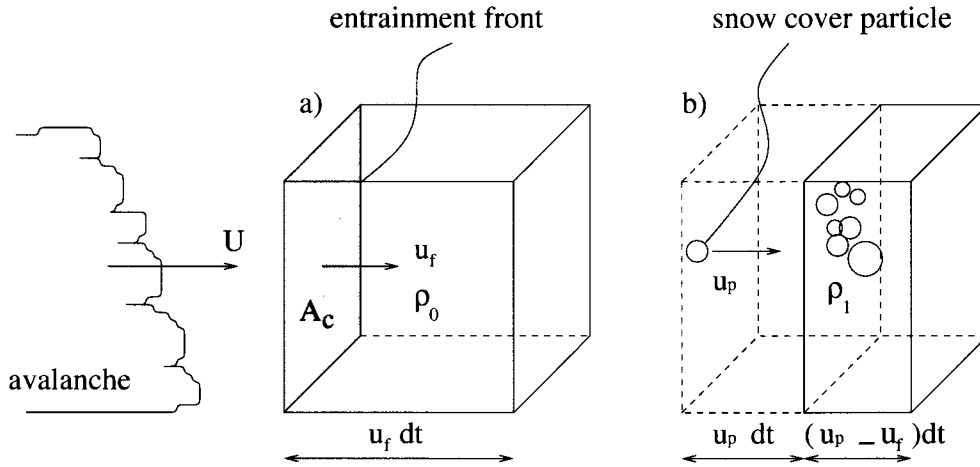
**Figure 4.11:** *Schematic view of a snow cover control volume during the impact with the avalanche. After the impact, the snow cover is either compacted or dilated. The figure shows the first case.*

control volume $A_c u_f dt$. This is shown in Fig. 4.11; $A_c$ is the cross-sectional area of the control volume. After the impact, particles start to move with a velocity $u_p$. The volume $A_c(u_f + u_p)dt$ is either compacted $(u_p > 0)$ or dilated $(u_p < 0)$. The mass is constant.

Ostroumov (1972) and Grigorian & Ostroumov (200) describe the entrainment problem by applying mass and momentum conservation to the control volume. Considering the control volume shown in Fig. 4.11 and with the approximation of one-dimensional flow, the conservation of mass equation applied at the snow cover can be written as:

$$m_e = A_c u_f \rho_0 dt = A_c(u_f + u_p)\rho_1 dt \tag{4.8}$$

$$\Rightarrow m_e = u_f \rho_0 = (u_f + u_p)\rho_1 \tag{4.9}$$

The change in momentum for the volumes in Fig. 4.11 is given by:

$$\bar{F} dt = m_e u_p - m_e u_{p0} \tag{4.10}$$

in which $\bar{F}$ is the time average value of the external force $F$ exerted on the system, $m_e u_p$ and $m_e u_{p0}$ are the final and initial momentum of the snow cover. Since at the beginning the snow cover is at rest, the expression $m_e u_{p0} = 0$.

The time averaged value $\bar{F}$ of the external force $F$ acting on the system is given by the impact pressure exerted by the avalanche on the snow cover perpendicular to the erosion front.

Ostroumov (1972) and Grigorian & Ostroumov (200) assumed that the applied stress is composed of the hydrostatic pressure and a velocity squared term. In this case entrainment is primarily a function of the avalanche flow height.

In our approach it is assumed that the main stress responsible for entrainment is the impact pressure between avalanche and snow cover, as observed from the experimental data. However, it can be easily adapted to describe different processes, such as penetration resistance. The impact pressure $p_i$ is given by the relation

$$p_i = c_i \rho U^2 \tag{4.11}$$

where $\rho$ is the avalanche density and $c_i$ is an empirical constant.

Using equations 4.9 and 4.10 the entrainment front velocity can be written as (Ostroumov, 1972):

$$u_f = \sqrt{\frac{p_i}{\rho_0 \left(1 - \frac{\rho_0}{\rho_1}\right)}} = C_f \sqrt{\frac{p_i}{\rho_0}}. \tag{4.12}$$

The factor $C_f$ can be defined as:

$$C_f^2 = \frac{\rho_1}{\rho_1 - \rho_0} \tag{4.13}$$

and accounts for snow compaction or dilatation during the entrainment process. While the final density of the snow cover can differ from the avalanche density, it is often assumed that the entrained snow is compacted or dilated to the avalanche density.

Entrainment takes place when the impact pressure is high enough to destroy bonds in the snow cover. The volumetric snow entrainment rate $\dot{S}_e$ [m$^2$ s$^{-1}$] is

$$\dot{S}_e = u_f \frac{\rho_0}{\rho} w = \frac{C_f w}{\rho} \sqrt{p_i \rho_0} \tag{4.14}$$

where $w$ is the avalanche width and the factor $\frac{\rho_0}{\rho}$ takes into account the snow cover compaction or dilatation when entrained in the avalanche. The entrainment rate is proportional to the avalanche speed, $U$. Finally, the entrainment depth $d_e$ can be calculated as:

$$d_e = u_f \frac{\rho_0}{\rho} dt. \tag{4.15}$$

Seite Leer /
Blank leaf

# 5 Modelling dense snow avalanche flow with entrainment

The aim of this chapter is to introduce entrainment into a numerical model in order to investigate the influence of mass variations on dense avalanche calculations. Accordingly, the entrainment theory illustrated in §4.3 will be included in flow models used to describe the avalanche dynamics. A quasi one-dimensional depth-averaged continuum model (Bartelt et al., 1999) has been modified to consider snow entrainment. Different constitutive equations have been tested. Fluid flow is described by a Voellmy-fluid flow law (Voellmy, 1955) and by a modified Criminale-Ericksen-Filbey fluid constitutive equation (Norem et al., 1989). The suitability of the different equations in describing the avalanche motion is highlighted.

The parametrization of a model including entrainment is generally more complex since additional input parameters are required. In particular, following the results of the experiments, the models with entrainment should account for the characteristics of the erodible snow cover such as: (1) depth $d_e$ and layering, (2) snow cover strength $p_{lm}$ and (3) snow distribution along the avalanche path. To investigate the sensitivity of the input parameters on the results, calculations have been performed by introducing input parameter perturbations up to 30%.

Finally, the model is validated by comparing the calculation results against experimental data. In particular, the model is applied to calculate flow velocities, runout distances, flow depths, deposition distributions with and without entrainment for some of the previously discussed avalanche events. Small, large and extreme avalanches are considered and the ability of the model to simulate different avalanche dimensions is discussed.

## 5.1 A one dimensional depth-averaged model with entrainment

Bartelt et al. (1999) presented a quasi one-dimensional depth-averaged continuum model developed to simulate the dense-avalanche motion. This model is used to predict avalanche

runout distances, flow heights and velocities as well as the distribution of snow deposition in the runout zone given an initial starting mass and shape, the values of physical parameters and the terrain coordinates of the avalanche path. The model numerically solves the mass (volume) and momentum balance equations (Sartoris & Bartelt, 2000).

A coordinate system is defined according to the definition given in §1.2 (see Fig. 1.4). The mass balance equation is described as:

$$\frac{\partial A}{\partial t} + \frac{\partial Q}{\partial x} = \dot{S}_e - \dot{S}_d \tag{5.1}$$

where:

- $x$ is the length along the avalanche path.

- $t$ is the time.

- $A(x,t)$ is the cross-sectional flow area given by $A(x,t) = w(x)h(x,t)$.

- $w(x)$ is the known flow width.

- $h(x,t)$ is the avalanche flow height.

- $Q(x,t)$ is the depth-averaged discharge flow corresponding to the average velocity $U(x,t)$ through the cross section area $A(x,t)$, i.e. $Q(x,t) = A(x,t)U(x,t)$.

- $\dot{S}_e$ and $\dot{S}_d$ are the volumetric snow entrainment and deposition rates respectively.

The right-hand side of the mass equation (5.1) contains the volumetric snow entrainment $\dot{S}_e$ and deposition $\dot{S}_d$ rates. In the original version of the model (Bartelt et al., 1999) these terms were set equal to zero assuming constant avalanche mass.

The volumetric snow entrainment rate $\dot{S}_e$ is computed using eq. 5.2, where the dependence from space and time is now made explicit, namely:

$$\dot{S}_e(x,t) = u_f(x,t)\frac{\rho_0}{\rho}w(x) = \frac{C_f w(x)}{\rho}\sqrt{p_i(x,t)\rho_0}. \tag{5.2}$$

It is assumed that avalanches deposit snow when the flow velocity $U$ drops below a critical velocity $U_c$. Thus the volumetric snow deposition rate $\dot{S}_d$ is given by:

$$\dot{S}_d(x,t) = 0 \qquad for \quad U(x,t) \geq U_c$$

$$\dot{S}_d(x,t) = C_d A(x,t) \quad for \quad U(x,t) < U_c \tag{5.3}$$

where the deposition coefficient $C_d$ varies between 0 and 1. Usually $C_d{=}1$, which implies the entire mass is being deposited within a calculation step $\Delta t$. The entrainment and deposition mass rates are found by multiplying $\dot{S}_e$ and $\dot{S}_d$ with the avalanche density $\rho$, which is assumed to be constant (300 kg m$^{-3}$).

The momentum equation is described as:

$$\frac{\partial Q}{\partial t} + \frac{\partial}{\partial x}\left[\alpha\frac{Q^2}{A}\right] = A\left[gF_0 - gF_f\right] - \lambda gA\frac{\partial h}{\partial x}\cos\varphi \qquad (5.4)$$

where:

- $\alpha(x,t)$ is the velocity profile factor.

- $g$ is the acceleration due to gravity.

- $\lambda$ is the active-passive pressure coefficient; this parameter governs the amount of longitudinal stress introduced via longitudinal straining of the flow body (Bartelt et al., 1999).

- $gF_0$ ($g\sin\varphi$) is the gravitational acceleration.

- $\varphi(x)$ is the track segment inclination.

- $F_f$ is the flowing friction.

- $F_e$ is the entrainment friction.

Voellmy-fluid (Swiss Voellmy-fluid model) law (Bartelt et al., 1999) and a Criminale-Ericksen-Filbey (Norwegian NIS model) (Norem et al., 1989) constitutive equations have been tested to understand which can better describe the dense avalanche behavior when considering mass variations. The choice of model determines the form of the friction term, $F_f$. The $F_f$ definition will be discussed in the following for both constitutive laws.

## 5.1.1 The Voellmy-fluid model

The Voellmy-fluid friction law assumes that the flow resistance can be divided into three main components: a Coulomb-type friction, a viscous resistance that varied with the square of the flow velocity and an internal friction accounting for compressive-tensile longitudinal strain inside the avalanche body (Salm, 1993).

# 5. MODELLING DENSE SNOW AVALANCHE FLOW WITH ENTRAINMENT

The flow friction $F_f$ is given by

$$F_f = \mu \cos \varphi + \frac{U^2}{\xi h} \tag{5.5}$$

where the first term in the equation is the Coulomb-type friction and the second term is the shear stress.

The flow parameter $\mu$ is mainly connected to snow properties whereas $\xi$ depends mainly on terrain geometry. See (Salm, 1993) and (Salm et al., 1990) for a more detailed explanation.

The Voellmy-fluid model assumes that the shear stress is concentrated at the avalanche-snow cover interface and that no shear deformation takes place in the avalanche body. The flow body moves as a plug where the same mean velocity is applied over the flow height, i.e. $\alpha(x, t) = 1$.

The basal shear resistance is defined by the equation:

$$\tau_{xz}(0) = \mu \sigma_z(0) + \frac{\rho g}{\xi} U^2 \tag{5.6}$$

which consists of an overburden pressure $\sigma_z(0)$ that, by definition, implicitly assumes a hydrostatic pressure distribution:

$$\sigma_z(0) = b\rho g h \cos \varphi \tag{5.7}$$

and a Chézy-like resistance which is proportional to the velocity squared (Bartelt et al., 1999).

Although the shear deformations are zero, longitudinal straining of the flow plug can occur. Resistance to active (tensile) and passive (compressive) flow states is given by the active/passive pressure coefficient $\lambda$ governed by the relation:

$$\left. \begin{matrix} \lambda_a \\ \lambda_p \end{matrix} \right\} = \tan^2 \left( 45° \pm \frac{\phi}{2} \right) \tag{5.8}$$

with:

$$\lambda = \begin{cases} \lambda_a & for \quad \frac{\partial U}{\partial x} > 0 \\ \\ \lambda_p & for \quad \frac{\partial U}{\partial x} \leq 0 \end{cases} \tag{5.9}$$

where $\phi$ is the internal friction angle of the snow. Typical internal friction angle are in the range $20° \leq \phi \leq 40°$, leading to active/passive values in the range $0.2 \leq \lambda_a \leq 0.5$ and $2.0 \leq \lambda_p \leq 4.6$. See (Savage & Hutter, 1989) and (Bartelt et al., 1999) for more details.

## 5.1.2 The Norwegian NIS model

The NIS model uses the modified Criminale-Ericksen-Filbey fluid constitutive equations to describe the avalanche flow, which are defined as:

$$\tau_{xz} = c + bp_e^k + \rho m \dot{\gamma}^n \tag{5.10}$$

$$\sigma_x = -(p_e + p_u) + \rho(\nu_1 - \nu_2)\dot{\gamma}^n \tag{5.11}$$

$$\sigma_z = -(p_e + p_u) + \rho\nu_2\dot{\gamma}^n \tag{5.12}$$

$$\sigma_y = -(p_e + p_u) \tag{5.13}$$

$$\tau_{yz} = \tau_{yx} = 0 \tag{5.14}$$

where $c$ is the snow cohesion [N m$^{-2}$], $b$ is the dry friction coefficient, $p_e$ is the effective pressure [N m$^{-2}$], $p_u$ is the pore pressure [N m$^{-2}$], $\rho$ is the flow density [kg m$^{-3}$], $m$ is the shear viscosity [m$^2$ s$^{n-2}$], $\nu_1$, $\nu_2$ are the normal stress viscosities [m$^2$ s$^{n-2}$], $k{=}1$ and $n{=}2$ are material constants and $\dot{\gamma}$ is the shear rate. It is assumed that for dry fully fluidized flow the material has no cohesion, $c = 0$, and the pore pressure $p_u$ is much smaller than $p_e$ (Bartelt et al., 1997). Implicit in these constitutive snow equations is the assumption that snow avalanches can be treated as a granular material in which single snow particles have the possibility to move relative to neighboring particles. The avalanche is treated as a fluidized layer and, unlike the Voellmy-fluid model, the shear deformation rates, $\dot{\gamma}$, are nonzero:

$$\dot{\gamma} = \frac{\partial U}{\partial z} = \frac{3}{2}\frac{(u_h - u_0)\sqrt{1 - \frac{z}{h}}}{h} \tag{5.15}$$

where $u_0$ is the velocity at the base of the avalanche and $u_h$ the velocity at the top surface. The vertical speed profile is not constant and the velocity profile factor is given by the relation:

$$\alpha(x,t) = \frac{5}{4}\left[\frac{9u_h^2 + 6u_hu_0 + 5u_0^2}{(3u_h + 2u_0)^2}\right] \tag{5.16}$$

The ratio $R$ between these velocities is:

$$R = \frac{u_h}{u_0} = \left[1 + \frac{2h}{3}\sqrt{\frac{s}{\rho(m - b\nu_2)}}\right] \tag{5.17}$$

where $s$, $m$, $b$, $\nu_1$, $\nu_2$ are the model parameters; $s$ [kg m$^{-3}$] is the velocity-squared dynamic friction coefficient. The flow friction $F_f$ is given by:

$$F_f = b\cos\varphi + \frac{su_0^2}{\rho g h} - \frac{9\nu_1(u_h - u_0)}{4h^2}\frac{\partial(u_h - u_0)}{\partial x} \tag{5.18}$$

135

and the passive pressure by the relation:

$$\lambda = \left[ 1 + \frac{9v_1(u_h - u_0)^2}{8gh^3 \cos \varphi} \right] \tag{5.19}$$

In the NIS model the slip condition at the bed surface is described by the relation:

$$\tau_{xz}(0) = -b\sigma_z(0) + su_0^2 \tag{5.20}$$

The basal friction consists of a dry-friction term proportional to the overburden pressure $\sigma_z(0)$, which by definition implicitly assumes a hydrostatic pressure distribution:

$$\sigma_z(0) = b\rho gh \cos \varphi \tag{5.21}$$

and a viscous term, which is proportional to the velocity squared.

For a complete description of the model see (Norem et al., 1989), and (Harbitz et al., 1998).

## 5.1.3 Numerical implementation

The governing system of avalanche equations is solved using a second order TVD (Total Variation Diminishing) finite difference scheme. The specific procedure is described in Sartoris & Bartelt (2000).

The avalanche track is divided into grid points having coordinates $x_n$ and $z_n$ and the governing equations are numerically solved for each of these points.

The model input consists of the initial conditions and the model parameters. Initial conditions are defined by the release mass and by a definition of an $m$-layer snowpack defined along the track. At each point $x_n$ along the avalanche path, the layer depth $d_m$ and strength $p_{lm}$ are defined. The erodible snow cover can be characterized by up to three layers (m=1, 2, 3).

The flowchart of the entrainment routine is shown in Fig. 5.2. Snow cover is defined when one or more layers have depth $d_m$ different from zero. The routine defines the active layer as the most superficial layer, coming in contact first with the avalanche. In Figure 5.2 the active layer is defined with the suffix $m$. If the strength of this layer $p_{lm}$ is lower than the stress exerted by the avalanche on the snow cover $p_i$, entrainment takes place. Depending on snow cover and avalanche characteristics, a part of a layer, an entire layer or multiple layers can be entrained on the basis of equation 4.15.
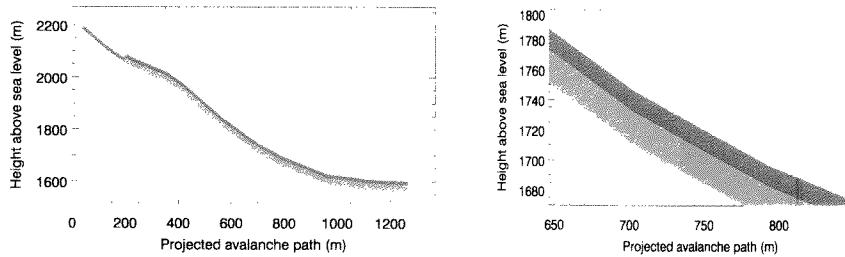
**Figure 5.1:** *Erodible snow cover graphical interface. On the left: the snow cover can be defined along the entire avalanche path: different snow depths $d_m$ and strengths $p_{lm}$ can be associated to each topography segment. In the release zone the interface shows only the release layer; the erodible snow cover is not defined (see upper part of the avalanche track). On the right: detail of the snow cover, which can be defined as up to three layers.*

If the applied avalanche stress is able to entrain only one part of a layer, in the next calculation steep the layer depth $d_m$ is diminished by the relation:

$$d_m = d_m - \frac{\dot{S}_e \Delta t}{w} \tag{5.22}$$

If the avalanche entrains an entire layer, the routine checks the characteristics of the next underlying layer and determines whether it can be entrained. The calculation is iterated since the snow cover strength is smaller than the avalanche stress and at least one layer depth is different from zero.

Different stresses exerted by the avalanche on the snow cover $p_i$ can be easily implemented in the routine to investigate different entrainment mechanisms. The model has been adapted to run with or without entrainment in order to make comparisons between the two cases.

Figure 5.1 shows an example of the graphical interface used to represent the erodible snow cover layers. The layers can be defined for the entire avalanche track and different snow cover characteristics can be associated to each topography segment. The interface allows the visualization of the entrainment and deposition processes. The entrainment location and the nature of erosion (progressive or sudden) can be observed and directly compared with field observation, when available (see Fig. 5.3).

137

# 5. Modelling dense snow avalanche flow with entrainment

For time t and coordinate position $x_n$

Begin

| | |
|---|---|
| Set $m_e = 0$ <br> $m = 0$ | /* Set entrainment mass <br> to zero */ <br> /* Initialize layer */ |

$m = m + 1$ → $m > 3$ layers → Return

No ← $d_m > 0$    /* Does snow exist */

Yes

$p_i = $ different equations    /* Calculate avalanche stress */

$p_i > p_{lm}$ → No → Return ($m_e = 0$)    /* Snow layer resists */

Yes

$u_f = $ eq. 4.12 <br> $d_e = $ eq. 4.15    /* Calculate entrainment depth */

$d_e = d_m$ <br> $m_e = d_e w l \rho_e$ <br> $d_m = 0$ ← No ← $d_e \leq d_m$

/* Entire layer is entrained */

Yes

$m_e = d_e w l \rho_e$ <br> $d_m = d_m - d_e$    /* Part of a layer is entrained */

Return
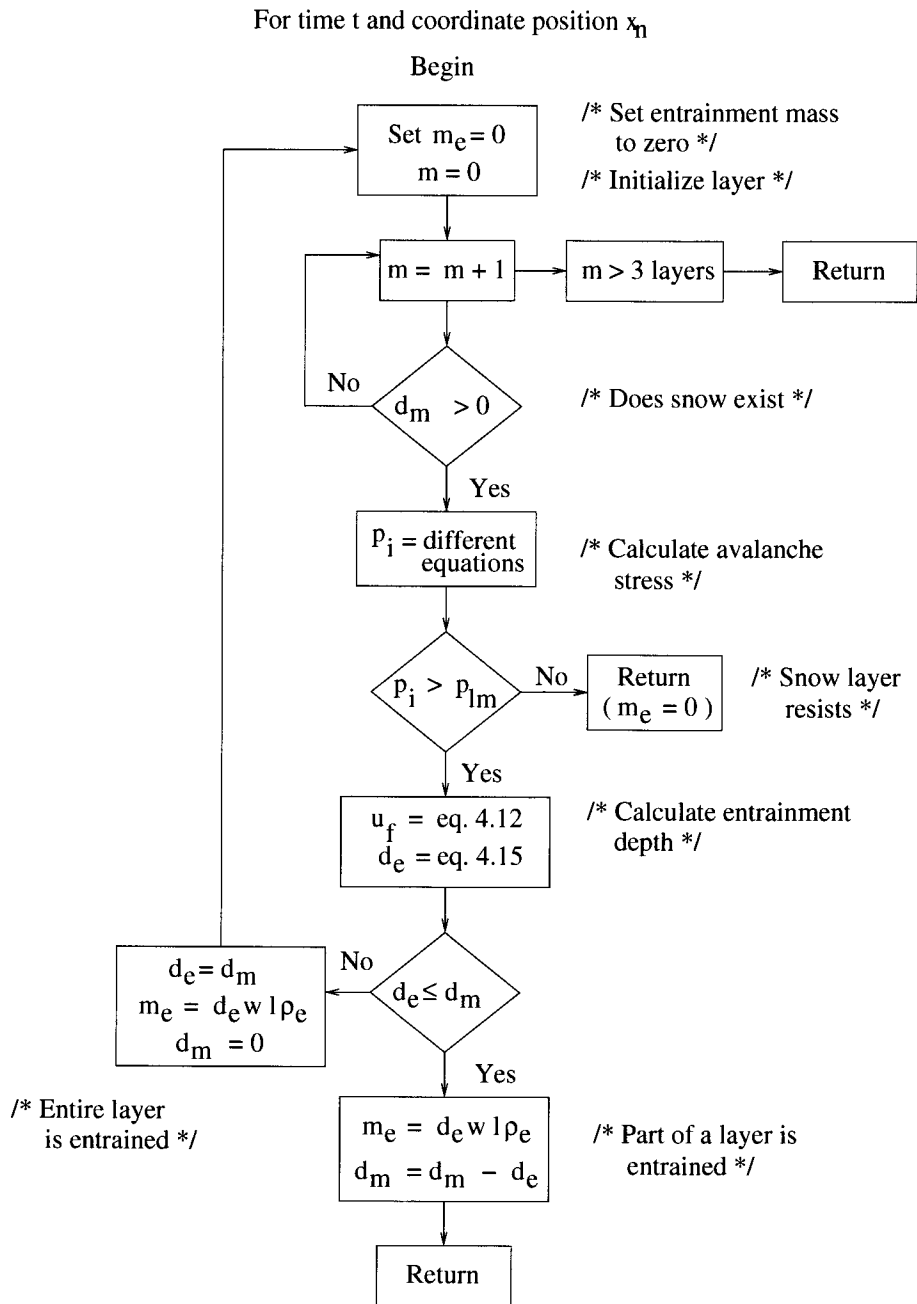
**Figure 5.2:** *Flowchart for the implementation of entrainment.*

138
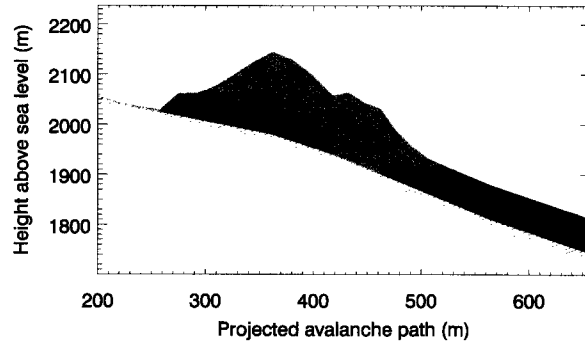
**Figure 5.3:** *The graphical interface showing details of entrainment in process. Entrainment can be observed directly at the contact interface between avalanche and snow cover.*

## 5.2 Model sensitivity

At present, uncertainties in the input parameter values is one of the main weaknesses still connected with the use of dynamical models for practical applications (Barbolini et al., 2002). For this reason a sensitivity analysis of the most common models used in practice (without entrainment) was carried out by Barbolini et al. (2000). The analysis pointed out that the model results, either in terms of runout distance or impact pressure, are remarkably sensitive to both the model parameters (friction coefficients) and the initial conditions (release area and release depth). The analysis was performed varying the input parameters by ±15–30% and observing the corresponding variations in the output parameters.

In addition to the parameters above, the model outputs including entrainment are influenced by the characteristics of the erodible snow cover such as depth $d_m(x)$, snow cover strength $p_{lm}(x)$ and snow layer distribution along the avalanche path.

In simulations without entrainment the avalanche mass is defined solely by the release mass; in simulations with entrainment the avalanche mass is defined by the release mass and the mass changes due to entrainment and deposition. Observations of real avalanches (see Chapter 3) revealed that the initial release can be quite small in comparison to the mass entrained along the avalanche path (in the case studies, the maximum growth index was $I_g = 12$). However, in calculations performed defining the release on the basis of the Swiss Guidelines, a larger part of the avalanche mass is defined as the release mass; the entrainment mass is therefore smaller (the maximum practice growth index was $I_{g_p} = 2.7$

139
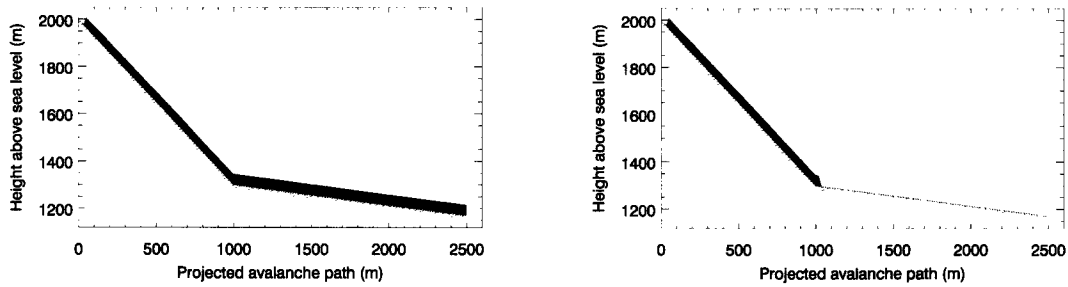
**Figure 5.4:** *Simplified topography used to assess the influence of varying the entrainment parameters. On the left: an erodible snow cover is defined for the entire avalanche track. On the upper part of the track the different color indicates the release zone. On the right: an erodible snow cover is defined only for the steeper part of the track.*

in the case studies).

In simulations with entrainment one has the option of choosing a large release area with a small entrainment area or a small release area and a large entrainment area. How do these choises influence the calculation results?

To better understand the effects that changes in the entrainment variables within the model can have on the model predictions (velocities, flow depth and runout distances) an example calculation is provided and described below. In particular, we vary the entrainment parameters and observe the subsequent effects on the model results.

To perform this analysis we use a simplified topography composed of two segments having constant slope angle of 35° and 5°, respectively (Fig. 5.4). The avalanche width is constant; calculations are performed with the NIS model.

## Sensitivity to release/entrainment length

Simulations are performed where the maximum avalanche mass is constant but the snow mass is introduced alternatively as release mass or as entrainment mass. The first simulation is performed defining a release length of $L_0 = 100$ m and an erosion length of $L_e = 900$; the last simulation by defining a release length of $L_0 = 500$ m and an erosion length of $L_e = 500$ m.

In Figure 5.5 the bold line (no perturbation) shows the outputs: flow velocity, flow depth and runout distance obtained by increasing the release length $L_0$, i.e. decreasing the entrainment length $L_e$. On the $x$-axis the dimensionless ratio $L_0/L_e$ is proportional to the release length. The release depth is 1 m and the release density 300 kg m$^{-3}$.

140
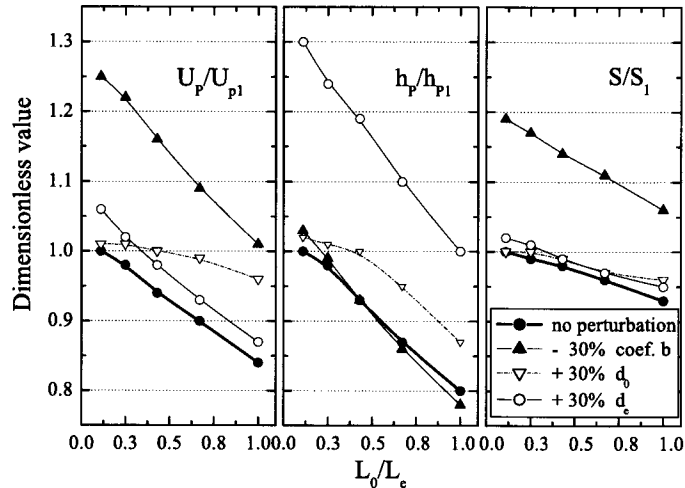
**Figure 5.5:** *Model sensitivity to changes in release $L_0$/entrainment $L_e$ length (x-axis) and $\pm 30\%$ variations of the friction parameter $b$, release depth $d_0$ and entrainment depth $d_e$. See text for explanation of $U_P$, $U_{P1}$, $h_P$, $h_{P1}$, $S$ and $S_1$*

The first diagram on the left in Fig. 5.5 shows the dimensionless ratio $U_P/U_{P1}$ where $U_P$ is maximum avalanche speed at the point $P$ located at the change in slope along the avalanche path (see Fig. 5.4) and $U_{P1}$ is the speed at $P$ calculated for the case $L_0/L_e = 0.1$.

The middle diagram of Fig. 5.5 shows the dimensionless ratio $h_P/h_{P1}$ where $h_P$ is maximum avalanche flow depth at the point $P$ and $h_{P1}$ is the flow depth in $P$ calculated for the case $L_0/L_e = 0.1$.

The diagram on the right in Fig. 5.5 shows the dimensionless ratio $S/S_1$ where $S$ is the runout distance and $S_1$ is the runout distance calculated for the case $L_0/L_e = 0.1$.

For all cases shown, varying the release/entrainment length changes the output. The avalanche flow depths appear to be most sensitive to these changes (see Fig. 5.5, middle). Increasing the release length by a factor of five reduces the flow depth by approximately 20%. The flow velocity at $P$ and runout distances are reduced by approximately 16% and 7%, respectively.

The reason for this behavior is that when a large part of the mass is defined as release mass, it is spread out over a long length and the avalanche depth remains small. In contrast, when the majority of the mass is defined as entrainment the snow accumulates at the front where it is entrained resulting in higher flow depths. As a result, the speed

**Table 5.1:** *Summary of the sensitivity analysis performed changing release/entrainment length $(L_0 + 400\%, L_e - 45\%$ respectively) and varying the parameter $b$, release depth $d_0$ and entrainment depth $d_e$ of $\pm 30\%$.*

| Perturbation | $L_0 = 0.1 L_e$ | | | $L_0 = L_e$ | | |
|---|---|---|---|---|---|---|
| | $U_P$ | $h_P$ | $S$ | $U_P$ | $h_P$ | $S$ |
| $L_0$ +400% ($L_e$ −45%) | - | - | - | 16% | 20% | 7% |
| $d_0$ +30% | 1% | 2% | 0% | 12% | 7% | 3% |
| $d_e$ +30% | −6% | 30% | 2% | 3% | 20% | 2% |
| $b$ −30% | 25% | 3% | 20% | 17% | −2% | 13% |

and runout distances are higher.

## Sensitivity to perturbations on input parameters

The simulations are then recalculated introducing $-30\%$ perturbations on the more sensitive friction parameter $b$ (Barbolini et al., 2000) (see Fig. 5.5, $-30\%$ coef. $b$) and $+30\%$ perturbation on the release depth $d_0$ and entrainment depth $d_e$ (see Fig. 5.5, $+30\%$ $d_0$ and $+30\%$ $d_e$ respectively). Changes were always performed individually, with the other parameters held at their reference value.

Simulations with entrainment show that velocity and runout distance are strongly sensitive to the variation of the friction parameter $b$, which mainly controls velocity and runout distance. Variations of approximately 25% for the speed and 19% for the runout were calculated.

Perturbing $b$ has little influence on the avalanche depth. However, avalanche flow depths are strongly sensitive to the entrainment depths. For an entrainment depth perturbation of 30%, flow depth variations of up to 30% were calculated.

It is interesting to observe that, especially for avalanches with small release areas and large entrainment masses $(L_0/L_e = 0.1)$, simulations with entrainment are still remarkably sensitive to the friction parameters (a perturbation of 30% on $b$ produced a 19% variation on the runout distance and 25% on the maximum velocity) but are barely sensitive to variations of the release depth and area. A perturbation of 30% on $d_0$ produced a 2–3% variation on the maximum velocity and flow depths and 1% on the runout distance. Similar values were calculated for a perturbation of the release area of 30% (corresponding to the $x$-axis value 1.3).

## 5.2.1 Effect on critical avalanche quantities

Special attention has been dedicated to the effects of introducing entrainment in the flow model on runout distances, flow velocities, pressures and flow heights.

### Effects on the runout distance

To study the effects of the entrainment on runout distances, simulations were performed using the following criteria:

- Without entrainment.

- With entrainment: variable snow cover strength ($p_{lm} = 0$ kPa and $p_{lm} = 10$ kPa), snow cover density 300 kg m$^{-3}$, variable erodible snow cover depth (see Fig. 5.4, left).

- Entrainment only in the upper part (steeper part) of the track: variable snow cover strength ($p_{lm} = 0$ kPa and $p_{lm} = 10$ kPa), snow cover density 300 kg m$^{-3}$, variable erodible snow cover depth (see Fig. 5.4, right).

Figure 5.6 shows the correlation between erodible snow cover depths and dimensionless projected runout distances $S/S_0$ for the cases listed above. The entrainment depth $d_e = 0$ m corresponds to the case without entrainment. The friction parameters used for the calculation are: $m = 0.0055$ m$^2$, $b = 0.45$, $s = 3.0$ kg m$^{-3}$, $\nu_1 = 0.1$ m$^2$ and $\nu_2 = 0.01$ m$^2$, those suggested by calculations for the Aulta avalanches (Bartelt et al., 1997).

In Figure 5.7 the dimensionless projected runout distances $S/S_0$ are then plotted as a function of the avalanche growth index $I_g$. In this case only the predictions obtained by entrainment in the upper part of the track are used and simulations are performed using two different parameter sets. The shaded bands represent the envelope of the above simulations; the upper envelope concerns simulations performed using the parameter set $m = 0.0060$ m$^2$, $b = 0.35$, $s = 3.0$ kg m$^{-3}$, $\nu_1 = 0.1$ m$^2$ and $\nu_2 = 0.01$; the lower envelope to the parameter set $m = 0.0055$ m$^2$, $b = 0.45$, $s = 3.0$ kg m$^{-3}$, $\nu_1 = 0.1$ m$^2$ and $\nu_2 = 0.01$ m$^2$.

It is observed that:

- The simulations with the entrainment produce longer runout for the same initial conditions and friction parameters than the simulations without entrainment. For reasonable entrainment depths, the runout distance grows by at most 20% (see Fig. 5.7, the case without entrainment corresponds to $d_e$=0).

143
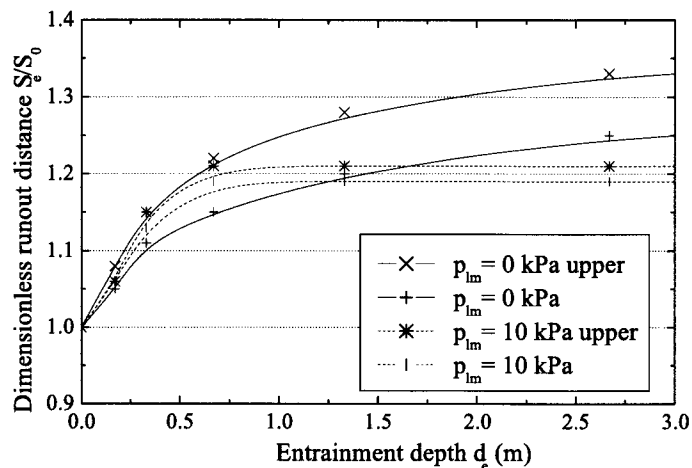
**Figure 5.6:** *Dimensionless projected runout distances are plotted in function of entrainment depth. NIS model calculation parameters:* $m = 0.0055$ $m^2$, $b = 0.45$, $s = 3.0$ $kg$ $m^{-3}$, $\nu_1 = 0.1$ $m^2$ and $\nu_2 = 0.01$ $m^2$. *"Upper" indicates that entrainment occurred only in the upper segment of the path.*

- For entrainment depths up to approximately 1 m, the maximum runout distance is obtained by the case with entrainment only in the steeper part of the track and low snow strength (see Fig. 5.6, $p_{lm} = 0$ kPa, upper), followed by the case with entrainment only in the steeper part of the track and high snow strength (see Fig. 5.6, $p_{lm} = 10$ kPa, upper). When the snow is distributed along the entire path, maximum runout distances are obtained as the avalanche entrains all of the low-strength snow.

- Increasing the snow cover strength ($p_{lm} = 10$ kPa) makes the snow more difficult to entrain. The capacity of the avalanche to entrain reaches a limit, and also the runout distance is limited (see Fig. 5.6). This also occurs if the erodible snow cover depth is increased.

- The runout distances calculated using the two parameter sets and no entrainment were similar ($d_e = 0$). In contrast, the simulations performed with entrainment are more sensitive to the calibration parameters. The sensitivity increases with the growth index. For a growth index $I_g = 2$ the runout variability of the different simulations is about 5%. However, for larger growth indices it reaches 20–30%.
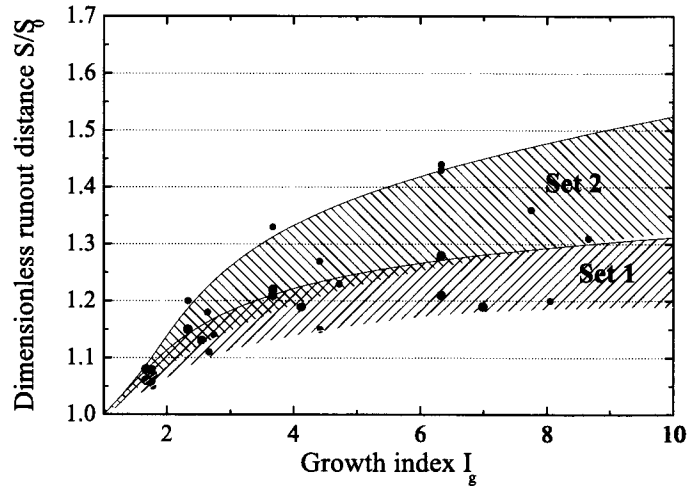
**Figure 5.7:** *Dimensionless runout distances plotted as a function of the avalanche growth index $I_g$. The parameters for set 1 are: $m = 0.0055$ $m^2$, $b = 0.45$, $s = 3.0$ $kg$ $m^{-3}$, $\nu_1 = 0.1$ $m^2$ and $\nu_2 = 0.01$ $m^2$ and for set 2 are: $m = 0.0060$ $m^2$, $b = 0.35$, $s = 3.0$ $kg$ $m^{-3}$, $\nu_1 = 0.1$ $m^2$ and $\nu_2 = 0.01$.*

This means, not only that the range of the calibration parameters must be strongly reduced in order to control the runout of an avalanche, but also that the entrainment depth and snow cover strength can play an important role in calculating runout distances.

**Effect on avalanche speed and pressure**

The effect of entrainment and its sensitivity to input parameters has also been investigated by estimating the variation on the output values velocity and pressure.

Avalanche velocities were calculated using the following approaches:

- Without entrainment.

- With constant release (characteristics) and friction parameters but varying the characteristics of the entrained snow: snow cover strength $p_{lm} = 1$ kPa and $p_{lm} = 10$ kPa, snow cover density 300 kg $m^{-3}$, snow cover depth $d_e = 2.0$ m (see Fig. 5.4, left). Entrainment along the entire path or only in the upper part of the track. Calculation parameters: $m = 0.0055$ $m^2$, $b = 0.45$, $s = 3.0$ kg $m^{-3}$, $\nu_1 = 0.1$ $m^2$ and $\nu_2 = 0.01$ $m^2$.

145

- With constant release and entrained snow characteristics but varying the friction parameters to reach the same runout distance: snow cover strength $p_{lm} = 1$ kPa, snow cover density 300 kg m$^{-3}$, snow cover depth $d_e = 2.0$ m. Entrainment limited to the upper part of the track.

- A simulation is also performed using the Voellmy-Salm procedure according to the Swiss Guidelines. The friction parameters for a large avalanche ($\mu = 1000$ and $\xi = 0.155$ m s$^{-1}$) were used. The position of the point $P$ is at the intersection of the two segments composing the avalanche path (see Fig. 5.4).
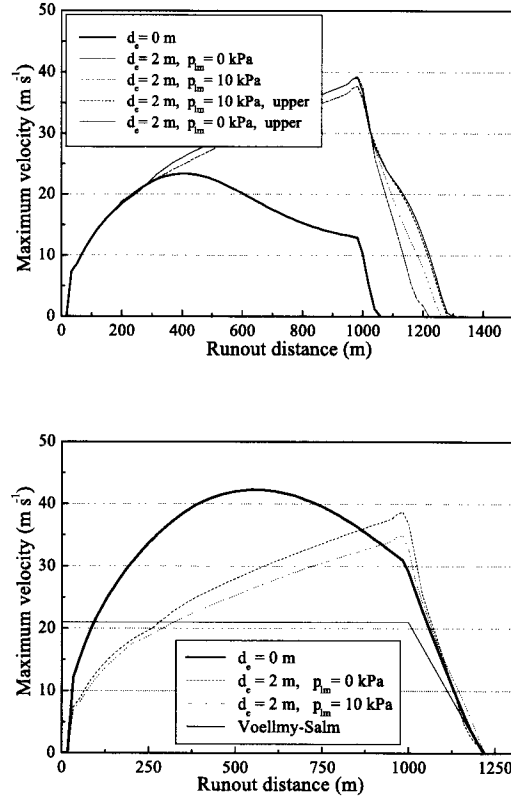
Figure 5.8, upper panel, shows the maximum velocity distributions along the avalanche path for cases 1 and 2 listed above. The bold full line shows the results of the simulation without entrainment. It is observed that the avalanche without entrainment starts to decelerate while still within the steeper part of the track. Avalanches entraining snow along the path increase their velocity until reaching the change in slope of the avalanche track. All simulated avalanches start to decelerate when the flatter part of the track is reached ($x = 1000$ m). The longer runout distance was reached by the avalanches that entrained mass only in the first part of the track. Figure 5.8 also shows that the avalanche that entrains snow on the flatter zone decelerates faster. The highest maximum speeds are reached by the simulations with entrainment.

Figure 5.8, bottom panel, shows the maximum velocity distribution for the cases 1, 3 and 4 (straight line). To obtain the runout distance calculated with the Voellmy-Salm model (215 m from point $P$) the simulation parameters were varied from case to case. In particular, the following parameters sets have been used:

- Case $d_e = 0$ m: $m = 0.0007$ m$^2$, $b = 0.20$, $s = 3.0$ kg m$^{-3}$, $\nu_1 = 0.01$ m$^2$ and $\nu_2 = 0.001$ m$^2$.

- Case $d_e = 2$ m, $p_{lm} = 0$ kPa: $m = 0.006$ m$^2$, $b = 0.45$, $s = 3.0$ kg m$^{-3}$, $\nu_1 = 0.1$ m$^2$ and $\nu_2 = 0.01$ m$^2$.

- Case $d_e = 2$ m, $p_{lm} = 10$ kPa: $m = 0.006$ m$^2$, $b = 0.48$, $s = 3.0$ kg m$^{-3}$, $\nu_1 = 0.1$ m$^2$ and $\nu_2 = 0.01$ m$^2$.

It is observed that to obtain the same runout distance, the parameters used in the simulation without entrainment are lower, i.e. the avalanche reaches the runout calculated with the Voellmy-Salm model only if the friction value is reduced. The avalanche without entrainment increases its speed, reaching a maximum velocity at about the half-way point

**Figure 5.8:** *Maximum velocity distribution along the avalanche path. Comparison between simulations without (bold straight line) and with entrainment. Calculations are performed with the NIS model. Upper panel: simulation parameters: $m = 0.0055$ m$^2$, $b = 0.45$, $s = 3.0$ kg m$^{-3}$, $\nu_1 = 0.1$ m$^2$ and $\nu_2 = 0.01$ m$^2$. Bottom panel: the parameters varied from case to case to match the runout calculated with the Voellmy-Salm model.*

of the steeper part of the track and then decelerates. In comparison, the avalanche with a mass variation slowly increases its speed, reaching a maximum at the point $P$. At the slope change the avalanches entraining mass have higher speed; however, the absolute maximum speed is reached by the avalanche without entrainment, at about half way along the steeper part of the track.

The pressure exerted by the avalanche is proportional to the square of the avalanche speed $U$. In Figure 5.9 the dimensionless ratio $U^2/U_P^2$, proportional to the avalanche pressure, is plotted as a function of the distance. The velocity $U_P$ is the avalanche speed at the point $P$ calculated using the Voellmy-Salm model. The square velocity term is calculated for the runout zone starting from the point $P$.

147
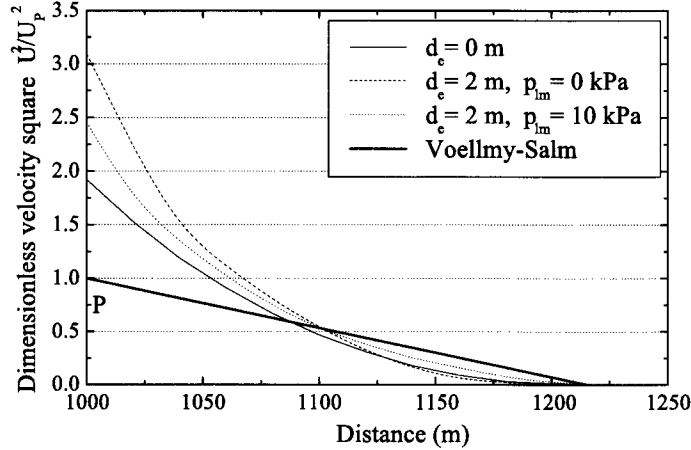
**Figure 5.9:** *The dimensionless ratio $U^2/U_P^2$ is plotted as a function of the distance.*

In Figure 5.9 the straight bold line represents the calculations performed using the Voellmy-Salm model (Swiss Guidelines). The other curves display the calculations performed using the Voellmy-fluid model with and without entrainment. It is observed that at the point $P$ the square velocity term calculated using the Voellmy-fluid model is considerably higher; however, it decreases below the Swiss Guidelines curve in the second part of the runout. In the first part of the track the highest ratio is calculated with the Voellmy-fluid model including entrainment.

This behavior shows that the avalanche speed and the avalanche pressure, in the first part of the runout zone reach higher values if calculated with the continuum models. However, the avalanches decelerate faster in the second part of the runout, resulting in lower overall speeds and pressures. The deceleration rate depends on the characteristics of the snow cover. In our case the avalanche that arrives at $P$ with the highest velocity (easily erodible snow conditions) has a faster deceleration along the second (flatter) part of the track.

### Effect on flow and deposition depths

Fig. 5.10 shows a comparison between the maximum flow depths calculated using the same parameters as in Fig. 5.8, upper panel. Comparing Fig. 5.8, upper panel, and Fig. 5.10 it is clear that the maximum speed is reached by the avalanches having the maximum flow depth, i.e. by the avalanches entraining mass. The entrained snow accumulates at
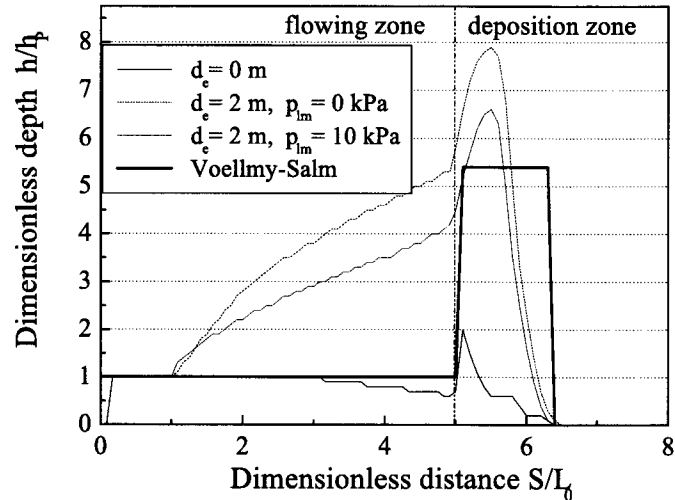
**Figure 5.10:** *The dimensionless maximum avalanche depth is plotted as a function of the dimensionless projected distance. $h_P$ corresponds to the avalanche flow depth calculated at P using the Voellmy-Salm model (Swiss Guidelines).*

the front where it is entrained, increasing the flow depth and, as a result, the speeds.

Thus, the models are very sensitive to the entrainment location within the avalanche body. Figure 5.11 shows an example of different flow depth distributions obtained by performing simulations in which the same amount of mass is entrained using different approaches. The example corresponds to the back calculation of the Pizzac event of March $5^{th}$, 1999. A point along the avalanche path has been chosen and the flow depth distribution is plotted as a function of the time. The three curves correspond to three different entrainment approaches: 1) the snow is entrained immediately at the avalanche front, 2) the snow is entrained at an area localized close to the avalanche front and 3) the mass is entrained along the entire avalanche length. The time shift along the $x$-axis indicates that the lower the avalanche depth the slower the avalanche speed; that is if the avalanche reached the observed point later, the speed was lower.

# 5.3 Model validation

A qualitative validation is performed by comparing model predictions to the experimental data with the aim to determine if the model gives a valid representation of the observed
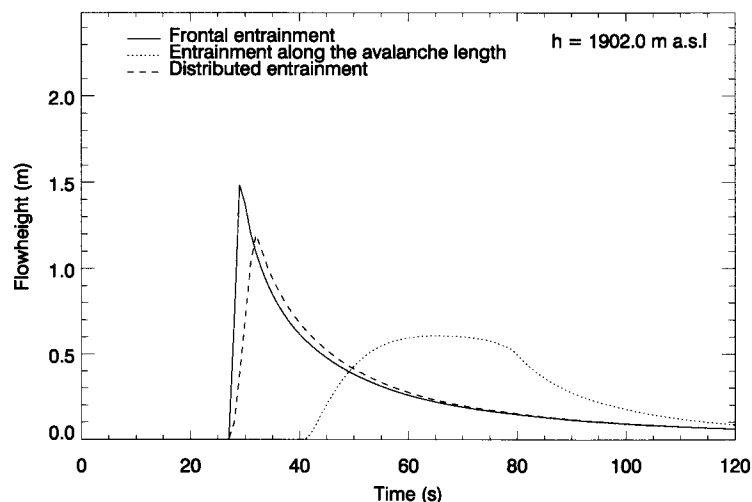
**Figure 5.11:** *Flow height simulations of March $5^{th}$, 1999, Pizzac avalanche using the NIS model. The same snow mass is entrained using three different erosion methods: frontal erosion (solid line), erosion distributed along all the avalanche length (dotted line) and erosion distributed over a part of the avalanche length (dashed line - distributed entrainment). Dashed line gives the best fit between experimental data and simulation.*

avalanches. In particular we want to answer the following questions:

- Does the model reproduce the physical behavior observed in snow avalanches?

- How different are the model predictions from the observations?

- Can the model accurately predict extreme avalanche runout distances, velocities and flow depths?

To examine the correspondence between model predictions and the experimental data simulations are performed using both the Voellmy-fluid and NIS models.

## 5.3.1 The Braemabuel avalanche

The Braemabuel avalanche represents an interesting case study (see §3.6). Field observations revealed that the snow cover had a well defined, layered structure with constant characteristics along the entire path. The avalanche entrained different layers, making this data set ideal for the verification of the entrainment theory and modelling. Figure 3.24 shows a simplified description of the data.

Simulations were performed using both Voellmy-fluid (see §5.1.1) and NIS (see §5.1.2) models. The volumetric snow entrainment rate $\dot{S}_e$ is calculated using equation 5.2.

In the simulations the snow layers were defined according to field measurements. The snow cover formed two layers having density and depth of $\varrho_1 = 200$ kg m$^{-3}$, $h_1 = 0.4$ m and $\varrho_2 = 300$ kg m$^{-3}$, $h_2 = 0.5$ m, respectively. The two layers are separated by a snow crust.

The strength of the layers was determined using the shear strength measurements of Brun & Rey (1987): the dry snow layer having $\varrho_1 = 200$ kg m$^{-3}$ had a mean shear strength of about $\tau_{s1} = 2.5$ kPa and the dry snow layer having $\varrho_2 = 300$ kg m$^{-3}$ had a mean shear strength of about $\tau_{s2} = 10$ kPa.

**The NIS simulations**

Two types of simulations were carried out. The first assumes that frontal impact forces dominate the erosion process, the second assumes a pure shear stress between the avalanche and snow cover.

Assuming that the main avalanche stress responsible for entrainment is given by the frontal impact pressure between the avalanche and the snow cover, the stress $p_i$ can be described as:

$$p_i = c_i \rho U^2 \tag{5.23}$$

The simulations were performed using the parameters: $m = 0.055$ m$^2$, $b = 0.43$, $s = 0.4$ kg m$^{-3}$, $v_1 = 1$ m$^2$ and $v_2 = 0.1$ m$^2$. The simulation results are shown in Fig. 5.12, upper panel.

The layer strength in the simulations were set according to the Brun & Rey (1987) values: 2.5 kPa and 10 kPa for the new and old snow layers respectively. The snow crust strength was 50 kPa.

The comparison between field measurements and calculations shows good agreement. In particular:

- The new snow layer is entrained.

- The old snow layer is not entrained in the flatter upper part of the track and below the main deposit at the bottom of the valley, in agreement with the field measurements.

- There is good agreement between avalanche stress and snow cover strength.
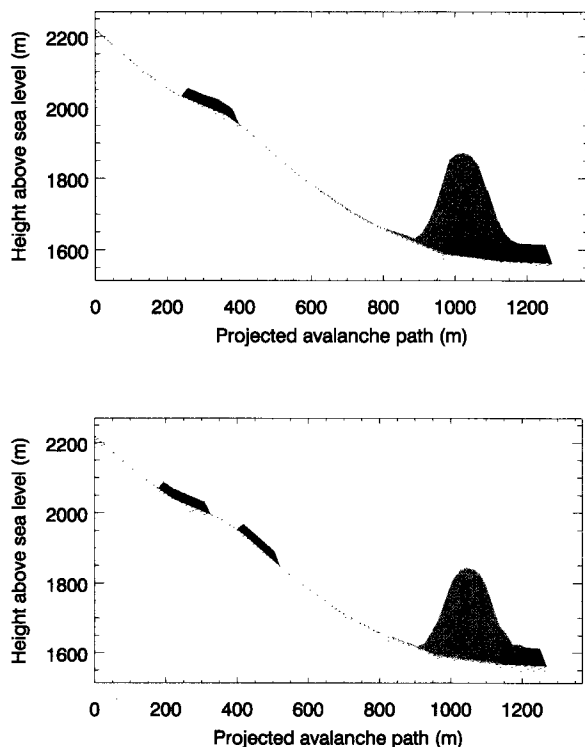
**Figure 5.12:** *Braemabuel simulations using the NIS model. Upper plot: The correct erosion is obtained by assuming a frontal impact between avalanche and snow cover. Lower plot: The assumption of a pure shear stress between avalanche and snow cover produces an incorrect erosion pattern.*

It is observed that the erosion was controlled by the snow crust; without it most of the snow cover would be entrained immediately at the avalanche front.

A second simulation was performed assuming that the avalanche exerts a pure shear stress on the snow cover. The stress $p_i$ is defined by the slip conditions in equations 5.20 and 5.22. The simulation was performed using the parameters $m = 0.055$ m$^2$, $b = 0.39$, $s = 0.4$ kg m$^{-3}$, $v_1 = 1$ m$^2$ and $v_2 = 0.1$ m$^2$. Results are shown in Fig. 5.12, below.

To obtain the layer erosion shown in Fig. 5.12, below, the layer resistances were set to 0.3 kPa and 1.7 kPa for the new and old layers respectively, i.e. considerably lower than the values given by Brun & Rey (1987). If the resistance were set to the values measured by Brun, the calculated shear stress would not be enough to entrain the layers.

In this case the comparison between field measurements and calculations does not show good agreement. In particular:

- The avalanche entrains the old snow cover in both the flatter part of the track where avalanche depths are higher and below the deposits. To understand this behavior the slip condition has been divided into a hydrostatic component, which is a function of the flow height, and a dynamic component, which is a function of the velocity squared. The two terms were calculated separately and plotted on a graph (Fig. 5.13). The hydrostatic term $b\rho g h \cos \varphi$ was calculated using $b = 0.39$, $\rho = 300$ kg m$^{-3}$, $h$ variable between 0 and 8.5 m and $1° < \varphi < 41°$ as calculated in the simulation. The dynamic term $s u_0^2$ was calculated using $s = 0.4$ kg m$^{-3}$ and $0 < u_0 < 36$ ms$^{-1}$, corresponding to the minimum and maximum speeds in the simulation. Figure 5.13 shows that the dynamic component is an order of magnitude smaller than the hydrostatic component and that the erosion is controlled by this last component, i.e. by the flow height. The larger the flow height, the larger the erosion; therefore erosion is mainly localized beneath the deposits, completely in disagreement with the field observations.

- The avalanche left part of the old snow cover along the first part of the steeper gully.

- The avalanche applied a very low stress on the snow cover.

Our observation is that the contribution of the shear stress exerted by the avalanche on the snow cover is negligible in comparison to the impact pressure. In addition the shear stress produced entrainment is not in agreement with the observed data. For this reason we assume that the impact pressure is the stress responsible for entrainment.

## The Voellmy-fluid model simulations

The same simulations were performed using the Voellmy-fluid model. The stress $p_i$ is described by the relation:

$$p_i = \rho \left( gh + c_i U^2 \right) \tag{5.24}$$

This relation was first used by Grigorian & Ostroumov (200) to describe entrainment. The stress is composed of the hydrostatic pressure term $\rho g h$ and a dynamic-impact pressure term, as already defined by equation 5.23. The calculation was performed using (1) both terms and (2) only the term corresponding to the impact pressure (i.e. the velocity squared term).

Simulations were performed using the friction parameters $\mu = 0.36$, $\xi = 1500$ m s$^{-2}$ and $\lambda = 7$. The layer strength was fixed according to the Brun & Rey (1987) values at
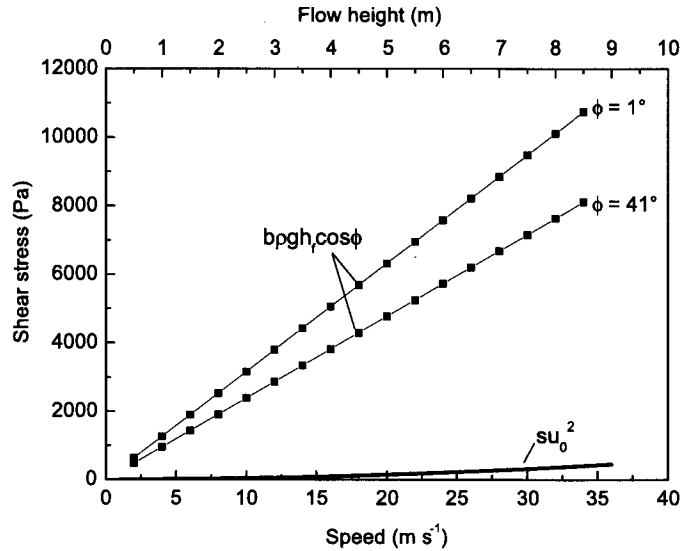
**Figure 5.13:** *Comparison between the hydrostatic (upper horizontal scale) and dynamic (lower horizontal scale) components as defined in the NIS slip condition.*

2.5 kPa and 10 kPa for the new and old snow layers respectively. The snow crust strength was 50 kPa. Results were the same as obtained by using the NIS model (see Fig. 5.12, above), and further indicate that the hydrostatic pressure is negligible in comparison to the impact pressure.

Also, in this case, the correct entrainment can be described by the stress relation 5.23.

## 5.3.2 Small avalanche: Pizzac simulations

Small avalanches with short return periods, which lose mass on steep slopes and quickly come to a halt, are difficult to calculate with current dynamical models. The Pizzac events are typical examples of this problem.

In the following we back-calculate an avalanche event recorded at the Pizzac avalanche test site on March $5^{th}$, 1999. This event was chosen because it was the largest and best documented event recorded at this site (i.e. largest runout distance, mass involved in the motion, flow velocity and pressure).

The simulation of the avalanche using the Voellmy-Salm model (without entrainment) shows that the frontal speed, height of flow, avalanche length and deposits are strongly
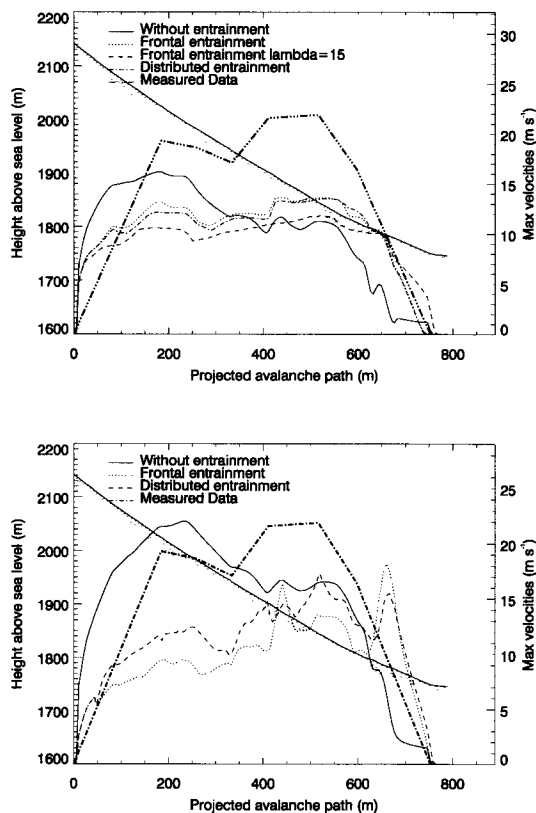
**Figure 5.14:** *Speed simulations of a small avalanche (Pizzac event of March 5th, 1999) using the Voellmy-fluid (VS, upper panel) and the NIS Norwegian model (lower panel). Simulations without entrainment, with frontal entrainment (for the VS $\lambda = 2.5$ and $\lambda = 15$) and with entrainment distributed along the avalanche length are compared with experimental data.*

underestimated ($\mu = 0.35$, $\xi = 3000$ m s$^{-2}$ and $\lambda = 2.5$). The speed results are shown in Fig. 5.14, upper panel. The measured and calculated flow heights are shown in Fig. 5.15; deposition heights are shown in Fig. 5.16, upper panel.

The same measurements were also back-calculated using the NIS model (without entrainment). The simulation was performed using friction values close to the smallest values within the range specified by Norem et al. (1989) ($m = 0.005$ m$^2$, $b = 0.4$, $s = 0.5$ kg m$^{-3}$, $v_1 = 0.001$ m$^2$ and $v_2 = 0.0001$ m$^2$). Fig. 5.14, lower panel, shows the comparison between model results and measurements. We note that calculated and measured speeds are in good agreement, as well as the runout distances. However, using constant parameters, it is not possible to obtain the acceleration measured in the second part of the track. In addition, flow height, avalanche length and depositions are unrealistic (see
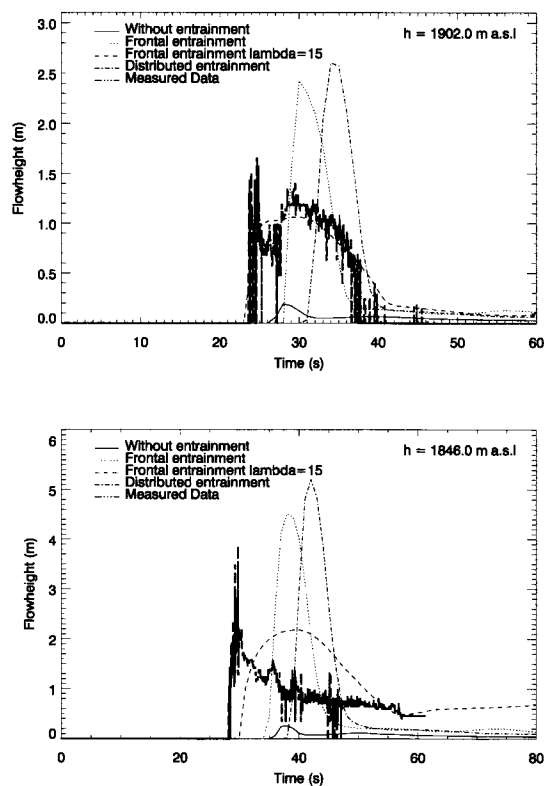
**Figure 5.15:** *Flow height simulations of a small avalanche (Pizzac event of March 5$^{th}$, 1999) using the Voellmy-fluid model. Simulations without entrainment, with frontal entrainment ($\lambda$ = 2.5 and $\lambda$ = 15) and with entrainment distributed along the avalanche length are performed in two positions along the avalanche path. Calculated data are compared with experimental data. Upper panel: point located at 1902 m a.s.l. where the gradient is about 29°. Lower panel: point located at 1846 m a.s.l. where the slope angle is about 38°.*

Figs. 5.17 and 5.16, bottom panel).

This particular avalanche was characterized by strong erosion, in that it increased its mass up to 9 times with respect to the released mass. To demonstrate the mass variation effect, simulations with entrainment were also performed. The densities used for these calculations ranged between 160 and 320 kg m$^{-3}$; the entrainment depth $d_m$ ranged between 0.4 and 0.7 m. In agreement with the measurements, all of the user-specified snow cover was entrained in the simulations.

Since front entrainment processes appear to dominate (see §3.3.3), in the first simulation the mass is entrained at the avalanche front. The model assumes that the eroded mass is instantaneously accelerated to the avalanche speed. A second simulation is performed

**Figure 5.16:** *Simulated deposits for a small avalanche (Pizzac event of March $5^{th}$, 1999) using the Voellmy-fluid and the NIS model. Simulations without entrainment, with frontal entrainment (for the VS $\lambda=2.5$ and $\lambda=15$) and with entrainment distributed along the avalanche length are compared with experimental data. Note the difference between simulations with and without entrainment.*

in which the acceleration requires a specified amount of time (indicated in the figures as *distributed entrainment*).

The results of the simulations performed using the NIS model are shown in Figs. 5.14, bottom panel, 5.16 and 5.17 ($m = 0.055$ m$^2$, $b = 0.5$, $s = 3$ kg m$^{-3}$, $v_1 = 1$ m$^2$ and $v_2 = 0.1$ m$^2$). The friction parameters used in the simulation with entrainment are higher than the parameters used in the case without entrainment in order to stop the avalanche at the same runout distance. In the simulation with entrainment the calculated speed in the runout zone is also higher than in the simulation without entrainment.

In general, the calculations with entrainment show that the calculated speeds are lower than the observed data and, in the first part of the track, also lower than the calculated
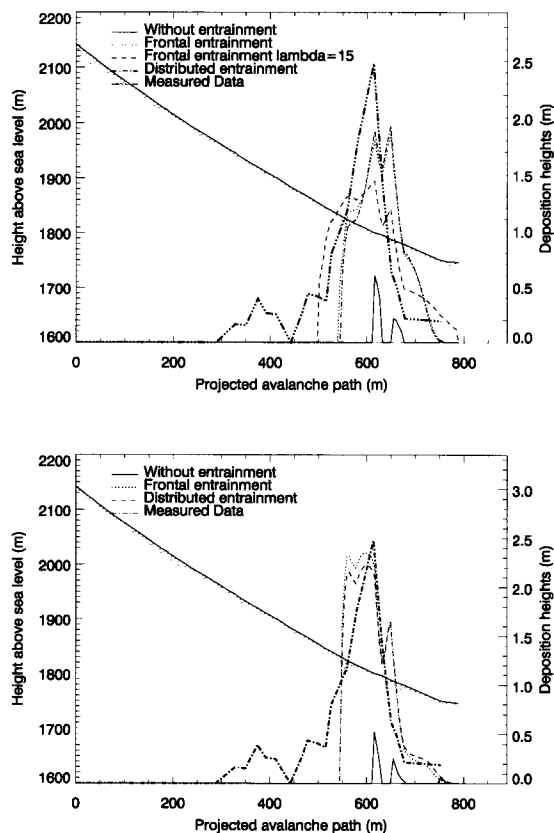
157
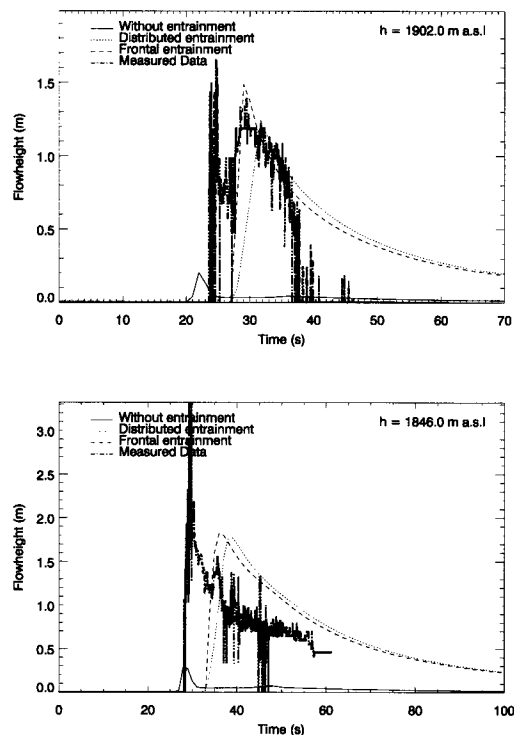
**Figure 5.17:** *Flow height simulations of a small avalanche (Pizzac event of March $5^{th}$, 1999) using the NIS model. Simulations without entrainment, with frontal entrainment and with entrainment distributed along the avalanche length are performed in two positions along the avalanche path and compared with experimental data. Upper panel: a point located at 1902 m a.s.l. where the gradient is about $29°$. Lower panel: a point located at 1846 m a.s.l. where the gradient is about $38°$. Note the very good agreement between calculated (with entrainment) and measured flow heights.*

speeds without entrainment. However, simulations with snow entrainment better reproduce the avalanche acceleration observed in the second part of the track. Recall that in this particular event the avalanche started to accelerate in spite of the lower gradient (see §3.3.2 and Fig. 3.4 for more details on the event).

The flow height over steep slopes and the distribution of deposit match the field measurements for both simulations containing entrainment (see Fig. 5.17). Over gentle slopes, in order to reach good agreement between measured and calculated heights, a time-delay, or distributed entrainment is necessary (see Fig. 5.17, upper panel). Depositions heights are also in good agreement with measured data (see Fig. 5.16, lower panel).

Interestingly, by increasing the time over which the collected snow is accelerated to the avalanche speed, maximum flow heights move back into the avalanche body and away

from the avalanche front. If the time delay is too large the avalanche dynamics can change substantially (see Fig. 5.11). In this figure the same snow mass is entrained using three different erosion methods: frontal erosion (solid line), erosion distributed along all the avalanche length (dotted line) and erosion distributed over a part of the avalanche length (dashed line). The erosion distributed over only a part of the avalanche length (distributed entrainment in Fig. 5.11) gives the best fit between experimental data and simulation.

The same simulations have been performed with the Voellmy-fluid model ($\mu = 0.48$, $\xi = 1600$ m s$^{-2}$ and $\lambda = 2.5$) (see Figs. 5.14, upper panel, 5.15, 5.16, upper panel). The results of these simulations are not as good as the simulation performed with the NIS model. Flow heights are strongly over-estimated and, although the simulated maximum heights are behind the front (see §3.3.3), the mass is distributed more in the height than in the length (see Fig. 5.15). This suggests that the assumption of no shear deformation together with the longitudinal straining do not describe the physical phenomenon appropriately because the mass transfer of entrained snow to the avalanche body is not correctly modelled. To calculate the correct height of flow, the $\lambda$ parameter must be increased to a value of 15. This could be physically explained by assuming an internal friction angle of about 60° or by considering the influence of the snow cohesion. However, although the introduction of a high $\lambda$ value helps simulate the measured flow heights, it also decreases the speed and increases the runout distance, making the simulations incorrect with respect to these results.

The NIS model, which accounts for a non-zero shear deformation rate and a longitudinal straining governed by a passive pressure depending on the shear deformation rate, describes and simulates small avalanche behavior better.

## 5.3.3 Large avalanche: Vallée de la Sionne simulations

It has been already demonstrated that the lack of snow entrainment in the models is one of the reasons why they function poorly for small avalanches events where mass evolution is significant. On the other hand, it has been observed that large avalanches also entrain most part of the snow cover lying on the ground. To investigate the influence of the entrained mass on the behavior of large avalanches, model simulations with and without entrainment were performed.

During the winter 1998/99 three very large avalanches events were artificially triggered at the VDLS test site. The largest avalanche was released on February 25$^{th}$. It was characterized by an average fracture depth of about 1.5 m that extended over a length of about 1 km. By the use of photogrammetric measurements (Vallet et al., 2001), the

159

total release mass was estimated to be 63,300 tons. The deposition volume was also determined. The avalanche travelled more than 4000 m. The image processing of a video recording gave the frontal speed of the event in the first 2000 m of track. FMCW radar, located in three positions along the avalanche path, allowed local entrainment rates and the distribution of flow height to be determined. The average height and density of the snow cover entrained by the avalanche have been estimated to be about 2.0 m and 200 kg $m^{-3}$, respectively.

In order to simulate a very large avalanche event with a one-dimensional model the spatial variability of the terrain profile, the frontal speeds, the flow heights and the deposit distributions were carefully analyzed in order to find the correct one-dimensional approximation.

As with the Pizzac avalanches, the February $25^{th}$ avalanche is also back-calculated using a Voellmy-fluid (VS) model and the NIS model. Simulations with and without entrainment were performed. The simulated avalanche entrains snow by eroding a user-specified snow cover. The snow cover is composed of one layer characterized by a height and density equal to the height and density of the layer entrained by the real avalanche. The average density value used for these calculations is 200 kg $m^{-3}$; the average entrainable height is 2.0 m. All the user-specified snow cover was entrained. Simulations have been compared with the height-intensity output of a FMCW radar located along the avalanche path. The radar plot interpretation was difficult because the boundary layer between the dense and the powder part of the avalanche was not clearly defined (we are simulating only the dense part of the avalanche). The maximum dense flow height was estimated at about 5 m. The avalanche took more than 90 seconds to pass over the radar.

Figures 5.18 and 5.19 show the results of these simulations.

Simulations without entrainment (NIS model parameters: $m$=0.003 m$^2$, $b = 0.34$, $s = 0.4$ kg $m^{-3}$, $v_1 = 0.001$ m$^2$ and $v_2 = 0.0001$ m$^2$ and VS parameters: $\mu = 0.16$, $\xi = 2700$ m s$^{-2}$ and $\lambda = 2.5$) clearly show discrepancies: flow heights and deposits are strongly underestimated (see Fig. 5.19). It is important to point out that the model does not account for density variations, meaning that the density of the avalanche along the avalanche path hs the same density as the avalanche deposit. A normal density value used in the simulations is 300 kg $m^{-3}$. This density should be a reasonable value during the flow phase. However, observations of densities in large avalanche deposits shows a much higher value: 400–600 kg $m^{-3}$. Since the model does not consider snow compression, the calculated deposition height should be reduced by about 50%–75%.

Better simulations are obtained by introducing entrainment. Figure 5.19 shows flow
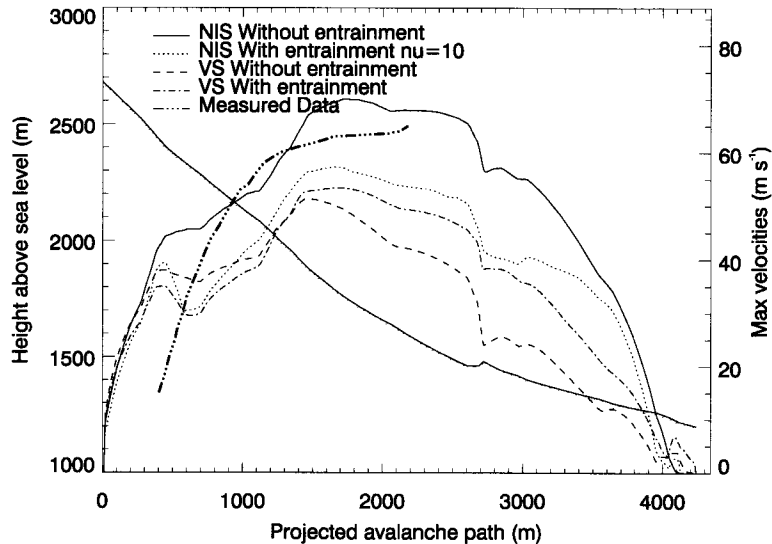
**Figure 5.18:** *Speed simulations of a large avalanche (VDLS event of February 25$^{th}$, 1999) using the Voellmy-fluid (VS) and the NIS model. Simulations without and with entrainment are compared to the observed data. Note that speeds calculated with the NIS model are in fair agreement with the observed data.*

height simulations using the NIS model ($m = 0.055$ m$^2$, $b = 0.34$, $s = 0.4$ kg m$^{-3}$, $v_1 = 0.0001$ m$^2$ $v_2 = 0.1$ m$^2$ and $m = 0.055$ m$^2$, $b = 0.34$, $s = 0.4$ kg m$^{-3}$, $v_1 = 10$ m$^2$ and $v_2 = 0.1$ m$^2$) and the VS model ($\mu = 0.23$, $\xi = 2500$ m s$^{-2}$ and $\lambda = 2.5$).

The better simulation is given by the NIS model with entrainment and a large longitudinal viscosity $v_1 = 10$ m$^2$ (see Fig. 5.19, upper panel). Note that without the introduction of a high value of normal stress viscosity, flow heights are too high. Also with the introduction of a large longitudinal viscosity the avalanche length is too short; more mass should be moved back into the tail. This means that internal shear deformations together with the longitudinal straining defined in the model are not sufficient to account for the backwards transfer of the entrained snow in large avalanches. In large avalanches the process of mass transfer inside the avalanche body appears to be stronger than in small avalanches.

It should be considered that the model uses constant friction values along all the avalanche length. It has been demonstrated that the distribution of the mass within the avalanche depends on the terrain/snow cover friction. Higher friction increases the snow transfer from the body to tail of the avalanche (see §3.3.3). In reality, the importance

161
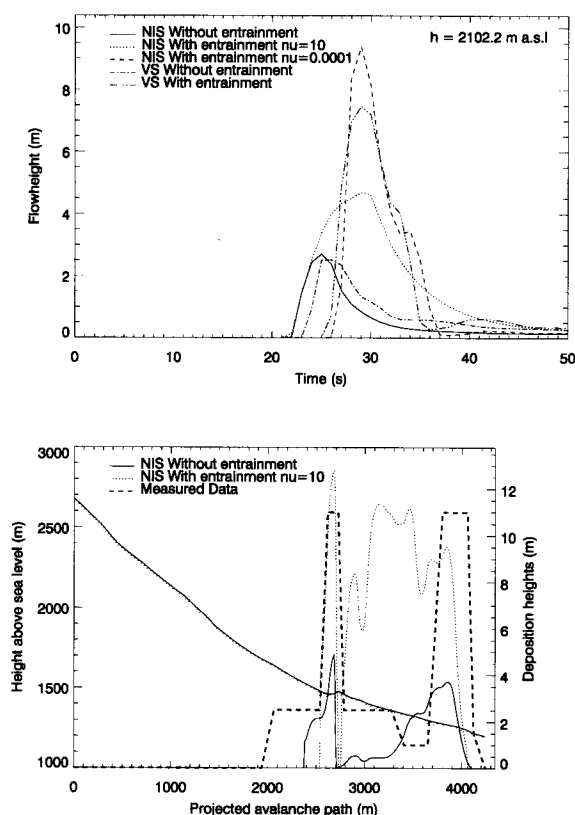
**Figure 5.19:** *Upper panel: flow height simulations of a large avalanche (VDLS event of February $25^{th}$, 1999) using the NIS model and the VS model. The better simulation is given by NIS model with entrainment and $\nu_1 = 10$ m². Lower panel: deposit simulations using the NIS model. Simulations with and without entrainment are compared with experimental data. Since the model does not account for density variations, calculated heights should be reduced by about 50%–75%.*

of the friction differs between the avalanche tail, where roughness and avalanche height are comparable, and the avalanche head, where the avalanche dimensions are an order of magnitude larger than the roughness. The application of a variable friction parameter could accelerate the avalanche front and decelerate avalanche tail, simulating the natural extension of the avalanche.

Observations of deposition heights show that only with entrainment are the real and calculated volumes in the deposition zone similar (see Fig. 5.19, lower panel). The simplified one-dimensional profile does not allow a precise deposit distribution to be obtained.

## 5.3.4 The extreme avalanches of the winter 1998/99

Avalanche dynamic models are primarily used to simulate extreme avalanches. For this reason six extreme avalanches of the winter 1998/99 have been back-calculated. The avalanche data are contained in Tables 3.11 (Loeuewenbach, Jungstafel, Cheer, Cheer-west and Aulta) and 3.8 (VDLS avalanche of February $25^{th}$). All avalanches have large dimension. Both open slope and channelled avalanches are considered.

Calculations are performed with the Voellmy-fluid continuum model using four different approaches:

1. *Case 1*: release area $A_r$, measured fracture depth $d_0$, entrainment along the path (the average entrainment depth $d_e$ is used), calibration parameters obtained by back-calculation of events. A snow cover having depth $d_e$ is defined as input for all the avalanche track having slope angle larger than 10°. All the defined snow cover is entrained at the avalanche front.

2. *Case 2*: release area $A_{r_{SG}}$, fracture depth $d_{SG300}$ as defined by the Swiss Guidelines (SLF, 1999), no entrainment, calibration parameters obtained by back-calculation of events. These simulations have been performed to directly compare simulations with (*Case 1*) and without (*Case 2*) entrainment.

3. *Case 3*: release area $A_{r_{SG}}$, fracture depth $d_{SG300}$ as defined by the Swiss Guidelines (SLF, 1999), no entrainment, calibration parameters given by the Swiss Guidelines for avalanches with a return time period of 300 years (SLF, 1999). Avalanches have been calculated using the calibration parameters defined by the Swiss Guidelines to simulate large avalanches (release volume larger than 60 000 m³). The parameters are given based on path topography (open slope, channel, narrow channel) and altitude (over 1500, between 1500 and 1000 m a.s.l. below 1000 m a.s.l.). These simulations correspond to the procedure actually used by practitioners to calculate avalanche pressure, runout distances, flow and deposition depths.

4. *Case 4* (only for the avalanches whose runout distance has been not correctly simulated in *Case 3*): extended release area to reach the observed runout, fracture depth $d_{SG300}$ as defined by the Swiss Guidelines (SLF, 1999), no entrainment, calibration parameters defined by the Swiss Guidelines.

The parameters used to back-calculate the events are shown in Fig. 5.20. The main simulation results for maximum velocities, runout distances, deposition depth and maximum

**Table 5.2:** *Calibration parameters for the Voellmy-fluid model used to back-calculate extreme avalanches of the winter 1998/99. Simulations with and without entrainment were performed. c= channelled, os= open slope.*

| | Type | with entrainment | | | | | without entrainment | | |
|---|---|---|---|---|---|---|---|---|---|
| | | $\mu_1$ | $\xi_1$ m s$^{-2}$ | $\mu_2$ | $\xi_2$ m s$^{-2}$ | $\lambda$ | $\mu_3$ | $\xi_3$ m s$^{-2}$ | $\lambda$ |
| Loeuewenbach | c | 0.30 | 2500 | 0.28 | 2000 | 7 | 0.28 | 2500 | 7 |
| Jungstafel | os | 0.27 | 2500 | 0.24 | 2000 | 7 | 0.13 | 2500 | 7 |
| Cheer | os | 0.24 | 2500 | 0.21 | 2000 | 7 | 0.13 | 2500 | 7 |
| Cheer-west | c | 0.26 | 2500 | 0.24 | 2000 | 7 | 0.19 | 2500 | 7 |
| Aulta | c | 0.26 | 2500 | 0.24 | 2000 | 7 | 0.25 | 2500 | 7 |
| VDLS | os | 0.22 | 2500 | 0.21 | 2000 | 7 | 0.15 | 2500 | 7 |

flow depth are shown in Figs. 5.21 and 5.22. Calculated deposition depths are compared against real deposition data. Avalanche speed measurements were available only for the VDLS avalanche.

In the *Case 1* simulations, in order to match the observed runout distances, the parameter $\xi$ was set to a constant value and the parameter $\mu$ was varied. The parameter combinations matching the observed runout are shown in Table 5.2. Simulations were performed twice assuming $\xi_1 = 2500$ m s$^{-2}$ and $\xi_2 = 2000$ m s$^{-2}$ respectively. The input avalanche mass in the calculation corresponds to the observed release avalanche mass.

For *Case 2*, simulations were performed assuming a constant $\xi_3 = 2500$ m s$^{-2}$ and a variable $\mu_3$ in order to match the observed runout distances. These parameter combinations are also shown in Table 5.2. The avalanche mass in the calculation does not correspond to the observed avalanche release mass but is defined on the basis of the Swiss Guidelines (SLF, 1999).

Comparison of flow height and velocities simulated with (*Case 1*) and without entrainment (*Case 2*) are shown in Figs. 5.21 and 5.22.

We find that when simulations with entrainment are performed, i.e. using the observed avalanche mass, the $\mu$ parameter range decreases substantially. In the box plot shown in Fig. 5.20, the parameter ranges used to back calculate all avalanches are shown.

In particular, for simulations without entrainment the parameters are sensitive to the type of path and tend to be higher in the case of channelled avalanches. It is also observed that the parameters used to back-calculate channelled avalanches without entrainment are similar to the ones used to calculate all avalanches (channelled or open slope) with entrainment. To simulate open-slope avalanches without entrainment, lower friction parameters

164
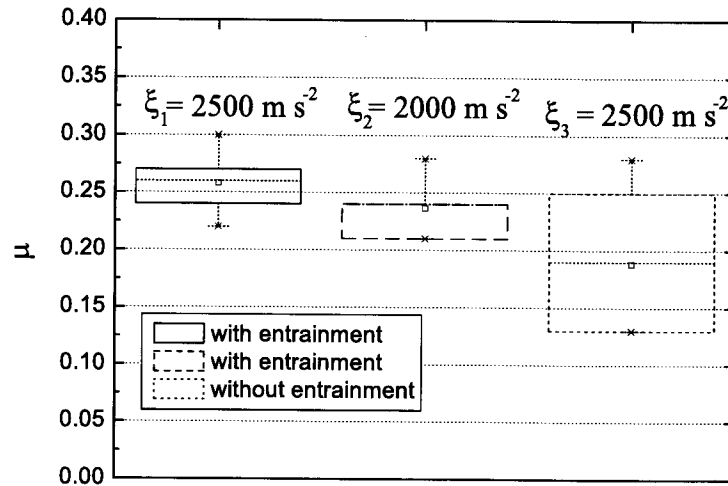
**Figure 5.20:** *Parameters used to back calculate the extreme avalanches of 1999. The range of the parameter $\mu$ is plotted for Case 1 (with entrainment, $\xi_1 = 2500$ m s$^{-2}$, $\xi_2 = 2000$ m s$^{-2}$) and for Case 2 (without entrainment, $\xi_3 = 2500$ m s$^{-2}$). The range of parameter $\mu$ in the case of the simulation with entrainment (Case 1) is significantly smaller than the simulation without entrainment (Case 2). The box plots show the mean (square in box), the median (line in box), 25/75% quantiles (box), 5/95% quantiles (whiskers) and 0/100% quantiles (cross).*

are needed.

In the case with entrainment, there is no evident distinction between the friction parameters for channelled and open slope avalanches.

The simulations also showed that maximum flow depths increase substantially when considering entrainment (see Fig. 5.22), the increase being more evident for open-slope avalanches. For open-slope avalanches with no entrainment, the snow can spread out over a large transversal length and the calculated snow depths are quite small. Including entrainment, however, can easily more than double the simulated flow heights. If the flow depth is increased, the second term in Eq. 5.5 becomes smaller and the influence of the parameter $\xi$ is reduced. Calculations performed using $\xi_1 = 2500$ m s$^{-2}$ and $\xi_2 = 2000$ m s$^{-2}$ are compared. Small velocity differences are observed.

Maximum avalanche velocities are also compared. It is observed that, initially, avalanches that entrain mass have a lower acceleration in comparison to avalanches that do not entrain snow. This behavior is observed for all examined avalanches and it is explained by the fact that the entrained mass must be accelerated to the avalanche speed, causing a

loss of velocity of the avalanche. However, when the entrainment significantly increases avalanche mass and flow depths, the loss in velocity is offset by reduction of the resistance force. Consequently the typical velocity for an avalanche with entrainment is lower in the first part of the track and higher in the second part.

In two cases avalanches entraining mass do not reach the velocities calculated without entrainment (see Fig. 5.21, Aulta and Loeuewenbach). This is mainly due to the ratio between released mass $M_r$ and entrained mass $M_e$. If most of the avalanche mass is defined as release mass as opposed to the entrained mass, as is the case in the Aulta ($M_e/M_r = 0.3$) and Loeuewenbach ($M_e/M_r = 0.4$) avalanches, a large flow depth change does not occur upon entrainment. Thus, the resultant deceleration effect is not overcome and overall velocities are lower. In contrast, when a larger part of the mass is defined as entrainment, as in the cases of Jungstafel ($M_e/M_r = 0.8$) and Cheer ($M_e/M_r = 1.0$) avalanches, the flow depths increase substantially and, as a result, the avalanche speed increases (see Fig. 5.21, Jungstafel and Cheer).

Simulations were also performed following the Swiss Guidelines, as used by practitioners for extreme avalanches (*Case 3*). The parameters used for these simulations are shown in Table 5.3. Simulations show that for three of the six examined avalanches, calculated runout distances are too short (see Fig. 5.21, Jungstafel, Cheer and VDLS).

In all of these cases, the released mass defined by the guidelines is larger than the observed release mass. However, the total mass reached by the avalanche is larger than the mass defined in the calculations following the guidelines. It the ratio between real mass and calculation mass $M_d/M_{r_{SG}}$ is smaller than 1.35, the runout is correctly predicted. In contrast, if the ratio $M_d/M_{r_{SG}}$ is larger than 1.35, the avalanche runout distance cannot be correctly simulated using the Swiss Guidelines (see Table 5.3, $R_1$).

The last (*Case 4*) simulations are performed by increasing the release mass in the practice calculations in order to reach the correct runout distances. The mass increase is obtained by extending the release area, which substantially decreases the ratio $M_d/M_{r_{SG}}$. Table 5.3, in the last column ($R_2$), shows the ratio used to reach the observed runout distances in the *Case 4* simulations.

The comparison between calculated deposition depth and maximum measured deposition depth shows that snow deposition depths reach a realistic value only in the simulations with entrainment (see Fig. 5.22). However, there is still a substantial difference between the average deposition depth calculated with the model and the real maximum deposition depths measured in the field.

In order to improve the calculations suggested by the Swiss Guidelines, it is necessary

**Table 5.3:** *Calibration parameters used for the Case 3 and Case 4 simulations, which follow the Swiss Guidelines used by practitioners. $R_1 = M_d/M_{r_{SG}}$, $R_2=$ correct $M_d/M_{r_{SG}}$*

| | Altitude m a.s.l. | Type | $\mu_1$ | $\xi_1$ | $\lambda$ | $R_1$ | Runout | $R_2$ |
|---|---|---|---|---|---|---|---|---|
| **Loeuewenbach** | 2105-1780 | os | 0.16 | 2500 | 7 | 1.35 | | - |
| | 1780-1520 | c | 0.20 | 1750 | 7 | | | |
| | 1520-1420 | c | 0.25 | 1500 | 7 | | | |
| | 1420-1360 | os | 0.18 | 2000 | 7 | | | |
| **Jungstafel** | 2060-1480 | os | 0.16 | 2500 | 7 | **1.76** | short | 1.35 |
| | 1480-1380 | os | 0.18 | 2000 | 7 | | | |
| **Cheer** | 2078-1500 | os | 0.16 | 2500 | 7 | **2.03** | short | 1.2 |
| | 1500-1360 | os | 0.18 | 2000 | 7 | | | |
| **Cheer-west** | 2183-1940 | os | 0.16 | 2500 | 7 | 1.31 | | - |
| | 1940-1500 | c | 0.20 | 1750 | 7 | | | |
| | 1500-1420 | c | 0.25 | 1500 | 7 | | | |
| | 1420-1360 | os | 0.18 | 2000 | 7 | | | |
| **Aulta** | 2570-2000 | os | 0.16 | 2500 | 7 | 1.30 | | - |
| | 2000-1540 | c | 0.20 | 1750 | 7 | | | |
| | 1540-1560 | os | 0.16 | 2500 | 7 | | | |
| **VDLS** | 2680-1500 | os | 0.16 | 2500 | 7 | **3.00** | short | 1.5 |
| | 1500-1200 | os | 0.18 | 2000 | 7 | | | |

to appropriately choose the initial mass. This was alternatively made by (1) extending the release beyond 500 m on slope angles smaller than 30° or (2) defining an erodible snow cover that was entrained by the avalanche. The second solution is obviously more realistic and is the one that yielded the best results.

As a result, practical calculations can be improved by using a rule for choosing the avalanche mass. A suggestion, based on the practice index analysis presented in Chapter 4, defines the avalanche mass $M$ as the sum of released mass $M_{r_{SG}}$ and entrained mass $M_e$ on the basis of the following relation:

$$M = M_{r_{SG}} + M_e = A_{r_{SG}}d_{SG300}\rho_0 + A_{e_{SG}}d_{e_{SG300}}\rho_e \qquad (5.25)$$

where $\rho_0 = \rho_e = 300$ kg m$^{-3}$ and

$$d_{e_{SG300}} = 0.5 d_{SG300} \qquad (5.26)$$

. The entrainment depth $d_{e_{SG300}}$ is the average entrainment depth measured for six extreme avalanches of the winter 1998/99 as shown in Fig. 4.2. It is important to remember that simulations including entrainment are almost insensitive to up to 30% variations in the release depth and the entrainment depth. This should guarantee that also avalanches with an above-average mass increase are also well represented by the relation 5.26.

In addition, it should be remembered that the introduction of entrainment decreases the friction parameter range, making it easier to choose them reasonably.
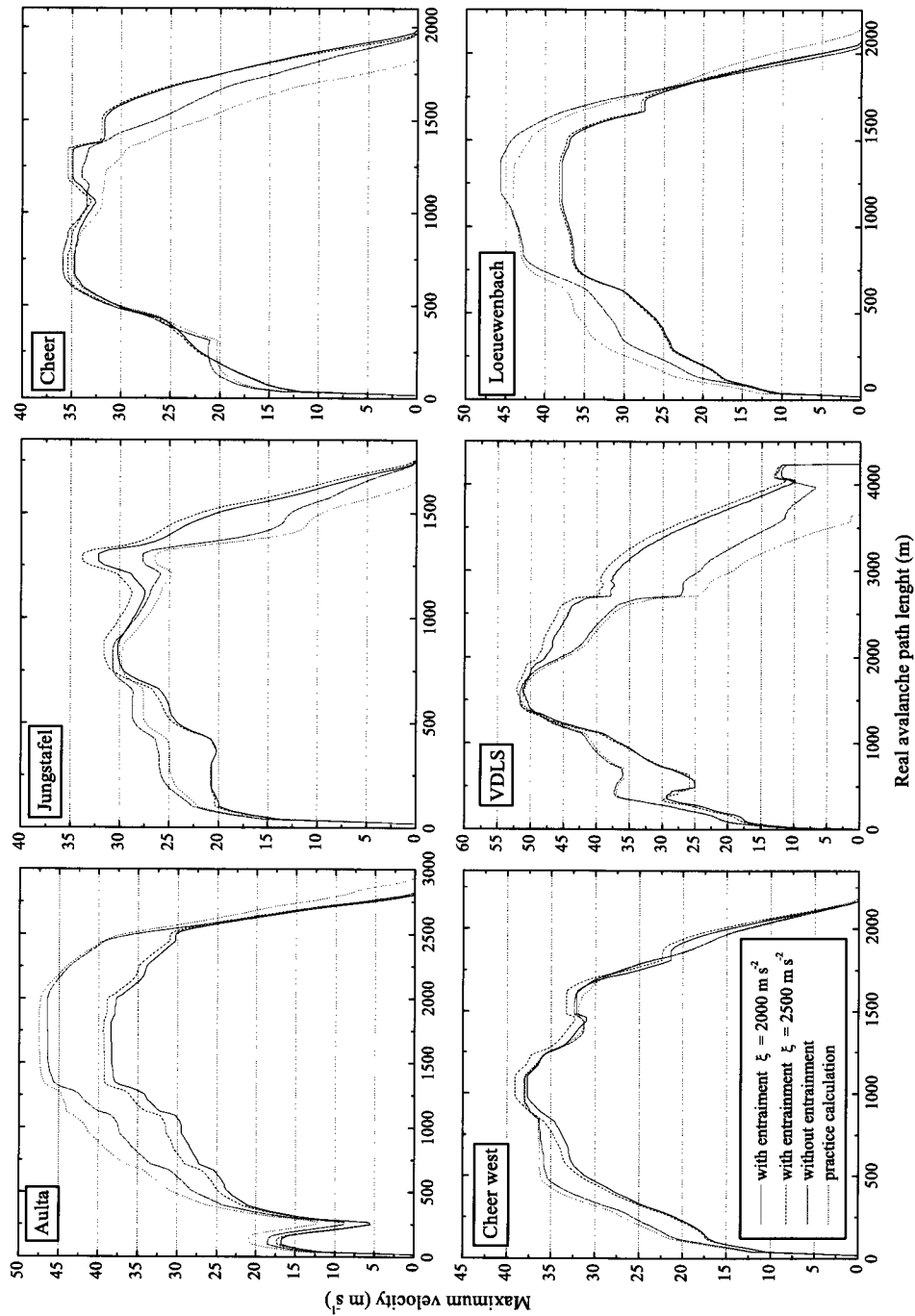
**Figure 5.21:** *Velocities simulated for extreme avalanches of the winter 1998/99 using the Voellmy-fluid model. Simulations with and without entrainment are performed. Calculations are also performed using the recommendations given in the Swiss Guidelines.*

169
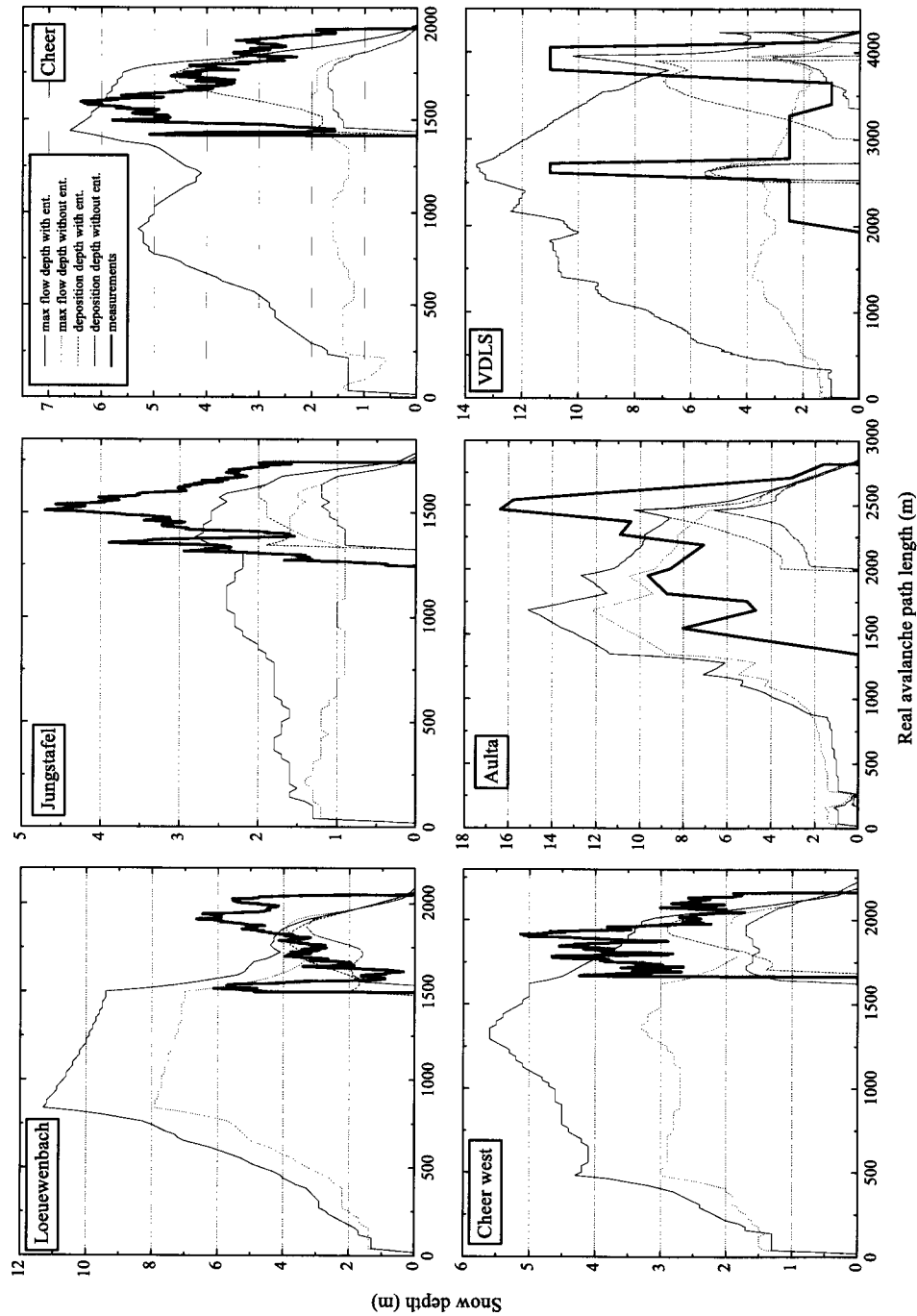
**Figure 5.22:** *Flow and deposition depths simulated for extreme avalanches of the winter 1998/99 using the Voellmy-fluid model. Simulations with and without entrainment are performed. Calculations are also performed using the recommendations given by the Swiss Guidelines. Deposition depths are compared to maximum depths measured in the field.*

170

# 6 Conclusions

The two main goals of this work were: (1) to understand the role of snow entrainment and deposition in snow avalanches and (2) to introduce entrainment and deposition into avalanche dynamics models in order to improve avalanche hazard assessment.

To achieve the first goal, the mass balance of seventeen avalanches of different dimension and characteristics was studied. Avalanche mass indices were defined.

The results show that:

- The avalanches increased their mass on average by a factor 4 through entrainment of snow.

- A maximum mass growth of up to a factor 12 is possible.

These growth values allow us to conclude that entrainment along the avalanche path plays a key role in avalanche dynamics. If the avalanche has the possibility to entrain mass, i.e. there are favorable snow conditions and a large potential entrainment area, the role of the initial conditions (release mass) becomes less important than assumed previously. In this case runout distances, flow depths and pressures are mainly governed by the entrainment process. Thus, a correct physical model for avalanche flow must contain snow entrainment.

The accuracy of the model calculations increases when entrainment is introduced in the models. However, some aspects still should be improved: simulations of small avalanches with entrainment underestimate velocities, and flow depths of large avalanches are sometimes overestimated.

The many simplifications contained in one-dimensional depth-averaged models and the actual constitutive equations that do not capture the real inner processes (mass transfer) in avalanches are the main causes for these problems. Since the nature of internal processes in avalanches is still largely unknown, it is clear that to further improve our capacity to model snow avalanches more experimental investigations concerning the internal avalanche motion in relation to entrainment processes (internal velocity profiles) are required.

# 6. Conclusions

New optical sensors for velocity measurements, capacitance sensors for density measurements and a higher FMCW radar resolution will allow a more precise determination of the avalanche constitutive behavior. With this new knowledge, it will also make sense to develop more complex dynamical models. A first step might be to make models that describe the full three-dimensional flow field. While the determination of the input fields such as snow erodibility for such an approach will become more difficult, the number of free parameters and assumptions will decrease. It is expected that an adequate description of snow entrainment and deposition processes will become even more important for these more realistic models.

Uncertainties in the values of the input parameters are one of the main weaknesses of all dynamical models. The models currently used for practical applications presented in this work are extremely sensitive to the input parameters such as release depth $d_0$ and area $A_r$, and friction parameters $\xi$ and $\mu$. The friction parameters $\xi$ and $\mu$ are clearly not physical but calibration parameters and can not be determined experimentally.

The introduction of entrainment in the models requires additional parameters such as snow cover depth $d_e$ and snow cover strength $p_{lm}$. The entrainment model and its two new parameters not only improves significantly the simulation results but also influences the sensitivity of the results on the parameters.

In particular, variations of up to 30% on release depth $d_0$, entrainment depth $d_e$ and $\xi$ do not produce sensitive variations in model output such as runout distances and speeds. The parameter $\mu$ can be held constant to simulate extremely large avalanches independently from path topography (open slope or channelled avalanches).

In others words, even if the number of parameters increases, the non-measurable parameters can be held constant and the two new parameters are physical values that can be measured. This fact suggests that models including entrainment are much more general.

At present, entrainment is not considered in practical applications. In this work it has been shown that neglecting the correct mass in the calculation leads to the following problems:

1. Runout distances are underestimated when the real avalanche mass is more than 30% larger than the mass defined by the Guidelines calculations (see 5.3.4). This can strongly influence hazard assessment.

2. Flow and deposition depth are in general underestimated. Defense structures such as deflecting and catching dams or gallery roofs cannot, therefore, be correctly dimensioned.

172

Even if entrainment can improve the accuracy of the calculations, the fact remains that model calibration for practical applications requires much experimental data on extreme avalanches. The data contained in this thesis are a unique and important contribution to the field of snow avalanche dynamics and they can be used to define basic guidelines to control errors in avalanche mapping procedures. However, additional and extended information for more events is needed to calibrate entrainment models.

Given the evidence for the importance of the phenomenon presented, avalanche dynamics research can no longer ignore entrainment and deposition processes. In future, research must focus on developing experimental techniques and theoretical models to gain deeper understanding of this phenomenon. However, the results of this dissertation show that entrainment can be introduced into practical hazard mapping calculations.

Seite Leer /
Blank leaf

174

# Notation

| Variable | Definition | Unit |
|---|---|---|
| **A** | | |
| $A$ | cross-sectional avalanche flow area | $m^2$ |
| $A_e$ | potential entrainment area | $m^2$ |
| $A_{e_{SG}}$ | potential entrainment area according to Swiss Guidelines | $m^2$ |
| $A_i$ | particle impact area | $m^2$ |
| $A_c$ | front entrainment control area | $m^2$ |
| $A_r$ | avalanche release area | $m^2$ |
| $A_{r_{SG}}$ | release area according to Swiss Guidelines | $m^2$ |
| $As_d$ | cross-sectional deposition area | $m^2$ |
| $As_e$ | cross-sectional entrainment area | $m^2$ |
| $A_{so}$ | area of the penetrometer tip | $m^2$ |
| $a_n$ | empirical constant | |
| | | |
| **B** | | |
| $b$ | coefficient of dry friction | |
| | | |
| **C** | | |
| $c$ | snow cohesion | kPa, Pa |
| $c_c$ | particle volume concentration | |
| $C_d$ | deposition coefficient | $s^{-1}$ |
| $C_f$ | compression/dilatation factor | |
| $c_f$ | form coefficient | m |
| $c_i$ | empirical constant | m |
| | | |
| **D** | | |
| $D$ | snow particle diameter | m |
| $d_d$ | deposition depth | m |
| $\bar{d}_d$ | average deposition depth in a cross-section | m |
| $d_e$ | entrainment depth | m |
| $\bar{d}_e$ | average entrainment depth in a cross-section | m |
| $d_m$ | depth of the snow layer $m$ | m |
| $d_m*$ | depth of the snow layer $m$ after avalanche passage | m |
| $d_{e_{SG}}$ | average entrainment depth according to Swiss Guidelines | m |

| | | |
|---|---|---|
| $d_{e_{SG300}}$ | Swiss Guidelines average entrainment depth for extreme avalanche | m |
| $ds$ | increment in tip penetration depth | m |
| $dt$ | time interval | s |
| $d_0$ | release fracture depth | m |
| $\bar{d}_0$ | average release fracture depth | m |
| $d_{SG}$ | Swiss Guidelines fracture depth | m |
| $d_{SG300}$ | Swiss Guidelines fracture depth for extreme avalanches | m |

**E**

| | | |
|---|---|---|
| $\dot{E}_c$ | kinetic energy consumption rate | J s$^{-1}$ |
| $E_i$ | impact kinetic energy intensity | J m$^{-2}$ |
| $E_p$ | penetration energy intensity | J m$^{-2}$ |

**F**

| | | |
|---|---|---|
| $F$ | force acting on the system | N |
| $\bar{F}$ | average force acting on the system | N |
| $F_e$ | entrainment friction | |
| $F_f$ | flow friction | |

**G**

| | | |
|---|---|---|
| $g$ | gravitational acceleration | m s$^{-2}$ |

**H**

| | | |
|---|---|---|
| $h$ | avalanche flow height | m |
| $h_P$ | maximum avalanche flow depth at the point $P$ | m |
| $h_0$ | vertical release fracture depth | m |

**I**

| | |
|---|---|
| $I_e$ | entrainment index |
| $I_{e_{SG}}$ | entrainment index according to Swiss Guidelines |
| $I_{e_{SG300}}$ | entrainment index for extreme avalanches according to Swiss Guidelines |
| $I_g$ | growth index |
| $I_{g_{SG}}$ | growth index according to Swiss Guidelines |
| $I_{g_{SG300}}$ | growth index for extreme avalanches according to Swiss Guidelines |
| $I_{pe}$ | potential entrainment index |
| $I_{pe_{SG}}$ | potential entrainment index according to Swiss Guidelines |
| $I_\rho$ | compression index |

**K**

| | | |
|---|---|---|
| $k$ | material constant | |

**L**

| | | |
|---|---|---|
| $L_0$ | avalanche release length | m |
| $L_e$ | avalanche erosion length | m |

**M**

| | | |
|---|---|---|
| $M$ | avalanche mass | kg, t |
| $m$ | shear viscosity | $m^2$ |
| $M_d$ | deposit mass | kg, t |
| $m_d$ | deposit mass between two consecutive sections | kg, t |
| $M_e$ | entrained mass | kg, t |
| $m_e$ | entrained mass between two consecutive sections | kg, t |
| $M_{max}$ | avalanche maximum mass | kg, t |
| $m_p$ | snow particle mass | kg, t |
| $M_r$ | avalanche release mass or initial mass | kg, t |
| $M_{r_{SG}}$ | release mass according to Swiss Guidelines | kg, t |
| $M_{r_{SG300}}$ | release mass for extreme avalanches according to Swiss Guidelines | kg, t |

**N**

| | | |
|---|---|---|
| $n$ | material constant, progressive number | |
| $N$ | noise in the measurements | |

**P**

| | | |
|---|---|---|
| $P$ | point representative of the beginning of the deposition zone | |
| $p_e$ | effective pressure | kPa, Pa |
| $p$ | impact pressure | kPa, Pa |
| $p_i$ | stress exerted by the avalanche on the snow cover | kPa, Pa |
| $p_{lm}$ | strength of the snow layer m | kPa, Pa |
| $P_r$ | return period | years |
| $p_u$ | pore pressure | kPa, Pa |

**Q**

| | | |
|---|---|---|
| $Q$ | depth-averaged discharge, flow rate | $m^3 \, s^{-1}$ |

**R**

| | | |
|---|---|---|
| $rms$ | root mean square error | |

## S

| | | |
|---|---|---|
| $S$ | runout distance | m |
| $s$ | velocity-squared dynamic friction coefficient | kg m$^{-3}$ |
| $sd$ | standard deviation | |
| $\dot{S}_d$ | volumetric snow deposition | m$^2$ s$^{-1}$ |
| $\dot{S}_e$ | volumetric snow entrainment | m$^2$ s$^{-1}$ |

## T

| | | |
|---|---|---|
| $t$ | time | s |

## U

| | | |
|---|---|---|
| $U$ | avalanche velocity | m s$^{-2}$ |
| $U_c$ | avalanche critical velocity | m s$^{-2}$ |
| $u_h$ | velocity at the top surface of the avalanche | m s$^{-2}$ |
| $u_f$ | entrainment front velocity | m s$^{-2}$ |
| $U_P$ | maximum avalanche velocity at the point $P$ | m s$^{-2}$ |
| $u_p$ | particle velocity | m s$^{-2}$ |
| $u_0$ | velocity at the base of the avalanche | m s$^{-2}$ |

## V

| | | |
|---|---|---|
| $V_d$ | deposit volume | m$^3$ |
| $V_r$ | avalanche release volume | m$^3$ |
| $V_{r_{SG}}$ | avalanche release volume according to Swiss Guidelines | m$^3$ |
| $V_{r_{SG300}}$ | avalanche release volume for extreme avalanches according to Swiss Guidelines | m$^3$ |

## W

| | | |
|---|---|---|
| $w_r$ | avalanche release width | m |
| $w$ | avalanche width | m |
| $w_p$ | avalanche width at the point P | m |

## X

| | | |
|---|---|---|
| $x, y, z$ | local coordinate system | m |
| $x', y', z'$ | global coordinate system | m |
| $x_n, z_n$ | grid points coordinates | m |

## Greek

### $\alpha$

| | |
|---|---|
| $\alpha$ | velocity profile factor |

## $\phi$

| | | |
|---|---|---|
| $\phi$ | internal friction angle | |

## $\varphi$

| | | |
|---|---|---|
| $\varphi$ | avalanche path slope angle | |
| $\varphi_p$ | avalanche path slope angle in a control section | |

## $\gamma$

| | | |
|---|---|---|
| $\dot{\gamma}$ | shear deformation rates | $\mathrm{s}^{-1}$ |

## $\lambda$

| | | |
|---|---|---|
| $\lambda$ | active/passive pressure coefficient | |
| $\lambda_a$ | passive pressure coefficient | |
| $\lambda_p$ | active pressure coefficient | |

## $\mu$

| | | |
|---|---|---|
| $\mu$ | model calibration parameter | |

## $\rho$

| | | |
|---|---|---|
| $\rho$ | avalanche core density | $\mathrm{kg\ m}^{-3}$ |
| $\rho_{air}$ | air density | $\mathrm{kg\ m}^{-3}$ |
| $\rho_d$ | deposit density | $\mathrm{kg\ m}^{-3}$ |
| $\bar{\rho}_d$ | average density of the deposited snow | $\mathrm{kg\ m}^{-3}$ |
| $\rho_e$ | entrained snow density | $\mathrm{kg\ m}^{-3}$ |
| $\bar{\rho}_e$ | average density of the entrained snow | $\mathrm{kg\ m}^{-3}$ |
| $\rho_m$ | density of the snow layer $m$ | $\mathrm{kg\ m}^{-3}$ |
| $\rho_m*$ | density of the snow layer $m$ after avalanche passage | $\mathrm{kg\ m}^{-3}$ |
| $\rho_{ice}$ | density of the ice | $\mathrm{kg\ m}^{-3}$ |
| $\rho_p$ | snow particle density | $\mathrm{kg\ m}^{-3}$ |
| $\rho_r$ | release average density | $\mathrm{kg\ m}^{-3}$ |
| $\rho_{sal}$ | saltation layer density | $\mathrm{kg\ m}^{-3}$ |

## $\sigma$

| | | |
|---|---|---|
| $\sigma_x,\ \sigma_y,\ \sigma_z$ | stress components | kPa, Pa |

## $\tau$

| | | |
|---|---|---|
| $\tau_{xz}$ | basal shear resistance | kPa, Pa |
| $\tau_s$ | snow cover shear strength | kPa, Pa |

## $\upsilon$

| | | |
|---|---|---|
| $\upsilon_1,\ \upsilon_2$ | normal stress viscosities | $\mathrm{m}^2$ |

179

| $\boldsymbol{\xi}$ | | |
|---|---|---|
| $\xi$ | model calibration parameter | m s$^{-2}$ |

| $\boldsymbol{\Delta}$ | | |
|---|---|---|
| $\Delta x$ | finite distance | m |
| $\Delta t$ | finite time interval | s |

# Acknowledgements

I would like to express my gratitude to all people who contributed to this work. I am very grateful to Perry Bartelt for the help, discussions and for the correction of this manuscript. Melissa Swartz and Dieter Issler for the English correction and the suggestions to improve my dissertation. Urs Gruber for the help in the elaboration of many experimental data. Marc Christen for the computer science support. Felix Tiefenbacher for the nice time we had during our dissertations, for the interesting discussions, for the many questions he answered in these three years. Dieter Issler and Massimiliano Barbolini for the encouraging suggestions at the beginning of this work and for the stimulating and fundamental discussions. The many people who have helped in the field experiments: all the surveyors of the Avalanche Centre of Arabba, the Alpine Guides and many others. The logistics and electronics staff of the SLF for their technical support in both field and laboratory experiments. The Arpav-Centro Valanghe di Arabba for the permission to use the experimental data of the Pizzac avalanche test site. Jürg Schweizer, Anselmo Cagnati, Stefan Margreth, Bruno Salm and many others to answer all my questions. I am very thankful to Prof. Paolo Burlando who supervised my thesis and Mohamed Naaim being examiner of my PhD thesis. I am also very thankful to Walter Ammann who gave me the opportunity to carry out this work. I would like to thank all the avalanche dynamics team and all the friends who during this period contributed to the pleasant atmosphere at the SLF. In particular Margherita, Sven, Andy, Barbara, Martin, Hans, Felix, Nicola, Jürg and many others. Finally, I want to thank my family and friends. In particular I would like to thank Michi for the discussions, for the good advices and especially for hiss great patience :-)).

# Bibliography

Ackroyd, P. (1987). Erosion by snow avalanches and implication for geomorphic stability, Torlesse range, New Zealand. *Arct. Alp. Res. 19*(1), 65–70.

Ammann, W. (1999). A new Swiss test site for avalanche experiments in the Vallée de la Sionne/Valais. *Cold Reg. Sci. Technol. 30*, 3–11.

Barbolini, M., Gruber, U., Keylock, C., Naaim, M., & Savi, F. (2000). Application of statistical and hydraulic-continuum dense-snow avalanche models to five real European sites. *Cold Reg. Sci. Technol. 31*, 133–149.

Barbolini, M., Issler, D., Sovilla, B., & Sommavilla, F. (1998). Erosion and deposition processes in dense-snow avalanche dynamics. Project proposal, Eidg. Inst. Schnee- und Lawinenforschung, Davos, Switzerland. Unpublished.

Barbolini, M., Natale, L., & Savi, F. (2002). Effects of release conditions uncertainty on avalanche hazard mapping. *Nat. Hazards 25*, 225–244.

Bartelt, P. & Lehning, M. (2002). A physical SNOWPACK model for the Swiss avalanche warning. PART I: numerical model. *Cold Reg. Sci. Technol. 35*, 123–145.

Bartelt, P., Salm, B., & Gruber, U. (1997). Modelling Dense Snow Avalanche Flow as a Criminale-Ericksen-Filbey Fluid without Cohesion. Mitt. 718, Eidg. Inst. Schnee- und Lawinenforschung, Davos, Switzerland.

Bartelt, P., Salm, B., & Gruber, U. (1999). Calculating dense-snow avalanche runout using a Voellmy fluid model with active/passive longitudinal straining. *J. Glaciol. 45*(150), 242–254.

BBF and SLF (1984). *Richtlinien zur Berücksichtigung der Lawinengefahr bei raumwirksamen Tätigkeiten.* Bern, Eidgenössisches Drucksachen- und Materialzentrale: Bundesamt für Forstwesen; Eidgenössisches Institut für Schnee- und Lawinenforschung.

Bell, I., Gardner, J., & Scally, F. D. (1990). An estimate of snow avalanche debris transport, Kaghan Valley, Himalaya, Pakistan. *Arct. Alp. Res. 22*(3), 317–321.

Birkeland, K., Hansen, K., & Brown, R. (1995). The spatial variability of snow resistance on potential avalanche slopes. *J. Glaciol. 41*, 183–190.

Bonnecaze, R., Huppert, H., & Lister, J. (1993). Particle-driven gravity currents. *J. Fluid Mech. 88*, 223–240.

Brugnot, G. & Pochat, R. (1981). Numerical simulation study of avalanches. *J. Glaciol. 27*(95), 77–88.

Brun, E. & Rey, L. (1987). Field study on snow mechanical properties with special regard to liquid water content. In *Avalanche Formation, Movement and Effect*, Volume 162, Symposium at Davos 1986, pp. 183–193. International Association of Hydrological Sciences.

Buser, O. & Frutiger, H. (1980). Observed maximum run-out distance of snow aavalanches and the determination of the friction coefficients $\mu$ and $\xi$. *J. Glaciol. 26*(94), 121–130.

Castelle, T. (1995). *Transport de la neige par le vent en montagne: approche expérimentale du site du Col du Lac Blanc*. Ph. D. thesis, École Polytechnique Fédérale de Lausanne. Thèse 1303, 1994.

Clement (1999). Photogrammetrische Auswertung Lawine Aulta. Technical report, CLEMENT Ingenieure + Geometer AG, Flims-Waldhaus, Switzerland.

Dawes, N. (1999). Project Vallée de la Sionne. Full scale experimentation and development of AVALDAT Radar Data Development and Interpretation Package. Master's thesis, University of Bath, Claverton Down, Bath, England.

Dent, J., Burrell, K., Schmidt, D., Louge, M., Adams, E., & Jazbutis, T. (1998). Density, velocity and friction measurements in a dry snow avalanche. *Annals Glaciol. 26*, 247–252.

Föhn, P. (1989). Snowcover stability tests and the areal variability of snow strength. In *ISSW'88. A merging of theory and practice. Proceedings of the International Snow Science Workshop*, Whistler, B.C., pp. 262–273. Canadian Avalanche Association, Vancouver, B.C.

Förster, M. (1999). Ausführliche Dokumentation ausgewählter Staublawinenereignisse und Bestimmung ihrer Eingangsparameter für die Verifikation von Staublawinenmodellen. Mitt. 730, Eidg. Inst. Schnee- und Lawinenforschung, Davos, Switzerland.

Gardner, J. (1983). Observations on erosion by wet snow avalanches, Mount Rae area, Alberta, Canada. *Arct. Alp. Res. 15*(2), 271–274.

Geldsetzer, T. & Jamieson, B. (2001). Estimating dry snow density from grain form and hand hardness. In *ISSW'2000. International Snow Science Workshop, 2-6 October 2000, Big Sky, Montana. Proceedings*, Bozeman, MT, pp. 121–127. American Avalanche Association.

Grigorian, S. & Ostroumov, A. (200?). Mathematical modelling of snow avalanches movement. In *Proceeding of the Symposium: 60 Years of Snow and Avalanche Research at Davos*, Davos, Switzerland. Eidgenössisches Institut für Schnee und Lawinenforschung.

Grigoryan, S., Eglit, M., & Yakimov, Y. (1967). A new formulation and solution of the problem of the motion of snow avalanches. *Trudy Vycokogornogo Geofizicheskogo Instituta 12*, 104–113. In Russian.

Gruber, U. (1998). *Der Einsatz numerischer Simulationsmethoden in der Lawinengefahrenkartierung.* Ph. D. thesis, University of Zurich.

Gruber, U. & Bartelt, P. (2001). Study of the 1999 avalanches in the Obergoms valley, Switzerland, with respect to avalanche hazard mapping. In *ISSW'2000. International Snow Science Workshop, 2-6 October 2000, Big Sky, Montana. Proceedings*, Bozeman, MT, pp. 495–500. American Avalanche Association.

Gruber, U., Dufour, F., Issler, D., Schaer, M., Dawes, N., Hiller, M., Stöckli, V., Tiefenbacher, F., & Sovilla, B. (2002). Final report of the avalanche winter 1998/1999 at the Vallée de la Sionne avalanche test site. Technical report, Eidg. Inst. Schnee-und Lawinenforsch. Not published.

Gubler, H. (1987). Measurements and modelling of snow avalanches speeds. In *Avalanche Formation, Movement and Effect*, Volume 162, Symposium at Davos 1986, pp. 405–420. International Association of Hydrological Sciences.

Gubler, H. & Hiller, M. (1984). The use of microwave FMCW radar in snow and avalanche research. *Cold Reg. Sci. Technol. 9*, 109–119.

Harbitz, C. (1998). A survey of computational models for snow avalanche motion. NGI Report 581220-1, Norwegian Geotechnical Institute, Oslo.

Harbitz, C., Issler, D., & Keylock, C. (1998). Conclusions from a recent survey of avalanche computational models. In E. Hestnes (Ed.), *25 Years of Snow Avalanche Research, Voss, 12–16 May 1998. Proceedings*, Volume 203 of *NGI Pubblication*, Oslo, pp. 128–139. Norwegian Geotechnical Institute.

Hungr, O. (1995). A model for the runout analysis of rapid flow slides, debris flow, and avalanches. *Canadian Geotechnical Journal 32*, 610–623.

Issler, D. (1999). European avalanche test sites. Overview and analysis in view of co-ordinated experiments. Mitt. 59, Eidg. Inst. Schnee- und Lawinenforschung, Davos, Switzerland.

Issler, D. (2003). Experimental information on the dynamics of dry-snow avalanches. In K. Hutter & N. Kirchner (Eds.), *Deformations and Failure in Granular and Porous Continua*, pp. in press. Berlin, Germany: Springer.

Issler, D., Gauer, P., Schaer, M., & Keller, S. (1996). Staublawinenereignisse im Winter 1995: Seewis (GR), Adelboden (BE) und Col du Pillon (VD). Mitt. 694, Eidg. Inst. Schnee- und Lawinenforschung, Davos, Switzerland.

Jamieson, B. & Johnston, C. (2001). Evaluation of the shear frame test for weak snowpack layers. *Annals Glaciol. 32*, 59–69.

Koelbl, O. (1991). Détermination photogrammétrique de l'épaisseur de neige lors de descentes d'avalanches. Publ. interne epfl-iphit, EPFL.

Kraus, K. & Waldhäusl, P. (1998). *Manuel de photogrammétrie. Principes et procédés fondamentaux* (Paris, Hermés ed.).

Kumar, A. (1994). Continuum approach to avalanche dynamics. In *Int. Symp. on Snow and Related Manifestations*, Snow and Avalanche Studies Enstablishment, Manali, India. Extended abstract.

Lauber, G. (1999). 17° Winterbericht 1998/99. Technical report, Lawinenwarndienst der Region Obergoms, CH-3981 Geschinen. 1999 report of the local avalanche security service.

Lehning, M., Bartelt, P., Brown, B., Fierz, C., & Satyawali, P. (2002a). A physical SNOWPACK model for the Swiss avalanche warning. PART II: Snow microstructure. *Cold Reg. Sci. Technol. 35*, 147–167.

Lehning, M., Bartelt, P., Brown, B., Fierz, C., & Satyawali, P. (2002b). A physical SNOWPACK model for the swiss avalanche warning. PART III: meteorological forcing, thin layer formation and evaluation. *Cold Reg. Sci. Technol. 35*, 169–184.

Louge, M., Steiner, R., Keast, S., Decker, R., Dent, J., & Schneebeli, M. (1997). Application of capacitance instrumentation to the measurement of density and velocity of flowing snow. *Cold Reg. Sci. Technol. 25*(1), 47–63.

Maeno, N. & Nishimura, K. (1987). Numerical computation of snow avalanche motion in a three-dimensional topography. *Low Temperature Science 46*, 99–110.

McClung, D. (1990). A model for scaling avalanche speeds. *J. Glaciol. 36*(123), 188–198.

McClung, D. & Schaerer, P. (1993). *The Avalanche Handbook* (The Mountaineers ed.). Seattle, WA.

Nishimura, K. & Maeno, N. (1989). Contribution of viscous forces to avalanche dynamics. *Annals Glaciol. 13*, 202–206.

Norem, H., Irgens, F., & Schieldrop, B. (1989). Simulation of snow-avalanche flow in run-out zones. *Annals Glaciol. 13*, 218–225.

Ostroumov (1972). *A model of the motion of snow avalanches of chute type*. Ph. D. thesis, Moscow University.

Perla, R., Beck, T., & Cheng, T. (1982). The shear strength index of alpine snow. *Cold Reg. Sci. Technol. 6*(1), 11–20.

Perla, R., Cheng, T., & McClung, D. (1980). A two-parameter model of snow-avalanche motion. *J. Glaciol. 26*(94), 197–207.

Pielmeier, C. & Schneebeli, M. (2002). Snow stratigraphy measured by snow hardness and compared to surface section images. In J. Stevens (Ed.), *ISSW'02. A merging of theory and practice. Proceedings of the International Snow Science Workshop 29 September–4 October 2002*, Penticton, B.C., pp. 345–352.

Rice, M., McEwan, I., & Mullins, C. (1999). A conceptual model of wind erosion of soil surfaces by saltating particles. *Earth Surf. Processes Landforms 24*, 383–392.

Salm, B. (1993). Flow, flow transition and runout distances of flowing avalanches. *Annals Glaciol 18*, 221–226.

Salm, B., Burkard, A., & Gubler, H. (1990). Berechnung von Fliesslawinen: eine Anleitung für Praktiker mit Beispielen. Mitt. 47, Eidg. Inst. Schnee- und Lawinenvorschung, Davos, Switzerland.

Sartoris, G. & Bartelt, P. (2000). Upwinded finite difference schemes for dense snow avalanche modeling. *Int. J. Num. 32*, 799–821.

Savage, S. B. & Hutter, K. (1989). The motion of a finite mass of granular material down a rough incline. *J. Fluid Mech. 199*, 177–215.

Savage, S. B. & Hutter, K. (1991). The dynamics of avalanches of granular materials from initiation to run-out. Part I. Analysis. *Acta Mech. 86*(1-4), 201–223.

Schaer, M. & Issler, D. (2001). Particle densities, velocities and size distribution in large avalanches from impact-sensor measurements. *Annals Glaciol. 32*, 321–327.

Schaerer, P. & Salway, A. (1980). Seismic and impact-pressure monitoring of flowing avalanches. *J. Glaciol. 26*(94), 179–187.

Schneebeli, M., Pielmeier, C., & Johnson, J. (1999). Measuring snow microstructure and hardness using a high resolution penetrometer. *Cold Reg. Sci. Technol. 30*, 101–114.

Schweizer, J. (1999). Review of dry snow slab avalanche release. *Cold Reg. Sci. Technol. 30*(1-3), 43–57.

Schweizer, J., Jamieson, J., & Schneebeli, M. (2003). Snow avalanche formation. *Rev. Geophys. 41*(4), 1–25.

Simpson, J. (1997). *Gravity currents in the environment and the laboratory.* Number ISBN 0-521-66401-2. Cambrige, U.K.: Cambridge University Press.

SLF (1951). Winterbericht 1951. Technical Report 15, Eidg. Inst. Schnee- und Lawinenforschung, Davos, Switzerland.

SLF (1999). *Neue Berechnungsmethoden in der Lawinengefahrenkartierung.* Davos, Switzerland: Eidg. Inst. Schnee- und Lawinenforschung.

SLF (2000). *Der Lawinenwinter 1999. Ereignisanalyse.* Davos, Switzerland: Eidg. Inst. Schnee- und Lawinenforschung.

Sommavilla, F. & Sovilla, B. (1998). The avalanche monitoring system of Mount Pizzac. In E. Hestnes (Ed.), *25 Years of Snow Avalanche Research, Voss, 12-16 May 1998. Proceedings*, Volume 203 of *NGI Pubblication*, Oslo, pp. 268–273. Norwegian Geotechnical Institute.

Sommavilla, F., Sovilla, B., & Tomaselli, A. (1997). Il sistema di monitoraggio per l'acquisizione dei parametri dinamici delle valanghe. *Neve e Valanghe 31*, 6–17.

Sovilla, B. & Bartelt, P. (2002). Observations and modelling of snow avalanche entrainment. *Nat. Hazards. 2*, 169–179.

Sovilla, B., Sommavilla, F., & Tomaselli, A. (2001). Measurements of mass balance in dense snow avalanche events. *Annals Glaciol. 32*, 230–236.

Suriñach, E., Furdada, G., Sabot, F., Biescas, B., & Vilaplana, J. (2001). On the characterization of seismic signals generated by snow avalanches for monitoring purposes. *Annals Glaciol. 32*, 268–274.

Tiefenbacher, F. (2003). *Vom konstitutiven Verhalten fliessenden Schnees.* Ph. D. thesis, Universität Basel.

Tiefenbacher, F. & Kern, M. A. (2003). Experimental devices to determine snow avalanche basal friction and velocity profiles. *Cold Reg. Sci. Technol.*. In press.

Turnbull, B. & Bartelt, P. (2003). Mass balance of a mixed flowing-powder snow avalanche. *Surveys in Geophysics*. Under review.

Unesco (1981). *Avalanche Atlas. Illustrated International Avalanche Classification.* Paris: UNESCO.

Vallet, J. (2002). *Saisie de la couverture neigeuse de sites avalancheux par des techniques aéroportées.* Ph. D. thesis, École Polytechnique Fédérale de Lausanne.

Vallet, J., Gruber, U., & Dufour, F. (2001). Photogrammetric avalanche volume measurements at Vallée de la Sionne. *Annals Glaciol. 32*, 141–146.

Voellmy, A. (1955). Über die Zerstörungskraft von Lawinen (On the destructive forces of avalanches). *Schweiz. Bauztg.* *73*(12/15/17/19), 159–162, 212–217, 246–249, 280–285.

Wilhelm, C., Bründl, M., Wiesinger, T., & Ammann, W. (2001). The avalanche winter 1999 in Switzerland–An overview. In *ISSW'2000. International Snow Science Workshop, 2–6 October 2000, Big Sky, Montana. Proceedings*, Bozeman, MT, pp. 487–494. American Avalanche Association.

# Curriculum Vitae

| | | |
|---|---|---|
| *Name:* | | Betty Sovilla |
| *Date of birth:* | | 14 January 1967 |
| *Place of birth:* | | Belluno, Italy |
| *Citizenship:* | | Italian |

| | | |
|---|---|---|
| **Education** | -1995 | Civil Engineer, spec. hydraulics. University of Padova, Italy. Professional qualification, University of Padova. |
| **Professional experience** | 1995 | Professional and scientific collaborator at the ENEL (National Electric Power Corporation) CRIS of Mestre, Hydraulics Research Centre. Project: Hydrological analysis of the Piave river. Determination of water deficit in relation to electricity and irrigation usage. |
| | 1996-1999 | Professional and scientific collaborator at the Avalanche Centre of Arabba, Veneto Region, Italy. Research project concerning avalanche dynamics and avalanche defence structures, collaboration in European projects. |
| | 2000-2004 | PhD student at the Swiss Federal Institute for Snow and Avalanche Research, Davos and at ETH Zurich, Department of Civil, Environmental and Geodetic Engineering. Institute of Hydromechanics and Water Resources Management. |
| | 2003-present | Scientific collaborator at the Eidg. Institut für Schnee und Lawinenforschung SLF, Davos, Switzerland. Scientific supervisor of the Vallèe de la Sionne project. |

| | | |
|---|---|---|
| **Teaching** | 1997 - present | AINEVA courses, Italy. Lectures on: a) avalanche dynamics and numerical simulation, b) snow mechanical properties, c) avalanche classification and d) snow-meteorological data analysis. Different Workshop and seminar concerning snow and avalanches. |
| **Awards during Phd** | | Award for the best presentation at the conference of the International Glaciological Society (IGS) 2000, INNS-BRUCK (A). Award for the best presentation at the International PhD meeting in the field of Natural Hazard 2001, Zürich (CH). |